

**KWAME NKRUMAH UNIVERSITY OF SCIENCE AND TECHNOLOGY,
KUMASI, GHANA**

**DROUGHT-HEATWAVES' DYNAMICS WITH LAND USE LAND COVER
TYPES UNDER THE WEST AFRICAN MONSOON SYSTEM**

By

DAKÉGA SABERMA RAGATOA

(B.Sc. Geography, M.Tech. Climate change and Adapted Land Use)

A Thesis submitted to the Department of Civil Engineering,

College of Engineering

in partial fulfilment of the requirements for the degree of

DOCTOR OF PHILOSOPHY

in

Climate Change and Land Use

August 2023

CERTIFICATION

I hereby declare that this submission is my own work towards the PhD in Climate Change and Land Use and that, to the best of my knowledge, it contains no material previously published by another person, nor material which has been accepted for the award of any other degree or diploma at Kwame Nkrumah University of Science and Technology, Kumasi or any educational institution, except where due acknowledgement has been made in the thesis.

Dakéga Saberma RAGATOA (PG PG9990219)
Student Name & ID Signature Date

Certified by:
Prof. Leonard K. AMEKUDZI
Supervisor(s) Signature Date

Certified by:
Prof. Dr. Andreas H. FINK
Supervisor(s) Signature Date

Certified by:
Prof. Kodjovi I. EDJAME
Supervisor(s) Signature Date

Certified by:
Prof. Kehinde O. OGUNJOBI
Supervisor(s) Signature Date

Certified by:
Prof. Samson ODURO-KWARTENG
Head of Department's Name Signature Date

DEDICATION

This work is dedicated to my beloved wife, Chantal K. M. Ragatoa (Born Tetevi),

my father, Mr Dyana Fetaba Ragatoa,

my mother Pascaline K. Ragatoa (Born Sakpala – of blessed memory),

and my sisters and brothers

.....

ABSTRACT

Heatwaves are prolonged periods of abnormal heat that can adversely impact human and animal well-being, public infrastructure, agriculture, wildfire occurrence and severity, and workplace efficiency. With increasing global warming, heatwaves and droughts are predicted to worsen. However, there are only a few documented cases of heatwaves in Africa, and less research in West Africa has explored the thermodynamics of heatwaves in the region. This study seeks to comprehensively investigate the dynamics of heatwaves, particularly their interaction with land-atmosphere processes and droughts as compound events in three climate zones in West Africa. The research compares heatwave and heat-stress occurrences and their coincidental intensity with drought, using satellite, reanalysis, and in-situ datasets from 1981 to 2020. The study uses Cumulative Heat (CumHeat or Heat_{cum}) and Universal Thermal Climate Index (UTCI) to measure heatwaves, Standardized Precipitation (Evapotranspiration) Index (SPI or SPEI) for drought, and Normalized CumHeat for temperature (T_{\max} and T_{\min}), UTCI, and Wet-Bulb Globe Temperature (WBGT) to examine heatwave dynamics. The study employs the ECMWF Year of Polar Prediction (YOPP) dataset to determine the main temperature advection and tendency terms that contribute to heatwaves in selected cases (2018, 2019, and 2020) covering different climate zones, from 1000 hPa, 925 hPa, to 850 hPa, and 700 hPa. The study also uses validated coupled RegCM-CLM simulation outputs initialized with soil moisture to compute SPEI and the normalized heatwave indices. The Drought-heatwave (D-HW) events from observational data showed lower frequency and intensity than the gridded dataset. The West African monsoon system is experiencing an increase in the intensity and duration of UTCI and T_{\max} heatwaves, mainly before or after the monsoon phase, with some occurrences during the monsoon phase. An increasing trend in the intensity and duration of heatwaves, up to 40 days, has been observed in the gridded dataset, and there is a higher likelihood of WBGT occurrence during the night. The study found that the differences in heatwave indices are primarily due to the sensitivity to moisture and wind. The intensity of heatwaves exhibits asymmetric statistical responses to moisture content deficits, particularly in the Guinea zone and some parts of Sudan (Coast of Senegal). In the Eastern part of West Africa, the opposite reaction to mid-latitudes is observed, where there is an increase in moisture before and during a high heatwave. The impact of soil moisture on heatwaves extends to the 6th level (8th level) about 0.492912 m (1.38283 m) into the soil. These findings could help improve weather forecasting, predict the impacts of heatwaves, and design adaptation strategies to reduce the vulnerability of populations to heatwaves. Additionally, the results contribute to developing more accurate and robust climate models that can better simulate the behaviour of heatwaves and their interactions with other climate variables.

TABLE OF CONTENT

| | |
|---|--------------|
| CERTIFICATION..... | ii |
| DEDICATION..... | iii |
| ABSTRACT..... | iv |
| TABLE OF CONTENT..... | v |
| LIST OF TABLES..... | x |
| LIST OF FIGURES..... | xii |
| LIST OF ABBREVIATIONS AND ACRONYMS..... | xxiii |
| ACKNOWLEDGEMENT..... | xxvi |
| CHAPTER 1: GENERAL INTRODUCTION..... | 1 |
| 1.1 Background..... | 1 |
| 1.2 Motivation of the Study (Rational)..... | 6 |
| 1.3 Problem Statement and Justification..... | 9 |
| 1.4 Aim and Objectives..... | 12 |
| 1.5 Research Questions..... | 12 |
| 1.6 Scope of the Study..... | 13 |
| 1.7 Organization of the Chapters..... | 13 |
| CHAPTER 2: LITERATURE REVIEW..... | 15 |
| 2.1 Overview of the Key Concepts..... | 15 |
| 2.2 Global Warming and Temperature Extremes..... | 28 |
| 2.2.1 Temperature Extremes and Land Feedback..... | 38 |

| | |
|---|-----------|
| 2.2.2 Recent Advancements in Africa and Specifically in West Africa..... | 48 |
| CHAPTER 3: METHODOLOGY..... | 57 |
| 3.1 Description of Study Area and Datasets..... | 57 |
| 3.1.1 Study Area..... | 57 |
| 3.1.2 Observation datasets..... | 58 |
| 3.1.3 ERA5 Pressure Levels and SST Dataset..... | 60 |
| 3.1.4 ERA5-Land Hourly Dataset..... | 61 |
| 3.1.5 Year of Polar Prediction (YOPP — Temperature tendency)..... | 62 |
| 3.1.6 Various Sources of Gridded Datasets..... | 65 |
| 3.2 Research Methodology..... | 66 |
| 3.2.1 Spatio-temporal Drifts patterns of Drought-Heatwave with the West African Monsoon..... | 66 |
| 3.2.1.1 Definitions and Characteristics of Drought indices..... | 66 |
| 3.2.1.2 Definition of heatwave and heat-stress indices..... | 68 |
| 3.2.1.2.1 The Universal Thermal Comfort index (UTCI)..... | 68 |
| 3.2.1.2.2 Cumulative Excess Heat (CumHeat)..... | 70 |
| 3.2.1.3 Statistical Analysis..... | 75 |
| 3.2.1.4 Combined Analysis of Drought and Heatwave..... | 76 |
| 3.2.2 Synoptic and Boundary layer scale Dynamics responsible for Heatwave in West Africa..... | 77 |
| 3.2.2.1 The Wet-Bulb Globe Temperature (WBGT)..... | 77 |
| 3.2.2.2 Recall of UTCI and CumHeat methods..... | 78 |
| 3.2.2.3 Temperature tendency..... | 78 |
| 3.2.2.4 Statistical Analysis..... | 81 |
| 3.2.3 Land Atmosphere Moisture (Energy) Fluxes in Different LULC Types.. | 83 |
| 3.2.3.1 The Regional Climate Model (RCM) Simulation..... | 84 |
| 3.2.3.2 Heatwave indices comparison over West Africa..... | 89 |
| 3.2.3.3 Moisture (Energy) fluxes in the different LULCT during Selected Heatwaves..... | 90 |
| 3.2.4 Summary of methodology..... | 91 |

CHAPTER 4: SPATIO-TEMPORAL DRIFTS OF DROUGHTS AND HEATWAVES WITH THE WEST AFRICAN MONSOON.....93

4.1 Introduction.....93

4.2 Analysis of Drought Indices Occurrence in West Africa: Insights and Trends 94

4.3 Cumulative Heatwaves Analysis considering UTCI and Tmax.....104

4.4 Analysing the Joint Occurrence of Drought and Heatwaves (D-HW): An Integrated Approach of Compound event in West Africa.....113

4.4.1 Concurrent D-HW at 3-month scale (SPI/SPEI and CumHeat Tmax/UTCI).....114

4.4.2 Concurrent D-HW at 6- and 12-month scale (SPI/SPEI and CumHeat Tmax/UTCI).....118

4.5 Discussion.....122

4.6 Summary.....126

CHAPTER 5: SYNOPTIC AND BOUNDARY LAYER SCALE DYNAMICS RESPONSIBLE FOR HEATWAVES IN WEST AFRICA.....128

5.1 Introduction.....128

5.2 Evaluation of Regional Heatwaves.....130

5.3 Thermodynamics during Selected Heatwave Case Studies over West Africa136

5.3.1 Principal Component Analysis (PCA): Dimensionality reduction of the variables and Pattern Detection.....138

5.3.2 Temperature tendency and temperature advection analysis: Trends and Patterns before, during and after Regional heatwaves.....144

5.3.3 The Vertical Profile of tendency terms and advections.....155

5.4 Discussion.....159

5.5 Summary.....165

| | |
|--|------------|
| CHAPTER 6: LAND-ATMOSPHERE MOISTURE (ENERGY) INTERACTION IN DIFFERENT LAND-USE AND LAND COVER TYPES DURING HEATWAVES..... | 167 |
| 6.1 Introduction..... | 167 |
| 6.2 Coupled RegCM-CLM Sensitivity analysis of Regional Heatwaves..... | 169 |
| 6.2.1 Regional heatwaves in West Africa..... | 169 |
| 6.2.2 Model sensitivity..... | 172 |
| 6.3 The Moisture role during Selected Heatwave cases over West Africa..... | 177 |
| 6.3.1 Surface Soil moisture with Temperature CumHeat..... | 177 |
| | 180 |
| 6.3.2 Surface Soil moisture with UTCI CumHeat..... | 180 |
| | 182 |
| 6.3.3 Surface Soil moisture with the WBGT CumHeat..... | 182 |
| 6.3.4 Normalised Temperature CumHeat Correlation with Soil Moisture Content (SMC) at different levels..... | 184 |
| 6.3.4.1 Normalised UTCI Correlation with Soil moisture Content (SMC) at different levels..... | 188 |
| 6.3.4.2 Normalised WBGT Correlation with Soil moisture Content (SMC) at different levels..... | 189 |
| 6.3.5 Moisture Advection during Heatwaves in West Africa..... | 192 |
| 6.4 Discussion..... | 199 |
| 6.5 Summary..... | 205 |
| CHAPTER 7: CONCLUSIONS AND RECOMMENDATIONS..... | 207 |
| 7.1 Introduction..... | 207 |
| 7.2 Conclusion and Summary of Key Findings..... | 208 |
| 7.2.1 What are the patterns of drought-heatwaves under the WAM?..... | 209 |
| 7.2.2 How well do synoptic and boundary layer scale temperature components explain heatwaves' dynamics in West Africa?..... | 210 |

| | |
|--|------------|
| 7.2.3 How sensitive is the coupled Regional Climate Model with a Land Model (RegCM-CLM) to heatwaves with moisture role in the different LULC types? | 211 |
| 7.3 Limitations of the Research Work | 213 |
| 7.4 Key Messages | 214 |
| 7.5 Recommendations | 216 |
| 7.5.1 Future Research | 216 |
| 7.5.2 Policy Actions | 218 |
| 7.6 Final Thoughts | 220 |
| REFERENCES | 222 |
| APPENDIXES | 249 |

LIST OF TABLES

| | |
|---|-----|
| Table 2.1. A concise summary of the various forms of compound extremes and the statistical methods utilised to analyse them: Adapted from Hao et al., (2018)..... | 18 |
| Table 3.1: Temperature Tendency terms and description..... | 64 |
| Table 3.2: Indices classification categories: a) SPI, SPEI severity index and levels; b) CumHeat index and levels of intensity adapted from Zittis et al.' HWMIId classification (Zittis et al., 2021) and c) UTCI conventional stress levels..... | 71 |
| Table 3.3: Description of the computed Indices with their input parameters, equations and references. For SPI ; $c_0= 2.515517$, $c_1 = 0.802853$, $c_2 = 0.010328$; $d_1 = 1.432788$, $d_2 = 0.189269$, $d_3 = 0.001308$. For SPEI , $c_0 = 2.515517$, $c_1 = 0.802853$, $c_2 = 0.010328$; $d_1 = 1.432788$, $d_2 = 0.189269$, $d_3 = 0.001308$. CumHeat: T_{anom} is the temperature anomaly relative to the 90 th percentile calendar-day on a given heatwave day..... | 73 |
| Table 3.4: Coupled RegCM-CLM set-up, parametrization, and data used..... | 88 |
| Table 4.1: Drought (SPI and SPEI) Mann Kendall decadal trends test for all climate zones (part 1); Bolded results are the statistically significant trends in the series. Here only the slope and the significance of the test are shown. The other results do not necessarily mean there is no trend, but indicates that the evidence is not sufficient to conclude with a 5% level of confidence that a trend exists. The dataset represent Tmax or UTCI for gridded dataset (grd) and observation dataset (obs)..... | 102 |
| Table 4.2: Drought (SPI and SPEI) Mann Kendall decadal trends test for all climate zones (part 2). Read as in Table 4.1..... | 103 |
| Table 4.3: Gridded and observation UTCI correlation and variances per zone. This table shows how good the gridded datasets represent the events in the observed dataset..... | 105 |

| | |
|---|-----|
| Table 4.4: Description of Gridded (grd) and Station (obs) UTCI. The table presents the variable and zones. There is also the mean, the available complete percentage data in the series (complete), the standard deviation (sd), the percentiles (p0 to p100) and a graphical distribution of the dataset (Dist., blue for the Guinea zone; red for the Sudan and black for the Sahel). The distribution (Dist.) is binned with the 20 percentiles range giving 5 bar-plots showing the distribution of the data..... | 105 |
| Table 4.5: CumHeat (Tmax and UTCI) Mann Kendall trend test. Bold results are the statistically significant trends in the series. Here only the slope and the significance of the test are shown. The other results do not necessarily mean there is no trend, but indicates that the evidence is not sufficient to conclude with a 5% level of confidence that a trend exists. The dataset represent Tmax/UTCI for gridded dataset (xxx.grd) and observation dataset (xxx.obs)..... | 110 |
| Table 5.1: Table Presenting the Heatwave Occurrence in the Case Study periods and for all the heatwave indices..... | 138 |
| Table 6.1: Soil layer levels and their depth from the Model Simulation (see Figure 6.13)..... | 185 |
| Table B1: Mean Frequency and Trend of heatwave (Heat stress) in West Africa. Presented per index and climate zones..... | 260 |
| Table B2: Mean Contribution of the temperature tendencies in the selected case studies (2018, 2019 and 2020) for each climate zone. Here are presented only the top 3 contributors irrespective of the model pressure levels..... | 261 |

LIST OF FIGURES

| | |
|--|----|
| Figure 3.1: Study Area covering the agroclimatic zones (Guinea, Sudan and Sahel) | 58 |
| Figure 3.2: Overview of West Africa showing ISD (stars) and GSOD (rounded dots) selected stations in the climate zones (colour-shaded); Climate zones are adapted from Earth Resources Observation and Science (EROS) Centre’s Climate zones distribution..... | 60 |
| Figure 3.3: Statistical reporting template using results from Welch’s t-test. At the top of each plot is the statistical report; (Patil, 2021)..... | 76 |
| Figure 3.4: Grid location in the model domain with model elevation at 20 km resolution. The rectangular strips in the plot represent the different climate zones. From bottom to top are the Guinea zone, the Sudan and the Sahel..... | 87 |
| Figure 3.5: Flowchart of research methodology..... | 92 |
| Figure 4.1: Drought indices: SPI and SPEI comparison at 3- (a, b, c), 6- (d, e, f) and 12- (g, h, i) month scales from gridded (xxx.grd) and observation (xxx.obs) data in the climatic zones. Combined violin and box plots with mean as centrality (red dot with tagged value); outliers (black dots) are tagged to the station name and data distribution. The statistical report for Kruskal–Wallis one-way ANOVA test for between group comparison is at the top of each plot. Only significant correlations have a p-value (Bonferroni corrected p-value)..... | 96 |
| Figure 4.2: Correlation plot between observation and gridded datasets drought indices per zone: (a) the Guinea zone, (b) the Sudan and (c) the Sahel zone. (d) is the overall correlation of all considered stations in West Africa. The cross over some correlation values show non-significant (at $\alpha = 0.05$) correlations..... | 97 |
| Figure 4.3: Drought trend in the climatic zones at 3-, 6- and 12-month for Gridded (.grid) and Observation (.obs) datasets. Yearly aggregated time series in dotted line for the Guinea zone in blue, red for the Sudan and black for the Sahel. The overlay corresponding colour lines are the linear trend for each zone. The full lines are the | |

corresponding smoothed non-linear trends. The transparent grey area is the 95% confidence interval of the trends. The values at the top are the trend's significance (p-value). Their colours are relative to their trend lines.....100

Figure 4.4: Compared occurrence proportion of Cumulative heat (CumHeat) for Tmax in the down panel and UTCI in the upper panel in the 3 climatic zones.....106

Figure 4.5: Seasonal Maximum values of Cumulative (excess) Heat (CumHeat) trends for all datasets (xxx.grd: gridded and xxx.obs Observation) and zones. Lines are the linear trends and dotted fine lines are the maximum values of the CumHeat. The blue line is the trend for Guinea zone, the red for the Sudan and the black for the Sahel. The transparent grey area is the 95% confidence interval of the trends The values at the top are: P = the statistical significance (p-value) of the trend. The colours are relative to their trend lines. The Labels are some stations that have more than 16 CumHeat values.....108

Figure 4.6: Seasonal Maximum values of Cumulative (excess) Heat (CumHeat) Duration trends for all datasets (xxx.grd: gridded and xxx.obs Observation) and zones. Lines are the linear trends and dotted fine lines are the maximum values of the CumHeat. The blue line is the trend for Guinea zone, the red for the Sudan and the black for the Sahel. The transparent grey area is the 95% confidence interval of the trends The values at the top are the trend results: $Y = \text{intercept} + \text{slope} \cdot X$. P gives the statistical significance (p-value) of the trend. The colours are relative to their trend lines. The labels are some stations that have more than 5 days.....109

Figure 4.7: Comparison of Annual maximum T_{\max} CumHeat in different climate zones; Gridded (A) and observation (B) datasets. The colours represent the different season of occurrence of each of the heatwave over the years. The colours of the dots shows the different occurrence seasons (Dry seas. is DJF, pre-mons. is MAM, JJA is considered the Monsoon season and SON the Post-mons.....111

Figure 4.8: Comparison of Annual maximum UTCI CumHeat in different climate zones; Read as in Figure 4.7.....113

| | |
|---|-----|
| Figure 4.9: Tmax CumHeat gridded D-HW at 3-month scale in West Africa from 1981 to 2020 : a) D-HW Occurrence over time with their levels of intensity/severity (the colours represent SPI and the bubble size are SPEI severity); b) is the frequency of occurrence over the years in the different climate zones (green is the Guinea, yellow is the Sudan and red is the Sahel zone). The trends equations are read as in Figure 4 (P gives the statistical significance (p-value) of the trend)..... | 115 |
| Figure 4.10: Tmax CumHeat observed D-HW at 3-month scale in West Africa from 1981 to 2020 : Read as in Figure 4.9..... | 116 |
| Figure 4.11: UTCI CumHeat observed D-HW at 3-month scale in West Africa from 1981 to 2020 : Read as in Figure 4.9..... | 117 |
| Figure 4.12: UTCI CumHeat gridded D-HW at 3-month scale in West Africa from 1981 to 2020 : Read as in Figure 4.9..... | 118 |
| Figure 4.13: D-HW frequency occurrence at 6-month scale in the different dataset at different the considered seasons. Colours represent the climate zones; on the vertical/horizontal are the combinations of datasets and seasons of occurrence..... | 120 |
| Figure 4.14: D-HW frequency occurrence at 12-month scale in the different dataset at different the considered seasons. Colours represent the climate zones; on the vertical/horizontal are the combinations of datasets and seasons of occurrence..... | 121 |
| Figure 5.1: Duration in the historical period (1981 - 2020). The Years of Occurrence (A-a,b,c); maximum (daytime) Temperature, UTCI and WBGT and (A-c,d,e) minimum (night-time) Temperature, UTCI and WBGT; The part B present (B-a,b,c) the duration for maximum daily Temperature, UTCI and WBGT, and the (B-c,d,e) duration for minimum daily Temperature, UTCI and WBGT; in West Africa..... | 131 |
| Figure 5.2: Cumulative Intensity in the historical period (1981 - 2020). The Years of Occurrence (A-a,b,c); maximum (daytime) Temperature, UTCI and WBGT and (A-c,d,e) minimum (night-time) Temperature, UTCI and WBGT; The part B presents (B-a,b,c) the maximum normalised Cumulative Intensity for Temperature , UTCI and WBGT, and the (B-c,d,e) minimum normalised Cumulative Intensity for Temperature, UTCI and WBGT; in West Africa..... | 133 |

| | |
|---|-----|
| Figure 5.3: Daytime Heatwave Monthly Relative Difference over the selected case study period (2018-2020) for Normalised Cumulative indices: (a-i) Temperature and UTCI; (m-x) Temperature and WBGT; (y-aj) UTCI and WBGT..... | 134 |
| Figure 5.4: Night-time Heatwave Monthly Relative Difference over the selected case study period (2018-2020) for Normalised Cumulative indices: (a-i) Temperature and UTCI; (m-x) Temperature and WBGT; (y-aj) UTCI and WBGT..... | 135 |
| Figure 5.5: Selected Heatwave Case Studies (red boxes) on the year of occurrence | 137 |
| Figure 5.6: PCA Applied to the 2018 Heatwave case study. Shown here are the (a) the scree plot that explain the total variation in the dataset by each component; (b) the biplot that give the direction of the individuals and the variables; (c) the biplot with classes focussed on the pressure levels and (d) the biplot with classes focused on the HW event periods..... | 140 |
| Figure 5.7: PCA Applied to the 2019 Heatwave case study. read as in Figure 5.6... | 142 |
| Figure 5.8: PCA Applied to the 2020 Heatwave case study. read as in Figure 5.6... | 143 |
| Figure 5.9: Variables evolution at 6 hourly over the whole selected period for heatwave case study in 2018. The values have been smoothed to daily for clarity. The pink bars are the totaltt. The black dotted vertical lines show the section of the beginning and the end of the detected heatwaves highest event in this particular period..... | 145 |
| Figure 5.10: 6 hourly correlation of variable at 850 hPa over the whole selected period for heatwave case study in 2018. On top the (absolute) value of the correlation plus the result of the correlation test as stars. On bottom, the bivariate scatter-plots, with a fitted line The bigger the absolute values the better the correlation (both positive or negative). The red crosses (correlation test) show the significance level of the p-values (0, 0.001, 0.01, 0.05, 0.1, 1) <=> symbols(“***”, “**”, “*”, “.”, “”). | 146 |
| Figure 5.11: 6 hourly correlation of variable at 925 hPa over the whole selected period for heatwave case study in 2018. Read as in Figure 5.10..... | 147 |

| | |
|---|-----|
| Figure 5.12: 6 hourly smoothed evolution over the 2018 detected heatwaves highest event in this particular period. Read as in Figure 5.9..... | 148 |
| Figure 5.13: Variables evolution at 6 hourly over the whole selected period for heatwave case study in 2019. Read as in Figure 5.9..... | 149 |
| Figure 5.14: Correlation of 6-hourly variables at 850 hPa over the whole selected period for heatwave case study in 2019. Read as in Figure 5.10..... | 150 |
| Figure 5.15: Correlation of 6-hourly variables at 925 hPa over the whole selected period for heatwave case study in 2019. Read as in Figure 5.10..... | 151 |
| Figure 5.16: 6 hourly smoothed evolution over the 2019 detected heatwaves highest event in this particular period. Read as in Figure 5.9..... | 152 |
| Figure 5.17: Variables evolution at 6 hourly over the whole selected period for heatwave case study in 2020. Read as in Figure 5.9..... | 152 |
| Figure 5.18: Correlation of 6 hourly variables at 850 hPa over the whole selected period for heatwave case study in 2020. Read as in Figure 5.10..... | 153 |
| Figure 5.19: Correlation of 6 hourly variables at 925 hPa over the whole selected period for heatwave case study in 2020. Read as in Figure 5.10..... | 154 |
| Figure 5.20: 6 hourly smoothed evolution over the detected 2020 heatwaves highest event in this particular period. Read as in Figure 5.9..... | 155 |
| Figure 5.21: Vertical profile of the different tendency terms and the computed advections during the selected heatwave events in West Africa. The lower troposphere is considered here (up to 700 hPa)..... | 156 |
| Figure 5.22: Vertical profile of the different tendency terms and the computed advections during the selected heatwave events in West Africa. The lower troposphere is considered here (up to 200 hPa)..... | 158 |
| Figure 6.1: Regional Heatwave duration and year of spatial occurrence. Comparison of the year of occurrence of the duration (upper panel I) and the duration (down | |

| | |
|---|-----|
| panel - II). All three indices are presented (CumHeat, UTCI and WBGT for maximum and minimum of the day)..... | 170 |
| Figure 6.2: Regional Heatwave duration. Comparison of the year of occurrence of the cumulative intensity. read as in Figure 6.1..... | 171 |
| Figure 6.3: Monthly relative difference between daytime heatwave indices. Case study from 2018 to 2020. Normalised Cumulative indices: (a-i) Temperature and UTCI; (m-x) Temperature and WBGT; (y-aj) UTCI and WBGT..... | 173 |
| Figure 6.4: Monthly relative difference between night-time heatwave indices. Case study from 2018 to 2020. Normalised Cumulative indices: (a-i) Temperature and UTCI; (m-x) Temperature and WBGT; (y-aj) UTCI and WBGT..... | 174 |
| Figure 6.5: Monthly Comparison of the relative difference between daytime heatwave indices from ERA5 computations and the RegCM-CLM model output. Case study from 2018 to 2020. Normalised Cumulative indices: (a-i) Temperature and UTCI; (m-x) Temperature and WBGT; (y-aj) UTCI and WBGT..... | 175 |
| Figure 6.6: Monthly Comparison of the relative difference between night-time heatwave indices from ERA5 computations and the RegCM-CLM model output. Case study from 2018 to 2020. Normalised Cumulative indices: (a-i) Temperature and UTCI; (m-x) Temperature and WBGT; (y-aj) UTCI and WBGT..... | 176 |
| Figure 6.7: Spearman rank correlations between normalised maximum CumHeat temperature months and current (a, c, e) and antecedent (b, d, f) surface moisture (SPEI) at 3-, 6- and 12 months scales. Cross-marked regions indicate significant correlations with a confidence level of 95%..... | 178 |
| Figure 6.8: Spearman rank correlations between normalised minimum CumHeat temperature months and current (a, c, e) and antecedent (b, d, f) surface moisture (SPEI) at 3-, 6- and 12 months scales. Read as in Figure 6.7..... | 180 |
| Figure 6.9: Spearman rank correlations between normalised maximum Cumheat UTCI months and current (a, c, e) and antecedent (b, d, f) surface moisture (SPEI) at 3-, 6- and 12 months scales. Read as in Figure 6.7..... | 181 |

| | |
|--|-----|
| Figure 6.10: Spearman rank correlations between normalised minimum CumHeat UTCI months and current (a, c, e) and antecedent (b, d, f) surface moisture (SPEI) at 3-, 6- and 12 months scales. Read as in Figure 6.7..... | 182 |
| Figure 6.11: Spearman rank correlations between normalised maximum CumHeat WBGT months and current (a, c, e) and antecedent (b, d, f) surface moisture (SPEI) at 3-, 6- and 12 months scales. Read as in Figure 6.7..... | 183 |
| Figure 6.12: Spearman rank correlations between normalised minimum CumHeat WBGT months and current (a, c, e) and antecedent (b, d, f) surface moisture (SPEI) at 3-, 6- and 12 months scales. Read as in Figure 6.7..... | 184 |
| Figure 6.13: Mean soil moisture showing different levels with moisture content extracted from the RegCM-CLM model..... | 185 |
| Figure 6.14: Spearman rank correlations between normalised maximum CumHeat T_{max} months and current (a, c, e, g, i, k, m, o, q, s) and antecedent (b, d, f, h, j, l, n, p, r, t) depth layer moisture content at 3-, 6- and 12 months scales. Read as in Figure 6.7..... | 187 |
| Figure 6.15: Spearman rank correlations between normalised minimum Cumheat T_{max} months and current (a, c, e, g, i, k, m, o, q, s) and antecedent (b, d, f, h, j, l, n, p, r, t) depth layer moisture content at 3-, 6- and 12 months scales. Read as in Figure 6.7 | 188 |
| Figure 6.16: Spearman rank correlations between normalised maximum CumHeat UTCI months and current (a, c, e, g, i, k, m, o, q, s) and antecedent (b, d, f, h, j, l, n, p, r, t) depth layer moisture content at 3-, 6- and 12 months scales. Read as in Figure 6.7..... | 189 |
| Figure 6.17: Spearman rank correlations between normalised maximum CumHeat WBGT months and current (a, c, e, g, i, k, m, o, q, s) and antecedent (b, d, f, h, j, l, n, p, r, t) depth layer moisture content at 3-, 6- and 12 months scales. Read as in Figure 6.7..... | 190 |
| Figure 6.18: Spearman rank correlations between normalised minimum CumHeat WBGT months and current (a, c, e, g, i, k, m, o, q, s) and antecedent (b, d, f, h, j, l, n, | |

| | |
|--|-----|
| p, r, t) depth layer moisture content at 3-, 6- and 12 months scales. Read as in Figure 6.7..... | 192 |
| Figure 6.19: PCA applied to the 2018 Heatwave case study. Shown here are the (a) the scree plot that explain the total variation in the dataset by each component (relative and specific humidity, temperature, humidity advection); (b) the biplot that give the direction of the individuals and the variables; (c) the biplot with classes focussed on the pressure levels and (d) the biplot with classes focused on the HW event periods..... | 193 |
| Figure 6.20: PCA applied to the 2019 Heatwave case study. Descriptions are read as in Figure 6.19..... | 194 |
| Figure 6.21: PCA applied to the 2020 Heatwave case study. Descriptions are read as in Figure 6.19..... | 195 |
| Figure 6.22: 6 hourly smoothed evolution over the 2018 detected heatwave highest event case study. The values have been smoothed to daily for clarity and plotted at 925 hPa, 850 hPa and 700 hPa. The pink bars are the temperature anomaly (°C). The black dotted vertical lines show the section of the beginning and the end of the detected heatwaves detected event in this particular period. Horizontal lines represent the parameters as indicated in the legend..... | 196 |
| Figure 6.23: 6 hourly smoothed evolution over the 2019 detected heatwaves highest event in this particular period. Descriptions are read as in Figure 6.22..... | 197 |
| Figure 6.24: 6 hourly smoothed evolution over the 2020 detected heatwaves highest event in this particular period. Descriptions are read as in Figure 6.22..... | 198 |
| Figure A.1: Heatwave (HWMId and AHWI) intensity (int) Correlation for the climate zones in West Africa (a- Guinea; b- Sahel; c- Sudan and d- overall average) | 250 |
| Figure A.2: HWMId zonal comparison; Gridded (a, b, c) and observation (d, e, f) datasets. BF10 is the Bayes Factor; The Highest Density Interval (HDI) formed from the posterior gives the 95% most credible values; r is the prior..... | 251 |

| | |
|---|-----|
| Figure A.3: UTCI Gridded and Station comparison; dataset distribution in the climatic zones and their relative level of heat stress at 32 °C strong heat stress in red dotted line (upper panel);Percentage of occurrence comparison in each climate zone with p-values at the top (lower panel)..... | 252 |
| Figure A.4: Seasonal Variation and distribution of UTCI (Gridded and Station) compared over the period 1981 to 2020 in the climate zones (Guinea, Sudan and Sahel). Red dotted line is the 32 °C strong heat stress..... | 253 |
| Figure A.5: Drought Heatwaves relationship and association in the Guinea Zone;association of heatwave / heat stress and drought at 3- (a), 6-(b) and 12-(c) months;each point represent an index, the path is the correlation between variable and the colours are the correlation strength; d- is the overall correlation between the indices,with correlation values in the upper triangle, a regression line on lower triangle and histogram with density on the diagonal..... | 254 |
| Figure A.6: Heatwave and Heat Stress Occurrence during Droughts in the Guinea zone;SPEI – HWMId (a), AHWI (b) and UTCI (c); SPI – HWMId (d), AHWI (e) and UTCI (f)..... | 255 |
| Figure A.7: Drought Heatwaves relationship and association in the Sudan Zone; Presented as Figure A.5..... | 256 |
| Figure A.8: Heatwave and Heat Stress Occurrence during Droughts in the Sudan zone; SPEI:AHWI vs HWMId (a), HWMId vs UTCI (c) and AHWI vs UTCI (d); SPI: AHWI vs HWMId(b), AHWI vs UTCI (e) and HWMId vs UTCI (f). The colours represent different drought intensity and the size represent the relative proportion of occurrence from the total series..... | 257 |
| Figure A.9: Drought Heatwaves relationship and association in the Sudan Zone; Presented as Figure A.5..... | 258 |
| Figure A10: Heatwave and Heat Stress Occurrence during Droughts in the Sahel ; Presented as in Figure A.8..... | 259 |

| | |
|--|-----|
| Figure B.11: Net total daytime temperature tendency at 925 hPa in the 2018 (January-March) heatwave case study. Appended are the temperature anomaly in contours (blue and red) and the wind direction (vector). The black box shows the case study..... | 263 |
| Figure B.12: Net total night-time temperature tendency at 925 hPa in the 2018 (January-March) heatwave case study. Appended are the temperature anomaly in contours (blue and red) and the wind direction (vector). The black box shows the case study..... | 264 |
| Figure B.13: Net total daytime temperature tendency at 925 hPa in the 2019 (November) heatwave case study. Appended are the temperature anomaly in contours (blue and red) and the wind direction (vector). The black box shows the case study | 265 |
| Figure B.14: Net total night-time temperature tendency at 925 hPa in the 2019 (November) heatwave case study. Appended are the temperature anomaly in contours (blue and red) and the wind direction (vector). The black box shows the case study | 266 |
| Figure B.15: Net total daytime temperature tendency at 925 hPa in the 2020 (January-March) heatwave case study. Appended are the temperature anomaly in contours (blue and red) and the wind direction (vector). The black box shows the case study..... | 267 |
| Figure B.16: Net total night-time temperature tendency at 925 hPa in the 2020 (January-March) heatwave case study. Appended are the temperature anomaly in contours (blue and red) and the wind direction (vector). The black box shows the case study..... | 268 |
| Figure C.17: Taylor Diagram of the 2018-2020 relative differences of Daytime Heatwaves indices. ERA5 HeatCum-UTCI is used as the reference dataset compared to the other ERA5 HeatCum-WBGT (represented as ERA2) and UTCI-WBGT (represented as ERA3) and the indices computed from the RegCM-CML model, HeatCum-UTCI (M1), HeatCum-WBGT (M2) and UTCI-WBGT (M3). The | |

| | |
|---|-----|
| correlation coefficient, the standard deviation, and the root mean square difference between the two datasets are displayed..... | 269 |
| Figure C.18: Taylor Diagram of the 2018-2020 relative differences of night-time Heatwaves indices. Read as in Figure C.17..... | 270 |
| Figure C.19: Taylor Diagram of the 2018-2020 relative differences of Daytime (night-time) Heatwaves indices. ERA and M are the datasets sources (ERA5 and Model output). Numbers that follow them are 1-3 (daytime) and 4-6 (night-time). So HeatCum-UTCI is used as the reference dataset compared to other datasets. The correlation coefficient, the standard deviation, and the root mean square difference between the two datasets are displayed. The ERA4, ERA5 and ERA6 are respectively..... | 270 |

LIST OF ABBREVIATIONS AND ACRONYMS

| | |
|-------------------|---|
| AHWI | Apparent Heat Wave Index |
| AMMA | Multidisciplinary Monsoon Analysis Model Inter-comparison Project |
| AOGCM | Atmosphere-Ocean General Circulation Model |
| BATS | Biosphere-Atmosphere Transfer Scheme |
| BL | Boundary layer |
| CAM | Community Atmosphere Model |
| CESM | Community Earth System Model |
| CLM | Community Land Model |
| CMI | Crop Moisture Index |
| CMIP | Coupled Model Inter-comparison Project (Phase) |
| DEWS | Drought Early Warning System |
| DRM | Disaster-Risk Management |
| EHF | Excess Heat Factor |
| ENSO | El-Niño-Southern Oscillation |
| ESP | Earth System Physics |
| ETCCDI | Expert Team on Climate Change Detection and Indices |
| ETSCI | Expert Team on Sector-Specific Climate Indices |
| GCM | Global Climate Model |
| HWMI | Heat Wave Magnitude Index |
| HWMI _d | Heat Wave Magnitude Index daily |
| ICTP | International Centre for Theoretical Physics |
| IPCC | Intergovernmental Panel on Climate Change |

| | |
|--------|--|
| ITD | Inter-Tropical Discontinuity |
| LA | land–atmosphere |
| LULC | Land Use Land Cover |
| LULCC | Land Use Land Cover Change |
| LULCT | Land Use Land Cover Type |
| MENA | Middle East and North Africa |
| NCAR | National Center for Atmospheric Research |
| PDSI | Palmer Drought Severity Index |
| PET | Physiological Equivalent Temperature |
| PMV | Predicted Mean Vote |
| PPD | Predicted Percentage Dissatisfied |
| RAI | Rainfall Anomaly Index |
| RCM | Regional Climate Model |
| SET | Standard Effective Temperature |
| SPEI | Standardized Precipitation Evapotranspiration Index |
| SPI | Standardized Precipitation Index |
| SREX | Special Report on Managing the Risks of Extreme Events and Disasters to Advance Climate Change Adaptation |
| SSP | Shared Socioeconomic Pathways |
| SST | Sea-Surface Temperature |
| UHI | Urban Heat Island |
| UNFCCC | United Nations Framework Convention on Climate Change |
| UTCI | Universal Thermal Climate Index |
| WAM | West African Monsoon |

| | |
|------|-----------------------------------|
| WBGT | Wet-Bulb Globe Temperature |
| WMO | World Meteorological Organization |
| WSDI | Warm Spell Duration Index |

ACKNOWLEDGEMENT

Bless the Lord, O' my soul!!!

My utmost appreciation goes to the Almighty God for the strength given throughout these challenging, but insightful times of research.

I am extremely grateful to my supervisors, Prof. Leonard K. Amekudzi from the department of Meteorology and Climate Science (KNUST, Kumasi, Ghana), Prof. Dr. Andreas H. Fink from the department of Meteorology and Climate Research (KIT IMK-TRO, Karlsruhe, Germany), Prof. Sidera Kodjovi Edjame (University of Lomé, Lomé, Togo) and Prof. Kehinde O. Ogunjobi (WASCAL Competence Centre, Ouagadougou, Burkina Faso) for their guidance, suggestions, comments, objective criticism, encouragement and motivation. They shaped this whole work and shaped me as an individual. I would like to thank my scientific advisors, Dr. Marlon Maranan (KIT, IMK-TRO, Karlsruhe, Germany) who acted as a mentor al-through this thesis work and gave insightful comments; Prof. Nana Ama Browne Klutse (University of Ghana / AIMS) for the continual support and guidance and providing access to the high performance computing system (CHPC) in South Africa for the model simulation. My sincere thanks go to Dr. Michael Thiel (University of Würzburg, Germany) for the support and the facilitation of activities such as connecting me to my German supervisor. I would also like to thank here Mr. Mthetho Sovara (CHPC) and Dr. Samuel Mabakane (University of Cape Town) for their assistance in setting the model up on the CHPC.

I extend my sincere appreciation to the Federal Ministry of Education and Research of Germany (BMBF) and the West African Science Centre on Climate Change and

Adapted Land Use (WASCAL) in Ghana, Accra, for providing the scholarship and financial support that made this research possible. I would like to acknowledge the support from the “Current and future risks of urban and rural flooding in West Africa – An integrated analysis and eco-system-based solutions (FURIFLOOD)” project, under which umbrella I was hosted and supervised in Germany.

I am deeply grateful to Prof. Wilson Agyei Agyare, the Director of the CCLU-KNUST program in Kumasi, and Prof. Eric Kwabena Forkuo, Deputy Director of the same program, for their guidance and support. I would also like to express my appreciation to the Climate Change and Land Use (CCLU) program staff and the Kwame Nkrumah University of Science and Technology for their management, assistance, and unwavering support throughout the completion of this thesis.

I extend my thanks to the KIT team and Prof. Dr. Peter Knippertz as the team lead for their valuable assistance during my research and data analysis. My gratitude also extends to those who contributed to my work in various ways, including my colleagues from WASCAL CCLU, batch 4.

CHAPTER 1: GENERAL INTRODUCTION

1.1 Background

The tropical climate is highly variable and is the main spot of distribution of the incoming solar energy on the earth. The variability is associated with the monsoon phenomenon that drives the climate in West Africa with daily, sub-seasonal cycles. Generally, two seasons are known and used in the climate context in West Africa: the wet (monsoon) and the dry (harmattan) seasons. The word “monsoon” originates from the Arabic word “*mousim*”, that is “season” describing the seasonal wind reversal over a region, usually accompanied by an increase in precipitation (Saroaha, 2017). Some research work have attempted to predict the West African Monsoon (WAM) phenomenon (e.g. the African Multidisciplinary Monsoon Analysis Model Inter-comparison Project (AMMA) (Janicot et al., 2008; Kergoat et al., 2011; Lafore et al., 2010; Polcher et al., 2011; Roehrig et al., 2013; Tompkins and Feudale, 2010)), but there are considerable inter-model variations in both the magnitude and the changes (Raj et al., 2019). The variability in rainfall, especially due to the side effects of global warming, is a challenge for farmers community about when exactly is the onset of the rainy season. This is paramount for agriculture in the region. On the other side, climate change increases the dry season’s intensity and duration and other extremes in the region already known for its elevated temperature (Kendon et al., 2019). There are also evidences of increasing temperature extremes in the region, namely heatwave, with impacts on infrastructures, agriculture and living beings (Ceccherini et al., 2017; Ragatoa et al., 2018; Russo et al., 2016). Efforts have been made to understand the physical causes of historical climate variability (Danuor et

al., 2011; Hourdin et al., 2010; Lafore et al., 2010) and the interaction of temperature extremes, especially when considering greenhouse gases, land cover and aerosols in West Africa.

With the global warming situation, the last decades recorded high extremes such as droughts and heatwaves all over the world, primarily due to human activities, especially the land use/cover change. Africa is not out of risk, considering its high vulnerability to global warming due to the high exposure and the low adaptive capacity. The principal extreme events in West Africa are floods, droughts and heatwaves that are expected to increase in the future (Ragatoa et al., 2018). The last two extremes are highly destructive for agriculture in the region, and they are considered dreadful in many countries because of their damaging effect on food production, health, and infrastructure. Temperature extremes negatively affect even more animals and ecosystems (Wilson and Boulder, 2019). It is imperative to grasp the association between temperature extremes and the West African Monsoon, the main driver of the West African climate. Thorough analysis of the WAM features and their interactions with the land surface can help in understanding the meteorological conditions that trigger heatwaves with droughts. That will considerably lead to better forecasts of climate extreme events in the region (Fink et al., 2011). The occurrence of one can be associated to the other and have serious consequences effect on livelihood. It is therefore needed to critically study their synoptic and climate conditions in relation to the high rate and non-controlled land use, to be able to predict them and act toward their reduction or adaptation.

Heatwaves also known as “the silent killer”, are projected to increase in the coming years in their frequency, duration and intensity, due to the increasing population and

demands for natural resources and also the pollution. There is a combination of natural and anthropogenic factors that trigger this extreme event, making it more intense under climate change. Heatwaves might entertain a synergy with the Urban Heat Island (UHI) and causes an increase in the stress in cities. A typical description of heatwaves involves the effects of stationary, high-pressure systems that generate an abnormal temperature for a given region over an extended period in the mid-latitudes. This results in an increase in air and surface temperatures across both urban and rural areas (Li and Bou-Zeid, 2013). The rural areas are as well affected, and the impacts are felt by the natural ecosystems, the agricultural production and by the populations. High humidity in the tropics can also increase the stress caused by heatwaves (e.g., humid heatwaves – high humidity during successive hot days may exacerbate the impact of extreme heatwaves (Russo et al., 2017a)). The public health implications of heatwaves are becoming more and more apparent and contribute to high infrastructures cost such as energy installations, roads, and even natural ecosystems and agriculture. Extreme heatwaves can lead to minor illnesses that impact plants (high temperature limits plants defence mechanism as well, leaving them more susceptible to attacks from pathogens and insect pests – (Kim et al., 2022)), animals and human beings (Aid et al., 1978; Langlois et al., 2013; Varghese et al., 2019). High heat illnesses are heat rash (prickly heat), heat oedema, heat cramps, and tetany, as well as serious illnesses as heat syncope, heat exhaustion and heat stroke that could lead to death (Cheng et al., 2019). Heat stroke is the most severe form of heat-related illness for humans. Heatwaves are known as prolonged periods (generally 3 or more days) of extreme temperature over an area. Unfortunately, they do not receive much attention and are not well understood

because of multiple and intrinsic atmospheric processes at play (Perkins, 2015; Perkins-Kirkpatrick and Lewis, 2020). If there are only a limited number of records available in West Africa, it may be due to the fact that a significant number of events are not observed or reported (Odoulami et al., 2017). In West Africa, there is no standard metric, except for the percentile-based method mostly used by researchers, and developed by the Expert Team on Climate Change Detection and Indices (ETCCDI) to provide indices relevant to climate change detection. Significantly less attention was given to West African heatwave in research though the few studies showed significant increase in the heatwave severity (Barbier et al., 2018; LARGERON et al., 2020; Moron et al., 2016; Oueslati et al., 2017).

The same is observed with droughts events across the globe. Drought refers to an extended duration when the total precipitation in a particular area is lower than the long-term average (Jesus et al., 2020), resulting in a disparity between the water demand and supply, thus leading to a hydrological imbalance as per the World Meteorological Organization's (WMO et al., 2016) definition. It is typically characterised as an extended period of limited water availability, typically resulting from inadequate precipitation or a drying up of agricultural land and water reserves due to abnormally high temperatures and low humidity. Drought hazards differ from other environmental hazards in three ways: the onset and cessation are difficult to determine because of the mechanisms that control it, there is no accepted universal conditions to define a drought condition. The related effects are less obvious and spread over a large geographic area (Haddow et al., 2017). Fundamentally, drought is a meteorological phenomenon characterised by a prolonged period of below-average precipitation amount, but its human impacts are much more complex and nuanced

than this simple climatic definition might suggest (Lybbert and Carter, 2015). Dry weather conditions prevailing over an area for a prolonged period characterize meteorological drought. There are four main types of drought, each with its own characteristics and impacts: (i) Meteorological Drought: meteorological drought is defined by a prolonged period of below-average precipitation. It is based on the amount of precipitation received in a given area over a certain period of time. This type of drought is primarily concerned with the deficit in precipitation and the duration of the dry period; (ii) Hydrological Drought: hydrological drought is related to the impact of rainfall deficits on the water supply. It is characterized by reduced stream flow, reservoir and lake levels, and groundwater. Hydrological droughts are typically detected by low water levels in streams, reservoirs, and groundwater, often after an extended period of meteorological drought; (iii) Agricultural Drought: agricultural drought is closely linked to meteorological or hydrological drought and focuses on the impact of these droughts on agricultural activities. It is characterized by precipitation shortages, differences between actual and potential evapotranspiration, soil water deficits, and reduced groundwater or reservoir levels. Agricultural drought can lead to crop damage and a general water shortage; (iv) Socioeconomic Drought: socioeconomic drought occurs when the demand for water surpasses the available supply. It is a type of drought that is often associated with the relationship between drought and its impact on various economic sectors, such as agriculture, industry, and households. Socioeconomic droughts can have significant social and economic consequences. It is important to note that these types of drought are interconnected and can overlap in their impacts. Droughts can have severe consequences on ecosystems, agriculture, water resources, and human societies,

making it crucial to monitor and manage them effectively. Droughts are one of the costly weather events in the West African countries (Ahmadalipour, 2017; IPCC, 2018; Partey et al., 2021). These drought definitions have been linked to the Atlantic sea surface temperature in West Africa and to the West African Monsoon (Shanahan et al., 2009), but their dynamics in relation with heatwave is not yet known under the WAM and the global warming.

Moreover, the co-occurrence of drought-heatwave events can cause severe damages, especially in cities with UHI and the high concentration of human beings, more than what they can cause when their effects are summed up (Li and Bou-Zeid, 2013), human and animal health, infrastructures and crops, thus impacting the environment and the land use knowing that climate responds to land use change creating an unending cycle. Understanding the causes of heatwaves in West Africa and their dynamics with drought and moisture content will help in forecasting the event, planning an effective and efficient management of the land in the region. This needs to be done in relation to the WAM under the global warming. Besides, it would serve as an early warning tool for forecasting.

1.2 Motivation of the Study (Rational)

The rationale for this research is anchored in the escalating concerns posed by global warming, which stands as a significant threat to both human society and ecological equilibrium. Evidence has shown that global warming (of about 1.5 °C) is a threat to the human society and the ecological environment (IPCC, 2018). During the 1970s and 1980s, West African nations have endured prolonged climate droughts, leading to dire consequences such as crop failures and inadequate rainfall. Escalating

population trends and increasing anthropogenic activities in the region have exacerbated the impact of these climatic shifts. The circumstance escalated into a crisis, exacerbated by surging food prices and the homecoming of 200,000 migrant labourers to West Africa due to the civil conflicts in Libya and Ivory Coast (Quenum et al., 2019; York, 2012). Furthermore, the increasing population in West Africa is having an impact on the climate through increased anthropogenic activities. A temperature increase of +1.5 °C has been documented during the April-May period in the Sahel region over the past 60 years. Despite these challenges, West African heatwaves remain an under-explored domain in scientific inquiry, often hindered by the scarcity of heatwave records and limited data availability. (Barbier et al., 2018) which is the transition period from the dry to the wet season (Inter-tropical Discontinuity movement); Barbier et al. (2018) added that heatwave events have been reported in the region at that season of the year over the last decades and health is one of the areas that can be severely affected by this event, and its impacts can also extend to ecosystems, transportation, and agriculture. This was already raised respectively by Ceccherini et al. and Russo et al. (2017; 2016). Very little attention is given to West African heatwaves in research (Barbier et al., 2018; Largeron et al., 2020; Moron et al., 2016; Oueslati et al., 2017). There is a scarcity of official heatwave records in Africa, as a considerable number of heatwave occurrences are frequently disregarded or unreported. (Odoulami et al., 2017). In contrast to developed nations, Sub-Saharan countries encounter numerous hindrances in implementing a robust heatwave detection framework, which encompass (i) inadequate governance structures, (ii) limited climate data observational networks, and (iii) a scarcity of proficiency to establish indigenous heatwave metrics that also

incorporate epidemiological information. (Harrington and Otto, 2020). However, increase in the frequency, duration and/or intensity of night-time and daytime heatwaves is observed in West Africa, especially in the Sahel. According to the IPCC (2019), concurrent events could happen and increase in frequency and duration in the future, especially in the Sahel (West Africa). But it is important to note here that the impact of the concurrent event together is greater than the sum of both events happening separately, because their positive feedback can worsen the rainfall deficit situation (Sharma and Mujumdar, 2017). In addition, Bastos et al. (2020) documented the influence that future land-management strategies could have on the patterns of summer heatwaves and droughts under long-term warming because of the land-atmosphere interaction. They are the local heating, the increase of urbanization (mainly due to population density) and the effect of the UHI that makes cities hotter than surrounding non-urban areas (Barbier et al., 2018; Katavoutas and Founda, 2019; Miralles et al., 2019). The synergy and interaction between UHI and heatwaves have been studied in some areas (Founda and Santamouris, 2017; Li and Bou-Zeid, 2013) and has been proved very harmful, therefore compelling research to understand the interactions between drought, heatwaves and the different land types (land surfaces) especially the urban area which concentrates the greater number of population and the most vulnerable area to temperature extremes. This study recognizes the crucial need to comprehend the intricate interactions between drought, heatwaves, and diverse land types, particularly within urban areas, to mitigate their adverse effects on the population. Through this research, a more accurate forecasting approach and the development of a heatwave early warning system are envisaged, offering significant potential for enhanced disaster-risk management and sustainable

urban planning. This also serves as a benchmark for UHI adaptation and mitigation, especially in cities where the greatest number of population lies and will reside in the future. The study aligns with the Sustainable Development Goals (SDGs) 11, 13, and 15, and contributes to a comprehensive understanding of these extreme events under the backdrop of global warming. Ultimately, the research aims to minimize the socio-economic, health, and security impacts of drought-heatwave events in West Africa. Finally, knowledge will be added to the West African climate system as well. The results of this research work will be valuable to policy- and decision-makers, on the quantification of these extremes under global warming in West Africa. It is the way to minimizing the impacts of drought-heatwave events on socioeconomic activities, human health and security in West Africa.

1.3 Problem Statement and Justification

The monsoon system in West Africa holds paramount importance, significantly influencing the climatology of the region. The unequivocal rise in global mean air temperature underscores the pressing nature of comprehending the intricate mechanisms of monsoons and their related climatic dynamics. Human-induced factors, including escalating greenhouse gas concentrations, substantiate the urgency to scrutinize the repercussions of temperature extremes and their interplay with land management practices. There is a strong evidence that the global warming observed over the last centuries is attributable to human activities. As a result, the concentrations of carbon dioxide (CO₂), methane (CH₄), and nitrous oxide (N₂O) have increased by 31%, 151%, and 17% since 1750, respectively (Fu et al., 2008; GreenFacts, 2006; IPCC, 2001). The concentrations of atmospheric greenhouse gases

(GHG) and aerosols, are expected to augment as well as their radiative forcing, and they will continue to increase as a result of human activities throughout the 21st century (Fu et al., 2008). Between 2006 and 2015, the Earth's temperature increased by 0.87 °C (± 0.12 °C) as a result of human activity, relative to pre-industrial levels (1850-1900). Should the present rate of warming persist, the world is expected to surpass the human-induced global warming threshold of 1.5 °C around the year 2040 (IPCC, 2018) which is almost reached (IPCC, 2021a).

Furthermore, The intricate nexus between changing climate patterns and their profound impact on agrarian societies, coupled with the evolving monsoon mechanism, necessitates thorough investigation. Land plays a significant role, especially in agrarian societies in West Africa. It has always been an important factor for agricultural production, industry and different economic activities. Their interactions with the changing climate and chiefly temperature extremes is earnestly affecting the economy (Deng et al., 2014). The changes affect temperature and precipitation, leading to possible changes in the mechanism of the monsoon and its related climate extremes. There have been works (AMMA project) that intended to predict the phenomenon in order to improve on agriculture and the economy in the subregion (Boone et al., 2009; Lebel et al., 2010; Polcher et al., 2011). Furthermore, climate extremes, especially droughts and heatwaves are crucial research topics nowadays because their potential impact and increase in the future (Ceccherini et al., 2015, 2016, 2017; Russo et al., 2013, 2015, 2016). In West Africa, there are few studies that have established the dynamics of heatwaves in relation to the WAM and very hardly the relationship between heatwaves and droughts (Feller and Vaseva, 2014; Guerreiro et al., 2018; Jones, 2018; Stefanon et al., 2012; Sutanto et al., 2020).

Droughts alone, have been studied to some extent as well as rainfall variability and dynamics in the region, but their association to heatwaves and relationships are very little known. Droughts and heatwaves are regarded as two of the most significant climate-related hazards globally, and their effects on both human societies and the environment are profound (Ciais et al., 2005; Easterling, 2000). In addition to recognizing the escalating consequences of heatwaves and their changes over time under global warming, comprehending the reasons behind heatwaves and the mechanisms of potential compound extreme weather events pose another mounting obstacle in both the scientific and decision-making communities (Harrington and Otto, 2020). Consequently, addressing the convergence and progression of heatwaves and droughts constitutes a distinct challenge for West African nations, particularly sub-Saharan countries, due to the prevalence of severe droughts that have adversely affected the area in recent years. Drought-heatwaves under the WAM system can be very detrimental since they threaten food security, health and infrastructures even when considered individually. Their impacts could be reduced with an improved understanding for meteorological purpose, forecast and with an integrated land use planning/measures.

According to Francesco Rocca, who is the President of the International Federation of Red Cross and Red Crescent Societies (IFRC), *“Heat waves are the silent killers of climate change, but they don’t have to be,”* says Rocca. *“The climate crisis is driving and intensifying humanitarian crisis in every region of the world, ... but when cities and communities are better prepared, extreme weather doesn’t have to become a disaster or a tragedy”*. Press release — <https://www.ifrc.org/press-release/ifrc-and-c40-cities-urge-cities-prepare-more-dangerous-and-deadly-heat-waves> (IFRC, 2022).

The urgency to combat these converging challenges is underlined by the silent but profound humanitarian crises triggered by heatwaves. Acknowledging the significance of this realm, this research endeavours to elucidate the intricacies of the West African Monsoon-related temperature extremes, delving into the intertwined dynamics of heatwaves and their multifaceted interactions with land use and land cover types. The present research contributes to bring light on questions pertaining to the WAM related temperature extremes with drought and seeks to establish the causes of heatwaves and their dynamics with the different land use and land cover types.

1.4 Aim and Objectives

This thesis research aims to investigate the drought-heatwaves dynamics with land Use Land Cover Types (LULCT) under the West African Monsoon (WAM) system.

Specifically, the research focuses on the following:

- i. Determine the spatio-temporal drifts patterns in the droughts-heatwaves within the WAM,
- ii. Investigate the synoptic and boundary layer scale dynamics responsible for heatwaves in West Africa,
- iii. Evaluate the land-atmosphere energy and moisture fluxes in different LULC types,

1.5 Research Questions

The inquiry into essential aspects of drought-heatwaves characteristics in West Africa, enunciated within this study, encompasses but is not limited to the following pivotal questions:

- i. What are the discernible patterns governing the occurrence of drought-heatwaves under the ambit of the West African Monsoon?
- ii. To what extent do the synoptic and boundary layer scale temperature components contribute to explicating the dynamics of heatwaves in the West African region?
- iii. How does the coupled Regional Climate Model with a Land Model (RegCM-CLM) respond to heatwaves, considering the interplay of moisture roles within different Land Use Land Cover Types (LULCT)?

1.6 Scope of the Study

The compass of this research endeavours to scrutinize the intricate dynamics of drought-heatwaves within the expanse of the West African Monsoon system, encompassing the timeline spanning from 1981 to the present day. In the pursuit of this study, particular emphasis is directed towards the West African landscape, with specific attention all-embracing Coastal to Savannah countries, Sudan, and Sahel regions. The geographical selection is meticulously crafted to facilitate meaningful comparisons, thereby expand on the diverse spectrum of climate extremes characteristic of West Africa. The variance in climatic and Land Use Land Cover Types (LULCT) across the Guinea, Savannah, and Sahel climate zones spawn anticipated disparities in the dynamics, driven by distinct energy fluxes and evapotranspiration mechanisms intrinsic to these regions.

1.7 Organization of the Chapters

The thesis is structured into a total of 7 chapters. The Chapter 1 introduces the whole work by presenting the general background, motivation, the justification and

objectives of the study. The research questions and scope of the study are also given. A detailed review of literature in the Chapter 2 covers specific concepts and theories pertaining to heatwaves (HW), drought, climate temperature extremes, and use land cover types (LULCT), compound drought-heatwaves (DHW), the Urban-Heat-Island (UHI), the West African Monsoon (WAM) system, Climate Change (CC), and Land-atmosphere interactions. The Chapter 3 specifically addresses the methodology with the theoretical background of extremes and heatwaves, particularly with underlying equations and validity for this study. This includes also the physical processes of temperature terms and advections, and their possible interaction with heatwaves in West Africa. The subsequent Chapters (4 to 6) report the analysis and results of the different research objectives. They are based on manuscripts in preparation or submitted to peer-review journals. Finally, the Chapter 7 lays out the findings, conclusions, limitations of the study and applicable recommendations from the research work.

CHAPTER 2:LITERATURE REVIEW

Embodied is the review of pertinent literature concerning the research theme and organized under the definition of key concepts. The state-of-the-art on topics such as heatwaves, drought, compound events, the West African Monsoon, atmospheric boundary layer, land-atmosphere interactions and the coupled models are explored.

2.1 Overview of the Key Concepts

An ‘extreme climate event’ or ‘extreme weather event’ or again ‘climate extreme’ is generally defined as “*the occurrence of a value of a weather or climate variable above (or below) a threshold value near the upper (or lower) ends of the range of observed values of the variable*” (IPCC, 2019). Various methods are available to assess the properties of extreme events or alterations in the frequency of extreme events. One such method involves examining whether records in observed time series occur with greater or lesser frequency than expected in a climate system that has not been perturbed (Seneviratne et al., 2012). In traditional studies, more attention was paid to extreme events caused by a single process. However, recent projections have highlighted the increase in severity, duration, and frequency of both precipitation and temperature extremes. Consequently, current research is focusing on investigating the occurrence of simultaneous or coincident extremes (also referred to as compound events), as they have the potential to cause more severe impacts on human society and the environment than individual extreme events alone. The changing patterns of weather-related hazards, partly attributed to climate change, and increasing exposure of buildings and infrastructure to such hazards have made it

necessary to characterize extreme events based on physical and socio-economic vulnerability to their impacts (Hao et al., 2018).

A temperature extremes could then be considered as the rarest events from the highest or lowest values range of temperature statistical distribution — the cold and hot extremes, whose occurrence are generally accompanied by significant socio-environmental impacts. Temperature extremes as well as all other extremes are traditionally defined in terms of their frequency of occurrence, or, in statistical terms, by the quantile of their distribution. Many temperature extremes' definition are based on the percentile distribution of their daily values (i.e., it is said to exceed the 90th percentile of the overall distribution). A symmetrical definition is used for abnormally cold days, and the seasonal temperature cycle is generally taken into account, so there are warm days in winter or cold days in summer (Cattiaux et al., 2020). In temperature extremes evolution studies, the frequency (number of days below or above the current temperature decile) or the evolution of the intensity, defined for example as the average temperature of the 10% of extreme days, are considered (usually with the duration, amplitude and magnitude). Furthermore, there is a growing emphasis on studying the interdependent nature of extreme events. It is worth noting that various interpretations exist for defining a compound extreme, and there are multiple drivers behind the recent surge of interest in this area. These include the heightened recognition of the non-stationary characteristics of the Earth's climate system, as well as advancements in high-performance computing systems and more sophisticated modelling techniques capable of accounting for multiple variables and their intricate interplay to some degree (Leonard et al., 2014).

In the field of climate science, compound events refer to multiple events that can occur in different ways. These events can either happen at the same time or sequentially, and they can involve extreme events combined with underlying conditions that intensify their effects. Moreover, they can also involve different types of events that lead to extreme impacts when combined. Such events can have a severe impact on society, and they can occur in different forms, such as high sea levels coinciding with tropical cyclone landfall or the combined effect of drought and heatwaves, which is typical for monsoon climate systems in West Africa. These events can have a significant impact on society and the environment, according to Seneviratne et al., (2012). According to Leonard et al. (2014), the Intergovernmental Panel on Climate Change (IPCC) special report on managing the risks of extreme events and disasters to advance climate change adaptation (SREX) which terms a compound event as multiple physical processes coming together, is ambiguous and proposes a more inclusive definition which addresses all the events:

“A compound event is an extreme impact that depends on multiple statistically dependent variables or events”.

This definition underscores the severity of the impact, the necessity for multiple variables or events, and the significance of statistical dependence. Considering this, the West African springtime heatwaves that occur at the end of the dry season could be called a compound event since it is a concurrent drought and heatwave condition — amplified (especially night-time heatwave in the Sahel) by the moisture intrusion in the night which magnifies also the impact on populations’ physiology (animals, plants and humans). Hao et al. (2018) in that regard summarized typical compound extremes as showed in Table 2.1, such as drought and hot extremes (drought-heatwaves), precipitation and temperature extremes, compound flood and

interestingly, the combined humidity and temperature extreme (heatwaves accounting for apparent temperature).

Table 2.1. A concise summary of the various forms of compound extremes and the statistical methods utilised to analyse them: Adapted from Hao et al., (2018).

| Type of Compound Extremes | Combined Variables / Events / Extremes | Approaches |
|---|---|---|
| Compound drought and hot extreme | Drought and heat wave (hot days or months, high temperature). | Empirical approach, Quantile regression, Multivariate distribution. |
| Compound precipitation and temperature extreme | Heavy precipitation and cold/warm condition | Empirical approach, Markov Chain approach, |
| | Low precipitation and high temperature | Empirical approach, Multivariate distribution, |
| Compound flood | Dry-warm/dry-cold/wet-warm/wet-cold condition. | Empirical approach. |
| | Heavy precipitation and cold/warm condition, | Multivariate distribution, |
| | Low precipitation and high temperature | Empirical approach, Indicator approach, Multivariate distribution, |
| Compound drought | Dry-warm / dry-cold / wet-warm / wet-cold condition. | Empirical approach, Indicator approach, Multivariate distribution. |
| | Deficit from precipitation, soil moisture, run-off, or other variables. | Indicator approach, Multivariate distribution. |
| Combined drought, moisture surplus, precipitation / temperature, and other extremes | Drought indices, precipitation extremes and temperature extremes. | Indicator approach. |

These compound extremes happen also in monsoon affected areas and conditions the moisture flow (in between the wet and dry season, heatwaves could happen during March-June) (Ratnam et al., 2016).

The West African Monsoon (WAM) is a vital climatic phenomenon in the tropical region and is the dominant climate feature or wind system in West Africa. It is characterised by a seasonal reversal of the prevailing surface winds that spans almost the entire region. This phenomenon entails the replacement of the north-easterly Harmattan winds during winter with the south-westerly monsoon winds in summer, transporting moisture from the Atlantic Ocean to the continent. Consequently, this supplies the crucial annual rainfall that sustains the local populations. The WAM is renowned for its four distinct weather zones, which are situated around the Inter-tropical Discontinuity (ITD), also known as the Inter-tropical Front (ITF) (Fink et al., 2017). The notion of four weather zones revolving around the ITD is well documented in Fink et al.'s (2017) works. In Roberts et al.'s (2015) research, the ITD is described as the interface between the dry Saharan northerly winds and the moist south-westerly monsoonal flow, thus defining it as a confluence of surface winds with significant near-surface moisture and temperature gradients. The same authors observe that the ITD is identifiable as the point at which the near-surface dew-point temperature reaches 14 °C. Additionally, the ITD moves in a northward direction, supplying moisture to the continent from its most southern point (approximately 5 °C) at the beginning of January. (Lyngsie et al., 2013). Throughout the boreal summer, the ITD advances northward over the region, subsequently receding during and after September, with a marked diurnal reliance. This phenomenon is caused by the suppression of circulation due to daytime dry convective turbulence resulting from surface heating, and increased stability at night, enabling the monsoon front to advance northward under the influence of the Saharan heat low (SHL) (Parker et al., 2005; Pospichal et al., 2010; Roberts et al., 2015). This movement of the ITD

appears to be important, especially when considering the diurnal pulsations and their synoptic scale dynamics that lead to heating (moisture is important in temperature variation and heat impact) during the spring over the Sahel. The Guinea Coast, especially the coastal zone, at the same period experiences mesoscale convective systems (MCSs) because the boundary layer moisture is known to increase south of the ITD, primarily in areas where the monsoon flow exhibits greater depth.

The Boundary Layer (BL), which is also known as the atmospheric or planetary boundary layer, is mainly distinguished by its thoroughly established mixing, known as turbulence. The turbulence is produced by the frictional drag caused by the atmosphere's movement over the harsh and sturdy surface of the Earth. Additionally, the Boundary Layer is characterised by the emergence of air packets from the heated surface, which gives rise to a 'bubbling-up' effect (Oke, 1987). The thickness of the Boundary Layer (BL) is not uniform and varies in space and time. Its thickness is dependent on the strength of the mixing generated by the surface. The turbulence allows the BL to obtain heat and water, as it is the part of the atmosphere that is most impacted by the earth's surface. This is supported by Oke (1987) and Stull (2005). Typically, the BL is around 1-2 km in depth, covering the lower 10 to 20% of the troposphere. However, it can range from tens of meters to over 4 km in depth, as stated by Stull (2005). A capping inversion separates the turbulent BL from the stable free atmosphere in the troposphere. This stable layer traps most of the surface friction, moisture, and pollutants from entering the free atmosphere. This BL by its physics and dynamics, governs the changes in temperature, humidity, pollen, and winds, as it is cool and calm in the night and warm and gusty in the day. Stull (2005) well documented the fact that the BL is "unstable" when it is in a state of free

convection, with vigorous thermal up-drafts and down-drafts, (i.e., the temperature of the surface is higher than that of the air in situations such as a sunny day with gentle breezes over land or when colder air is transported over a warmer body of water). When the opposite is seen then it is called “stable” (the surface is colder than the air, as during a clear night over land, or when warm air is advected over colder water). In addition, there are neutral boundary layers that occur when it’s windy and overcast. These layers experience forced convection, which is the movement of air caused by the tendency of hotter, less dense material to rise (free dry convection), while colder, denser material sinks due to gravity. As a result, heat is transferred within the layers (Honnert, 2019). The heat and humidity that get trapped within the boundary layer (BL) serve as significant sources of fuel for the development of convective clouds. Moreover, wind shear, which is the difference in wind speed or direction over a relatively short distance in the atmosphere, can be divided into both horizontal and vertical components. This phenomenon is also known as wind shift or gradient (Lester, 2013; Stull, 2005). In the atmospheric boundary layer (BL), wind shear arises from the friction near the ground, driven by factors like daytime surface heating intensifying deep mixing. This phenomenon generates horizontal vorticity, which, when combined with updrafts in convective clouds, can lead to the formation of tornadoes. The dissipation of kinetic energy within the boundary layer is crucial, and overnight radiative cooling can enhance wind decoupling, acting as a constraint on the movement of large-scale wind systems. During nighttime, the presence of a low-level jet becomes prominent, contributing to heightened low-level kinetic energy. In this context, daytime turbulence acts as a counterforce against the monsoon flow. Wind shear generally causes “mechanical turbulence” in the BL

because of the difference in speed between the wind aloft and the earth surface wind, slowed by the friction. Shinoda (1986) previously revealed the wind anomalies during the Sahelian 1980s drought and concluded that the decrease in rainfall leads to an increase in thermal wind and zonal wind shear, thus the intensification of the African Easterly Jet (AEJ) in the mid- and upper-troposphere. A decrease (increase) in soil moisture levels in the Sahel region results in an increase (decrease) in wind speed, the drier soil conditions resulted in a maximum wind speed occurring in the late afternoon. This outcome can be attributed to the interplay between surface processes, boundary layer dynamics, and mesoscale phenomena, which are all strongly influenced by soil moisture availability. Specifically, when soil moisture decreases, the transfer of sensible heat increases at the expense of latent heat in land-atmosphere interactions, as previously noted by Jiménez et al. (2011). Land-atmosphere interactions refer to the exchange of moisture and energy between the earth's ecosystems and the atmosphere (Dickinson, 1995). Human activities, such as land use changes, significantly impact the regional climate by altering the surface reflectivity and the distribution of absorbed energy towards evapotranspiration or heating at the near-surface (Phillips et al., 2009; Pongratz et al., 2009). It is worth noting that land system changes can also lead to increased carbon sequestration, for example, through the land-sparing effects of intensification, unless they are overcompensated by rebound effects (Lambin and Geist, 2006; Lambin and Meyfroidt, 2011). Moisture and heat fluxes from the land surface play a critical role in determining the atmospheric temperature, water vapor, precipitation, cloud properties, and the downward radiative fluxes at the surface. The energy and moisture budgets at the land surface are primarily linked to evaporation, which

represents a simultaneous expenditure of both energy and water mass, resulting in a negative correlation between the soil's heat and moisture states (Brubaker and Entekhabi, 1996). During warm and dry anomalies, the feedback mechanism whereby elevated temperatures prompt an increased demand for evaporation to cool the surface, while at the same time, limiting the evaporation due to low soil moisture content, is a well-known and fundamental concept (Brubaker and Entekhabi, 1996). Other feedback mechanisms also exist, such as moist soil, which provides water for evaporation when energy is available, leading to increased precipitation through the provision of moisture and subsequent condensation into droplets. If this process continues, it can reinforce the moist anomalies. Conversely, dry soil suppresses moisture, resulting in reduced evaporation and precipitation over the region, leading to further drying. However, it is unclear to what extent the drying will continue if the dry anomaly persists. In a similar scenario, the drying of soil or removal/conversion of vegetation can increase the albedo, resulting in a net radiative heat loss that enhances sinking motion of the air and suppresses precipitation, thereby exacerbating drying in regions such as the Sahel (Brubaker and Entekhabi, 1996). According to the authors, the onset or cessation of hydrological droughts may be influenced by large-scale causes such as circulation patterns or teleconnections. However, local positive feedback within the land-atmosphere system may contribute to the persistence and intensification of droughts. Once a drought occurs, the soil becomes drier, vegetation cover is reduced, and surface roughness is lowered, leading to alterations in surface temperature and albedo. In an extensive review of the interactions between the atmosphere and surface hydrology, Nicholson (2000a) highlighted that the surface hydrology fundamentally delays and prolongs the effects

of meteorological droughts. Each component of evaporation within the surface water balance possesses its distinct temporal scale, and vegetation emerges as a key influencer, contributing to both the prolongation and postponement of the soil moisture's return to the atmosphere. Furthermore, vegetation expedites this process through the evaporation of canopy-intercepted water. Thus, the configuration of vegetation, encompassing root depth, emerges as a governing factor in shaping land-atmosphere interactions. These intricate mechanisms gain particular significance within the Sahel region, characterized by heightened atmospheric moisture recycling. Here, meteorological processes spanning boundary layer evolution to the generation of mesoscale disturbances are markedly influenced by moisture dynamics. The study was conducted in the Sahel of Niger. In the same line of discussion, Cameron (2001) brought more insight on the importance of vegetation in the Sahel, regulating the soil moisture desiccation rate and their relative proximity to buildings effect in the drying process. The deep root uptake could be called here since the soil water content reduces but not the entire water content dissipates. The deep root uptake is considered because of the depth to which some plants/vegetation cover in arid and semi-arid region could go for moisture. The process of soil moisture depletion occurs from the soil surface down to deeper layers. A pertinent question to ask is: what is the rate and intensity of this depletion during a drought event? Based on scientific evidence, it can be stated that soil moisture is significantly reduced during drought events (depending on the severity and duration of the event), but it does not reach a level of complete depletion that would eradicate all living organisms. As a result, plant and microbial activities are reduced, as well as soil respiration (carbon uptake during drought and/or heatwaves). The impact of drought on vegetation varies

perceptibly across different areas, primarily determined by the location of land-cover types (Agnew and Chappell, 1999; de Freitas, 1994; Doughty et al., 2015; Li et al., 2020; Markewitz et al., 2010; Rossato et al., 2017; Vicente-Serrano, 2007; Wajid et al., 2007; Wenda and Hanks, 1981). In the context of extreme temperatures, the IPCC (2019) has observed that an increase in temperature leads to a reduction in soil moisture and latent heat flux, while increasing sensible heat flux. This alteration in the Bowen ratio results in a further rise in surface air temperature. However, the report notes that this feedback can be mitigated if the land surface is irrigated and evapotranspiration is enhanced. In the Sahel, where irrigation is increasingly being adopted, this is of particular relevance. Additionally, it has been found that trees are more resilient to heat stress than grasslands as they are able to better retain moisture during drought or heatwave conditions (Teuling et al., 2010). Nevertheless, different types of forests exhibit varying responses to drought and heatwaves (Babst et al., 2012). To investigate these complex land-atmosphere interactions, researchers have developed statistical models and numerical models integrating atmospheric primitive equations (such as the conservation of mass and energy). Some models have even been coupled to study these interactions in greater depth.

As per the IPCC 2019 glossary, climate models are computational tools that provide a numerical representation of the climate system. These models are constructed based on the physical, chemical, and biological properties of the various components of the climate system, including their interactions, feedback processes, and some of their known characteristics (IPCC, 2019). Climate models are essential tools for representing and investigating the response of climate systems to various forcing. They are used to making predictions about future climate patterns over short-term

(seasonal to decadal) and long-term (century and beyond) time scales (Flato et al., 2014). Climate models can range in complexity, depending on the number and type of components they represent, such as the Atmosphere, Hydrosphere, Biosphere, Lithosphere, and the Cryosphere. When multiple components are combined, they are referred to as coupled models. In Earth-system models, the concept of “coupling” is often used in two ways: offline and online. Offline coupling involves passing output from one model to another for computation of a variable, while online coupling allows for feedback to pass between the two models. Fully coupled models, or shared model inputs, employ online coupling. The Community Earth System Model (CESM) is a set of models that are designed to simulate interactions between the earth's land, air, and water components as a single system. Climate models can be broadly divided into two categories: Global climate models (GCMs) and regional climate models (RCMs). GCMs, also known as general circulation models, are comprehensive models that represent the global climate system and its interactions with the atmosphere, ocean, and land surface. On the other hand, RCMs are limited-area models that simulate climate processes in a specific region with a resolution similar to that of the atmospheric and land surface components of AOGCMs, but without interactive ocean and sea ice components (Flato et al., 2014). Regional Climate Models (RCMs) are coupled to ocean and ice nowadays. The coupling of RCMs with other models of the climate system, such as ocean and sea ice models, is necessary to downscale the global climate models and project the surface climate at a regional scale (Flaounas et al., 2018). The Earth System Physics (ESP) section of the International Centre for Theoretical Physics (ICTP) in Trieste, Italy maintains the Regional Climate Model system RegCM. This model, developed at the National

Center for Atmospheric Research (NCAR), has undergone evolutionary improvements and is the first limited-area model created for long-term regional climate simulation. RegCM is a community model and has been specifically designed to be accessible to a diverse group of scientists from around the world. It is a publicly available, open-source, user-friendly, and portable code that can be applied to any region globally (Elguindi et al., 2014; Giorgi et al., 2016). RegCM was used to investigate the West African monsoon feature in the Guinea coast and Sahel considering the heat fluxes (latent and sensible heat) and the dry spells (Diba et al., 2019), and to examine heatwaves interaction with forests in West Africa (Odoulami et al., 2017). The Biosphere-Atmosphere Transfer Scheme (BATS) is an important surface package integrated into RegCM, which accounts for the influence of vegetation and soil moisture on surface-atmosphere exchanges of momentum, energy, and water vapour. Surface fluxes of sensible heat, water vapour, and momentum are calculated using a standard surface drag coefficient formulation based on surface-layer similarity theory. RegCM models are often coupled with other land models to explore land-atmosphere dynamics, such as the Community Land Model (CLM). Originally designed as the land model for the Community Earth System Model (CESM) and the Community Atmosphere Model (CAM), CLM is now coupled with RegCM to provide more detailed land surface modules (Yang et al., 2019) and land-surface atmosphere interactions (Elguindi et al., 2014; Koné et al., 2018; Maurya et al., 2017). This allows for a more comprehensive understanding of the interactions between the land and atmosphere. Coupled RegCM-CLM model was already used for example to simulate the Indian summer monsoon (ISM) and showed better performance due to the interactions of a better representation of surface

processes (Kumar et al., 2020; Maharana et al., 2019; Rai et al., 2020). The coupling of these two models could reveal more about the land-surface interaction (especially land feedback) during temperature extremes in West Africa, as it can also be used for urban energy balance in urban tropical cities (Demuzere et al., 2017; Varentsov et al., 2018).

2.2 Global Warming and Temperature Extremes

According to the IPCC, global warming refers to the recent increase in global mean surface temperature (GMST) over a 30-year period, centred on a particular year or decade, since the pre-industrial revolution period of the 1950s. The IPCC expects this warming trend to persist (IPCC, 2019). Climate change, on the other hand, encompasses all changes and variability, although there are distinct differences between the two. It is defined as a change in the state of the climate that can be detected (using statistical methods) by changes in the mean and/or variability of its properties and persists over an extended period, typically for decades or longer. The United Nations Framework Convention on Climate Change (UNFCCC) distinguishes between climate change resulting from human activities altering the atmospheric composition and climate variability due to natural causes (IPCC, 2019, 2012a; UNFCCC, 1992). The consequences of both are not entirely dissociated, as they are directly or indirectly related to the undeniable and commonly agreed fact of rising temperatures. The direct effects of climate change are mostly related to the extreme temperature records observed worldwide.

According to recent research by Almazroui et al. (2020), the largest increase in mean annual temperature is expected over the Sahara in West Africa by the end of the

twenty-first century, estimated at 5.6 °C under the strong forcing of the Shared Socioeconomic Pathways (SSP) SSP1-2.6, SSP1-4.5 and SSP5-8.5 scenarios. This region is already one of the hottest and driest places in the Northern Hemisphere. Moreover, extreme weather events such as floods and droughts are strongly linked to the variability in precipitation trends under global warming. The research further indicated that the mean annual temperature is projected to rise by 1.2 °C (1.4 °C), 1.5 °C (2.3 °C), and 1.8 °C (4.4 °C) in the near- and long-term periods over subregions of Africa under the SSPs, based on a multimodel ensemble from 27 CMIP6 models. Aside from the Sahara which is hot and will warm the more, West Africa will continue to warm at 0.6 °C decade⁻¹ under the SSP5-8.5. This continuous warming will only lead to intense and severe heat related extremes.

Ahmadalipour and Moradkhani (2018), have highlighted the potential societal impacts of temperature extremes, particularly heatwaves, caused by global warming and climate change. In their study, they focused on the Middle East and North Africa (MENA) region, where the mortality risk among elderly people over 65 years is a major concern due to excessive heat stress. To quantify this risk, they employed 17 fine resolution Regional Climate Models (RCMs) using the wet-bulb temperature. The results showed that the severity of mortality risk is projected to increase by 8–20 times in the future, albeit with high uncertainties. However, limiting global warming to 2 °C could reduce this risk to 3–7 times, emphasizing the need for planning and adaptation measures to mitigate the heat-related mortality risk across the region.

The monitoring of drought as an extreme event has become increasingly important, despite being a natural phase of an area's climate regime. It is a costly hazard that has significant and widespread impacts, including economic losses in agriculture and

food security, hydropower generation, industry, human and animal health, livelihood, personal security, and access to education, where people may have to travel long distances to obtain water (WMO and GWP, 2016). Droughts are characterised by their spatial and temporal scales and their severity or magnitude. Drought impact is defined as a loss or change at a specific time due to drought, and risk management should involve hazard, exposure, vulnerability, and impact assessment. To monitor, manage or forecast drought, it is necessary to develop a Drought Early Warning System (DEWS) to track, assess and provide timely and relevant information on climatic, hydrologic, and water supply conditions and trends before or during the early onset of the event for efficient action. Preparedness and mitigation techniques are also crucial in dealing with drought.

Drought indicators and indices are essential tools for characterizing and quantifying drought conditions. Drought indicators typically include various climatic and hydrological parameters, such as precipitation, temperature, stream-flow, groundwater and reservoir levels, soil moisture, and snow-pack, depending on the specific region. In contrast, drought indices provide numerical representations of drought severity and are typically computed using these indicators (WMO and GWP, 2016). Examples of indices are the Crop Moisture Index (CMI) calculated along with the Palmer Drought Severity Index (PDSI) output, the Rainfall Anomaly Index (RAI), the WMO recommended Standardized Precipitation Index (SPI; (WMO, 2012)) and the Standardized Precipitation Evapotranspiration Index (SPEI; (Vicente-Serrano et al., 2010a)). The last two are mostly used in the world, especially in West Africa (Agnew and Chappell, 1999; Morel, 1995; Nicholson, 2000b, 2018). There

are many other indices which have themselves their own characteristics, indicators, applications, strengths, and weaknesses (WMO and GWP, 2016).

The 2003 European heatwave (HW), considered to be the most severe of the twentieth century, after the 2022 heatwave (Ballester et al., 2023), drew significant attention to the social impacts of extreme temperatures, resulting in high mortality rates. The summer of 2003 saw a series of strong, persistent heatwaves in Europe, which were some of the most intense and prolonged heatwaves since 1950 (Fink et al., 2004; Garcia-Herrera et al., 2010; Russo et al., 2015; Schär et al., 2004). These heatwaves have had notable impacts on human mortality, regional economies, and natural ecosystems, and are becoming increasingly frequent and intense due to global warming and climate change (Guido Ceccherini et al., 2017; Ragatoa et al., 2018; Russo et al., 2016). Heatwaves are a type of temperature extreme that is challenging to define due to the multiple characteristics and metrics used to identify them, making domain-specific impact and indicator use important. The World Meteorological Organization's definition is commonly used by meteorologists and defines a heatwave as occurring when the daily maximum temperature exceeds the average maximum temperature by 5 °C for more than five consecutive days, with the normal period being 1961-1990. The intense and frequent nature of heatwaves is not limited to Europe, as evidenced by recent studies in Africa.

But nowadays, the timescale of occurrence in this definition has been modified to “three or more consecutive days” and the normal has changed according to the newly defined climatology by the WMO (1981-2010 or 1991-2020). The House of Commons Environmental Audit Committee's Ninth Report of 2017-2019 session highlighted that heatwaves are responsible for causing various heat-related illnesses.

These include heat cramps, heat rash, heat oedema (swelling, typically in the ankles), heat syncope (dizziness and fainting due to dehydration), and heat exhaustion, which in severe cases can lead to heatstroke, a potentially fatal condition. Recognizing the early signs of heatstroke can avoid unnecessary death. Heatstroke is very dangerous for the health, caused when the body's thermoregulatory mechanism fails. Heatstroke can result in cell death, organ failure, brain damage or death. Initial symptoms indicate heat exhaustion, which usually gets better if addressed quickly. The documented signs include headaches, confusion and dizziness, loss of appetite, nausea, excessive sweating, pale and clammy skin, cramps in the arms, legs, and stomach, rapid breathing or heartbeat, a temperature of 38 °C or higher, and severe thirst (Environmental Audit Committee, 2018).

Heatwaves hit both land and oceans, but the one taking more attention is the land or terrestrial heatwaves where human population reside (Hobday et al., 2015). Perkins et al. (2012) highlighted the escalating occurrence of land-based heatwaves and warm spells worldwide, which is a growing cause of concern. The authors defined heatwaves as seasonally extreme (i.e., summer) events and warm spells as seasonally anomalous warm periods occurring annually. Using the HadGHCND gridded daily land data from 1950 to 2011, they calculated the 90th percentile of minimum and maximum temperatures and the Excess Heat Factor (EHF) for each grid, for warm spells and heatwaves. Their findings demonstrated that the intensity, frequency and duration of these events have been increasing and continue to do so. Furthermore, the appropriate index for a case study should be selected carefully, as some events that are not necessarily summer events could influence trends in various regions worldwide. For instance, percentile-based indices such as TX90 and TN90 are more

relevant for warm spells. Night-time trends were more significant than daytime trends, which explained the general warming of the Earth.

Ratnam et al. (2016), correspondingly, responded to the increasing trend of summer heatwaves (during March-June) in India. They sought to clarify the root causes of these heatwaves. Through statistical analysis of maximum temperature data, researchers in India have distinguished and characterised two types of heatwaves and their respective causes. The first type is linked to blocking over the North Atlantic, leading to a cyclonic anomaly to the west of North Africa at upper levels. The second type is attributed to the anomalous Matsuno-Gill response to anomalous cooling in the Pacific.

Furthermore, the 2010 Russian heatwave called the torrid weather, choked the Western Russia during summer killing about 55000 people. This was the worst of over 33 years heatwave occurrence. Rasmijn et al. (2018) conducted a study on the Russian heatwave and its severe consequences, linking it to an abnormal and persistent high-pressure circulation anomaly over western Russia, which was further strengthened by a lack of spring moisture in the soil. The authors concluded that as global warming progresses, large-scale atmospheric conditions that favour extreme warming will not be counteracted by adequate soil moisture, resulting in future heatwaves that will be even more intense than the 2010 event. It is projected that temperature extremes over western Russia could increase by 8.4 °C. As a result, the socioeconomic impacts of future heatwaves are expected to be more severe than current estimations.

As for drought, there are many indices that are used in the literature to define heatwaves. In that regard, Zare et al. (2018) conducted a study to compare the

Universal Thermal Climate Index (UTCI) with other commonly used thermal/heat indices such as Standard Effective Temperature (SET), Physiological Equivalent Temperature (PET), Predicted Mean Vote (PMV), Predicted Percentage Dissatisfied (PPD), and Wet Bulb Globe Temperature (WBGT), as well as environmental parameters. They analysed daily data for the year 2016, computing correlation and linear regression analyses to assess the relationship between UTCI and the other indices and environmental parameters. The results showed that UTCI had a strong correlation with PET ($r = 0.96$), WBGT ($r = 0.88$), and SET ($r = 0.87$), while also significantly correlating with environmental parameters such as dry temperature, relative humidity, and wind speed. The study found that UTCI and WBGT showed similar thermal perceptions from April to October, while PET had the most severe heat perception from May to September. The authors also noted that PMV was more effective at detecting severe cold than UTCI during all months except for June. Overall, the study suggests that UTCI is comparable to other widely used thermal/heat indices, with the added advantage of strong correlations with environmental parameters.

In the race of giving a robust heatwave definition, Russo et al. (2014) proposed a new index, after the hottest European summer in 2003 and the Russian 2010 summer extreme heatwave (more serious in amplitude and spatial extent and the strongest globally recorded), the Heat Wave Magnitude Index (HWMI) that can be compared over space and time. Effectively, the temperature percentile-based indices (Alexander et al., 2006; Meehl and Tebaldi, 2004) as well as the Heatwave Duration Index defined by Frich et al. (2002), a country specific threshold of 5 °C above the normal, group or sector-specific indices (Perkins and Alexander, 2012), are not

robust enough and could not capture some specificity of some regions and sectors, thus could not be compared across the globe. The 27 indices developed by the Expert Team on Climate Change Detection and Indices (ETCCDI; http://etccdi.pacificclimate.org/list_27_indices.shtml) seemed to come in as a solution, added to the Warm Spell Duration Index (WSDI) which is calculated using a percentile-based threshold.

However, because of its limitation to seasonal and annual computation, the HWMI is used to determine and compare heatwaves across regions and time taking into account both the magnitude and duration. The HWMI was improved by Russo et al. (2015), the Heat Wave Magnitude Index daily (HWMId) in order to solve the limitations in evaluating daily or sub-heatwaves in the considered three consecutive hot days. The HWMId is more robust and can assign magnitude to a single day composing a heatwave. This new formula was used to evaluate historical heatwave events across the whole European continent from 1950 to 2014. The event will increase in magnitude and frequency in Europe, as projected by the authors. The index in question was employed in Africa during various seasons (Guido Ceccherini et al., 2017; Ragatoa et al., 2019, 2018; Russo et al., 2016), the results revealed that Africa has been experiencing longer and more extent heatwaves than in the last two decades of the 20th century. Ceccherini et al. (2017) observed an increase in the frequency and spatial extent of extreme heatwaves. They reported that the frequency of extreme heatwaves had risen to 24.5 occurrences per year (60.1% of land area) between 2006 and 2015, compared to 12.3 occurrences per year (37.3% of land area) during the period from 1981 to 2005. The study projects that this trend will continue into the future, with extreme heatwaves becoming more regular by 2040. In the same

way, a modified version of the HWMI_d was formulated (Russo et al., 2017b) to account for humid-heatwaves where the humidity could amplify the event and strongly affect human health. With increasing warming levels under the global warming, heatwave magnitude and peak are amplified as well. The apparent temperature (AT) is then considered and used by replacing the maximum temperature by the AT for those heatwave days with $AT > T$, to bring in the Apparent Heat Wave Index (AHWI). This index is comparable to the Heat Index (HI) but more robust in terms of comparison and magnitude assessment. This paper states then the existence of a dry and a humid heatwave driven by blocking patterns, reduced cloudiness and advection of warm air for the first type and high relative humidity and/or hot and humid air being advected to the concerned area (i.e. Eastern US and China with high AT impact).

Geirinhas et al. (2019) sought to identify the causes of the 2010 heatwave in Rio de Janeiro, Brazil, by characterising the prevailing atmospheric conditions. The authors used weather and climate forecast models in the Metropolitan Region of Rio de Janeiro (MRRJ), which is densely populated and highly exposed to the health impacts of heatwaves. They found that elderly individuals, as well as women, were particularly vulnerable to heatwave-related mortality. The authors identified a quasi-stationary Rossby wave train in the westerly flow that initiated in January 2010 and persisted until the heatwave period (2–9 February 2010), explaining the large-scale atmospheric circulation associated with the development of heatwaves in the region. This Rossby wave is related to the teleconnection pattern between the Southeast Pacific Ocean, South America, and the South Atlantic Ocean, which is known as the Pacific-South America modes (PSA modes — PSA1 and PSA2, are atmospheric

patterns influenced by ENSO, with PSA1 affecting northeastern Brazil's rainfall during El Niño and PSA2 displaying a dipole rainfall pattern in the South Atlantic Convergence Zone). These modes are associated with anomalous sea surface temperatures and are related to El Niño-Southern Oscillation (ENSO) episodes. These atmospheric dynamics can lead to drought in certain regions. The soil-atmosphere feedback mechanisms were also found to be significant in the development of the heatwaves over southeastern Brazil, with observed large values of short-wave radiation incidence at the surface. The authors observed persistent short-wave radiation anomalies over southeastern Brazil and central Brazil during January 2010, which contributed to rapid soil drying through high evaporation rates, resulting in a positive feedback mechanism that promoted the amplification of hot and dry surface conditions, especially to the north of the MRRJ (the same mechanism was observed and documented for the 2003 summer heatwave). The authors concluded that heatwave events in the MRRJ were driven by atmospheric processes at different temporal and spatial scales, with several abnormal land-atmospheric conditions during the preceding weeks.

In their study on regional heatwaves Perkins-Kirkpatrick and Lewis (2020) made use of a new measure of heatwaves, the cumulative heat and showed significant increase in the heatwaves across the globe since 1950s driven by heatwave days. The authors employed the Berkeley Earth Surface Temperature (BEST) dataset with a key heatwave metric (T_{\max} heatwave definition – CTX90) aside the new cumulative heat which is key in the research work because it can be used for comparison between regional heatwaves on spatio-temporal scales for the assessment of impacts. The measure known as Cumulative Heat or Cumulative Excess Heat ($heat_{cum}$) quantifies

the additional heat generated by heatwaves within a given season. This value is determined by calculating the sum of the difference between each heatwave day and the corresponding calendar-day 90th percentile (i.e., the heatwave daily threshold for that year) across all heatwave days in that season.

It is worth noting that land-use changes (LUCs) and related land processes are significant contributors to global warming, leading to changes in extreme temperatures and water cycle patterns (Seneviratne et al., 2018).

2.2.1 Temperature Extremes and Land Feedback

Any doubt having been removed about the occurrence of temperature extremes all over the world, a situation confirmed by almost all the studies, and it is anticipated that with the current global warming trend, these heatwaves will intensify and persist for longer periods, these events have never been happening on themselves in the atmosphere even though they are atmospheric phenomena. Droughts are not just atmospheric phenomena, they have causes and/or catalysts at the earth's surface. In a normal scenario where there is a dense vegetation, unquestionably the albedo (fraction of incident solar radiation reflected by a surface) in that region will be higher than the one recorded in an ice-land or surface covered with snow. The same will be for the bright sand desert's albedo that is > 0.5 (equivalent to aged snow). Not only West African receives a high amount and intensity of energy directly from the sun, there is very less ice-land or snow coverage in the region to reflect the incoming energy, this is another contributing condition to the warming in the region (West Africa is mainly covered by forest, woodland, grassland, bare soil and the artificial places in urban area, settlements). The earth's albedo affects how much solar energy

it absorbs, and therefore how warm earth's surface is. The soil being a huge carbon reservoir of the earth, it is highly contributing to the concentration of the greenhouse gases in the atmosphere through the management that is done. Tropical deforestation for example, and its effects on the climate, are well known scenarios of land use changing the local climate. It is often observed that such areas in the tropics that transition from forests to cropland are often drier and warmer. In climate systems, the albedo determines the radiation balance of the surface and influences the surface temperature and boundary-layer structure of the atmosphere while in other physical sciences, the albedo controls the microclimate of plants and thus their biological and physio-chemical processes such as energy, water, and respiration balance (Wang and Davidson, 2007). This in return will determine the type of cover observed in the area, when considering a natural process. But it is not so, human being has been having such an impact on the land that, it is alarming how degraded the situation becomes. For example, Wang and Davidson (2007), when studying the impact of climate variations on surface albedo in temperate grassland, noted the importance of air temperature in controlling albedo during winter to summer transitions and vice versa. Precipitation amount also affects the albedo during winter. This research revealed that surface albedo varies even in the same land cover (temperate grassland) in response to climate variations. It also links the climate change impacts with the changes of surface albedo, and the feedback of the albedo response to the physical climate system, improving on the climate models for projection.

Rhee et al. (2014) investigated the relationship between land cover patterns and surface temperature in a Geographic Information System (GIS) environment using a Random Forest classifier and a simple linear regression for two urban areas in

Denver, Colorado, USA. Urban lands are known to have a higher temperature compare to the surroundings because of the material used for construction and the development requirement. But cities are gathering more and more people for their attractive centres and living conditions. In such circumstances, heat stress is presented as a significant issue in urban areas, especially when occurred with drought. Rhee et al. (2014) documented some crucial factors at the heart of temperature patterns specifically in urban areas (Dousset and Gourmelon, 2003; Xiao et al., 2007): The expansion of urban areas has brought about various changes that significantly impact the climate, including changes in albedo, enhanced evapotranspiration, increased radiative flux, and anthropogenic urban heat emissions. These factors contribute to the severity of heatwaves experienced in cities, especially due to the Urban Heat Island (UHI) effect, as noted by Smoyer-Tomic et al. (2003). Furthermore, changes in land cover and land use, especially through the development of impervious surfaces, affect thermal patterns by altering the exchange of energy flux between the surface and boundary layer. In a study conducted by McGarigal et al. (2012), the authors used the FRAGSTATS software to compute class-level spatial metrics and found that land cover patterns involving trees and roads and parking lots have a greater influence on surface temperature than grass and buildings. These findings highlight the potential for specific land cover types to mitigate the adverse impacts of heatwaves and drought, which are often closely related and mutually reinforcing. As such, strategies aimed at reducing the harmful impacts of urban drought can be employed to address the effects of heatwaves in cities.

Heatwaves are the most rapid spurts of temporary temperature change, and bring the highest of high temperatures. Knowing that cities are naturally hotter than the

surrounding rural areas, Li and Bou-Zeid (2013) were interested in the synergies between Urban-Heat-Islands (UHI) and Heatwaves. This study was intending to answer an interesting question, whether urban and rural temperatures respond in the same way to the excessively hot periods of heatwaves. The combination of observational and modelling indicated that there are synergies between UHI and heatwaves. The observed synergies are interactions whereby heatwaves amplify the temperature in the urban areas as well as in the environs or rural areas, increasing the gradient temperature in the two considered areas. Most interestingly, the findings revealed that the added heat stress in cities could be even higher than the sum of the background UHI and the heatwave effect taken individually and associated mathematically. The authors associated the high impacts of this phenomenon to the low surface moisture and wind speed in urban areas during heatwave events.

Likewise, Founda and Santamouris (2017) further clarified the UHI and heatwaves complex synergies but focusing on coastal cities, which represent the majority of the population in the world and especially in Africa. Taking the case of the 2012 summer heatwave in Athens (Greece), the findings shed light on the positive feedback between UHIs and HWs. The feedback suggests that there is a significant increase in the average UHI magnitude during heatwaves (HWs) compared to the background summer conditions, with a maximum increase of up to 3.5 °C. It is noteworthy that the diurnal variation of UHI magnitude is prominent due to the local circulation effects of the nearby sea, resulting in a daytime occurrence, which is contrary to the conventional perception of UHI as a night-time phenomenon. The differences in latent heat fluxes between urban and rural areas are also expected during HWs. As surface temperatures increase, evapotranspiration from the ground to the atmosphere

also increases, which contributes to the reduction of ambient temperature by releasing latent heat. The rate of evapotranspiration depends on surface moisture and vegetation, which are more abundant in rural areas than in urban zones. Therefore, rural areas have a higher potential for evapotranspiration and reducing ambient temperatures. During daytime HWs, the wind speed was slower than non HW (NHW) periods, with wind speeds of 4.4 and 11.5 m/sec during NHW and 4.2 and 8.4 m/sec during HW periods. However, the link between UHI intensity and the diurnal maximum ambient air is not synchronous. The magnitude of UHI intensity increases with temperature and decreases with increasing wind speed (depending on the direction). Thus, HW periods are associated with higher UHI intensity, as are southerly winds in Athens. The nocturnal UHI intensity is of particular interest as high night-time temperatures have been proven to have more significant physiological impacts than high daytime temperatures (Gabriel and Endlicher, 2011; Tan et al., 2010)). The researchers observed that low wind speeds prevailed at all sites, especially during HW periods, due to lower pressure gradients. This indicates that advection mechanisms, such as sea/land breezes, do not contribute to UHI intensity during night-time. Instead, radiative processes mainly control the magnitude of night UHI. It is important to consider the proximity of the sites to the sea, as coastal cities play a role in this process. The findings may differ in completely inland areas.

The research conducted by Zhou et al. (2019) focused on the role of land-atmosphere (LA) feedback in the occurrence of compound drought and aridity events. The authors acknowledged that soil droughts can persist for longer periods (months to years) compared to atmospheric aridity that usually lasts for weeks to months. They

assessed the physiological stressors that drive large vegetation mortality and reduced terrestrial carbon uptake at a monthly scale to understand the impacts of compound drought and aridity events. In addition to the large-scale atmospheric circulation and sea surface temperature anomalies that contribute to climate extremes, the LA feedback initiated by soil moisture anomalies can strongly influence near-surface heat and aridity, and thereby affect large-scale atmospheric circulation anomalies. This feedback creates an unending cycle that exacerbates the occurrence of concurrent soil drought and atmospheric aridity. This study demonstrated that the LA feedback leads to a strong negative coupling between soil moisture and vapour pressure deficit, which greatly exacerbates the occurrence of concurrent soil drought and atmospheric aridity. Changes in soil moisture and vapour pressure deficit are closely linked. This interaction intensifies the occurrence of simultaneous conditions of soil drought (low soil moisture) and atmospheric aridity (low vapour pressure), creating a stronger negative relationship between these two factors. The simulations in the CMIP5 models project that this coupling will increase, which could pose significant risks to ecosystem services and human well-being in the future.

Pertaining to land–atmospheric feedback during droughts and heatwaves, Miralles et al. (2019) provided an overview of the current state of knowledge regarding land–atmospheric feedback during droughts and heatwaves, highlighting the current and future challenges. Droughts and heatwaves are complex meteorological events that are often characterised by elongated periods of precipitation and/or moisture shortage and extremely high temperatures, respectively. The occurrence of these events can have significant socioeconomic consequences, including crop failure, plant mortality, air pollution, and water scarcity. They also pose a threat to the sustainability of

ecosystems and food production systems, and increase the likelihood of wildfires. The intensification of these events is linked to global warming, prompting researchers to examine them as individual and associated events. However, their onset, evolution, and cessation remain poorly understood, and the scientific community has yet to fully grasp the complexity of their driving processes in different regions of the world. Addressing these challenges will require a multidisciplinary approach, involving collaboration between climate scientists, ecologists, hydrologists, and other experts. Through improved understanding and predictive capabilities, we can better prepare for and mitigate the impacts of droughts and heatwaves on human societies and the natural environment. But the common agreement about the physics is that both events have similar land-atmosphere feedback and persistent large-scale circulation anomalies vital for their initiation. The feedback can be simplified into a soil and vegetation mechanism according to Miralles et al. (2019): as they dry out, land evaporation and/or evapotranspiration is reduced, making the air to dry the more, decreasing further the probability of rainfall and tend to a meteorological drought. As evaporation decreases, a greater proportion of incoming radiation is absorbed by the environment, resulting in an increase in sensible heat and potentially contributing to the development or amplification of a heatwave. This land-atmosphere interaction becomes very crucial in understanding these extreme events mechanism or physics and in defining their magnitude and why they often concur in their occurrence or relate in some ways to each other. Questions raised in the nowadays and reported in the work are critical to today's research and for Africa: Is it possible to use the understanding of the role of land feedback to develop geoengineering strategies aimed at preventing the worsening of droughts and

heatwaves during their initial stages? In order to address the questions raised in previous research, both coupled and statistical models have been employed. However, to explicitly solve for convection, high-resolution land-atmospheric coupled models must be integrated into the coupled models, as cloud feedback plays a crucial role in the climate system. The representation of evaporation in land surface schemes is still a limitation in land-atmosphere feedback studies. Exploiting knowledge of land-atmosphere feedback is crucial to the development of geoengineering mitigation strategies. Therefore, it is essential to quantify the impact of land-use change and management on atmospheric moisture transport and heat advection during droughts and heatwaves. This would enable the exploration of geoengineering solutions to mitigate the expansion and concatenation of extreme events. According to Miralles et al. (2019), ongoing research remains focused on the crucial role of land conditions in the evolution of droughts and heatwaves as extreme events.

However, the complexity of this analysis of LA interactions does not stop researchers, models are mostly developed and used for that purpose; to understand land-atmosphere interactions. Steiner et al. (2005) introduced the coupling of the Common Land Model (CLM0) to a regional climate model (RegCM). The study consisted of replacing the active land surface parametrization scheme, known as the Biosphere-Atmosphere Transfer Scheme (BATS), in a RegCM with the newly developed CLM0. The main reason of this combination, while the RegCM has already a land component, is that the regional climate modelling domains for land-atmosphere models supplies the model's lower boundary condition for more than 30 % of the Earth's surface which significantly impacts different transfers such as the

transfer of mass, momentum, and energy between the atmosphere and the land surface, which in turn affect prognostic climate variables ((Dickinson et al., 1993; Henderson-Sellers and Dickinson, 1993). For instance, the Community Land Model (CLM) computes several land surface variables (such as surface temperature, precipitation, and the vertical distribution of atmospheric water vapour and clouds) at every grid point using ten soil layers of varying thickness, one vegetation layer with a canopy photosynthesis-conductance model, and up to five snow layers, depending on the total snow depth. It processes other parameters such as the soil temperature and moisture, run-off and ocean surface fluxes. Steiner et al. (2005) expounded the difference between the BATS parametrization and the CLM0. The primary contrast between CLM0 and BATS lies in their surface representation. While CLM0 has 10 vertical soil layers, up to five snow levels, and one vegetation layer, BATS has three soil moisture levels, two soil temperature levels, one snow layer that is incorporated with the surface soil layer in temperature calculations, and one vegetation layer. As a result, the computation of albedo, surface fluxes, soil temperatures and moisture, run-off, canopy water storage, vegetation canopy, stomatal conductance, photosynthesis, and snow involves different approaches and/or theories of computation (Dickinson et al., 1993). The results of the study, when compared with station observations, indicate that CLM0 outperforms BATS in simulating root zone soil water content and other related processes, such as albedos and surface energy and water budgets, except for snow cover.

Maharana et al. (2019) employed the regional climate model (RegCM4.6) coupled with the latest version of the land-surface model (Community Land Model; CLM4.5) to assess the Indian summer monsoon (ISM) over 34 years. The study indicated a

suppression of moist convective activity over India, resulting in a decrease in rainfall and an eastward shift of convective systems from India towards the Bay of Bengal (BoB). However, the coupling between the land and atmosphere components in the model was found to be weak, and the longer spin-up period did not improve the ISM simulation in the RegCM-CLM model. Therefore, the authors concluded that the CLM4.5 was not yet adequate to represent the land-atmosphere interactions during ISM and recommended further improvements. Notably, soil moisture initialization was not carried out in the model simulation, despite its importance in the monsoon-affected regions' planetary boundary layer. Nevertheless, the latest version of CLM, CLM5, has already addressed some of the shortcomings of CLM4.5.

In a similar vein, a study by Rai et al. (2020) focused on investigating the North-east Monsoon (NEM) in India using the coupled land-atmosphere model RegCM4-CLM4.5. The study aimed to improve the reproduction of land-surface processes associated with the NEM. The study used RegCM4.7 coupled with different land-surface schemes (BATS, CLM and SUBGRID) from 1970 to 2005, for a period of 36 years. The results showed that the CLM land-atmosphere scheme better captured moisture convergence and transport over the NEM region (NEMR), resulting in a finer spatial distribution of rainfall compared to CON and SUB experiments. However, there was no agreement between the CLM and the other two experiments with regard to sensible and latent heat transfers. While the CLM showed high sensible (latent) heat over the eastern coast and central Tamilnadu (Kerala), the Control (BATS) and SUB (SubGrid) experiments showed the opposite. Despite this, since the CLM performed better in representing the NEMR over the southern Indian region as compared to the other schemes integrated in the study, the conclusion was

that it captures moisture fluxes and rainfall distribution better over the NEM. These results suggest that Maharana et al. (2019) could have improved their simulated model if they had examined the influence of forced soil moisture initialization in the coupled model environment.

2.2.2 Recent Advancements in Africa and Specifically in West Africa.

Drought and land surface processes/interactions have widely been studied all over the world, most in areas where there has been a record of extensive anthropogenic modification of land surface, such as the Great Plains, the Amazon and the Sahel. Nicholson (2000a) explored the impact of land surface atmosphere interactions on the variability of rainfall in the West African Sahel. The study found evidence of anthropogenic global warming and a significant decrease in mean rainfall of 25-40% between 1931-1960 and 1968-1997. Furthermore, it was observed that the region experienced wet years throughout the 1950s and mostly dry years since 1970, implying a potential role of land surface feedback in these variations (Nicholson, 2000a).

Quenum et al. (2019) investigated the impact of global warming on precipitation and drought patterns in West Africa. The study aimed to understand the shifts in seasons due to climate change. Using data from the Coordinated Regional Climate Downscaling Experiment (CORDEX) at different global warming levels (GWL, i.e., 1.5 °C, 2.0 °C, 2.5 °C, and 3.0 °C) above the pre-industrial level (PIL), the authors computed four different indices over the region. The results showed that the rising global temperature exacerbated extreme temperatures worldwide and affected precipitation patterns. There was a one-month shift in the rainy season, and increased

intensity was recorded in the Gulf of Guinea compared to historical records. The Sahel and Savannah regions suffered from extreme and severe droughts during certain years, with an increase in extreme droughts observed under GWLs (2.0 °C and 3.0 °C) in the coastal part of Liberia and Cameroon, Mali, Burkina Faso, Niger, Ivory Coast, Benin, Nigeria, and Chad. These results support the IPCC 2012 report, which states that precipitation variability under global warming would strongly be linked to temperature extremes, which could be a threat to the environment and society.

In digging into such questions, global warming brought in interrogations related to rainfall distribution and their effect on drought in the Sahel. As many studies suggested, this warming might intensify the drought events and make them recurrent, Salack et al. (2016) queried the attributions of the intensification of drought in the Sahel. They suggested a hybrid phenomenon where the increased frequency of intense rain could be associated at the same time to drought conditions in terms of spatial and temporal distribution of the rainfall. This hybrid configuration of the rainfall in the Sahel could explain this perspective on drought, but also more seriously threaten food security. The research paper investigated a new approach for drought definition and explored the contribution of both oceans warming and the low to mid-level atmosphere regional dynamic features in triggering the Sahel's droughts and hybrid rainfalls. The results of these investigations showed that, indeed, regional atmospheric patterns and oceans basin warming in the North Atlantic and the Mediterranean Sea effectively trigger hybrid rainy seasons (here, these mixed dry/wet seasonal rainfall features) in the Sahel and threatening the West African rain-fed farming systems.

In the Sahel region of West Africa, the hottest months of the year (April and May) have experienced a significant increase in temperature, according to Largeron et al.'s (2020) study. This warming has led to severe heatwaves with temperatures exceeding 45 °C in several countries, including Niger, Senegal, Mali, Burkina Faso, and Chad during the spring of 2010. The study suggests that the April 2010 North African heatwave was mainly due to the contribution of water vapour to the greenhouse effect, especially during night-time temperatures. The presence of clouds in the Sahara and both clouds and dust loadings in the Sahel resulted in strong positive anomalies of surface incoming long-wave fluxes and negative anomalies of incoming short-wave fluxes during the heatwave. Results show that humidity radiative effect (HRE) accounted for 64% of the total radiative warming during the heatwave, while aerosols radiative effect (ARE) and clouds radiative effect (CRE) accounted for 20% and 16%, respectively. Moreover, HRE led to a night-time increase of 2-m temperature up to 6.5 °C. These findings suggest that the combination of strong warming during the hottest months of the year and water vapour greenhouse effect may lead to severe heatwaves in the Sahel region.

Similarly, Guigma et al. (2020) investigated the fundamental thermodynamic causes of Sahelian heatwaves by analysing five different thermal indices from the fifth generation of the European reanalysis (ERA-5). The authors used temperature (T), the heat index (HI), the Steadman non-radiant Apparent Temperature (AT), the Net Effective Temperature (NET) and the Universal Thermal Comfort index (UTCI) to characterize the heatwaves between February and June, which corresponds to the hot period between the cool winter season and the monsoon season. The study found that the Sahel experiences high magnitude heatwaves every year, with the eastern region

experiencing more events than the western. Daytime heatwaves last longer than night-time, but the latter events are slightly more intense than the daytime events. The authors determined the thermodynamic processes by deriving the surface energy budget (SEB) from the ERA-5 data and assessed the role of clouds during some heatwave types by deriving the cloud radiative effect (CRE). Wind speed and cloud coverage were found to increase during T, HI, and NET heatwaves, while the low-level moisture increases significantly during AT and UTCI heatwaves, thereby affecting the associated thermodynamics. Notably, the highest wind speeds were recorded during the day when the boundary layer turbulence was great, while the night had lower speeds due to the surface-atmosphere decoupling, which left the floor to nocturnal low-level jets. The authors recommend using several indices rather than a single one to avoid missing out some heatwave events that other indices could have identified (mainly two categories, temperature related and humidity related). Tropical plumes are meteorological phenomena associated with the transport of moisture from the tropics to extratropical latitudes. They are known to be elongated cloud bands that extend from the tropics into the subtropics. Specifically, they are particular type of tropical–extratropical interaction that involves the equatorward penetration of subtropical upper-level troughs, strong subtropical jet (STJ) streaks, elongated cloud bands on their equatorward side (termed tropical plumes — Tps (Knippertz and Martin, 2005). They are likely to be favourable to the build-up stage of heatwave occurrence over the Sahel.

The Sahelian heat waves and their health impacts warning (ACASIS) project with the main objective to set up an early warning system for Sahelian heatwaves adapted to the population’s health risks is implemented in Senegal and Burkina Faso. The

project focuses on determining heatwaves' dynamics, atmospheric patterns and evolution over the last decades. As a multidisciplinary consortium, three challenges were facing the project, TN prediction for health issue in the region (nocturnal temperature being disturbed by many parameters such as near surface vertical gradient, humidity and aerosol distribution, boundary layer turbulence and clouds particularly which are not well represented in climate model), environmental conditions related to heatwaves that are likely to affect human health and finally the linkage between the environmental and local conditions. This project published several paper on extreme heatwaves' dynamics in West Africa (Barbier et al., 2018; Couvreur et al., 2014; Fontaine et al., 2013; Moron et al., 2016; Oueslati et al., 2017). They focused on temperature extreme and warm day and night trends, their occurrence and associated atmospheric circulation, their characterization and related physical mechanism. But a lot remains to do in the area as there are still questions needed to answer such as the land surface feedback.

Offerle et al. (2005) in the West African Sahel were rather interested in the urban modification of the surface energy balance, especially in Ouagadougou, Burkina Faso, during the globally hot 2003 year, in February. The UHI intensity increases during the dry period in Ouagadougou and start decreasing at the rainfall onset during the study period. The energy balance flux measurements reveal that the outskirts of the city experience a higher amount of all-wave radiation due to the presence of bare dry soil, which has a higher albedo, lower heat capacity and thermal conductivity as compared to the urbanized surface. On the other hand, the material and geometry of the urban area lead to a decrease in albedo. The increased urbanization, which involves the use of non-local materials, more paving, and the

construction of taller and denser buildings, has a significant impact on the surface energy balance by reducing albedo and increasing heat storage. As a result, nighttime urban temperatures are higher. It should be noted, however, that the authors did not consider the impacts of urbanization on the rainy season. The land surface plays a crucial role in the transfer of solar radiation into the atmosphere, which is described by the surface energy balance in Eq. 2.1:

$$R_{net} = SW_{inc}(1 - ALB) + LW_{inc} - \epsilon\sigma TS^4 = LH + SH + G \quad (2.1)$$

where SW_{inc} and LW_{inc} are the incoming short-wave (Wm^{-2}) and long-wave radiation (Wm^{-2}) and ϵ , σ and TS are the surface emissivity, Stefan-Boltzmann constant and the surface temperature (K), respectively (Klein, 2016). Surface conditions such as albedo, surface temperatures, and latent, sensible and ground heat flux can be determined by these variables. Consequently, the surface can significantly affect the energy budget of the planetary boundary layer (PBL) through the transfer of sensible or latent heat to the atmosphere. However, land-atmosphere interactions play a minor role under strong synoptic forcing or for saturated or wilting point soils (Eltahir, 1998; Ferguson and Wood, 2011; Teuling et al., 2010). Klein (2016) used the Weather Research and Forecasting model (WRF) driven by reanalysis data to investigate the relevance of regional moist processes, convection and vegetation patterns for the West African monsoon (WAM) regime. The study revealed the significant role of regional atmospheric and land surface processes in changes in precipitation amounts or shifts of the monsoon rain-band, and temperature changes at smaller scales, which affect local moisture convergence or divergence, particularly in the semi-arid Sahel region of West Africa where strong gradients of soil moisture, vegetation and surface temperature exist.

Odoulami et al. (2017) conducted a study on the potential impacts of forestation on the occurrence and characteristics of heatwaves over West Africa in the future. They used the excess heat factor (EHF) and the percentile-based index (TXI) to assess the impact of forestation on the Savannah zone (area between 8° N and 12° N), under the IPCC RCP4.5 scenario, for the past (1970-2000) and future (2030-2060). The study aimed to examine the possible effects of ongoing forestation activities and the associated ecological dynamics on the occurrence and characteristics of heatwaves over the region. The study employed regional climate model (RCM) simulations to investigate the effects of forestation on the characteristics of future heatwaves in response to the altered vegetation canopy. The authors collected and simulated maximum and minimum temperatures and precipitation data from the Climatic Research Unit (CRU TS3.23) gridded at 0.5° × 0.5° horizontal resolution and the Princeton University Global Meteorological Forcing Dataset for land surface modelling (PGF), produced by the Terrestrial Hydrology Research Group of Princeton University, using the ITCP RegCM4.3 model. The results of the study showed a general increase in the characteristics of heatwaves for the RCP 4.5 emission scenario. The forestation activities are likely to increase the number and days of heatwaves over the forested zone (Savannah) and decrease them over the Sahel and along the Guinea coast. The regional climate model captured the extreme temperature thresholds, but failed to capture the spatial distribution of heatwave number, days, and duration as observed in reality, indicating the superiority of observation data in capturing the characteristics of heatwaves. Therefore, the authors concluded that specific greening or cooling methods should be used for each zone in West Africa to avoid undesirable outcomes, and that the study of the possible effects

of forestation on the characteristics of heatwaves over West Africa could provide valuable information for policymakers to make informed decisions regarding the management of the region's forest resources.

In this literature review, we have investigated the impact of land surface processes on atmospheric dynamics in West Africa, with a particular focus on heatwaves and droughts. Global warming has led to an increase in the frequency, duration, and intensity of these extreme events, with significant consequences for human health, agriculture, water resources, and ecosystems. Studies have shown that deforestation and land-use change have exacerbated heatwaves and droughts in West Africa by increasing surface temperatures and decreasing moisture availability. Ongoing forestation activities in the region may have unforeseen consequences on the characteristics of heatwaves in the future, highlighting the importance of understanding the drivers and impacts of these events to develop effective adaptation strategies. Land surface properties such as vegetation cover, soil moisture, and surface temperature play an important role in modifying the energy budget of the planetary boundary layer and affecting regional weather and climate. Studies have highlighted the importance of land-atmosphere feedbacks in the semi-arid Sahel region, which is particularly prone to surface-atmosphere interactions. The literature reviewed used various methods to examine land surface processes, including regional climate models, remote sensing, and observational data. Overall, this literature review underscores the critical role of land surface processes in shaping weather and climate in West Africa. These findings highlight the need to consider land surface processes in climate modelling and policy decisions to develop effective adaptation

strategies and mitigate the adverse effects of extreme events such as heatwaves and droughts. Future research should continue to explore the complex interactions between land surface processes and atmospheric dynamics in the region to enhance our understanding of the underlying mechanisms and develop more robust adaptation strategies.

CHAPTER 3: METHODOLOGY

3.1 Description of Study Area and Datasets

3.1.1 Study Area

The climate in West Africa is strongly influenced by a south-north gradient, resulting in significant differences in annual precipitation. These variations have led to the classification of the region into three main agroclimatic zones (Fink et al., 2017; Yaro and Hesselberg, 2016). The northernmost Sahelian zone experiences irregular annual rainfall, with a maximum amount occurring in August, and receives less than 500 mm of precipitation annually, making it a semi-arid region located at approximately 12°N – 19 °N latitude. The Sudan zone, located further south, receives between 400 mm and 1000 mm of precipitation over a period of three to five months. Finally, the tropical humid Guinea zone, located along the Gulf of Guinea, receives an annual mean rainfall of over 1000 mm and has a bimodal regime (Nicholson, 2018). Climate vagaries in the region are of great importance, particularly in light of the predominant concern of drought, as well as the effects of extreme rainfall events, which can result in rapid flooding that impacts both agriculture and urban life. Evidence suggests that the Sahel has experienced an increase in extreme rainfall, which led to unprecedented floods between 2009 and 2013 (Panthou et al., 2014; Sanogo et al., 2015). It is, therefore, necessary to address both drought and heatwaves in the region (IPCC, 2019).

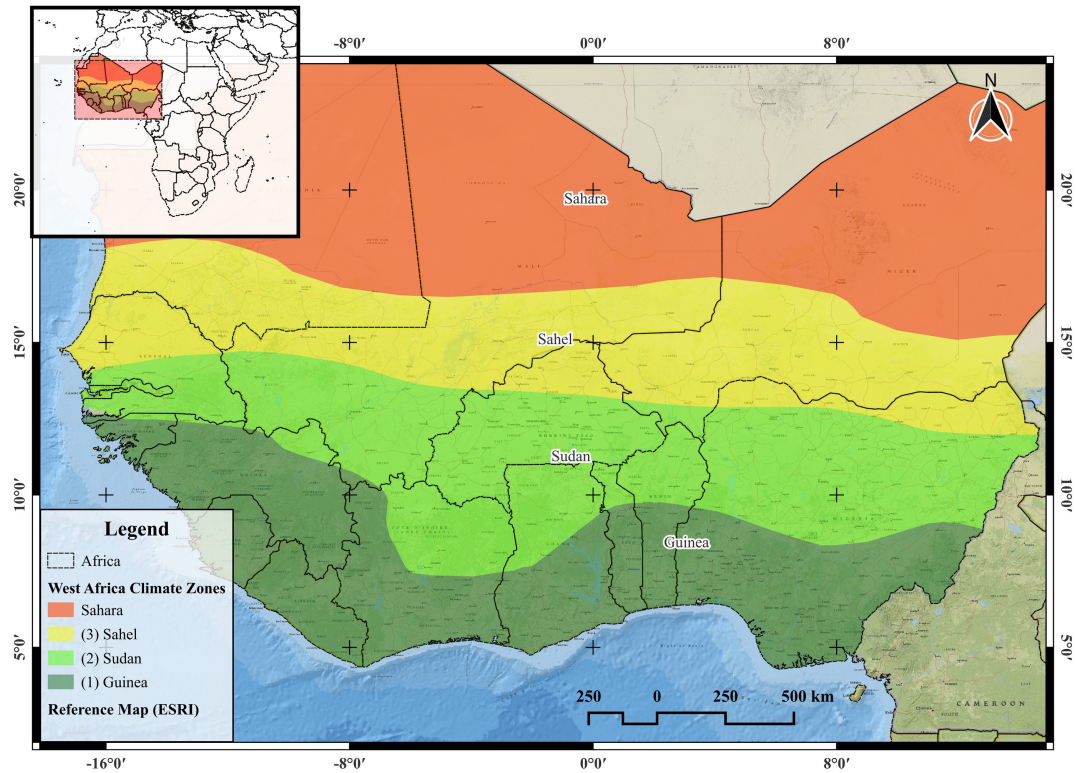


Figure 3.1: Study Area covering the agroclimatic zones (Guinea, Sudan and Sahel)

3.1.2 Observation datasets

The Global Surface Summary of the Day (GSOD) were retrieved from the National Oceanic and Atmospheric Administration (NOAA) National Centres for Environmental Information (NCEI). The latest daily summary data are normally available 1 to 2 days after the date-time of the observations used in the daily summaries. The dataset is organised from 1921 to present, over 9000 stations data. A number of parameters are available, but not all meteorological parameters are present in the database. The GSOD was used in several studies on heatwaves (Ceccherini et al., 2016; Guido Ceccherini et al., 2017). GSOD data are daily observations derived from ISD dataset (Lavigne and Liu, 2022). GSOD is quality checked but affected by

missing values, even though the data from 1973 to the present is the most complete of the dataset. GSOD observations before 1980 (in some regions) appeared to be unrealistic, constraining to some extent the use of pre-1980 data (Matsuura and Willmott, 2012). Thereof, stations with less than 80% of the available data are removed. Thirty-four (34) stations are then selected and further processed. Maximum daily temperature (T_{max}) are retrieved as well as precipitation. Due to the fact that the initial synoptic and hourly data are recorded and established in GMT, the GSOD data is also reported and consolidated based on Greenwich Mean Time (GMT, 0000Z – 2359Z).

The Integrated Surface Database, (ISD, also known as Integrated Surface Hourly, ISH (Lavigne and Liu, 2022)) is a global hourly and synoptic surface observations data compiled from different sources to an ASCII format and common data model (<https://www.ncei.noaa.gov/products/land-based-station/integrated-surface-database>). ISD includes numerous parameters such as cloud cover and various other parameters as recorded by weather stations.

The GSOD and ISD data were retrieved from 1981 to 2020 for the whole region ($4^{\circ}N - 21^{\circ}N$ and $-18^{\circ}W - 16^{\circ}E$, Figure 3.2). The ISD data is retrieved solely for the Universal Thermal Climate Index (UTCI) computation because the GSOD data, which is a daily averaged dataset, does not have all the required parameters (e.g., cloud cover fraction) for UTCI computation. The total cloud fraction is then collected along with the air temperature (T_a), relative humidity (RH) and wind speed (w_s) at 12:00 and 18:00 UTC. Only the stations with a minimum of 60% of the total cloud cover fraction available from the whole series are used. Here, 36 stations met

the requirements. Then, the highest UTCI of the day which is at 12:00 was selected for further analysis. The dataset was used specifically for the objective 1.

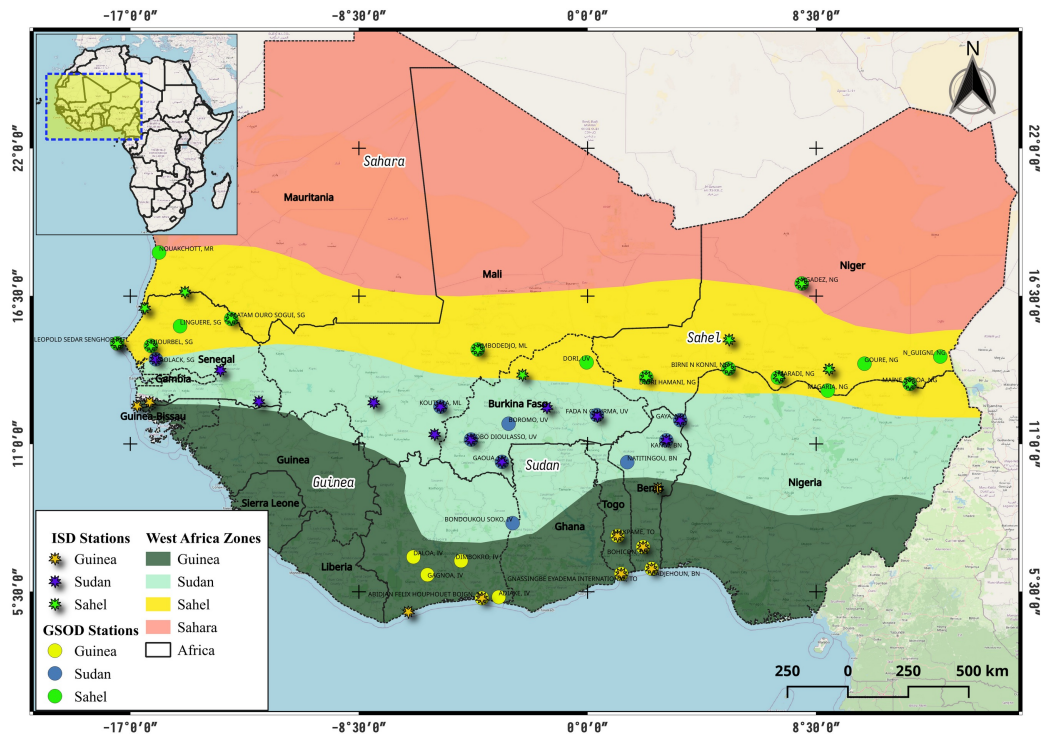


Figure 3.2: Overview of West Africa showing ISD (stars) and GSOD (rounded dots) selected stations in the climate zones (colour-shaded); Climate zones are adapted from Earth Resources Observation and Science (EROS) Centre’s Climate zones distribution

3.1.3 ERA5 Pressure Levels and SST Dataset

ERA5, the fifth generation global climate and weather reanalysis by the European Centre for Medium-Range Weather Forecasts (ECMWF), covers the past 4 to 7 decades, from 1950 onwards. It replaces the ERA-Interim reanalysis and provides hourly estimates for various atmospheric, oceanic, and land parameters by integrating model data and observations worldwide. The data is updated daily and includes sets of datasets for different research fields, including pressure levels and Sea Surface Temperature (SST). Compared to other reanalysis products, ERA5 is an

improved version of ERA-Interim, as reported by Oueslati et al. (2017), which can well capture the annual cycles and inter-annual variability of the Heat-Index in the US. ERA5 is suitable for model data validation and driving models such as the RegCM4.5 and its recent versions (Anwar et al., 2022). It accurately represents near-surface meteorological parameters like moisture, wind, etc. ERA5 was used for evaluating 2m air temperature, sensible, and latent heat fluxes (Hersbach et al., 2020). This dataset was mainly used for the objective 3 to drive the coupled RegCM-CLM model. It provides hourly estimations of land, atmospheric and oceanic variables at $0.25^\circ \times 0.25^\circ$ grid resolution with 137 vertical levels (~ 80 km in altitude). So the ERA5 dataset was used because of the horizontal grid and the vertical levels. Parameters such as the convective rain rate, surface solar net radiation, surface thermal downward etc. for the RegCM model simulation at 20 km resolution are used for the simulation.

3.1.4 ERA5-Land Hourly Dataset

ERA5-Land is an enhanced resolution of ERA5 dataset. Air temperature and humidity are used as atmospheric forcing to control the simulation. ERA5-Land dataset is widely used for diverse analysis related to climate change and climate variability. ERA5 is a gridded dataset projected on a regular latitude-longitude grid of $0.1^\circ \times 0.1^\circ$ (~ 9 km). The dataset cover many climate parameters at the surface. The spatial and temporal resolution of this dataset makes it suitable for all kinds of land surface applications (Muñoz-Sabater et al., 2021). The data is retrieved from 1981 to 2020 and several parameters were collected: 2 m Temperature, 2 m dew-point temperature, surface pressure, surface solar radiation downwards, total

precipitation and 10 m U and V wind components. The dataset is collected hourly over the whole West Africa (4°N – 21°N and -18°W – 16°E). ERA5-Land dataset has been proven to be reliable for climate analysis and especially for Drought and heatwaves (Dirmeyer et al., 2020; Li and Wang, 2022; Wang et al., 2022). ERA5-Land dataset is proven to be close to station (observation) dataset than the ERA5 in some area. Even though there are some differences especially in the highest altitudes, they highly match the observation data (Barbosa and Scotto, 2022). They are recently used for heatwaves detection and analysis (Ye et al., 2022). These datasets are used for the objective 2 analysis over West Africa on heatwaves causes.

ERA5-Land is preferred because the land surface plays a crucial role in the coupled Earth-atmosphere system. The resolution offered by the land component of ERA5 (spatially 0.1° x 0.1° or approximately 9 km and temporally hourly) is better suited for detailed analysis (Muñoz-Sabater et al., 2021). The 2 m temperature, 2 m dew-point temperature, 10 m wind components ((\vec{U}) and (\vec{V})) and the solar downwelling short-wave radiation are retrieved and re-gridded to 0.25° x 0.25° for computation of CumHeat and WBGT and later comparisons with the ERA5 Thermal Comfort. ERA5-Land is used in the present work to compute heatwave metrics.

3.1.5 Year of Polar Prediction (YOPP — Temperature tendency)

The Year of Polar Prediction (YOPP) is the flagship initiative of the Polar Prediction Project (PPP), which operates under the World Weather Research Programme (WWRP) of the World Meteorological Organization (WMO). Due to the polar regions' increased sensitivity to climate change and their unknown effects on regional and global weather patterns and social and economic impacts, investing in

international polar research is imperative. The primary objective of the YOPP is to improve the understanding of Earth-system processes at high latitudes and to enhance numerical models' representation. The European Centre for Medium-Range Weather Forecasts (ECMWF) archives provide freely available atmosphere, ocean, and sea-ice output from the world's leading global medium-range numerical weather prediction system datasets. The non-operational output provided by the ECMWF permits a more in-depth analysis of individual model process contributions to the evolution of state, facilitating the identification and characterization of key sources of model error (Bauer et al., 2020). The YOPP core phase and MOSAiC field campaign spanned from July 2017 to October 2020, allowing for the study of consecutive seasons in consecutive years. However, only the July 2017 to March 2020 period is available on the ECMWF for surface, pressure, and model levels in the forecast-type datasets. The dataset has its identifiers and is located in ECMWF's MARS archive. It consists of 3-hourly output at an 18 km resolution in the atmosphere/land-surface and 1/4 degree resolution in ocean and sea-ice covered areas. A research experiment using the same set-up runs parallel to the operational system and outputs additional fields for the first 48 hours (with a 3-hour frequency, 0 - 48 h) containing tendencies of the atmospheric physical and dynamical processes (see Table 3.1). The sum of these tendencies explains the change of state between consecutive model output times. The tendencies allow users to break down the overall change of state into the contribution from each process.

The process tendencies refer to the accumulated values from the start of the forecast. As a result, the tendencies at the 24th forecast step represent the accumulated tendencies over the first 24 hours, or a day, of the model integration. In this study, the

researchers used the tendencies from forecast step 0 to 24 hours for comparing with temperature evolutions. The model level parameters involve temperature tendency terms that are listed in Table 3.1. This dataset is utilized for the objective 2 analysis.

Table 3.1: Temperature Tendency terms and description.

| Long Name | Short Name | Description |
|---|-------------------|--|
| Temperature tendency from Dynamics | ttendd* | Refers to the change in temperature mainly caused by the horizontal and vertical motion |
| Temperature tendency from Radiation | ttendr* | Change in temperature of the atmosphere due to short and long-wave radiation, the absorption and emission of radiation by atmospheric gases, clouds, and the Earth's surface |
| Temperature tendency from Subgrid Orography | ttends | Change in temperature due to the effects of unresolved topographic features on atmospheric circulation, including the generation of turbulence and gravity waves, the blocking of air flow, and the interaction with vertically propagating gravity waves. |
| Temperature tendency from Turbulent Diffusion & Subgrid Orography | ttendts | Caused by the turbulent mixing of air, as well as the influence of small-scale surface features on the atmospheric flow |
| Temperature tendency from convection (deep + shallow) | ttendcds | Change in temperature over time due to the effects of deep and shallow convection, including the vertical movement of air and the associated heating and cooling effects. |
| Temperature tendency from cloud scheme | ttendcs | Refers to the impact of cloud processes on temperature changes in the atmosphere. Clouds can absorb and emit radiation, affecting the balance of energy in the atmosphere and leading to changes in temperature. |
| Temperature tendency from Turbulent Diffusion | ttendt* | Calculated index by subtracting dT_subgrid_orog from dT_turb_diff_subgrid_orog. Refers to the change in temperature caused by the turbulent mixing of air molecules. Turbulent diffusion is the transport of mass, heat, or momentum within a system due to random and chaotic time-dependent motions. |

| Long Name | Short Name | Description |
|----------------------------|------------|--|
| Total temperature tendency | totaltt* | Calculated index by summing all 6 T-tendency terms from YOPP archive. It represents the overall change in temperature at a given location over a certain time period, taking into account the contributions from all the different physical processes. |

“*” represent the important terms or used T-tendency terms in the present case studies; The grey coloured rows are the computed terms for analysis purpose.

3.1.6 Various Sources of Gridded Datasets

Gridded datasets are also retrieved for the same period and region and remapped to the nearest grid-point of the selected stations (coordinates location). Precipitation data is retrieved from the Climate Hazards Group Infrared Precipitation with Station data (CHIRPS v2.0, $0.05^\circ \times 0.05^\circ$ — (Funk et al., 2015)). CHIRPS dataset is a second version of the satellite observations at high resolution for precipitation variations and drought monitoring analysis from 1981 to near-present. The daily dataset is retrieved for the purpose of this research work. T_{\max} is acquired from the Berkeley Earth Surface Temperature dataset (BEST, $1^\circ \times 1^\circ$ — (Rohde et al., 2013)). It is originally a gridded reconstruction of land surface air temperature, with an experimental version that provides users with daily dataset for 1880 to present. The dataset is intended to assess temperature change. The data is proven to be good because in contrast to other data sets incorporating records from roughly 5000-7000 land stations, the Berkeley data set incorporates approximately 39,000 records, making it suitable for this analysis.

The UTCI data used in this study were obtained from the ERA5-HEAT (Human thErmAl comforT, $0.25^\circ \times 0.25^\circ$) dataset, which was downloaded from the Copernicus Climate Change Service (C3S) ERA5 reanalysis dataset (Di Napoli et al., 2020). This dataset was derived using parameters from the European Centre for

Medium-Range Weather Forecasts (ECMWF). As with the observation dataset, the UTCI values were computed using 2m air temperature (T_a), 2m dew point temperature (T_d), wind speed at 10m above ground level (v_a), solar radiation, and thermal radiation at the Earth's surface. The data covers the Mean Radiant Temperature (MRT) and the UTCI, which are stored in Kelvin from 1 January 1979. The data underwent a conversion process where it was transformed from Kelvin to degrees Celsius ($^{\circ}\text{C}$) by subtracting 273.15.

The datasets cited above are used for the objective 1 and are for indices' calculation for gridded dataset.

3.2 Research Methodology

The research methodology is presented following the objectives. So, the first objective's methodology is presented, then the second and the last objective follows.

3.2.1 Spatio-temporal Drifts patterns of Drought-Heatwave with the West African Monsoon

There are numerous metrics for drought and heatwaves that are used for different reasons and different objectives. In this study the drought and heatwave metrics used are described giving the reasons why they are used.

3.2.1.1 Definitions and Characteristics of Drought indices

According to the definition provided by the World Meteorological Organization (2016) drought refers to an extended period during which the total amount of precipitation received in a particular region is below the long-term average, leading to an imbalance between water supply and demand. Based on that, the standardized

Precipitation Index (SPI) is used. It is a widely used index to characterize observed precipitation within a given timescale (monthly in this case). It is recommended (WMO, 2012) for its power, flexibility, and simplicity in calculation (uses only precipitation; (McKee et al., 1993)). The standardization of the index removes regional dependency.

In addition, the Standardized Precipitation Evapotranspiration Index (SPEI) is employed. SPEI uses the water balance principle obtained by calculating the difference between precipitation (P) and potential evapotranspiration (PET) (Beguería et al., 2014; Vicente-Serrano et al., 2010b). The PET is computed using the modified form of Hargreaves' equation (Hargreaves, 1994) as given in Droogers and Allen (2002). It includes the rainfall as a proxy for insolation to improve the estimate of PET. At the same time, SPEI has the advantages of the Palmer drought severity index (PDSI) and SPI (Wang et al., 2020). Both SPI and SPEI are multi-scalar drought metric and are employed at relatively short timescales (3-months, for meteorological drought and 6-months for agricultural drought). A longer timescale is used to include hydrological drought for water resources (12-months) (Mishra and Singh, 2010; Pei et al., 2020).

The truncation level used here for the drought index is -1. Values below -1 are reckoned a drought event, where more negative values indicate more severe drought relative to average long-term conditions (Schwalm et al., 2017). CHIRPS and BEST datasets are also used to compute SPI and SPEI indices (see the indices' classification in Table 3.2). The indices are further analysed.

3.2.1.2 Definition of heatwave and heat-stress indices

3.2.1.2.1 *The Universal Thermal Comfort index (UTCI)*

Likewise, UTCI is mainly used in this study as a human bio-meteorology parameter to measure the linkages between the outdoor environment and human heat-related conditions (Di Napoli et al., 2020, 2018). It is deemed important in this study due to the role of humidity in Sahelian heatwave (reported by Tomasini et al. (2022)). The Mean Radiant Temperature (T_{mrt}) is necessary to calculate UTCI, but it is difficult to compute with accuracy for West Africa due to the non-availability of observation data, especially the global radiation. So, the total cloud fraction is used as a surrogate to compute the global radiation and then the T_{mrt} . Within the accepted range (wind speed ranging from 0.5 m/s to 17.0 m/s), UTCI is very sensitive to wind speed but, besides T_a , also T_{mrt} strongly influences UTCI. It is expressed as follows in Eq. 3.1:

$$UTCI = T_a + Offset(T_a, T_{MRT}, U_{wind}, P_{vapour}) \quad (3.1)$$

where T_a is the ambient air temperature, T_{mrt} is the mean radiant temperature (calculated from radiation), U_{wind} is the wind speed and the P_{vapour} is the water vapour pressure or relative humidity (RH). The index is now applied on a spatial gridded data covering the whole West Africa. This is to determine the duration, intensity, and most importantly here, the spatial extent of heatwave. The UTCI is a heat stress index that has been developed with several important features in mind. Firstly, it is designed to be thermophysiologicaly significant across the entire range of heat exchange. Additionally, it is applicable in all climates, seasons, and scales, which makes it a useful tool for a range of applications in human bio-meteorology, including daily forecasts, warnings, regional and global bio-climatic mapping,

epidemiological studies, and climate impact research. Moreover, the index is independent of individual characteristics such as age, gender, specific activities and clothing, making it a versatile and reliable tool for use in diverse contexts. These characteristics make it well-suited for the case study at hand.

In the present case study, the Rayman model is used for the computation of UTCI (Matzarakis et al., 2010, 2007). The model considers cloud coverage in octas as a replacement for radiation, with specifically used parameters (air temperature, wind speed, relative humidity/water vapour). There are particular requirements for every location of each station, which are the geographical latitude, longitude and the elevation (see Table 3.2 for classification).

The Rayman Model: Matzarakis et al. (2010, 2007) proposed the Rayman Model as a tool to calculate the Mean Radiant Temperature (T_{mrt} °C) and thermal indices, which are used in human-bio-meteorology. T_{mrt} is an important parameter that summarizes the impact of all short- and long-wave radiation fluxes and represents the equivalent surface temperature of a perfect black and equal surrounding environment. It summarizes the effect of all the different short- and long-wave radiation fluxes. Although T_{mrt} cannot be directly measured, it can be calculated based on different measured parameters. The Rayman Model employs the global radiation $G(\frac{W}{m^2})$ to calculate the T_{mrt} using time, date, geographic position, and cloud cover. In this model, cloud cover is measured on an octas scale, where 0 represents clear sky and 8 represents an overcast sky. The octas scale is a convenient way to quantify cloud cover and is widely used in meteorology and climatology. It is based on dividing the visible sky into eight equal parts and estimating the fraction of

the sky covered by clouds. The hypothesis is that direct solar irradiation assumes a clear sky with no clouds.

3.2.1.2.2 *Cumulative Excess Heat (CumHeat)*

A heatwave is a prolonged period of hot weather above a temperature threshold, spanning 3 or more days over an area. As in Perkins-Kirkpatrick (2020), a heatwave is defined here as a period of at least three successive days when daily T_{\max} is above the daily threshold for each calendar day (90th percentile for a 31-day moving window surrounding this day) for the reference period 1981–2010. The cumulative (excess) heat (CumHeat) is calculated as the accumulation of the heat difference between a heatwave day and the temperature threshold of the 90th percentile of the corresponding calendar day. In contrast to Europe, solar radiation intensity is generally high all through the year in West Africa and heatwaves can occur in any season (Russo et al., 2016); so CumHeat is applied across all heatwave days in the year (see the classification of heatwaves based on the Russo heatwave classification in Table 3.2). The Cumulative Excess Heat (CumHeat) is applied to the maximum temperature (gridded and observation datasets). It is also applied to the UTCI and the WBGT. This was done to make all the indices comparable and avoid disparities. The formula is expressed as:

$$Heat_{cum} = \sum_1^n T_{anom} \quad (3.2)$$

The equation involves three variables, namely $Heat_{cum}$, n , and T_{anom} , where $heat_{cum}$ represents the cumulative heat exposure, n denotes the number of heatwave days in a given year, and T_{anom} represents the temperature anomaly relative to the calendar-day 90th percentile on a specific heatwave day. The $Heat_{cum}$ or CumHeat metric utilizes

heatwave days rather than the total temperature of days surpassing moderate extreme thresholds, as suggested by Russo and Sterl (2011). This method avoids overstating the heat exposure, as it considers only the excess heat over a specific number of consecutive days that defines a heatwave (Perkins et al., 2012). The indices are then compared to each other in the different climate zones.

Table 3.2: Indices classification categories: a) SPI, SPEI severity index and levels; b) CumHeat index and levels of intensity adapted from Zittis et al.' HWMIId classification (Zittis et al., 2021) and c) UTCI conventional stress levels

| Categories | Index value |
|---|---------------------------|
| a) SPI and SPEI (for Drought values above -1 are not considered) | |
| Extremely wet | ≥ 2 |
| Very wet | < 2 to ≥ 1.5 |
| Moderately wet | < 1.5 to ≥ 1 |
| Near normal | < 1 to ≥ -0.99 |
| Moderately dry | < -0.99 to ≥ -1.49 |
| Severely dry | < -1.49 to ≥ -1.99 |
| Extremely dry | < -1.99 |
| b) Cumulative (excess) Heat; values below 2 are not considered) | |
| Normal | 0 – 5 |
| Moderate | 5 – 10 |
| Severe | 10 – 15 |
| Extreme | 15 – 30 |
| Very extreme | 30 – 50 |
| Super extreme | 50 – 80 |
| Ultra extreme | > 80 |
| c) Heat-stress (UTCI; values below 9 are not considered (Zare et al., 2019)) | |
| No thermal stress | +9 – +26 |
| Moderate heat-stress (HS) / caution | +26 – +32 |
| Strong heat-stress / Extreme caution | +32 – +38 |
| Very strong HS | +38 – +46 |
| Extreme heat-stress / Danger | $> +46$ |

The CumHeat is applied to the UTCI and the WBGT indices after extracting the calendar day 90th percentile threshold of daily UTCI for comparison with the T_{\max} CumHeat previously computed. The computed UTCI from the Rayman model for station datasets are compared with the retrieved indices from ERA5-HEAT (gridded dataset). Then the spatial gridded datasets (CumHeat T_{\max} and CumHeat WBGT from

ERA5-LAND with CumHeat UTCI from ERA5-HEAT) are compared between themselves in the objective 2.

The table Table 3.3 provides a comprehensive description of the indices employed to achieve the study's objectives, outlining the relevant climate parameters used in their computation, along with the corresponding equations.

Table 3.3: Description of the computed Indices with their input parameters, equations and references. For SPI ; $c_0=2.515517$, $c_1 = 0.802853$, $c_2 = 0.010328$; $d_1 = 1.432788$, $d_2 = 0.189269$, $d_3 = 0.001308$. For SPEI $\omega = \sqrt{-2 \ln(p)}$, $c_0 = 2.515517$, $c_1 = 0.802853$, $c_2 = 0.010328$; $d_1 = 1.432788$, $d_2 = 0.189269$, $d_3 = 0.001308$. CumHeat: T_{anom} is the temperature anomaly relative to the 90th percentile calendar-day on a given heatwave day.

| N° | Index Name | Description/Reference | Variables | Equation |
|----|--|--|--|---|
| 1 | Standardized Precipitation Index (SPI) | Measure of drought on time scales of 3, 6 and 12 months. (McKee et al., 1993) | <ul style="list-style-type: none"> P: Precipitation S: is the probability density plus or minus coefficient. If $F > 0.5$, then $S=1$; if $F \leq 0.5$, then $S = -1$ | $SPI = S \frac{t - (c_2 t - c_1) + c_0}{[(d_3 t + d_2)t + d_1]t + 1}$ |
| 2 | Standardized Precipitation Evapotranspiration Index (SPEI) | Measure of drought on time scales of 3, 6 and 12 months. (Vicente-Serrano et al., 2010a) | <ul style="list-style-type: none"> P: Precipitation PET: Evapotranspiration $D_i = P_i - PET_i$, with D_i the moisture deficit. | $SPEI_i = \omega - \frac{c_0 + c_1 \omega + c_2 \omega^2}{1 + d_1 \omega + d_2 \omega^2 + d_3 \omega^2}$ |
| 3 | Universal Thermal Climate Index (UTCI) | The equivalent perceived temperature. The index is suitable as a method for calculating outdoor thermal comfort levels (Blazejczyk et al., 2012; Bröde et al., 2012) | <ul style="list-style-type: none"> T_{max}: maximum temperature (deg C) ws: wind speed (m/s) T_{mrt}: mean radiant temperature (deg C) or cloud cover/global radiation RH: relative humidity ratio (0 – 100) or water vapour | $UTCI = T_a + Offset(T_a, T_{MRT}, U_{wind}, P_{vapour})$ <p>Polynomial accessible at https://james-ramsden.com/calculate-utci-c-code/</p> |

| N° | Index Name | Description/Reference | Variables | Equation |
|----|--|---|--|---|
| 4 | Cumulative (Excess) Heat (CumHeat or Heat _{cum}) | It is the sum of the anomaly between each heatwave day and the calendar-day 90 th percentile across all heatwave days in the year (Perkins-Kirkpatrick and Lewis, 2020). | Applied to : <ul style="list-style-type: none"> • T_{max}: maximum temperature • UTCI: Universal Thermal Climate Index | $\text{Heat}_{\text{cum}} = \sum_1^n T_{\text{anom}}$ |

3.2.1.3 Statistical Analysis

The Mann Kendall monotonic trend (Kendall, 1970; Mann, 1945) test with the Sen's Slope (Sen, 1968) are used to determine trends in climate zones and linear trends are used for the plots. Statistical performance tests are applied to assess the differences between gridded and the observation datasets. Working with and comparing several datasets compels to the use of Bonferroni correction of p-values (the p-values are multiplied by the number of comparisons), the Games-Howell pairwise comparison (multiple pairwise comparison test between datasets in an inhomogeneity of variances' case). The distribution of the data is analysed considering the median differences (non-parametric difference metrics (Patil, 2021)). Figure 3.3 explains the different statistical analysis on the plots and how to interpret them. For example in the Figure, are the t_{welch} which is Welch's one-way ANOVA parametric test with the test used and the statistics; the p-value with the significance level, the effect size type (ANOVA's Omega — ω squared) and its estimate (represent how much variance in the variables is accounted for), the confidence interval (CI at 95%) and finally the number of observation (nobs). At the bottom are the Bayesian reporting style with the logarithm Bayes Factor, the posterior type, estimate, intervals and prior type.

To compare the results of Universal Thermal Climate Index (UTCI), the Mean absolute error (MAE), coefficient of determination (R^2), and Root Mean Squared Error (RMSE) are employed as performance evaluation metrics.

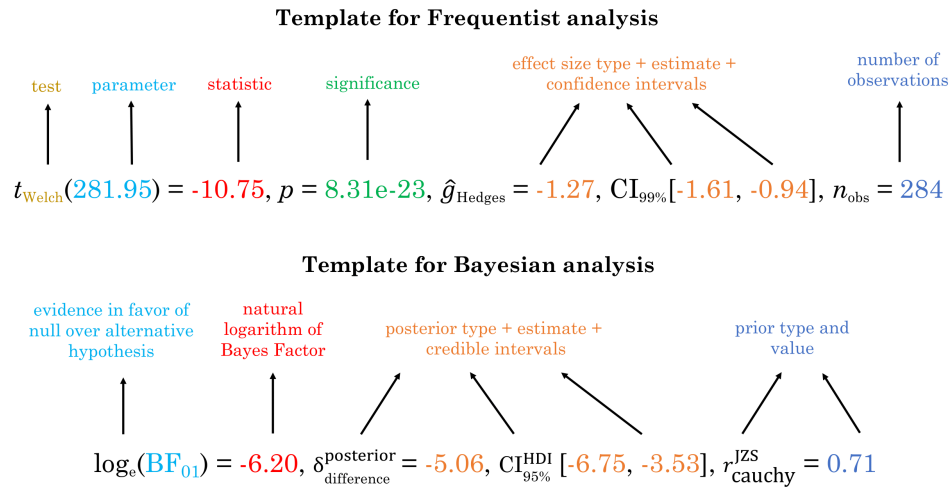


Figure 3.3: Statistical reporting template using results from Welch’s t-test. At the top of each plot is the statistical report; (Patil, 2021)

3.2.1.4 Combined Analysis of Drought and Heatwave

Considering that a heatwave is a hot period of consecutive days with $T_{\text{max}}/\text{UTCI}$ greater than the 90th percentile and a drought is on a monthly scale (3, 6 and 12-month), this work used a simple and effective compound drought-heatwave (D-HW) event detection. Thus, a D-HW event is defined as a heatwave episode occurring during a month under drought conditions (a month with an associated 3, 6 or 12-month SPI/SPEI value ≤ -1 and $\text{CumHeat } T_{\text{max}}/\text{UTCI} \geq 2$) (Geirinhas et al., 2021; Mukherjee and Mishra, 2021). Here, the different time scales are preserved. This could show which of the drought scales (associated to meteorological, agricultural and hydrological drought) and drought index (SPI or SPEI) has experienced more (or intense) heatwave. The datasets are compared for D-HW co-occurrence differences. The frequency trends are also assessed.

3.2.2 Synoptic and Boundary layer scale Dynamics responsible for Heatwave in West Africa

In this study, the Universal Thermal Climate Index (UTCI) is used with the Wet-Bulb Globe Temperature (WBGT) and the Maximum Temperature to which is applied the Cumulative Excess Heat (CumHeat). The CumHeat is applied to not only the maximum of the temperature (or UTCI or WBGT) but to the Daytime (night-time) heatwaves. The average from 06:00 to 18:00 defines the daytime and from 18:00 to 06:00 next day defines the night-time heatwave for each index.

3.2.2.1 The Wet-Bulb Globe Temperature (WBGT)

The Wet-Bulb Globe Temperature (WBGT) is developed more than 50 years ago (during the 1950s) and was first used to control heat illness (during physical exercises) in training camps of the United States Army and Marine Corps. So the WBGT is used as a replacement to the “effective Temperature including Radiation component” (ETR) to measure Human thermal discomfort. Various indices are used to measure discomfort in both indoor and outdoor environments, each with its own advantages and drawbacks (Budd, 2008). The WBGT is commonly used as a heat index for outdoor workplaces, as it is calculated using standard meteorological data (Zare et al., 2018). The WBGT is used in this work because it is a well constituted heat index for workplaces. Even though the UTCI uses the heat balance mechanisms of human body, it does not account for differences in metabolic rates during work, or the impact of specialized protective clothing, or even the constant change in position and movement during real work situations (Lemke and Kjellstrom, 2012). The

WBGT outdoor (takes into account the dew point temperature, air temperature, solar radiation and the wind speed) is calculated based on the following equation (Eq. 3.3):

$$WBGT = 0.7 T_{nwb} + 0.2 T_g + 0.1 T_a \quad (3.3)$$

where T_{nwb} is natural wet bulb temperature T_g is radiation temperature and, T_a is dry temperature. From the equation it comes out that the natural wet bulb temperature (T_{nwb}) is the largest component (70%) of the WBGT, but the T_g can be up to three times higher than T_{nwb} . So on balance both components can have a similar influence on WBGT (Lemke and Kjellstrom, 2012). On the other side, low wind speeds have a considerable effect on T_g .

3.2.2.2 Recall of UTCI and CumHeat methods

The CumHeat method is described in the previous objective as well as the UTCI. They were used in this objective for spatio-temporal analysis and comparison. Furthermore, the Cumulative Excess Heat is applicable to both daytime and night-time temperatures, as well as to other heat indices like UTCI and WBGT.

3.2.2.3 Temperature tendency

The temperature tendency terms are used to understand the causes of heatwaves in West Africa. The YOPP dataset is available only from 2018 to 2020 in the core phase. The six tendency terms are evaluated during the heatwave case studies with the temperature anomaly and wind direction. The case studies covered January – March 2018, November – December 2019 and January – March 2020. The pre- and post-monsoon heatwaves are then covered in these case studies. The analysis considered model levels converted to nearest-pressure levels at 1000 hPa, 925 hPa, 800 hPa, 700 hPa and 500 hPa, 400 hPa, 300 hPa, 250 hPa and 200 hPa using the

geo-potential height for vertical profiles. Only the 925, 850 and the 700 are used for the analysis.

The temperature tendencies are analysed to determine the terms that contribute to the selected case heatwaves. For that purpose, the total tendency is computed from the sum of all the 6 tendency terms. The temperature horizontal advection is also computed from the wind (\vec{u} and \vec{v}) components and the temperature at the same levels. Temperature gradients and wind vectors together can give the temperature advection, resulting in a time-rate of change of temperature at a given location. The rate of change of temperature with respect to time at a given location may be estimated using the temperature gradient and the wind vector. The formula is given in Eq. 3.4 and Eq. 3.5 hereafter:

$$-V \cdot \nabla T = - \left(u \frac{\partial T}{\partial x} + v \frac{\partial T}{\partial y} \right) \quad (3.4)$$

The discretised advection is used to plot the above formula on a map. The formula is:

$$- \left(u \frac{\partial T}{\partial x} + v \frac{\partial T}{\partial y} \right) = - \left(u \frac{\Delta T}{\Delta x} + v \frac{\Delta T}{\Delta y} \right) \quad (3.5)$$

The temperature gradient is a vector whose magnitude is the rate of change of temperature with distance $\frac{\Delta T}{\Delta d}$ and points in the direction of the greatest decrease in temperature. This is because temperature typically decreases as we move in the direction of the temperature gradient. However, it's important to note that temperature advection is not solely a cooling or warming process based on the temperature gradient. In fact, adiabatic processes, such as expansion and compression, can also cause changes in temperature. For instance, when air rises and

expands, it cools, and when it descends and compresses, it warms. Therefore, the temperature can change even when moving along the temperature contour (in a direction tangent to the contour at that point). The direction of the greatest increase is perpendicular to the temperature contour at the location where the gradient is determined. The computation of the gradient involves the use of central differences that are accurate up to the second order in interior points, while either forward or backward one-sided differences are used at the boundaries that are accurate up to the first or second order.

A box area centred on the case study heatwave development is used to extract the time series of each of the terms that are found important in the temperature change. These are the used temperature tendency by dynamics (*ttendd*), temperature tendency by radiation (*ttendr*) and the temperature tendency by turbulent diffusion (*ttendt*). The total tendency (*totaltt*) is also used, as well as the Meridional (Merid) and Zonal (Zonal) advections. Finally, another variable is added: the temperature tendency from dynamics minus the total horizontal advection, referred to as the residual temperature tendency dynamics or “*rttd*” written as in Eq. 3.6:

$$rttd = ttendd - total . adv \quad (3.6)$$

It represents the remaining contribution to the temperature tendency dynamics after accounting for the effects of horizontal advection, which is assumed to be the vertical advection in this context.

Vertical profiles are afterwards used to analyse the behaviour of each of the tendency terms by altitude. Measuring the vertical profile of temperature tendencies can help to determine the relative contributions of different physical processes to atmospheric temperature changes, such as radiation, convection, and advection. This information

is useful for improving weather forecasting models and understanding the mechanisms driving the changes.

3.2.2.4 Statistical Analysis

The daytime (night-time) average daily gridded data over West Africa are re-gridded from $0.1^\circ \times 0.1^\circ$ to $0.25^\circ \times 0.25^\circ$ to fit with the ERA5-HEAT dataset. From the ERA5-Land, the CumHeat T_{\max} and the WBGT are computed spatially. Case studies are selected from January 2018 – December 2020. The case studies are selected from 2018 to 2020 because of the availability of the Year of Polar Prediction (YOPP) dataset. Indeed, the YOPP dataset is available in its core phase from 2018 to 2020 in the ECMWF archives. Furthermore, the absolute and Relative differences are computed between indices to determine the monthly differences and the affected area. The absolute and relative difference between two indices (t and x) are expressed in Eq. 3.7 as:

$$Absdiff(t, x) = i_1(t, x) - i_2(t, x) \quad (3.7)$$

This equation represents the absolute difference between two images or signals of two datasets (i_1 and i_2) at a specific time t and location x. The function calculates the absolute value of the difference between the pixel values of two datasets at each corresponding location (t, x).

$$Reldiff(t, x) = \frac{i_1(t, x) - i_2(t, x)}{\max(i_1(t, x) - i_2(t, x))} \quad (3.8)$$

The relative change (in Eq. 3.8) expresses the absolute change as a percentage of the value of the index in the first index. Here, the equation is calculating the relative difference between the pixel values (i_1 and i_2) at each corresponding location (t,

x) in a datasets. The numerator is the absolute difference between the pixel values at that location. The denominator is the maximum absolute difference between the two datasets at that location. Dividing the absolute difference by the maximum absolute difference normalizes the difference between the two images and gives a value between -1 and 1, which represents the relative difference between the two datasets at that location.

In this study, correlation analysis is conducted to investigate the relationship between the tendency terms and the temperature meridional and zonal advection. The closely correlated terms are further cross-correlated to characterize their relationship. Cross-correlation analysis involves exploring the relationship between two time series (y_t and x_t), which may be related to past lags of the x -series. The sample cross-correlation function (CCF) is used to identify lags of the x -variable that may be useful predictors of y_t . In this study, it is used to understand type of correlation between $x_{(t+h)}$ and x_t for $h = 0, \pm 1, \pm 2, \pm 3$, and so on. When one or more $x_{(t+h)}$, with positive lags (h), are predictors of y_t , it is referred to as x leads y . In the opposite case, with a negative lag (h), it is a correlation between the x -variable at a time before t and the y -variable at time (t). Then, when h *negative*, are predictors of y_t , it is referred to as x leads y . In this case, it is to determine whether change in temperature advection leads to change in tendency.

Furthermore, on the different temperature tendency variables, a Principal Component Analysis (PCA), also known as Empirical Orthogonal Function Analysis (EOF), is a statistical technique used to identify patterns in high-dimensional data, applied to detect the general tendency and contribution of each of the variable to the selected

heatwave cases (Jiang et al., 2020). It is a method of dimensionality reduction that transforms the data into a smaller number of uncorrelated variables called principal components (PCs), while still retaining the most important information in the original data. PCA identifies the directions of maximum variance in the data and projecting the data onto these directions, thus creating the principal components. The first PC captures the largest amount of variation in the data, followed by the second PC, and so on. Each PC is a linear combination of the original variables, with coefficients known as loadings. PCA is commonly used in various fields such as meteorology, economics, and biology to identify underlying patterns in large datasets. Overall, PCA is a powerful technique for exploring the structure of complex data sets and extracting the most important information, while reducing the dimensionality of the data.

3.2.3 Land Atmosphere Moisture (Energy) Fluxes in Different LULC Types

To achieve this objective, the Universal Thermal Climate Index (UTCI) is used with the Wet-Bulb Globe Temperature (WBGT) and the Maximum Temperature to which is applied the Cumulative Excess Heat (CumHeat). The CumHeat is applied to Daytime (night-time) heatwaves. The indices are computed on the RegCM-CLM model simulation outputs. The average from 06:00 to 18:00 defines the daytime, and from 18:00 to 06:00 the next day defines the night-time heatwave for each index as described in the previous objective. Case studies are also selected from January 2018 – December 2020 to understand the moisture and energy budget during heatwave events in West Africa.

3.2.3.1 The Regional Climate Model (RCM) Simulation

According to the American Meteorological Society glossary, a regional climate model (RCM) is a computational model used for climate prediction, which is constrained by lateral and oceanic conditions from a general circulation model (GCM) or observation-based data set (reanalysis). It aims to simulate the atmospheric and land surface processes, while also considering various factors such as high-resolution topographical data, land-sea contrasts, surface characteristics, and other elements of the Earth-system. [From the AMS site at: http://glossary.ametsoc.org/wiki/Regional_climate_model]. Therefore, an RCM has the capability to generate high-resolution outputs within a specified region. In RCMs, the initial conditions are defined and controlled by lateral atmospheric boundaries and time-varying lower surface boundaries. Consequently, global reanalysis or GCM can be downscaled in an RCM simulation to enhance the regional representation of climate variability. (Elguindi et al., 2014). In GCMs the Land-Atmosphere interface is supplied with more than 30% of Earth surface, but this percentage can be greater in RCMs domains. The specification of boundary conditions can have a substantial impact on the exchange of mass, momentum, and energy between the land surface and the atmosphere. Consequently, this can affect various prognostic variables, including surface temperature, precipitation, and the distribution of atmospheric water vapour and clouds (Steiner et al., 2005). The differences between RCMs and GCMs mainly arise due to the stronger and more realistic topographic forcing in RCMs, which results in changes in circulation and moisture flux (Gao et al., 2008). RCMs have the capability to represent atmosphere-surface energy exchanges at fine

scales, making them a valuable tool for studying the assessment of heatwaves and land use/cover types.

In this study, the Abdus Salam International Centre for Theoretical Physics (ICTP) Regional Climate Model version 4 (RegCM4.7) is employed for simulations due to its various relevant land-surface schemes. The model is detailed by Giorgi et al. (1993a, 1993b) and Giorgi and Shields (1999). The Non-hydrostatic core is employed coupled with the Community Land Model (CLM). The Biosphere-Atmosphere Transfer Scheme (BATS by Dickinson et al. (1993)) has been replaced by the third generation model (CLM), which is a community model developed to improve several components of widely used land surface schemes. (Dai et al., 2003; Oleson et al., 2008). The version of CLM used for the coupled model is RegCM4.7-CLM4.5, and it includes the CLMU4.5 (CLM Urban scheme) that draws on urban land-use fraction data from the LandScan2004 dataset to provide urban ravine factors and surface features. (Jackson et al., 2013). The configuration of the model is described in Table 3.4. The CLM4.5 has incorporated many recent scientific advances in understanding and representing land surface processes, expanded model capabilities, and improved surface and atmospheric forcing datasets, similar to its predecessor CLM4.

The CLM4.5 model has undergone several updates to improve its accuracy. The updates include enhancements to the canopy radiation scheme, canopy scaling of leaf processes, and photosynthesis processes. Additional updates have been made to the wetland units, which have been replaced by surface water store, facilitating the modelling of prognostic wetland distribution. To calculate surface energy fluxes, the model employs distinct methods for each type of land cover, as described by Bonan

et al. (2012, 2011). The model simulates numerous processes, such as surface characterization, absorption, reflection, and transmittance of solar radiation, absorption and emission of long-wave radiation, momentum, sensible heat (ground and canopy), and latent heat (ground evaporation, canopy evaporation, transpiration) fluxes, heat transfer in soil and snow (including phase change), urban energy balance and climate, crop dynamics and irrigation, land cover and land use change (including wood harvest), and dynamic global vegetation distribution.

The Figure 3.4 presents the elevation of the model, where the highest elevations are located in the Eastern part of the region and the lowest in the Coastal part that covers almost all the southern and western parts. But in the Guinea, there are relatively high elevations around the Guinea, Liberia, and Sierra Leone and also around the Atakora mountains in across Togo, Benin and the western centre of Nigeria. This configuration has an effect on the heatwave and especially moisture availability and advection. The rectangular strips are the climate zones defined for further analysis.

Unlike the previous version CLM4, CLM4.5 introduces several urban density classes to the urban land unit to enhance the modelling of urban areas. This development allows for a more comprehensive simulation of the urban environment and, in particular, the temperature of inhabited regions within a climate model. The urban parametrization of CLM4.5 (CLMU4.5) includes a detailed description of urban canopy heat and air-conditioning, which is a critical component of the model.

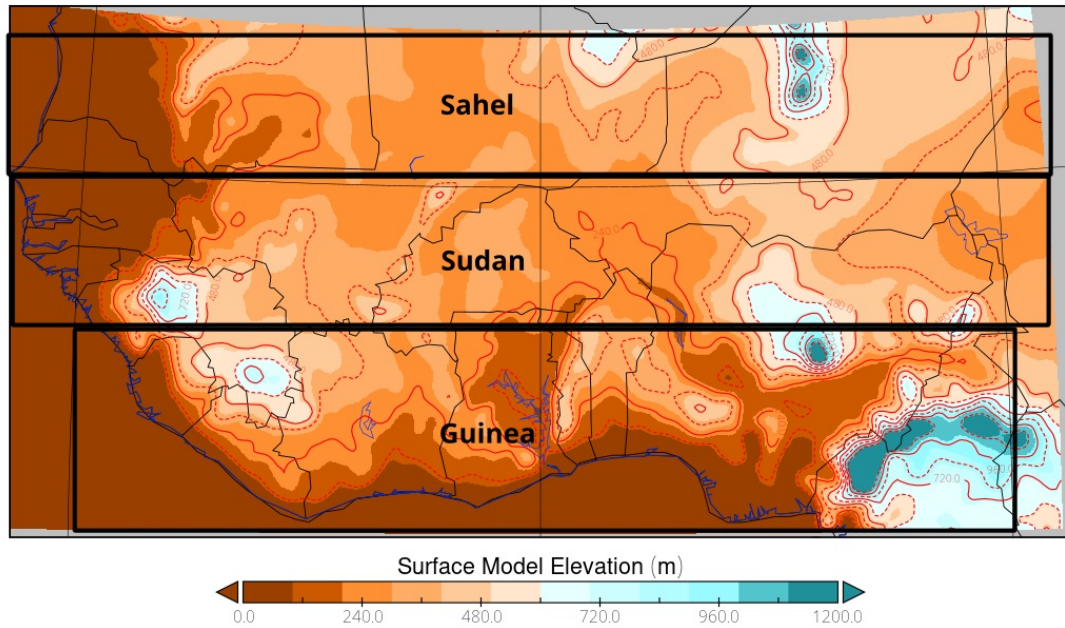


Figure 3.4: Grid location in the model domain with model elevation at 20 km resolution. The rectangular strips in the plot represent the different climate zones. From bottom to top are the Guinea zone, the Sudan and the Sahel

The city parametrization of CLM4.5 is constructed using a canyon-like design for the city zones, which is conceptually comparable to the single-layer urban canopy model of the SLUCM (Kusaka et al., 2001; Oleson et al., 2013). The model is able to simulate the effects of urban surfaces on surface characteristics parameters, including air temperature, building roof temperature, building wall temperature, and road temperature. Table 3.4 provides a summary of the model configuration used in this study.

Table 3.4: Coupled RegCM-CLM set-up, parametrization, and data used

| Model parameter | Set-up |
|---|---|
| RegCM | Version 4.7 |
| Dynamics | Non-Hydrostatic core |
| Vertical levels and Model top | 23 layers; 50 hPa |
| Map projection | Normal Mercator |
| Planetary Boundary layer | (Holtslag et al., 1990) |
| Cumulus parametrization | MIT-Emanuel scheme (Emanuel, 1991) |
| Microphysics parametrization | Subgrid Explicit Moisture Scheme (SUBEX; (Pal et al., 2000)) |
| Radiation parametrization | The National Center for Atmospheric Research (NCAR), Community Climate System Model (CCM3) (Kiehl et al., 1998) |
| Ocean flux parametrization | (Zeng et al., 1998) |
| Time step | 10 |
| Initial and lateral boundary conditions | ERA5 0.25° x 0.25° Reanalysis dataset (Dee et al., 2011) |
| Soil moisture initialization | CPC Soil Moisture V2 (van den Dool et al., 2003) |
| Topography data | The Global Multi-resolution Terrain Elevation Data 2010 (GMTED2010) |
| Oceanic boundary condition | Six hourly updated, Optimum Interpolated (OI) ERA5 Daily SST data |
| Land surface treatment | Community Land Model (CLM) 4.5 |
| CLM Urban Scheme | ON |

It also considers several components of the urban environment, including sensible heat exchange at the reference height, sensible heat flux from the canyon to the atmosphere, sensible heat flux from the wall to the canyon space, sensible heat flux from the road to the canyon space, and sensible heat flux from the roof to the

atmosphere. In addition, the model accounts for anthropogenic heat fluxes resulting from building heating and air conditioning, as well as heat transfer in roofs, building walls, and roads, and hydrology (Ahmad et al., 2021). To represent the land surface, CLM employs a hierarchical sub-grid system consisting of several types, such as glacier, lake, wetland, urban, and vegetated land. The vegetated land type is further subdivided into a mosaic of plant functional types (PFTs).

3.2.3.2 Heatwave indices comparison over West Africa

The output dataset from the model is used for further analysis. The Cumulative excess heat (CumHeat), the Universal Thermal Climate Index (UTCI) and the Wet-Bulb Globe Temperature (WBGT) are computed from the output. They are normalized and case studies are selected during the period 2018 to 2020.

The daytime (night-time) average daily gridded data over West Africa ($0.25^\circ \times 0.25^\circ$). The selected case studies are from January 2018 – December 2020. The case studies are selected from 2018 to 2020 because of the availability of the dataset from the Year of Polar Prediction (YOPP) initiative. Furthermore, the absolute and Relative differences are computed between indices to determine the monthly differences and the affected area. The absolute and relative differences between two indices (t and x) is expressed as in the equations 3.7 and 3.8. But the Relative difference was extracted from the relative differences of the ERA5 dataset computations (previous objective) and the model output. The absolute difference was then taken as the comparative relative difference.

The relationship between heatwave and antecedent soil moisture to determine the heatwave index that relates better. Generally, it has been demonstrated that

heatwaves and soil moisture deficit have asymmetric relations, but this is done with the soil moisture output from the RegCM-CLM model and the SPEI drought index (Herold et al., 2016; Lorenz et al., 2010). The probability distribution is also analysed.

3.2.3.3 Moisture (Energy) fluxes in the different LULCT during Selected Heatwaves

The moisture advection and energy budget (sensible and latent heat) are also evaluated during the breaking-records heatwaves. Moisture advection is the horizontal transport of water vapour by the wind. Measurement and knowledge of atmospheric water vapour, or “moisture”, is crucial in the prediction of all weather elements, especially clouds, fog, temperature, humidity thermal comfort indices and precipitation. Regions of moisture advection are often co-located with regions of warm advection.

The relationship between heatwave and antecedent soil moisture to determine the heatwave index that relates better. Generally, it has been demonstrated that heatwaves and soil moisture deficit have asymmetric relations, but this is done with the soil moisture output from the RegCM-CLM model and the SPEI drought index (Herold et al., 2016; Lorenz et al., 2010). The probability distribution is also analysed.

The moisture horizontal advection is computed from the wind (\vec{U} and \vec{V}) components and the moisture at the same levels. Humidity gradients and wind vectors together can give the humidity advection, resulting in a time-rate of change of humidity at a given location. The rate of change of moisture with respect to time at

a given location may be estimated using the moisture gradient and the wind vector. The formula is similar to Eq. 3.4 and Eq. 3.5 applied to humidity (relative and specific). The formula is (Eq.3.9 and Eq.3.10):

$$-V \cdot \nabla H = -\left(u \frac{\partial H}{\partial x} + v \frac{\partial H}{\partial y}\right) \quad (3.9)$$

The discretised advection is used to plot the above formula on a map. The formula is:

$$-\left(u \frac{\partial H}{\partial x} + v \frac{\partial H}{\partial y}\right) = -\left(u \frac{\Delta H}{\Delta x} + v \frac{\Delta H}{\Delta y}\right) \quad (3.10)$$

The humidity gradient is a vector whose magnitude is the rate of change of humidity with distance $\frac{\Delta H}{\Delta d}$ and points in the direction of the greatest increase in temperature.

3.2.4 Summary of methodology

Figure 3.5 presents a summary of the methodology employed to address each research objective, as well as the sequence in which the study was conducted. First, heatwave and heat-stress occurrences with drought were compared using various datasets including satellite, reanalysis, and in-situ data from 1981 to 2020. Second, the study uses different indices to measure heatwaves, droughts, and temperature, including Cumulative Heat, Universal Thermal Climate Index, Standardized Precipitation (Evapotranspiration) Index, and Wet-Bulb Globe Temperature for gridded datasets. The ECMWF Year of Polar Prediction (YOPP) was employed to determine the main temperature advection and tendency terms contributing to heatwaves in selected cases, and finally, the coupled RegCM-CLM was configured to simulate heatwaves in West Africa.

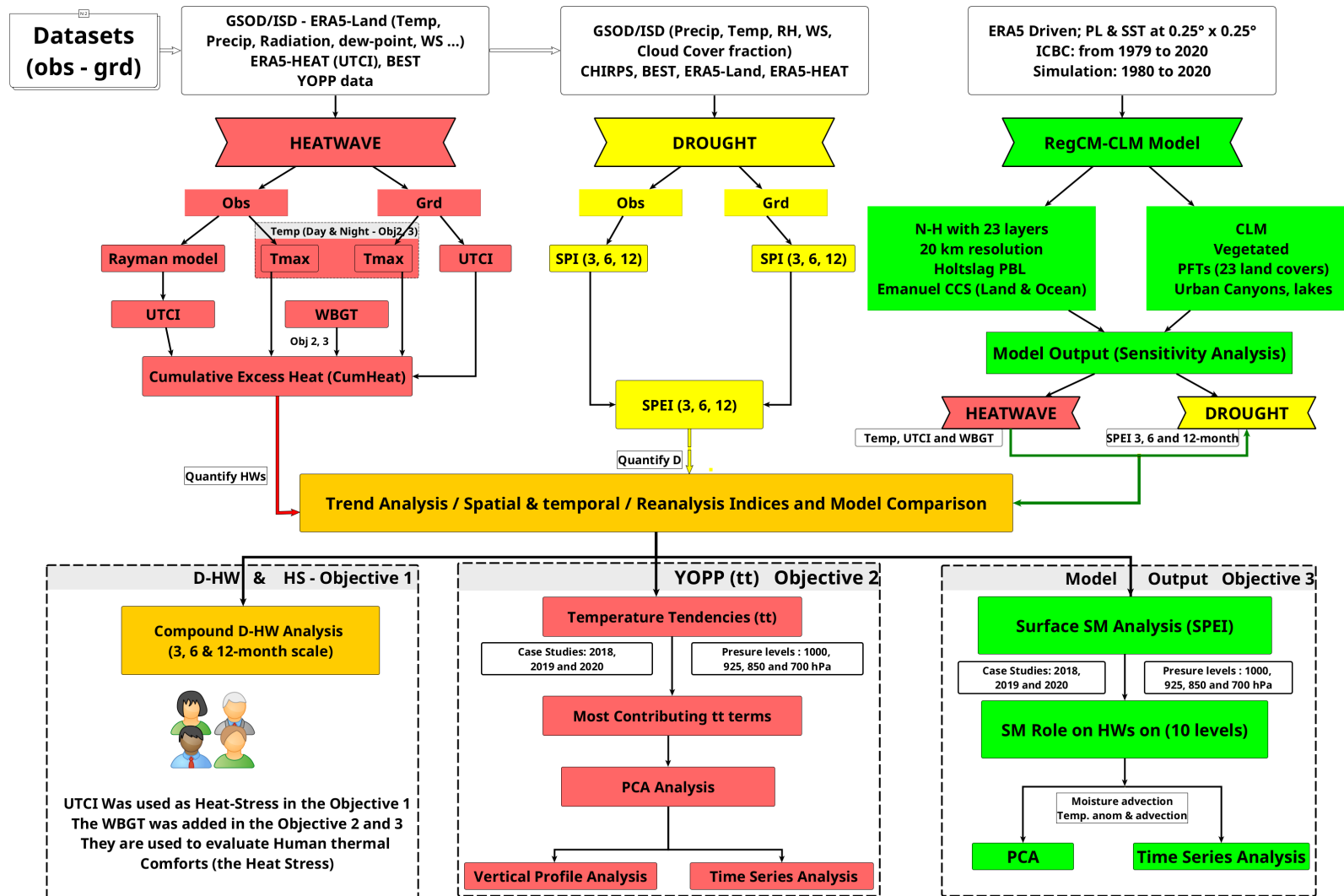


Figure 3.5: Flowchart of research methodology

CHAPTER 4: SPATIO-TEMPORAL DRIFTS OF DROUGHTS AND HEATWAVES WITH THE WEST AFRICAN MONSOON

This chapter comparatively assesses the trends, evolution of drought and heatwaves and their co-occurrence in West Africa by using the SPI/SPEI and the Cumulative Excess Heat (CumHeat) on maximum temperature and the Universal Thermal Climate (UTCI). Both gridded, and observation datasets were used from 1981 to 2020.

4.1 Introduction

West Africa experienced temperature extremes in the last decades and sometimes longer intense droughts episodes. This climatic variability affects the livelihoods of the growing African population, a continent identified since 2007 by the Intergovernmental Panel on Climate Change (IPCC) as one of the most vulnerable in the world (Danuor et al., 2011; IPCC, 2021a). Increased rainfall variability and long-lasting drought triggered regional scale famine in the 1970s and 1980s (IPCC, 2012b; Quenum et al., 2019). There is also evidence of increasing temperature extremes in the region, namely heatwave, impacting infrastructures, agriculture, and living beings (G. Ceccherini et al., 2017; Ragatoa et al., 2018; Russo et al., 2016). Efforts have been made to understand the physical causes of historical climate variability (Danuor et al., 2011; Hourdin et al., 2010; Lafore et al., 2010) and the interaction of temperature extremes especially, when considering greenhouse gases, land cover and aerosols in West Africa.

In this objective covering West Africa's ($4^{\circ}\text{N} - 21^{\circ}\text{N}$ and $-18^{\circ}\text{W} - 16^{\circ}\text{E}$) investigates the occurrence of heatwave and drought and the combined D-HW event using both

observation and gridded datasets. Observation data is very scarce in West Africa, making heatwave studies challenging. Specifically, The SPI and SPEI are used as drought indices. The cumulative (excess) heat (CumHeat) of maximum temperature (T_{\max}) and UHCI as heatwave indices are compared in West Africa climate regions. Analysis was then carried on the datasets to detect trends and differences in the trends for both datasets. Finally, an evaluation of the simultaneous occurrence was conducted to ascertain D-HW events in the region.

4.2 Analysis of Drought Indices Occurrence in West Africa: Insights and Trends

Drought occurred in the region, with differences within and between datasets at different scales for the different considered indices. The correlations' results are also presented with their trends. There are differences in the distribution of drought datasets in the different climate zones at the three (3) considered scales (Figure 4.5). The main point is that there are more variations in the observation data, mainly denoted by the extreme values ported by some stations. There are substantial differences in the datasets for each zone (differences in the median of the datasets). For example, The mean difference in the Guinea is very low, from 0.00129 for SPEI-3 station to 0.00361 for the gridded dataset at 3-month scale. This difference increases as one goes to the Sudan and the Sahel. The Sahel experiences extreme dryness for some stations. Both datasets consider SPI, especially in Agadez and Goure (red tagged outliers in Figure 4.5), mainly seen in observation data and Guinea. Only the significant Bonferroni corrected p-values (all values are multiplied by the number of comparisons (Cabin and Mitchell, 2000)) are shown (Figure 4.5b, c

and f). The Games-Howell pairwise comparison test is applied because of the difference in variance and the higher power results provided (Sauder and DeMars, 2019). Observation data in Guinea and Sudan have many of these extremes. While SPEI is more or less homogeneous over time and for both datasets, SPI is not that homogeneous. This shows the differences in the datasets at different scales. Relatively high differences are generally observed between SPI datasets at all scales, especially in the Sahel, due to the extreme dryness recorded by some stations.

Typically, observation datasets in all the climate zones in Figure 4.5 present more variations than gridded datasets. The Kruskal-Wallis rank sum tests the H_0 that the distribution location parameters of droughts are the same in each dataset. The alternative is that they differ in at least one, which is true in this case. The effect size (rank epsilon squared, $\epsilon_{ordinal}^2$) the gridded dataset accounts for, shows the level of variance in the observation data. The differences in the observation and the gridded are noticeable, and while SPI shows a slightly positive median, SPEI shows a slightly negative median in Guinea. The median and the rank epsilon squared presents some differences in the datasets.

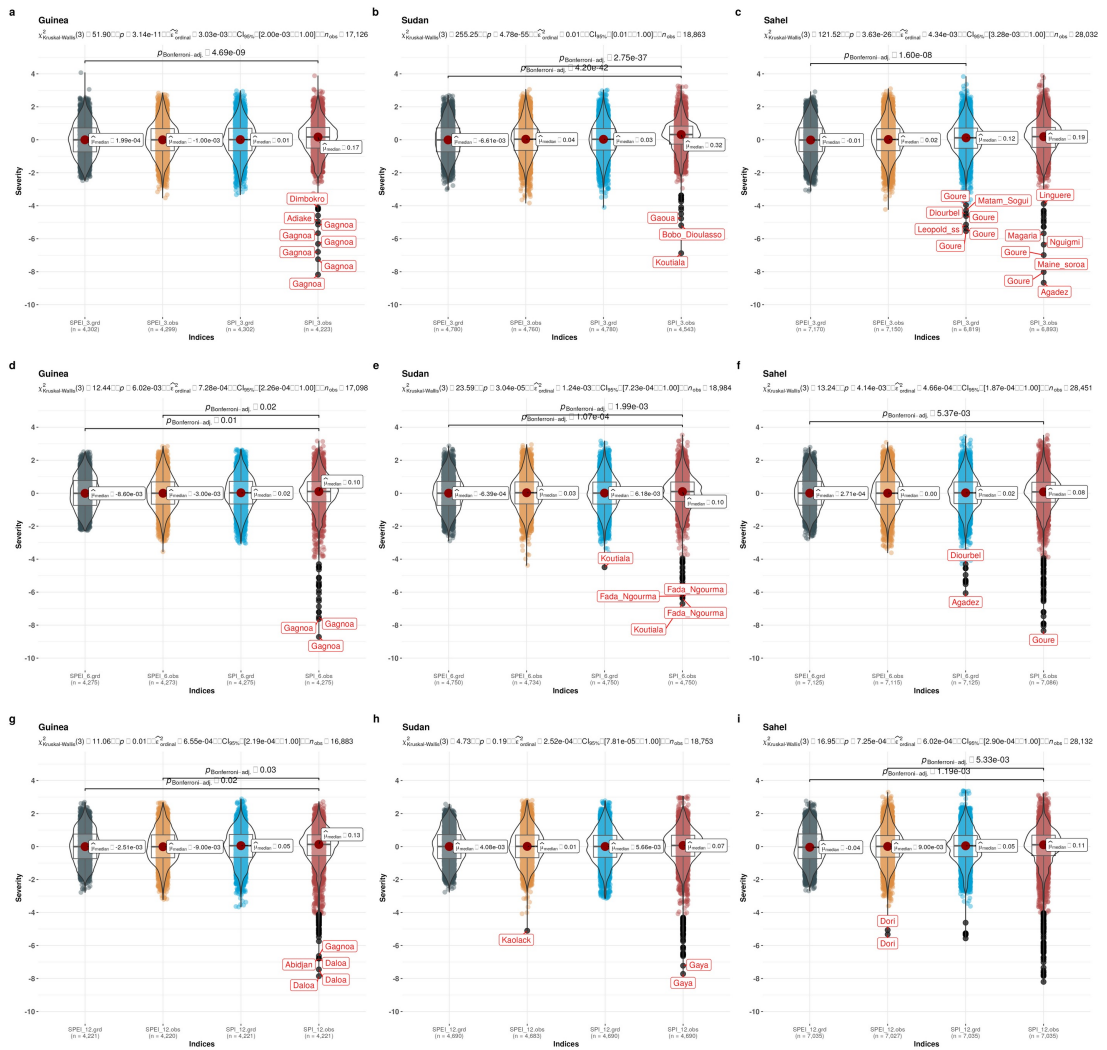


Figure 4.1: Drought indices: SPI and SPEI comparison at 3- (a, b, c), 6- (d, e, f) and 12- (g, h, i) month scales from gridded (xxx.grd) and observation (xxx.obs) data in the climatic zones. Combined violin and box plots with mean as centrality (red dot with tagged value); outliers (black dots) are tagged to the station name and data distribution. The statistical report for Kruskal–Wallis one-way ANOVA test for between group comparison is at the top of each plot. Only significant correlations have a p-value (Bonferroni corrected p-value)

Using the Spearman rank correlation in Figure 4.2 to check the level of relation in the datasets at different scales, SPI and SPEI generally give different results within stations datasets. Figure 4.2a-c reveal the correlation between and within gridded and observation drought indices in the climate zones in West Africa at different temporal scales, and Figure 4.2d gives the overall correlation over climate regions.

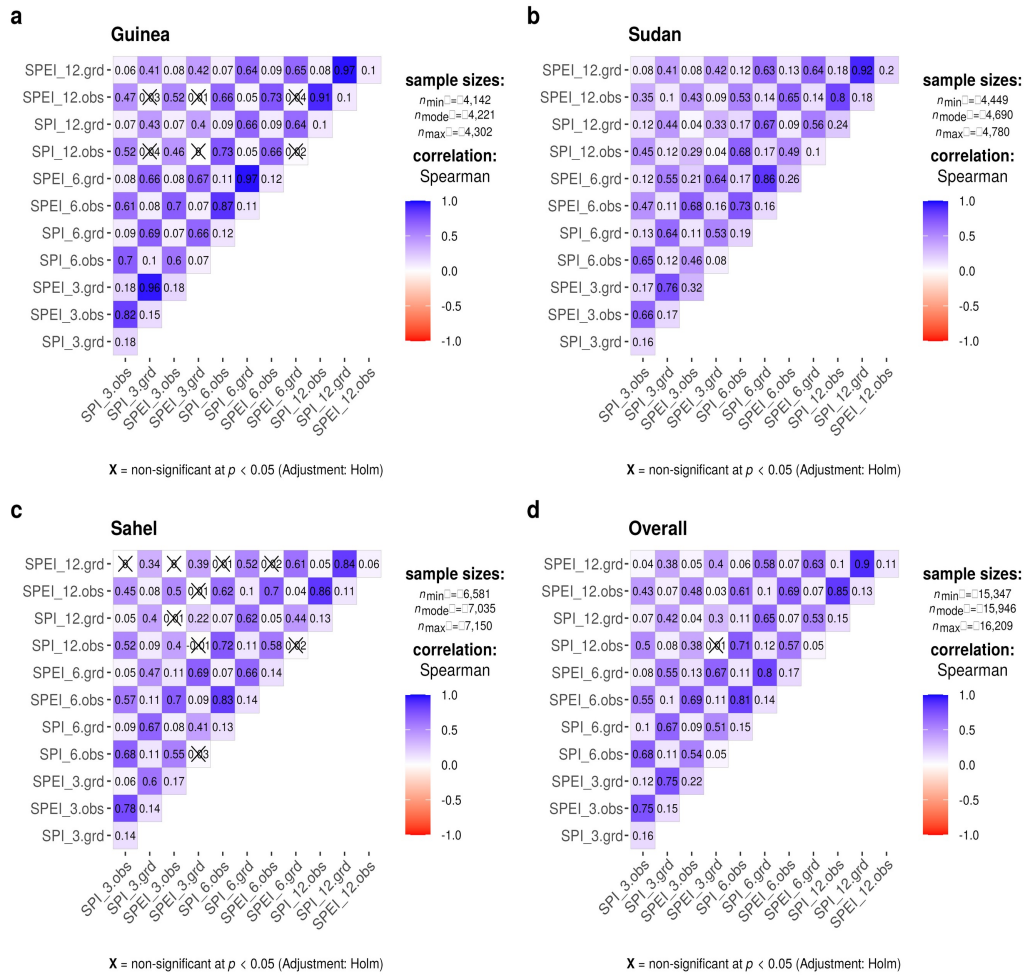


Figure 4.2: Correlation plot between observation and gridded datasets drought indices per zone: (a) the Guinea zone, (b) the Sudan and (c) the Sahel zone. (d) is the overall correlation of all considered stations in West Africa. The cross over some correlation values show non-significant (at $\alpha = 0.05$) correlations

The correlations vary from 0.03 to 0.97. The highest are recorded in the Guinea and the Sudan within datasets of the same scale (i.e., SPI-12 gridded and SPEI-12 gridded has 0.97 in the Guinea zone). Gridded data shows higher correlations between indices of the same scale.

The higher the temporal scale, the higher the correlation. SPEI and SPI indices are strongly correlated at the same scale within datasets, and the correlations agree better

with the timescale, as in Tefera et al. (2019) and Pei et al. (2020). The observed higher correlations for 6- and 12-month scale drought indices denote the implication of prolonged meteorological drought in the area, reducing the soil moisture. In the Sahel, these correlations are lower. The low correlation is affected by the low precipitation rate and intensity. According to Tsige et al. (2019), the high correlation between SPI and SPEI means precipitation plays a considerable role in controlling intra-seasonal drought. On the other hand, the near surface dryness caused by the temperature highly affects the correlation (as in the Sahel, Figure 4.2c), making it weaker in comparison. This may indicate that moisture storage capacity (precipitation accumulation) of the soil in some zones (Guinea) could alleviate the intensity of the short term drought.

The general tendency presents lower correlations between observation and gridded drought indices at different temporal scales. Observation and gridded datasets show lower correlations, which are mostly not significant across scales. The higher the temporal scale, the lower the general correlation between observation and gridded indices. This could be due to the high variations in the observation dataset with outliers, while the gridded dataset is more/less homogeneous. There are notable correlation differences between the datasets. BEST dataset is combined with CHIRPS to compute SPEI index, the index with higher correlation values in all zones.

When looking at the trend in the drought dataset, Figure 4.3 shows the trend in each zone for aggregated annual minimum SPI and SPEI at the temporal scales. The general tendency is for an increase in the trend, showing a general recovery for SPI indices at all scales and for both datasets. The slope becomes higher in the Sudan and

the Sahel zone with the timescale, and is steeper for the gridded dataset. The trends are significant at some scales for some climate zones like the Figure 4.3e. The Sahelian SPI trend shows more significance.

For SPEI index, the pattern is different. The tendency is generally decreasing toward dryer periods, but most of the trends are not significant as per the values. Indeed, unlike SPI, SPEI uses precipitation and temperature for its calculation, thereby considering the influence of global warming to some extent. Meteorologically, SPI shows a slight regain of precipitation and the SPEI denotes a reduction of the soil moisture for plants due to temperature fluctuation (mean increase).

Only SPEI 12-month observation dataset has increasing trend for the Sahel and the Guinea zone. The Sahel has the most pronounced trend. Changes in temperature could drive the observed discrepancies in the SPEI results, but in areas with low temperature variations, SPI can perform as well as SPEI does (Tefera et al., 2019). From the literature, the Guinea, and Sudan zones have dry peaks in 2000s but with higher intensity. A recovery period (tending to 0 or higher) is observed from 2005 onwards, but the Sahel experienced some recovery from 1985, peaking in 1994-1995 and 2014 to 2016 mainly for SPI. Bamba et al., (2015) documented the low amount of rainfall over West Africa in the 1980s. The increased tendency of rainfall in West Africa was in the 1990s, especially in the Sudan and Sahel for SPEI where the trend is more pronounced.

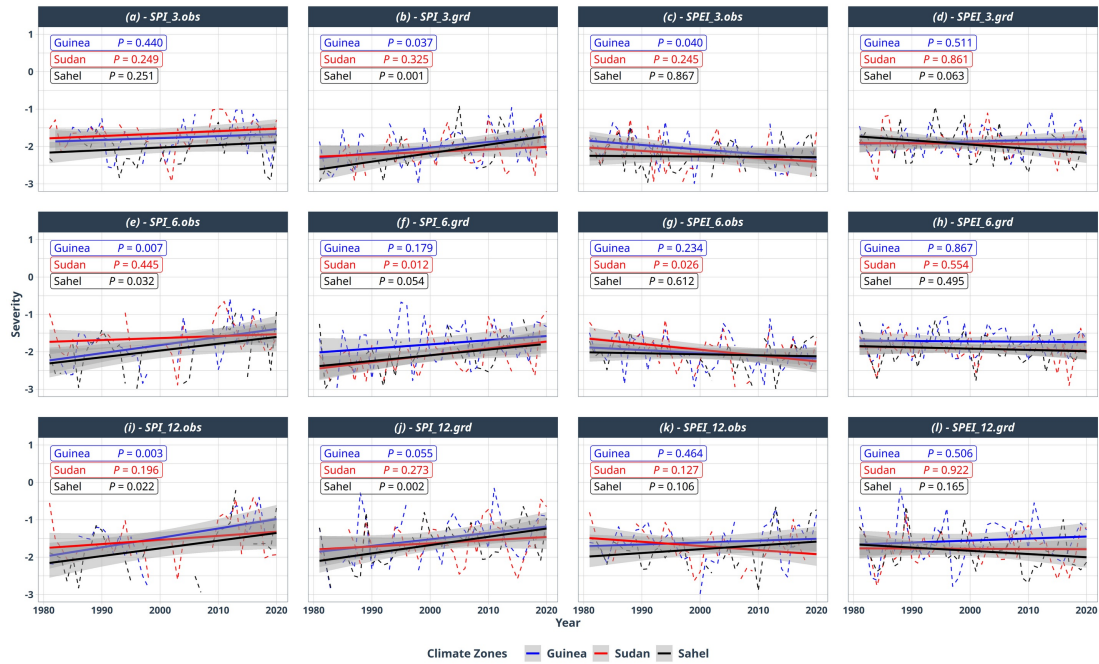


Figure 4.3: Drought trend in the climatic zones at 3-, 6- and 12-month for Gridded (.grd) and Observation (.obs) datasets. Yearly aggregated time series in dotted line for the Guinea zone in blue, red for the Sudan and black for the Sahel. The overlay corresponding colour lines are the linear trend for each zone. The full lines are the corresponding smoothed non-linear trends. The transparent grey area is the 95% confidence interval of the trends. The values at the top are the trend's significance (p-value). Their colours are relative to their trend lines.

That period coincides with the increased precipitation in some part of the Sudan Savannah zone (Bobadoye, 2018). This configuration could affect the occurrence of heatwaves in the different regions.

The gridded dataset does not capture the same tendencies for drought with both SPI and SPEI. Variability is instead presenting a general recovery for all zones in SPI with a dry peak period in 2015 (corresponding to a slight reduction in precipitation) as in 1981-1985 for SPEI. The gridded datasets could hardly show the dry peak period in 2000 for both SPI and SPEI at all scales. The uncertainty statistically reduces with the temporal drought scale. The disparities in the datasets could also be

due to the combination of BEST and CHIRPS data records (rainfall increasing intensity in some stations).

The tables Table 4.1 and Table 4.2 present the Sen's slope and P-value for different decades (1981-1990, 1990-2000, 2000-2010, 2010-2020) across the three climate zones (Guinea, Sudan, Sahel). The SPI and SPEI at different time scales (3-, 6- and 12-month) and for observed and gridded datasets are considered. The Sen's slope indicates the trend over time and the P-value is a statistical measure of the hypotheses, typically, a smaller P-value (below 0.05) indicates strong evidence that the trend is significant.

In the 1981-1990 period, the Sen's slope values for Guinea and Sahel are mostly negative, suggesting a decreasing trend in these indices, while Sudan shows a mixed trend. However, the P-values are mostly above 0.05, indicating that these trends are not statistically significant.

In the 1990-2000 period, the Sen's slope values for Guinea are negative, indicating a decreasing trend. In contrast, Sudan and Sahel show a mixed trend. The P-values for Guinea and Sudan are mostly below 0.05, indicating that these trends are statistically significant.

In the 2000-2010 decade, the Sen's slope values for Guinea are mixed, while Sudan shows a mostly negative trend, and Sahel shows a positive trend. The P-values for Guinea and Sahel are mostly below 0.05, indicating that these trends are statistically significant.

Table 4.1: Drought (SPI and SPEI) Mann Kendall decadal trends test for all climate zones (part 1); Bolded results are the statistically significant trends in the series. Here, only the slope and the significance of the test are shown. The other results do not necessarily mean there is no trend, but indicates that the evidence is not sufficient to conclude with a 5% level of confidence that a trend exists. The dataset represent Tmax or UTCI for gridded dataset (grd) and observation dataset (obs)

| Decade | Zones | Test | SPI3 | | SPEI3 | | SPI6 | |
|-----------|--------|-------|----------------|-----------------|-----------------|-----------------|-----------------|-----------------|
| | | | obs | grd | obs | grd | obs | grd |
| 1981-1990 | Guinea | SS | 0.00002 | 0.00007 | 0.00016 | 0.00007 | 0.00003 | 0.00016 |
| | | p-val | 0.81961 | 0.56071 | 0.15953 | 0.59783 | 0.79584 | 0.20992 |
| | Sudan | SS | -0.00015 | -0.00029 | -0.00011 | -0.00039 | -0.00028 | -0.00046 |
| | | p-val | 0.07399 | 0.00250 | 0.14123 | 0.00004 | 0.00165 | 0.00000 |
| | Sahel | SS | -0.00004 | 0.00002 | -0.00021 | 0.00001 | -0.00016 | 0.00004 |
| | | p-val | 0.43521 | 0.75476 | 0.00001 | 0.81252 | 0.00148 | 0.49484 |
| 1990-2000 | Guinea | SS | -0.00016 | -0.00019 | -0.00013 | -0.00019 | -0.00018 | -0.00023 |
| | | p-val | 0.07128 | 0.03338 | 0.14193 | 0.04829 | 0.04215 | 0.01220 |
| | Sudan | SS | 0.00041 | 0.00008 | 0.00041 | 0.00002 | 0.00048 | 0.00014 |
| | | p-val | 0.00000 | 0.30897 | 0.00000 | 0.83620 | 0.00000 | 0.06972 |
| | Sahel | SS | 0.00006 | 0.00003 | 0.00002 | 0.00007 | 0.00004 | 0.00004 |
| | | p-val | 0.17006 | 0.54557 | 0.55061 | 0.06508 | 0.34669 | 0.39785 |
| 2000-2010 | Guinea | SS | 0.00030 | 0.00002 | 0.00017 | -0.00014 | 0.00040 | -0.00009 |
| | | p-val | 0.00032 | 0.83613 | 0.04748 | 0.05471 | 0.00001 | 0.21149 |
| | Sudan | SS | -0.00010 | 0.00021 | 0.00000 | 0.00031 | -0.00007 | 0.00033 |
| | | p-val | 0.15889 | 0.00184 | 0.97332 | 0.00000 | 0.34748 | 0.00000 |
| | Sahel | SS | 0.00019 | 0.00009 | 0.00020 | 0.00016 | 0.00023 | 0.00014 |
| | | p-val | 0.00000 | 0.02218 | 0.00000 | 0.00000 | 0.00000 | 0.00040 |
| 2010-2020 | Guinea | SS | -0.00002 | 0.00022 | 0.00010 | 0.00035 | -0.00002 | 0.00029 |
| | | p-val | 0.75877 | 0.01070 | 0.07810 | 0.00001 | 0.81055 | 0.00095 |
| | Sudan | SS | -0.00004 | -0.00001 | -0.00028 | 0.00001 | -0.00008 | 0.00003 |
| | | p-val | 0.59500 | 0.92702 | 0.00000 | 0.93726 | 0.23922 | 0.66396 |
| | Sahel | SS | -0.00007 | -0.00006 | 0.00009 | -0.00008 | 0.00004 | -0.00011 |
| | | p-val | 0.06195 | 0.12024 | 0.00109 | 0.02019 | 0.27079 | 0.00893 |

* "SS" is the Sen's Slope; "p-val" is the P-value; bold values are the significant values at 5% level confidence

Table 4.2: Drought (SPI and SPEI) Mann Kendall decadal trends test for all climate zones (part 2). Read as in Table 4.1.

| Decade | Zones | Test | SPEI6 | | SPI12 | | SPEI12 | |
|-----------|--------|-------|----------------|-----------------|-----------------|-----------------|-----------------|-----------------|
| | | | obs | grd | obs | grd | obs | grd |
| 1981-1990 | Guinea | SS | 0.00002 | 0.00007 | 0.00016 | 0.00007 | 0.00003 | 0.00016 |
| | | p-val | 0.81961 | 0.56071 | 0.15953 | 0.59783 | 0.79584 | 0.20992 |
| | Sudan | SS | -0.00015 | -0.00029 | -0.00011 | -0.00039 | -0.00028 | -0.00046 |
| | | p-val | 0.07399 | 0.00250 | 0.14123 | 0.00004 | 0.00165 | 0.00000 |
| | Sahel | SS | -0.00004 | 0.00002 | -0.00021 | 0.00001 | -0.00016 | 0.00004 |
| | | p-val | 0.43521 | 0.75476 | 0.00001 | 0.81252 | 0.00148 | 0.49484 |
| 1990-2000 | Guinea | SS | -0.00016 | -0.00019 | -0.00013 | -0.00019 | -0.00018 | -0.00023 |
| | | p-val | 0.07128 | 0.03338 | 0.14193 | 0.04829 | 0.04215 | 0.01220 |
| | Sudan | SS | 0.00041 | 0.00008 | 0.00041 | 0.00002 | 0.00048 | 0.00014 |
| | | p-val | 0.00000 | 0.30897 | 0.00000 | 0.83620 | 0.00000 | 0.06972 |
| | Sahel | SS | 0.00006 | 0.00003 | 0.00002 | 0.00007 | 0.00004 | 0.00004 |
| | | p-val | 0.17006 | 0.54557 | 0.55061 | 0.06508 | 0.34669 | 0.39785 |
| 2000-2010 | Guinea | SS | 0.00030 | 0.00002 | 0.00017 | -0.00014 | 0.00040 | -0.00009 |
| | | p-val | 0.00032 | 0.83613 | 0.04748 | 0.05471 | 0.00001 | 0.21149 |
| | Sudan | SS | -0.00010 | 0.00021 | 0.00000 | 0.00031 | -0.00007 | 0.00033 |
| | | p-val | 0.15889 | 0.00184 | 0.97332 | 0.00000 | 0.34748 | 0.00000 |
| | Sahel | SS | 0.00019 | 0.00009 | 0.00020 | 0.00016 | 0.00023 | 0.00014 |
| | | p-val | 0.00000 | 0.02218 | 0.00000 | 0.00000 | 0.00000 | 0.00040 |
| 2010-2020 | Guinea | SS | -0.00002 | 0.00022 | 0.00010 | 0.00035 | -0.00002 | 0.00029 |
| | | p-val | 0.75877 | 0.01070 | 0.07810 | 0.00001 | 0.81055 | 0.00095 |
| | Sudan | SS | -0.00004 | -0.00001 | -0.00028 | 0.00001 | -0.00008 | 0.00003 |
| | | p-val | 0.59500 | 0.92702 | 0.00000 | 0.93726 | 0.23922 | 0.66396 |
| | Sahel | SS | -0.00007 | -0.00006 | 0.00009 | -0.00008 | 0.00004 | -0.00011 |
| | | p-val | 0.06195 | 0.12024 | 0.00109 | 0.02019 | 0.27079 | 0.00893 |

* “SS” is the Sen’s Slope; “p-val” is the P-value; bold values are the significant values at 5% level confidence

And finally, in the 2010-2020 decade, the Sen’s slope values for Guinea and Sahel are mostly positive, suggesting an increasing trend, while Sudan shows a mixed

trend. The P-values for Guinea and Sahel are mostly below 0.05, indicating that these trends are statistically significant.

In conclusion, the trends in these indices vary across different periods and zones. While some trends are statistically significant, others are not, indicating the complex nature of climate extremes in West Africa. These findings could be crucial for understanding the impact of climate change on these regions and informing mitigation and adaptation strategies.

The decadal trend test shows more significance in the trends.

4.3 Cumulative Heatwaves Analysis considering UTCI and Tmax

A characterization of UTCI for both ERA5-HEAT and the computed Rayman model from observation/station data (ISD) over West Africa is established (Błażejczyk et al., 2013). The categories determine the level of stress and its physiological implications or response to human heat homeostasis. Gridded UTCI data is then compared to the computed UTCI from station data. The Pearson's correlation (see Table 4.3) coefficient is highly positive in all climatic zones (varying from 0.77 in the Guinea zone to 0.80 in the Sudan and 0.88 in the Sahel). The linear model R^2 is above 0.6 except for the Guinea zone (0.59), implying that the Sudan and Sahel zones datasets had a stronger correlation than the other datasets, and the gridded dataset accounts for more of the variance. The perfect R^2 values are attributable to the overestimated wind values (Molina et al., 2021). Also, the cloud difference due to the overcast conditions of low cloud cover (low cloud cover) and the underestimation of coastal stratocumulus shift in the ERA5 datasets (Danso et al., 2019; Jakob, 1999). The RMSE between gridded and computed UTCI is also given in Table 4.3 for each

zone showing the difference between the computed UTCI and gridded UTCI datasets. The RMSE values (bellow 10% of the number of observation) show the gridded datasets' performance to accurately represent the observed heat stress in the region.

Table 4.3: Gridded and observation UTCI correlation and variances per zone. This table shows how good the gridded datasets represent the events in the observed dataset.

| Index | Zone | Pearson's Statistics | p.value | R² | MAE | RMSE |
|--------------|-------------|-----------------------------|----------------|----------------------|------------|-------------|
| UTCI | Guinea | 0.77 | 523.31 | < 0.00 | 0.59 | 2.62 |
| | Sudan | 0.8 | 636.97 | < 0.00 | 0.63 | 2.78 |
| | Sahel | 0.88 | 1029.64 | < 0.00 | 0.78 | 2.91 |

The Table 4.4 summarizes the UTCI compared results and reveals small differences in the mean values in each zone where gridded UTCI has a higher mean value in all zones except for the Guinea zone.

Table 4.4: Description of Gridded (grd) and Station (obs) UTCI. The table presents the variable and zones. There is also the mean, the available complete percentage data in the series (complete), the standard deviation (sd), the percentiles (p0 to p100) and a graphical distribution of the dataset (Dist., blue for the Guinea zone; red for the Sudan and black for the Sahel). The distribution (Dist.) is binned with the 20 percentiles range giving 5 bar-plots showing the distribution of the data.

| UTCI | Zones | mean | sd | p0 | p25 | p50 | p75 | p100 | Dist. |
|-------------|--------------|-------------|-----------|-----------|------------|------------|------------|-------------|--------------|
| grd. | Guinea | 30.15 | 4.81 | 9.53 | 26.66 | 29.62 | 33.60 | 43.65 | |
| | Sudan | 34.12 | 5.19 | 10.72 | 30.77 | 34.52 | 37.85 | 48.24 | |
| | Sahel | 32.63 | 8.17 | -2.86 | 27.60 | 33.63 | 38.90 | 52.48 | |
| obs. | Guinea | 30.36 | 4.99 | -10.60 | 26.80 | 30.60 | 34.40 | 50.10 | |
| | Sudan | 32.75 | 5.32 | -6.00 | 29.40 | 33.30 | 36.60 | 52.60 | |
| | Sahel | 32.43 | 7.4 | -15.60 | 28.00 | 33.50 | 37.80 | 58.10 | |

The Sudan and the Sahel have a close stress level, but the gap between them is larger with the gridded dataset (see mean and p100 values in the zones in Table 4.4). What is agreed in both UTCI datasets is that the Sudan generally experienced more heat-stress. Di Napoli *et al.* (2020) documented the same and evaluated the deviation of

UTCI by 5.2 ± 2.5 °C, which is close in the present case (1.37 ± 0.21 °C) in the climate zones.

In Figure 4.4 below, the proportion of occurrence of each severity level of the cumulative heat indices are shown. The results are close in the two indices for the different climate zones.

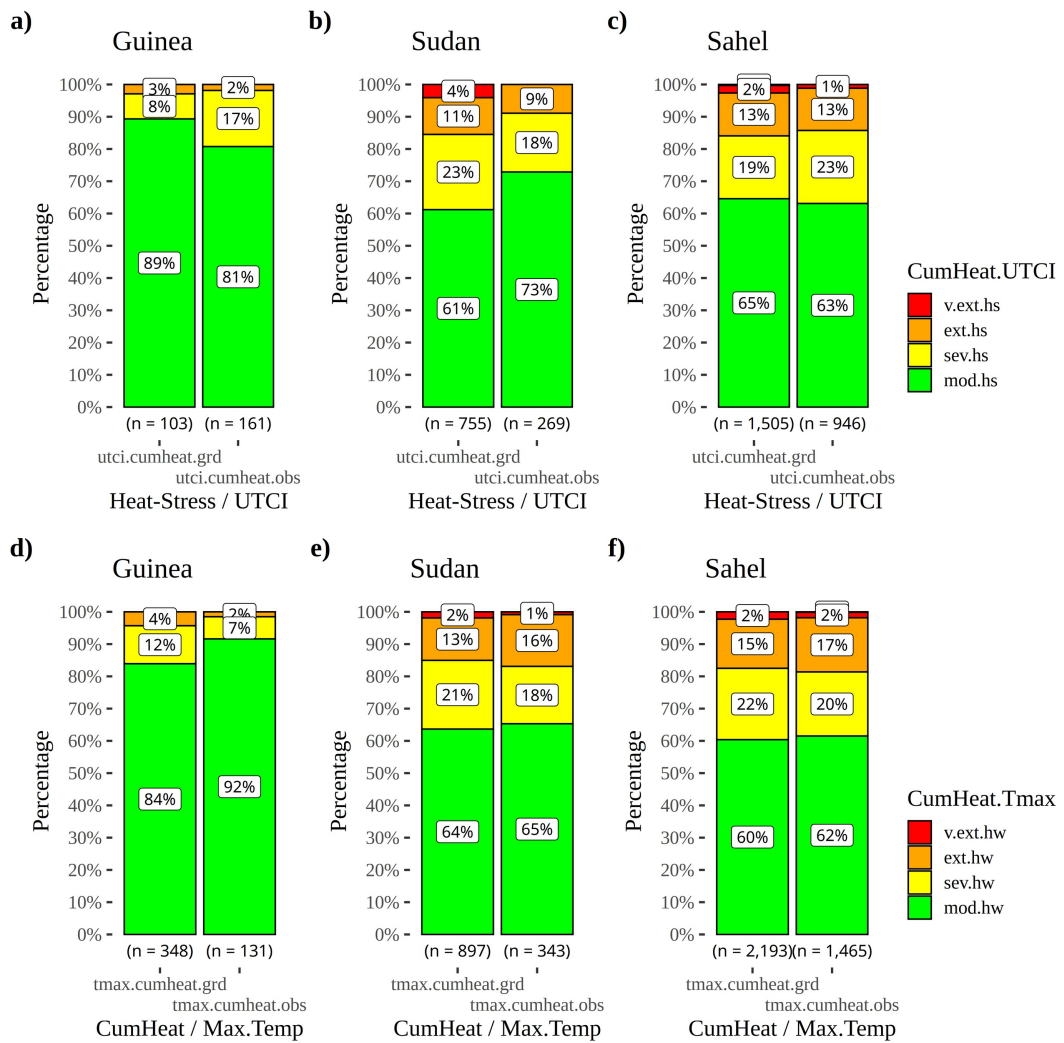


Figure 4.4: Compared occurrence proportion of Cumulative heat (CumHeat) for Tmax in the down panel and UTCI in the upper panel in the 3 climatic zones

There is no “Super Extreme” or “Very Extreme” heatwaves in the Guinea zone for UTCI and T_{max} for both observation and gridded dataset. But the proportion of

severity are quite close in the Guinea for the different datasets and the heat indices. The Sudan presents the same configuration with 4 % of “Very Extreme” heat-stress in the UTCI and T_{\max} gridded dataset, while there is only 1 % in observation T_{\max} and no record of such severe heatwave/heat-stress in the UTCI dataset (in Sudan). In the Sahel, only a small percentage (Leopold Sedar Senghor in Senegal) recorded a “Super Extreme” heatwave in January February 2008. But only an increased percentage of “Extreme” and “Very Extreme” heatwave/heat-stress are recorded compared to the Sudan (for both T_{\max} and UTCI). Overall, the proportion towards higher percentages of more severe heatwaves increases from the Guinean zone to the Sahelian zone. The Sahel and the Sudan have almost the same configuration of heatwave occurrence with tendency to higher percentages in the Sahel. The CumHeat applied to the indices makes them comparable, and the results are very close. This leads to analysing the trend of each index over time.

The cumulative (excess) heat method (CumHeat) is applied using the 90th percentile threshold on both UTCI and T_{\max} datasets. The CumHeat for T_{\max} and UTCI are analysed from 1981 to 2020 and comparison is done for the gridded and observation dataset. The trends reveal increasing tendencies for both observation and gridded dataset and indices cumulative heat. In Figure 4.5 the Sahel show higher increasing trend (black full line) followed by the Sudan (red line).

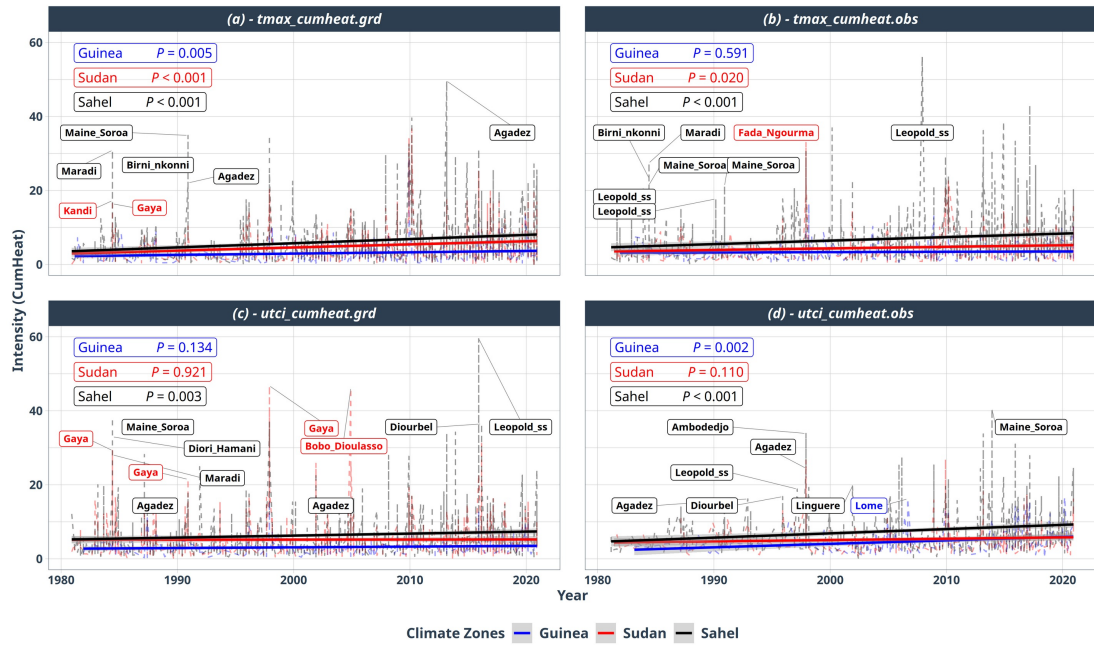


Figure 4.5: Seasonal Maximum values of Cumulative (excess) Heat (CumHeat) trends for all datasets (xxx.grd: gridded and xxx.obs Observation) and zones. Lines are the linear trends and dotted fine lines are the maximum values of the CumHeat. The blue line is the trend for Guinea zone, the red for the Sudan and the black for the Sahel. The transparent grey area is the 95% confidence interval of the trends. The values at the top are: P = the statistical significance (p-value) of the trend. The colours are relative to their trend lines. The Labels are some stations that have more than 16 CumHeat values.

The gap is increasing between the different zones (especially the Sahel zone having a more abrupt slope) from 2000 for T_{\max} datasets. UTCI, on the other hand, shows a similar pattern, but the Guinea zone has a steeper slope compared to the Sudan zone in the observation dataset (Figure 4.5d). This denotes a fast increasing trend in the Guinea zone relative to the high humidity. Overall, the differences in the datasets trends are very low.

The duration of the trends is also increasing for T_{\max} CumHeat gridded dataset. Some trends are not significant, like in the Guinea zone in Figure 4.6b.

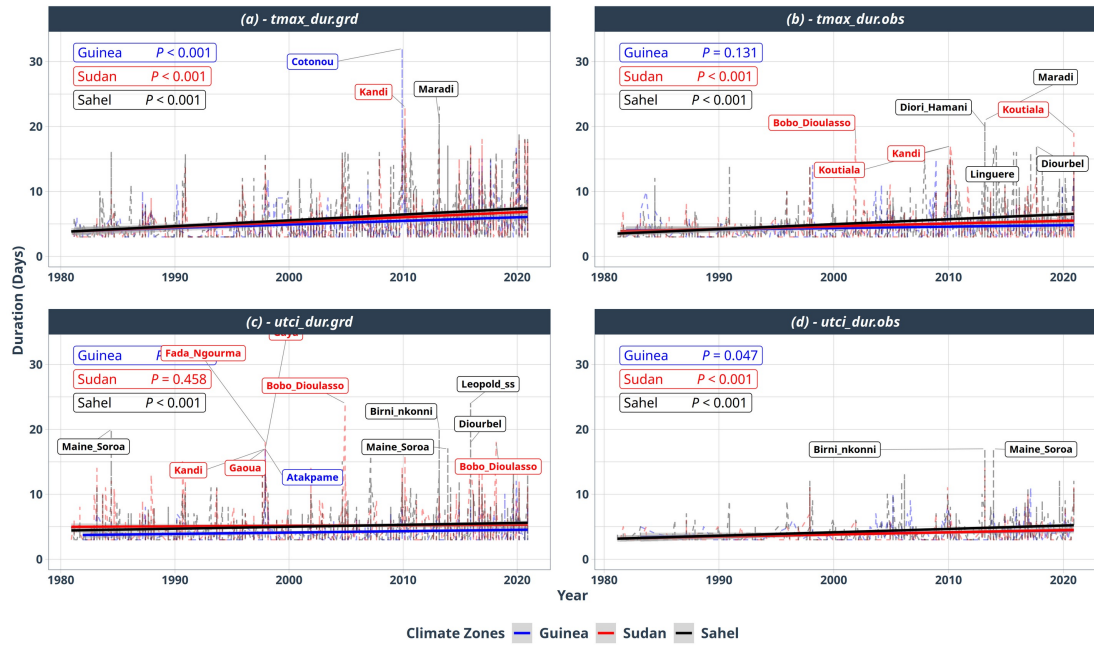


Figure 4.6: Seasonal Maximum values of Cumulative (excess) Heat (CumHeat) Duration trends for all datasets (xxx.grd: gridded and xxx.obs Observation) and zones. Lines are the linear trends and dotted fine lines are the maximum values of the CumHeat. The blue line is the trend for Guinea zone, the red for the Sudan and the black for the Sahel. The transparent grey area is the 95% confidence interval of the trends. The values at the top are the trend results: $Y = \text{intercept} + \text{slope} \cdot X$. P gives the statistical significance (p-value) of the trend. The colours are relative to their trend lines. The labels are some stations that have more than 5 days.

The gridded data shows higher trends compared to the observation. In all the datasets and climate zones, the Sahel has a higher trend followed by the Sudan and the Guinea has the lowest trends even for UTCI. The tagged stations show some of them that have high trends in the different zones.

Differences presented in the trend of the datasets are obtained from a linear trend. The Table 4.5 presents the Mann Kendall monotonic trend test for all the indices considering the mean, max and cumulative intensity of daily values over the whole period. The T_{\max} observation trends are significant for all the climate zones, but only the Sahelian zone seem to have significant trend for the gridded dataset. The Sahel

and the Guinea are significant for UTCI in gridded and observation datasets respectively.

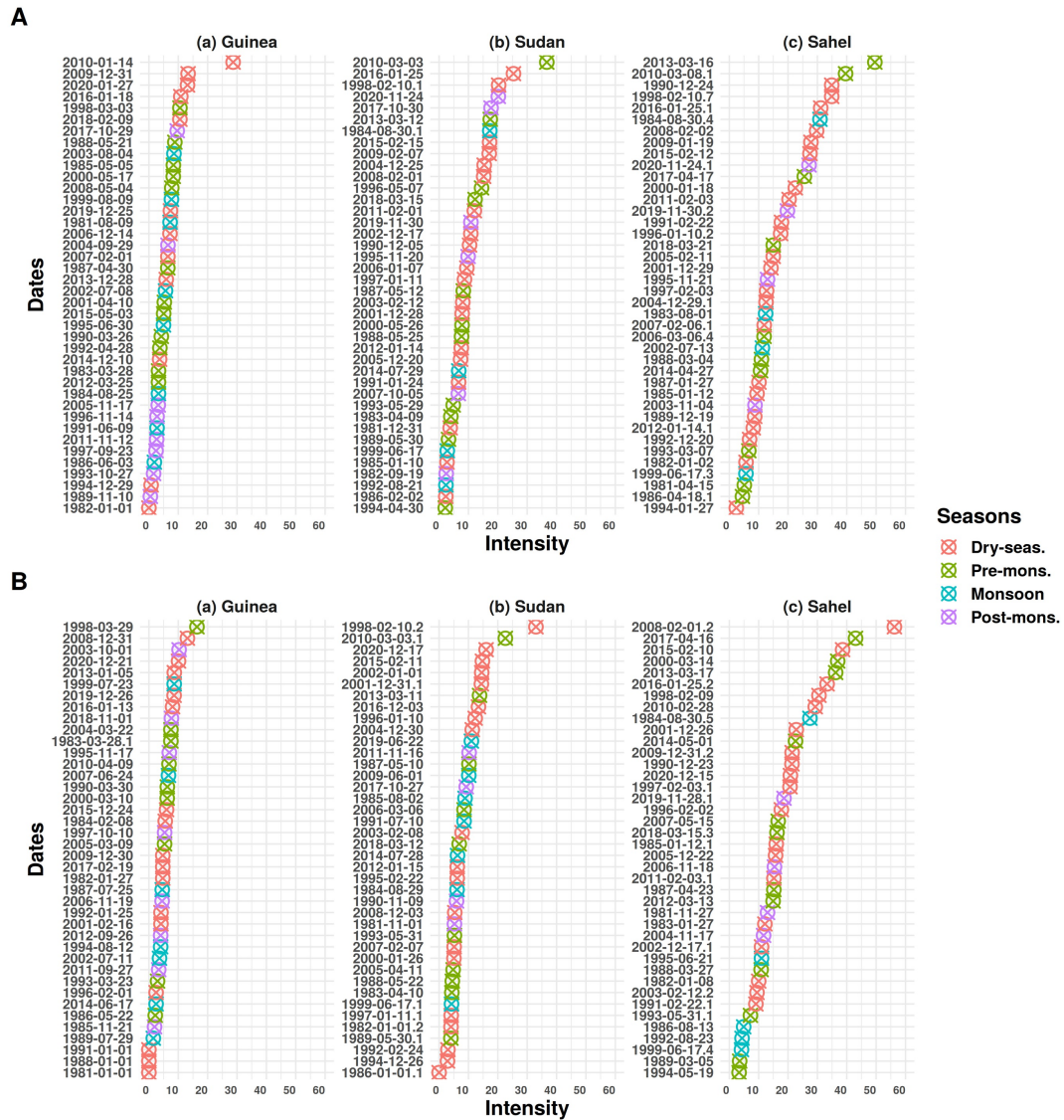
Table 4.5: CumHeat (Tmax and UTCI) Mann Kendall trend test. Bold results are the statistically significant trends in the series. Here only the slope and the significance of the test are shown. The other results do not necessarily mean there is no trend, but indicates that the evidence is not sufficient to conclude with a 5% level of confidence that a trend exists. The dataset represent Tmax/UTCI for gridded dataset (xxx.grd) and observation dataset (xxx.obs)

| Dataset | Climate zones | Test | Mean Intensity | Max Intensity | Cumulative Intensity |
|----------|---------------|-------|-----------------|-----------------|----------------------|
| tmax.grd | Guinea | SS | 0.00003 | 0.00005 | 0.00004 |
| | | p-val | 0.09473 | 0.07167 | 0.55539 |
| | Sudan | SS | 0.00000 | 0.00000 | -0.00001 |
| | | p-val | 0.88684 | 0.92713 | 0.86023 |
| | Sahel | SS | 0.00005 | 0.00009 | 0.00022 |
| | | p-val | 0.00000 | 0.00000 | 0.00008 |
| tmax.obs | Guinea | SS | 0.00013 | 0.00014 | 0.00040 |
| | | p-val | 0.01849 | 0.04763 | 0.10616 |
| | Sudan | SS | 0.00015 | 0.00002 | 0.00041 |
| | | p-val | 0.01107 | 0.18227 | 0.12677 |
| | Sahel | SS | 0.00013 | 0.00018 | 0.00036 |
| | | p-val | 0.00000 | 0.00003 | 0.00587 |
| utci.grd | Guinea | SS | -0.00006 | 0.00012 | -0.00021 |
| | | p-val | 0.62297 | 0.60634 | 0.68976 |
| | Sudan | SS | -0.00007 | -0.00011 | -0.00019 |
| | | p-val | 0.08338 | 0.09896 | 0.30953 |
| | Sahel | SS | 0.00011 | 0.00020 | 0.00036 |
| | | p-val | 0.01860 | 0.01153 | 0.10333 |
| utci.obs | Guinea | SS | -0.00150 | -0.00199 | -0.00526 |
| | | p-val | 0.00051 | 0.00605 | 0.00266 |
| | Sudan | SS | 0.00000 | 0.00000 | 0.00014 |
| | | p-val | 0.99514 | 0.83065 | 0.82708 |
| | Sahel | SS | -0.00024 | -0.00026 | -0.00063 |
| | | p-val | 0.20934 | 0.35281 | 0.43118 |

* “SS” is the Sen’s Slope; “p-val” is the P-value; bold values are the significant values at 5% level confidence

Furthermore, the student’s t-test in Figure 4.7 and 4.8 show heatwaves’ highest annual intensity differences along with the year and month of occurrence. The season

of occurrence is also shown by the colours of the dots. The seasons are categorised using the conventional seasonal cycles (DJF, MAM, JJA and SON). As expected in West Africa, heatwaves occurred at different periods/seasons in the year.



Source: Gridded (BEST; top panel) vs Observed (GSOD; down panel) Datasets

Figure 4.7: Comparison of Annual maximum T_{max} CumHeat in different climate zones; Gridded (A) and observation (B) datasets. The colours represent the different season of occurrence of each of the heatwave over the years. The colours of the dots shows the different occurrence seasons (Dry seas. is DJF, pre-mons. is MAM, JJA is considered the Monsoon season and SON the Post-mons.

Over the considered period, heatwaves occurred with different intensity which varies also with the dataset (gridded Figure 4.7A and observation Figure 4.7B).

The most severe magnitudes occurred in the last decades. Gridded data, generally show higher intensity compared to observation (except for the Sahel where the opposite is observed), and the highest intensity are recorded in the Sahel for both datasets. It shows important differences, but observation data present less internal deviation. Across the years, the intensity of CumHeat significantly varied. The highest difference between datasets is statistically recorded in the Guinea zone and then in the Sahel.

The mean of maximum CumHeat (the blue vertical dotted line) is also increasing from the Guinea zone to the Sahel (Figure 4.7 and 4.8) but the biggest values are observed in the Sahel.

The year of the highest heatwave is recorded in 2010 for the gridded dataset in Guinea and Sudan zones and 2013 in the Sahel. A careful look into the plots shows a shift in the months when they occurred (January in the Guinea, March in the Sudan and the Sahel. The observation dataset revealed rather different occurrence dates, 1998 in the Guinea, 1998 and 2008 in the Sudan and the Sahel respectively. The years of highest CumHeat for UTCI are 1998 and 2016 in the gridded dataset and 2020, 2010 and 2013 for the Guinea, Sudan and Sahel zones respectively. The predominant seasons of occurrence are the dry season (DJF) and the pre-monsoon (MAM).

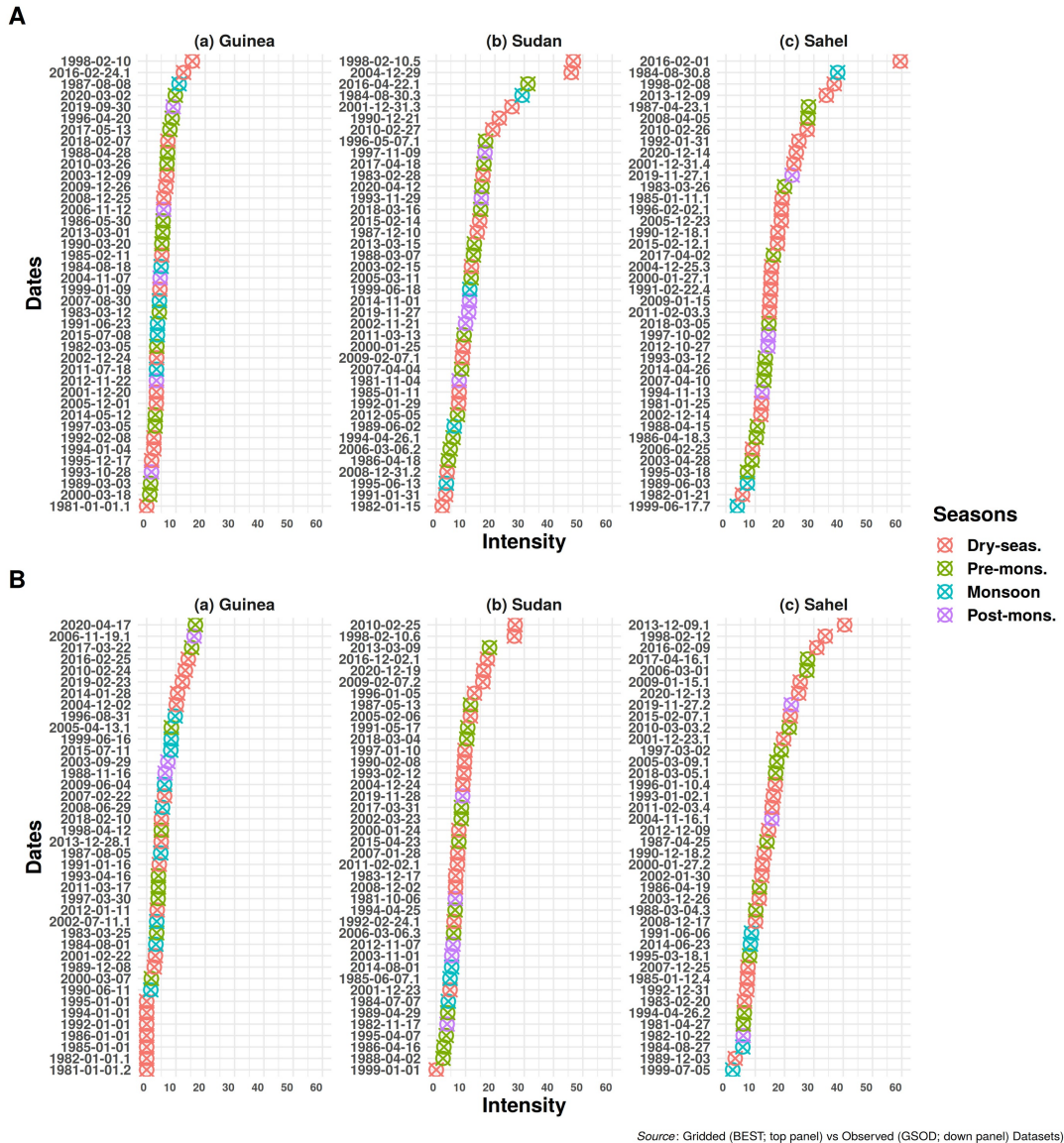


Figure 4.8: Comparison of Annual maximum UTCI CumHeat in different climate zones; Read as in Figure 4.7

4.4 Analysing the Joint Occurrence of Drought and Heatwaves (D-HW): An Integrated Approach of Compound event in West Africa

Heatwave/heat-stress and drought events are calculated by capturing both events' occurrences over the whole year. Heatwaves can happen at any period in the year in Africa, the same is assumed for West Africa even though the intensities seem to be higher between January to April. The analysis is performed per climate regions for

concurrent occurrence of heatwaves with SPEI and SPI with their frequency trends. The D-HW occurred in almost every month in the year but with focus on November-March and some during June-October depending on the climate zone and the intensity.

4.4.1 Concurrent D-HW at 3-month scale (SPI/SPEI and CumHeat Tmax/UTCI)

For gridded data, T_{\max} CumHeat co-occurrence with drought at 3-month scale presents increasing trend of D-HW from the Guinea zone to the Sahel where there are most of the records. In all the zones, there is an increasing trend of the frequency of occurrence (Figure 4.9b and 4.10b). The period 1980s recorded some concurrent events but became more frequent from 1998 and on.

Particularly in the Guinea zone, D-HW events intensity is low compared to the Sudan and the Sahel. Lomé and Atakpame in Togo, Bohicon in Benin and Abidjan in Côte d'Ivoire are tagged in their different representative SPI level colours. The highest intensity recorded is in the Sudan going up to Super Extreme heatwave during a moderate SPI and a severe SPEI. Some stations that recorded that high level of heatwave are Koutiala (Mali), Gaoua and Bobo Dioulasso (Burkina Faso — to mention a few). The periods of severe occurrence are 1980s, 2000s and 2015/2018. The same scheme is presented in the Sahel with more occurrence in the 1980s, then some less intense in the 2000-2010 and finally in 2014/2020 in Maradi (Niger), Leopold Sedar Senghor, Diourbel (Senegal) among others. Most heatwave occurrence are during moderate to extremely dry SPI/SPEI with increasing frequency from 2000 and especially 2015.

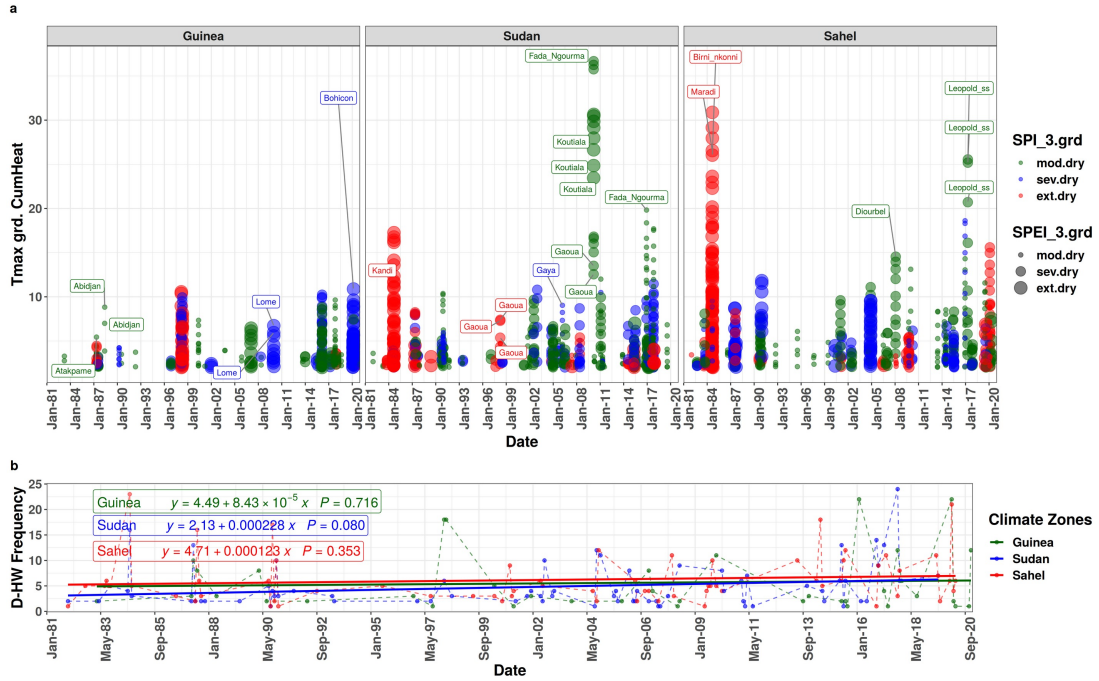


Figure 4.9: Tmax CumHeat gridded D-HW at 3-month scale in West Africa from 1981 to 2020 : a) D-HW Occurrence over time with their levels of intensity/severity (the colours represent SPI and the bubble size are SPEI severity); b) is the frequency of occurrence over the years in the different climate zones (green is the Guinea, yellow is the Sudan and red is the Sahel zone). The trends equations are read as in Figure 4 (P gives the statistical significance (p-value) of the trend)

In the observation dataset (see Figure 4.10), a decreasing frequency is rather noticed in all zones, with a general reduced frequency compared to the gridded dataset. The Sahel has a decreasing trend even though there are high frequency and intensity D-HW as it is in the Sudan. Most of the co-occurrences happened during moderate dry SPI and/or moderate to severe SPEI. The gridded dataset shows higher frequencies and drought intensities. In the 1980s D-HW could be explained by the dry years in West Africa, especially in the Sudan and the Sahel.

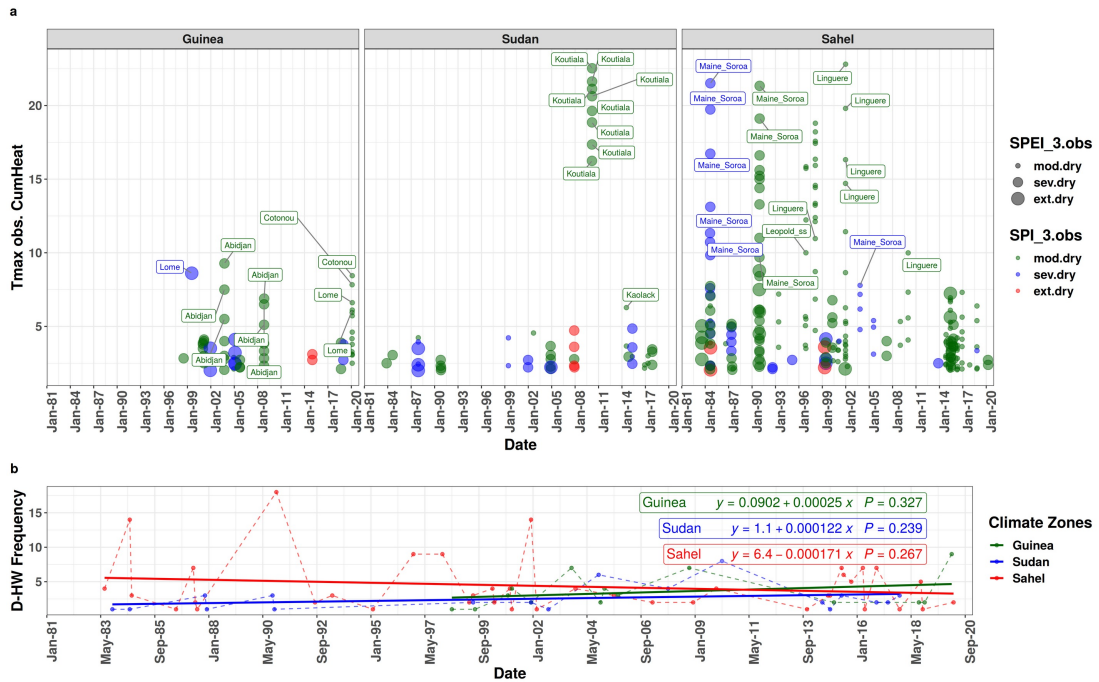


Figure 4.10: Tmax CumHeat observed D-HW at 3-month scale in West Africa from 1981 to 2020 : Read as in Figure 4.9

Overall, the intensities are not the highest T_{max} CumHeat of the data. This could induce the reflection that D-HW event do not really increase the intensity of drought or heatwave in the zones for the 3-month scale droughts. The difference in occurrence from the gridded and observation datasets could come from the precipitation amount recorded at the time by the dataset.

Similarly to the T_{max} , UCI CumHeat present different patterns of co-occurrence in the 3 zones. The intensity and frequency is reducing for all the zones for D-HW gridded dataset (Figure 4.12b) while it is increasing for observation dataset except the guinea zone (Figure 4.11b). All the stations recorded intense and frequent heatwave in the years 1980s (most of which are during extreme SPI/SPEI) and have decreased in the subsequent years, even though there are more records in the Sudan and the Sahel.

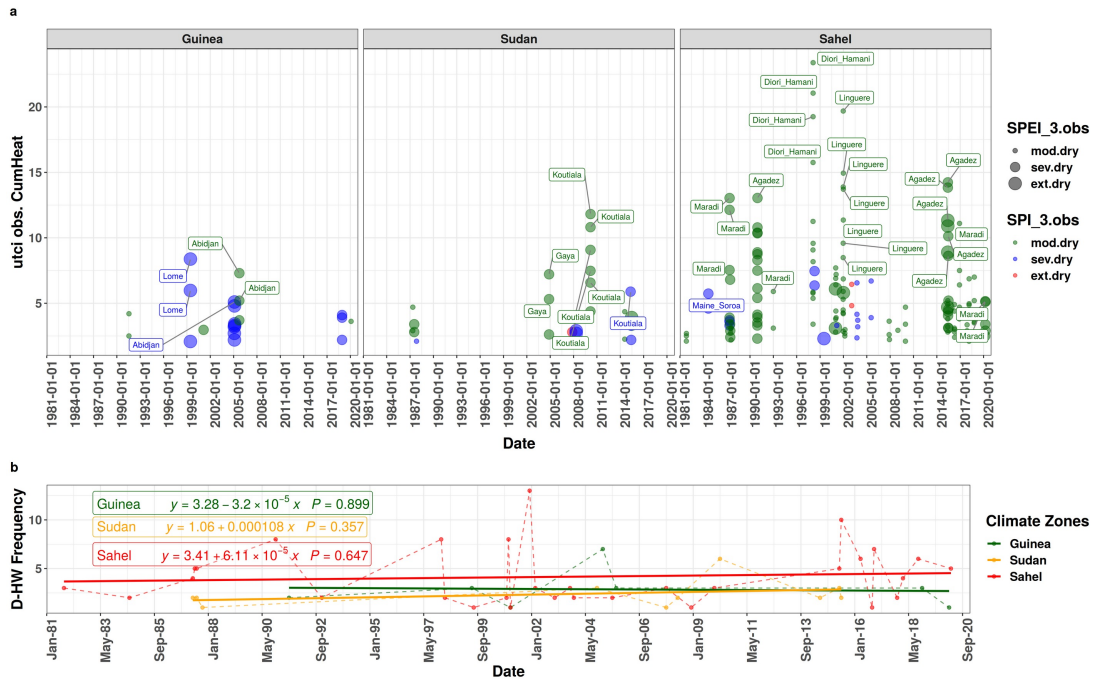


Figure 4.11: UTCI CumHeat observed D-HW at 3-month scale in West Africa from 1981 to 2020 : Read as in Figure 4.9

Here again, the highest intensities are very extreme (Sudan) and super extreme (Sahel) UTCI CumHeat during extreme dryness for SPI/SPEI. Most of the D-HW occurred during a moderate SPI and moderate to severe SPEI. But in the observation dataset, the intensities are reduced with a slight increase in the frequency for the Sahel and the Sudan. Although the frequency have slightly increased, they are similar to what is observed at the end of the trend in the gridded dataset. The decreasing trend of the frequency and intensity of UTCI CumHeat in all zones for the gridded dataset (as seen in Figure 4.12b), follows the same pattern as SPEI, especially in the Sahel at 3-month drought scale. This could be more related to the SPEI because of the combination of evapotranspiration (water vapour) and temperature (radiation) in both indices. UTCI uses humidity in the equation, but the SPEI seems to be reducing, meaning that the evapotranspiration is high and the amount of water (humidity) is reducing.

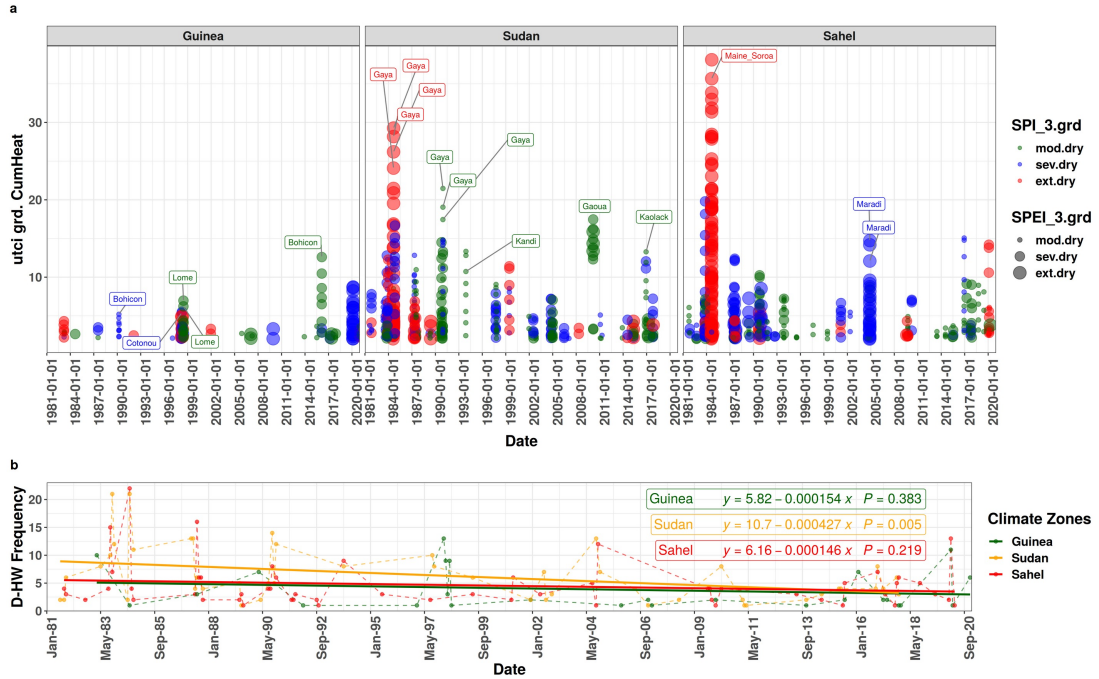


Figure 4.12: UTCI CumHeat gridded D-HW at 3-month scale in West Africa from 1981 to 2020 : Read as in Figure 4.9

There probably is an exaggeration of the 1980s droughts and heatwaves in the gridded dataset. Precipitation is increasing in the zones for SPI and slightly decreasing for SPEI (due to evapotranspiration and temperature variations in the Sudan and the Sahel especially). Zare et al.(2018) showed that there is a strong correlation of UTCI with dry temperature and negative relationship with relative humidity. This means, a decreasing relative humidity might lead to an increase in the UTCI value but the temperature increases with UTCI (SPEI).

4.4.2 Concurrent D-HW at 6- and 12-month scale (SPI/SPEI and CumHeat Tmax/UTCI)

In the 6-month scale drought occurrences, T_{max} Cumheat gridded and observation agreed on the general more or less static frequency trend of D-HW in the Guinea and the Sudan, even though the intensities are reducing for the Sudan zone. The Sahel has

higher frequency over the years with a slight increasing trend. It is also worth noting the 1980s high intensities of D-HW for the gridded dataset compared to the observation. The observation dataset has the same increase in the T_{\max} CumHeat frequency but a reducing trend for the Guinea and a more/less static pattern for the Sudan zone. The Guinean zone shows a decreasing trend of the frequency of observed heatwaves, while the Sahel still present a slight increase. T_{\max} CumHeat seem to be agreeing on the same tendencies in the frequency of the D-HW for both datasets. With the scale, both dataset get closer in the frequency trends of D-HW in the different zones. The UTCI CumHeat show a rather different pattern (not shown here). The gridded dataset frequency is reducing in all zones while the observation is increasing in the Sahel, slightly increasing in the Guinea and more/less null in the Sudan. The gridded data could not capture here the higher intensities in the last two decades in the Sahel. The frequencies are close, but the intensities are different. The 1980s D-HW seem to have been exaggerated in the gridded dataset here too. The same observation and analysis is carried on the 12-month scale D-HW. The highest intensities are recorded in the 1980s and the year 2000s for the Sudan and the Sahel and the frequency is rather decreasing slightly with the T_{\max} CumHeat observation dataset. As the timescale increases, the UTCI CumHeat keeps its pattern of decreasing trend for the gridded dataset in the Sudan and the Sahel and a relatively increasing trend for the Guinea zone. At the same time, the observation dataset shows increasing trend for the Sudan and mostly the Sahel with decreasing trend for the Guinea. The T_{\max} CumHeat presents a different pattern. There is an increasing trend for almost all the zones and time scales with the exception in the Sahel at 3-month scale, in the Guinea at 6 and 12-month scale.

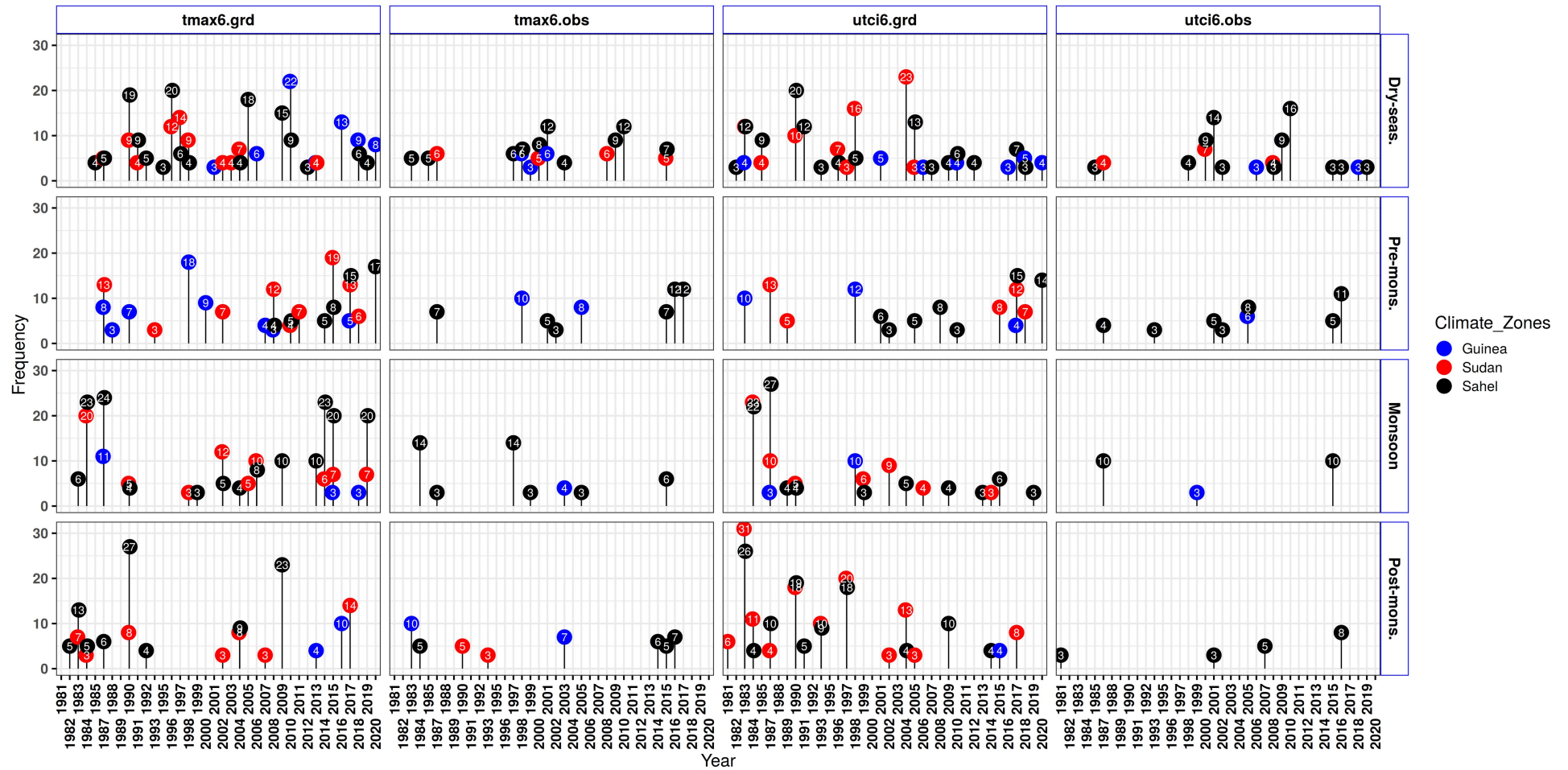


Figure 4.13: D-HW frequency occurrence at 6-month scale in the different dataset at different the considered seasons. Colours represent the climate zones; on the vertical/horizontal are the combinations of datasets and seasons of occurrence.

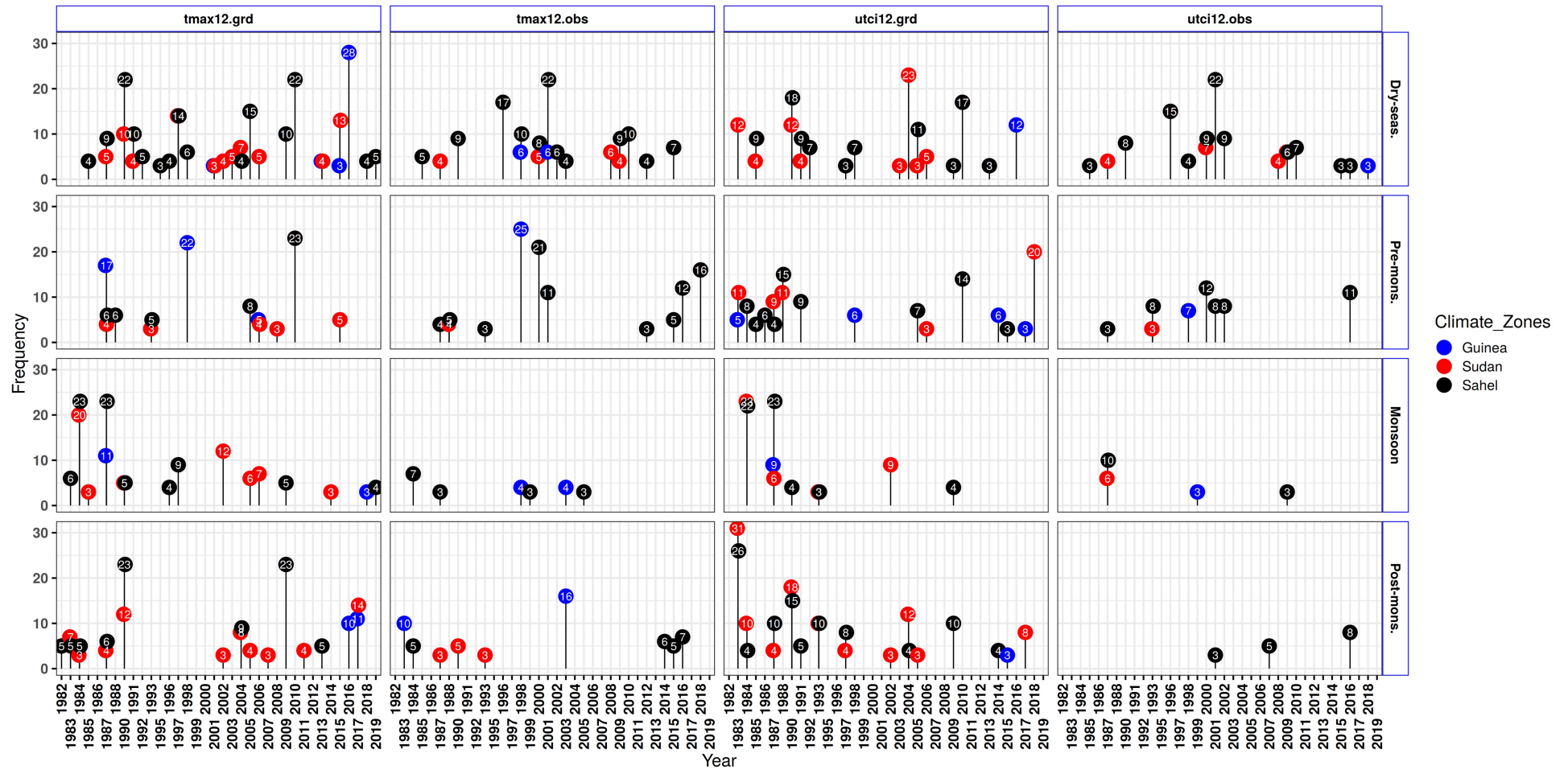


Figure 4.14: D-HW frequency occurrence at 12-month scale in the different dataset at different the considered seasons. Colours represent the climate zones; on the vertical/horizontal are the combinations of datasets and seasons of occurrence.

4.5 Discussion

Under global warming, West Africa's livelihood is affected by longer intense temperature extremes (heatwaves and drought). Heatwave/heat stress could have dramatic impacts on health, humans, natural ecosystems and anthropogenic activities. Most heatwaves in West Africa go unnoticed/unreported, making it difficult for decision-making and fore-preparation. The main findings of this objective are as follows:

- Correlation between drought datasets is very low for both indices at all considered scales. But the within dataset correlations show good agreement even though there are small differences (SPEI takes into account evapotranspiration, it is more sensitive to changes in drought) (Liu et al., 2021; Tefera et al., 2019). The Guinea zone recorded in general mild to moderate SPEI but extreme SPI. Sudan and Sahel all recorded extremes. The combination of CHIRPS and BEST datasets could be a good fit in some stations for SPEI analysis (but with care).
- Station data has less number of heatwaves (CumHeat) and lower intensity compared to Gridded data which is very homogeneous while stations present extreme values (Kozubek et al., 2020). This is also effecting the difference in trends and occurrences of heatwave/heat-stress over the region (Ngoungue Langué et al., 2022).
- The computed UTCI from Rayman model is very close to the ERA5-HEAT data (1.37 ± 0.21 °C) (Di Napoli et al., 2020; Matzarakis and Nastos, 2011). There is almost a very good compatibility. The gap could be linked to the fact

that low clouds in ERA5 are underestimated in West Africa (Kniffka et al., 2019). It could affect the discrepancies that exist between the computed UTCI from Rayman model and the ERA5-HEAT data (ISD observation also has some missing values for cloud fraction cover).

- The Sahel is experiencing more stress than the other zones. The same is observed for T_{\max} CumHeat in some stations, and this is concluded from both datasets (station and gridded). Heatwave/heat-stress intensity are increasing (for both datasets) (Engdaw et al., 2022; Largeron et al., 2020; Moron et al., 2016; Oueslati et al., 2017).
- The Sahel reveals particular tendencies of D-HW. The frequency is increasing or decreasing depending on the index (Tmax/UTCI), the zones and the dataset. Heatwave/heat-stress do not frequently occur during very severe drought conditions with the highest intensity. This aspect is relatively new information in the region but agrees with some previous work (Guigma, 2021) on UTCI or T_{\max} heatwaves occurrence in the Sahel at specific periods of the year that could be considered drought periods (Njoku et al., 2021).

From the above results in the different drought time scales, the D-HW is determined by the frequency and intensity of occurrence. UTCI is a heat budget index that has strong positive correlation with air temperature and solar radiation with a negatively strong correlation with relative humidity (no good correlation with wind; (Njoku et al., 2021; Zare et al., 2018)). At 3-month scale, UTCI and T_{\max} CumHeat show various patterns of D-HW occurrence in all three considered zones. When UTCI seem to be decreasing, T_{\max} is increasing for the gridded dataset, denoting a similar tendency to the 3-month scale SPEI gridded dataset. Indeed, SPEI is influenced by

temperature (potential evaporation due to solar radiation and temperature). Most of the highest T_{\max} CumHeat values are recorded either in the dry season (December to February), the pre-monsoon (January to March-April) or the post-monsoon period (October to December). The same is observed with UTCI, but it is worth noting that UTCI could occur with higher values during May to October in all zones when the relative humidity and/or water vapour are high with soil moisture content (Matzarakis and Nastos, 2011; Njoku et al., 2021). The global warming and the increasing temperature could have been affecting the evapotranspiration and the accelerated depletion of soil moisture and leading to the decreasing frequency (not necessarily intensity) trend of the UTCI especially in the Sahel. Air temperature has the most substantial influence on UTCI in all climate zones as in hot-humid climate (Akinbobola et al., 2017), and in arid or temperate climate (Balogun et al., 2019; Blazejczyk et al., 2012; Vatani et al., 2016). In the work conducted by Largeron et al. (2020) on the April 2010 heatwave, they noted the strong link between heatwaves and the incoming heat surface fluxes over the Sahara and the radiative effect of water vapour especially on minimum temperature. The case under study considers only the maximum temperature, so most of the effect is due to heat advection/fluxes, as stated also by Guigma et al. (2020). As for the 2010 heatwave, there was an increased incoming long-wave radiation and reduced incoming short-wave radiation due respectively to enhanced cloud formation and northward transport of tropical plumes and monsoon flow. Effectively, tropical plumes (first incursion of moist monsoon flow in spring) have an effect during the night (Guichard et al., 2009; Knippertz and Martin, 2005). This happens with a variation of the daily incoming long-wave flux. According to Engdaw et al. (2022), the inter-annual variability of the sea surface

temperature (SST) have a great impact on the causes of heatwaves in the coastal West Africa. There is then a contribution from the oceanic forcing that enhances the occurrence of heatwaves in the coast (Russo et al., 2016), but this is out of the scope of the present study.

Engdaw et al. (2022) analysed the trends of heatwaves in Africa from 1980 to 2018 using observation dataset (CRU TS4.03 and BEST) and reanalysis dataset from ERA5, MERRA-2 and the Japanese Meteorological Agency's 55-year reanalysis (JRA-55). They reported important differences in the datasets trends and temporal evolutions of heatwave with the reanalysis datasets, but pointed to the years of reference in West Africa that are 1998, 2008, 2010, 2016, 2019 and 2020 (mainly indices that use the 90th percentile) as in the current work. They also highlighted the high variability in the bimodal temperature (a maximum in March-April and another one in September-October) pattern.

High temperatures and humidity could lead to intense UTCI but drought periods are known to reduce the humidity, thence the heat-stress. Heatwaves can occur during both drought and non-drought conditions (Wreford and Adger, 2010) as shown in the present work. The relatively reduced intensity of both T_{\max} and UTCI CumHeat as the drought becomes intense could mean that they are less prone to be intensified during very severe drought (Lageron et al., 2020). Moron et al. (2016), when documenting warm extremes in the northern part of the continent, came to the fact that March – June are the warmest season across the Sahelian and Sudanian belts, implying that heatwaves mostly occur between the end of the dry season and the onset of rainfall. This is also observed in the results (Dry and pre-monsoon seasons) of this work, and there are heatwaves that occurred during the monsoon and post-monsoon phase.

The Guinean zone has experienced very extreme heat-stress (UTCI) and heatwave (T_{\max}) especially from January to May (Błażejczyk et al., 2013; Jendritzky et al., 2012). Urban heat island (given the many developing cities in the coastal region) could exacerbate the effects of increasing temperatures' frequency of heatwave/heat-stress in stations close to cities (Fischer et al., 2012). The periods where the heat-stress is low in Sudan and Sahel zones, are mainly where the precipitation generally peaks over the year, temperature has relatively decreased. The Guinea zone, having much humidity, experience less frequent stress between June – September corresponding to the relative reduction of temperature and the start of the little dry season (peaks in August) (Pante et al., 2021). March – May in the Guinea zone are prone to heatwaves/heat-stress because of the moisture (greenhouse effect of moisture according to Guichard et al. (2009)). The Sudan-Sahel zone is a hot and semi-arid region in West Africa experiencing heatwaves with a high risk during springtime and autumn season prior or after the summer monsoon. This is probably facilitated by the springtime Saharan dust from the northern part of the region and/or tropical plumes leading to moisture advection (Knippertz and Fink, 2006; Knippertz and Martin, 2005). Heatwaves are related to drought, but with a configuration different from what is observed in the mid-latitudes regarding the atmospheric dynamics and the soil moisture role.

4.6 Summary

This study investigated the occurrence of heatwave/heat stress and 3, 6 and 12-month drought in three (3) major zones in West Africa: Guinea, Sudan, the transition zone and the Sahel. The study is carried on by comparing the station and gridded datasets.

The cumulative (excess) heat was used for T_{\max} and UTCI values to make them comparable over the selected stations in West Africa. The comparison could be done because UTCI perfectly agrees with air temperature (Bröde et al., 2010) and the 90th percentile is extracted to get the excess heat from the reference daily thresholds. This work goes beyond to check the co-occurrence of heatwave/heat stress with drought. The zones differently experience heatwave/heat stress even to the station level with different pattern in the datasets. There is a low variation of temperature in the tropics, which affects the occurrence of heatwaves in West Africa. There is a need to revisit the physical formation of heatwaves in the region for the development of early warning systems and the probable particular relationship with the West African monsoon system. The physical processes of heatwaves in West Africa relies now on the temperature and moisture roles in the continent, regulating the relative humidity/water vapour. In order to consider all aspects, orography and wind velocity could be an addition to understanding these events in the region.

CHAPTER 5:SYNOPTIC AND BOUNDARY LAYER SCALE DYNAMICS RESPONSIBLE FOR HEATWAVES IN WEST AFRICA

This chapter assesses the physical processes of the atmosphere responsible for heatwaves in West Africa, by using the Universal Thermal Climate (UTCI), the Wet-Bulb-Globe Temperature (WBGT) and Cumulative Excess Heat (CumHeat) on maximum and minimum temperature. Night-time (daytime) heatwaves are considered in this work in the lower atmosphere (Planetary Boundary Layer, PBL). Heatwave case studies are selected for in-depth analysis of temperature tendencies in 2018, 2019 and 2020. This investigation is part of a manuscript under review.

5.1 Introduction

Heatwaves are considered as periods of abnormally hot weather, with temperature targeted as the main driver of the extreme weather event. During a heatwave, the temperature is higher than the average temperature of the affected area. Heatwave have been extensively studied in Europe and many other parts of the world, but in Africa, there has been less attention given to the event. West Africa is described as part of the tropical warmest and driest region, especially the Sudan and the Sahel. Over the Sahel and the Sahara, heatwave events are associated with temperature positive anomalies in spring with westward moisture (movement of moist air or water vapour towards the west, typically driven by prevailing wind patterns) and weaker positive anomaly in summer with weaker moisture. Indeed, the Africa warming is more rapid compared to other regions due to human activities (IPCC, 2021b). This situation is already an alarming one, with the weak adaptation strategies of the populations living in many affected areas. Surface temperatures in West Africa

have risen significantly over the last few decades, with the highest increases occurring in the Sahara and Sahel regions. Specifically, the average annual and seasonal surface temperatures have increased by 1 – 3 °C since the mid-1970s. If global warming reaches 1.5 °C, 2 °C, or 3 °C, average annual surface temperatures in West Africa are expected to be higher than the global average. Heatwaves in West Africa have become more intense and longer in the 21st century compared to the last two decades of the 20th century. From 1961 to 2014, the frequency of very hot days (over 35 °C) has increased by 1 – 9 days per decade, while tropical nights (minimum temperature above 20 °C) have increased by 4 – 13 nights per decade. Furthermore, due to night warming, cold nights have become less frequent. At 1.6 °C and 2.5 °C global warming, the number of potentially lethal heat days is projected to reach 50 – 150 and 100 – 250 per year, respectively, with the highest increases occurring in coastal regions (CDKN Global, 2022). According to recent research, children born in West Africa in the year 2020 will experience a significantly greater number of heatwaves in their lifetime compared to those born in 1960, in the event of 1.5 °C global warming. The projected increase in heatwave frequency is estimated to be between 4 and 6 times higher. Furthermore, the risk of heat-related mortality over tropical West Africa is anticipated to rise to 6–9 times higher than the 1950-2005 average in the event of 2 °C global warming. This alarming trend is particularly prevalent in urban areas such as Lagos, Niamey, Kano, and Dakar due to their increasing level of urbanization. (CDKN Global, 2022). The Sahel is reported to have high numbers of frequency, intensity, and duration of heatwaves in the year, and this will become more in the near future (Deme et al., 2020; Roehrig et al., 2013). The last decades are becoming hotter, according to Fontaine et al. (2013). The strong

warming of temperature in West Africa mainly occurs during April–May, at the interface of the dry and wet season. Even though the progressive soil desiccation has been pointed out as a major process during high magnitude heatwaves in the mid-latitudes, in West Africa the theory might not completely hold in the Sahel and Sahara because they are already dry zones (Largeron et al., 2020). Largeron et al. (2020) and Guichard et al.(2009) reported that moisture frequently advects into Sahelian heatwaves, but the main driver remains the temperature. The objective of this investigation is to analyse the modifications in atmospheric state processes through the use of temperature tendencies dataset obtained from the Year of Polar Prediction (YOPP) initiative spanning from 2018 to 2020. The study defines specific case studies to identify the impact of each temperature tendency term, and calculates the sum of these tendencies to explain the state change between consecutive model output times. By breaking down the overall state change into the contribution from each process, the tendencies enable users to gain a comprehensive understanding of the changes in atmospheric state.

5.2 Evaluation of Regional Heatwaves

A comparative analysis is performed on the spatial grid scale (grid points) over the period 1981 to 2020 (Figure 5.1). This is done for all computed and normalized indices (cumulative excess heat for Temperature, the Universal thermal Climate Index – UTCI and the Wet-Bulb Globe Temperature – WBGT) including the duration and the cumulative intensity. The duration in days is displayed as well as the years of occurrence at regional scale for both maximum and minimum daily indices.

The top panel (Figure 5.1A) visual aspect gives a hint that the largest heatwave coverage (Coastal and Northern part of the region) happened after the years 2000s and particularly after 2010. This is mainly for the T_{\max} and max daily UTCI. In the Sahel, it can be observed some heatwave pockets (Figure 5.1A-d, e) in 1983, but the largest coverage is after 2007-2010.

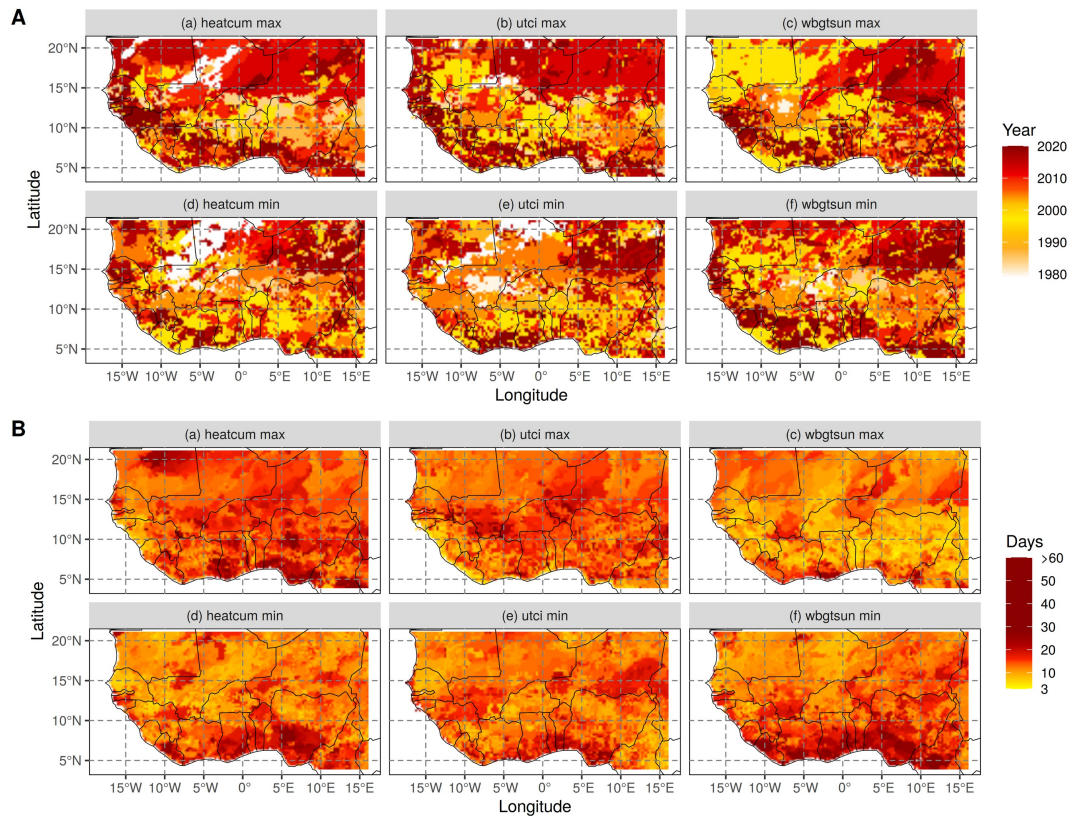


Figure 5.1: Duration in the historical period (1981 - 2020). The Years of Occurrence (A-a,b,c); maximum (daytime) Temperature, UTCI and WBGT and (A-c,d,e) minimum (night-time) Temperature, UTCI and WBGT; The part B present (B-a,b,c) the duration for maximum daily Temperature, UTCI and WBGT, and the (B-c,d,e) duration for minimum daily Temperature, UTCI and WBGT; in West Africa

Looking at the duration of the events in the region, they vary with the different indices, but the coastal area seems to present high intensities going up to 60 days (Figure 5.1B-a, f) as well as the Sahel (Figure 5.1B) and some part of the Sudan (Figure 5.1B-b, d, e, f). The longest day max heatwave recorded 50 days (WBGT),

48 days (T_{\max}) and 44 days (UTCI). The daily minimum heatwave recorded rather high values, 66 days (WBGT), 54 days (UTCI) and 47 days (T_{\min}). The minimum daily indices recorded higher values except for the Temperature where the values are closer. The intensity varies as well.

The Figure 5.2 reveals the normalized cumulative intensity for comparison. Between the different indices, there are slight differences in the year of occurrence. For example, the 1983 maximum temperature Cumheat in the Northern part of the region (Northern Mali and Mauritania) is carried in the UTCI maximum CumHeat and their minimum CumHeat (Temperature and UTCI) with a slight shift in the location (Figure 5.2I-a, b, d, e). The WBGT remains locally consistent in the 1981 heatwave for both maximum and minimum heatwave located in the central part of Mali (see Figure 5.2I-c, f).

Most heatwaves that occurred in or after 2010 are located either in the Sahel or in the Coastal area, a few in the Sudan. But their intensity is also proportional, going up to 40 in the cumulative intensity. The records present for daily heatwaves 34 (T_{\max}), 43 (UTCI) and 37 (WBGT) against 29 (T_{\min}), 37 (UTCI) and 44 (WBGT) for night-time heatwaves. It is also interesting to appreciate the variations in the cumulative intensity, where the night-time heatwaves present higher intensities compared to the daytime heatwaves for the WBGT.

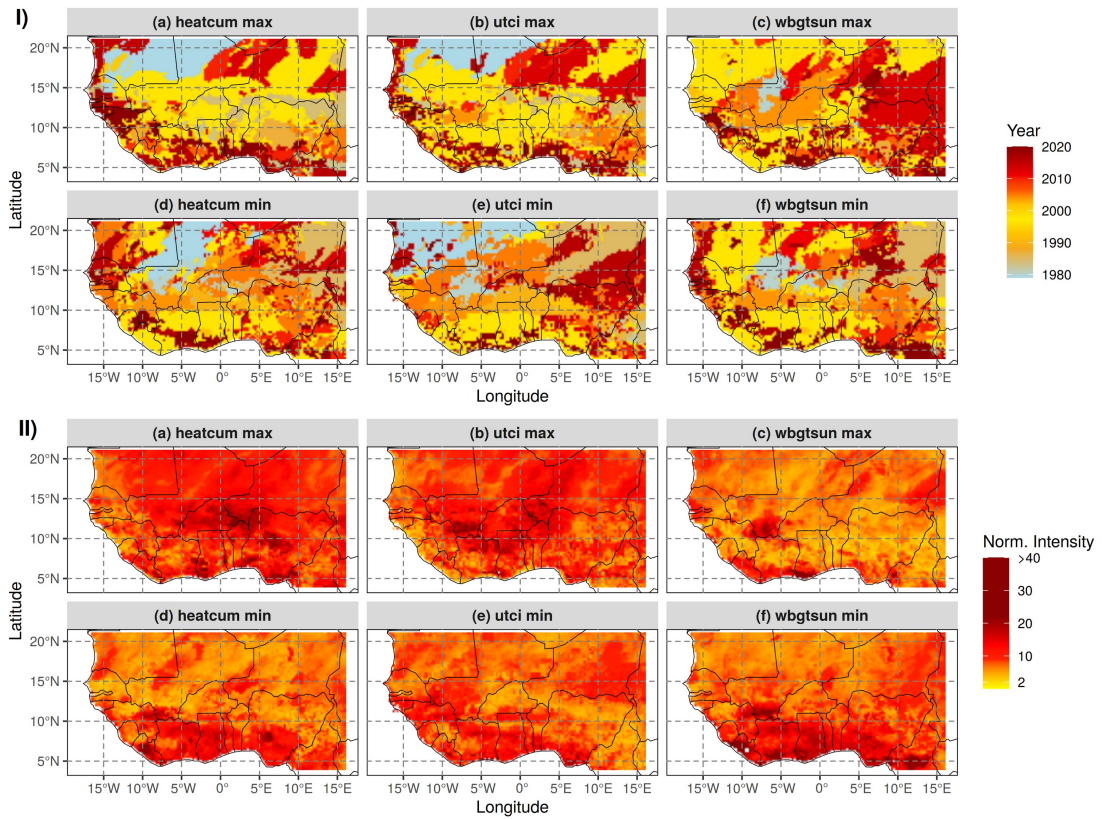


Figure 5.2: Cumulative Intensity in the historical period (1981 - 2020). The Years of Occurrence (A-a,b,c); maximum (daytime) Temperature, UTCI and WBGT and (A-c,d,e) minimum (night-time) Temperature, UTCI and WBGT; The part B presents (B-a,b,c) the maximum normalised Cumulative Intensity for Temperature , UTCI and WBGT, and the (B-c,d,e) minimum normalised Cumulative Intensity for Temperature, UTCI and WBGT; in West Africa

Thus, to appreciate the differences between the different indices at daytime (Figure 5.3) and night-time (Figure 5.4) periods, the relative difference is computed at regional scale (spatial).

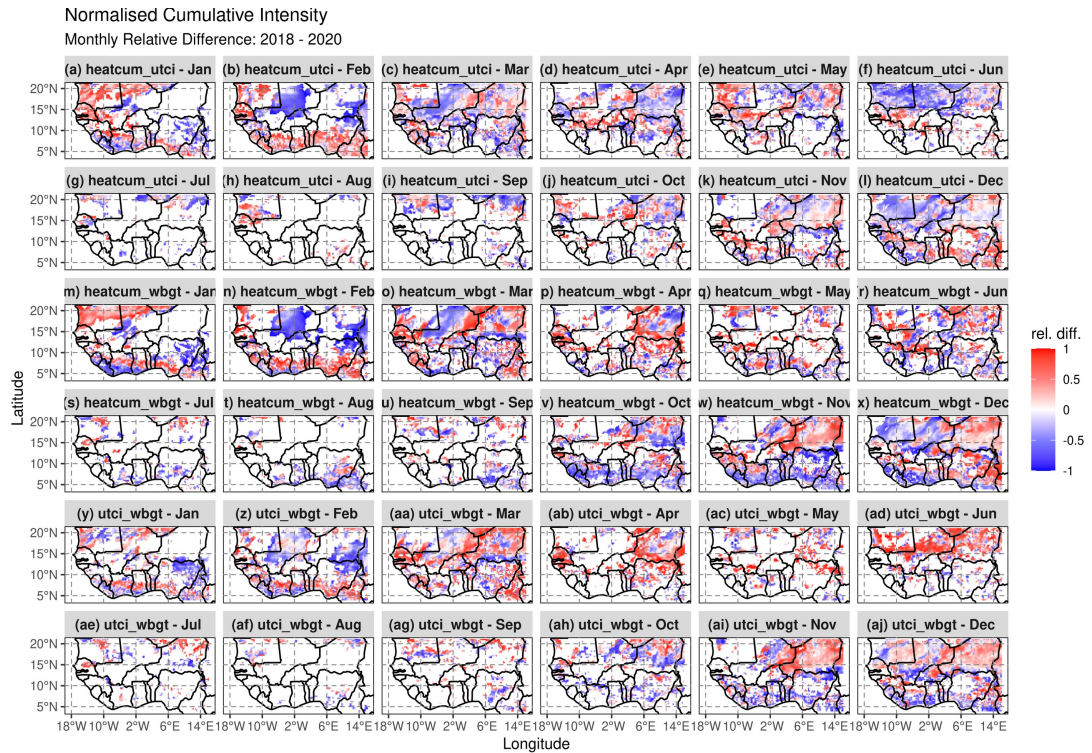


Figure 5.3: Daytime Heatwave Monthly Relative Difference over the selected case study period (2018-2020) for Normalised Cumulative indices: (a-i) Temperature and UTCI; (m-x) Temperature and WBGT; (y-aj) UTCI and WBGT

The daytime differences are mainly positive in the coastal part between T_{max} and UTCI in January-February. UTCI affect the Sudan and the Sahel with more intensity compared to the T_{max} (the negative relative difference dominate). The end of the year rather shows a distinction between the West (negative, Figure 5.3a-i) and the East (positive, Figure 5.3a-i). The pattern is not very clear for the T_{max} and WBGT combination but January-March and October-December present major differences in terms of area coverage (Figure 5.3v-x).

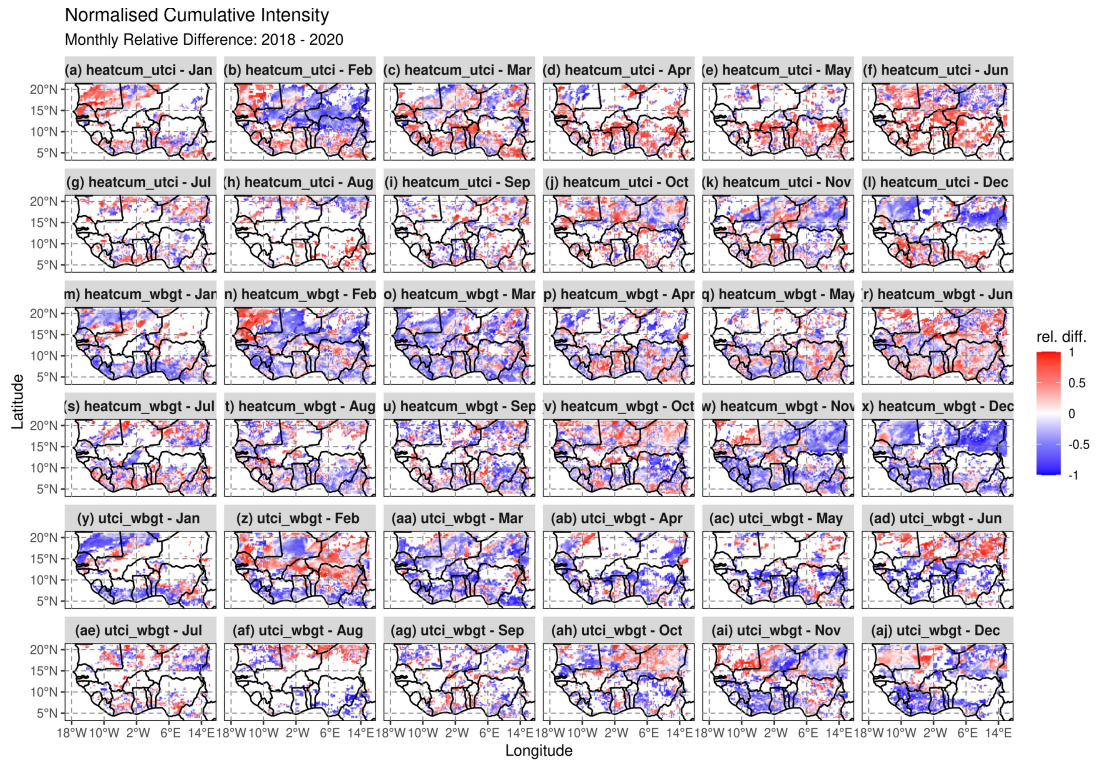


Figure 5.4: Night-time Heatwave Monthly Relative Difference over the selected case study period (2018-2020) for Normalised Cumulative indices: (a-i) Temperature and UTCI; (m-x) Temperature and WBGT; (y-aj) UTCI and WBGT

In general the pattern shows positive correlation between T_{\max} -UTCI, T_{\max} -WBGT and UTCI-WBGT in the Coastal area and negative in the Sudan and the Sahel for the first 2 months, while the opposite is presented from March onward. There are a few coverage differences between UTCI and the WBGT except during March, November and December.

The night-time differences are mainly negative between T_{\min} and the WBGT (temperature lower than the WBGT in general Figure 5.4m-x) but positive between T_{\min} and UTCI (temperature higher than UTCI Figure 5.4a-i).

There is a mix between UTCI and the WBGT but the Guinea zone reveals that the UTCI is higher than the WBGT while the opposite is observed in the Sudan and the Sahel.

From the previous heatwave comparison it can be determined the seasonal occurrence and location of severe heatwaves, even though it is not clear how they develop. In order to see the development in the selected case studies (January-March 2018; October-December 2019 and January-March 2020) single day window plots have been made (not shown).

5.3 Thermodynamics during Selected Heatwave Case Studies over West Africa

This section assesses the thermodynamics at the root of heatwaves in the region. For the analysis, the ECMWF Year of Polar Prediction (YOPP) model levels at 91, 80, 77 and 71 which roughly correspond to 1013.25, 925, 850 and 700 hPa or 25 m from the surface to ~900 m, then to ~1.4 km (about the highest height of a convective boundary layer – CBL height) and 3 km (higher than the boundary layer level) in altitude are used (Aryee et al., 2020).

The case studies considered the period of January to March 2018 in the Niger and Mali which is the central part of the region, October to December 2019 in Niger located more in the Easter part of the region and the whole Coastal part in the Guinea zone in January to March 2020 (see Figure 5.5). The case studies do not present the most extreme heatwave events over the period 1981 to 2020 but due to the ECMWF YOPP data availability, this work is limited to the heatwave development from 2018 to 2020 (using the duration, extent, and severity).

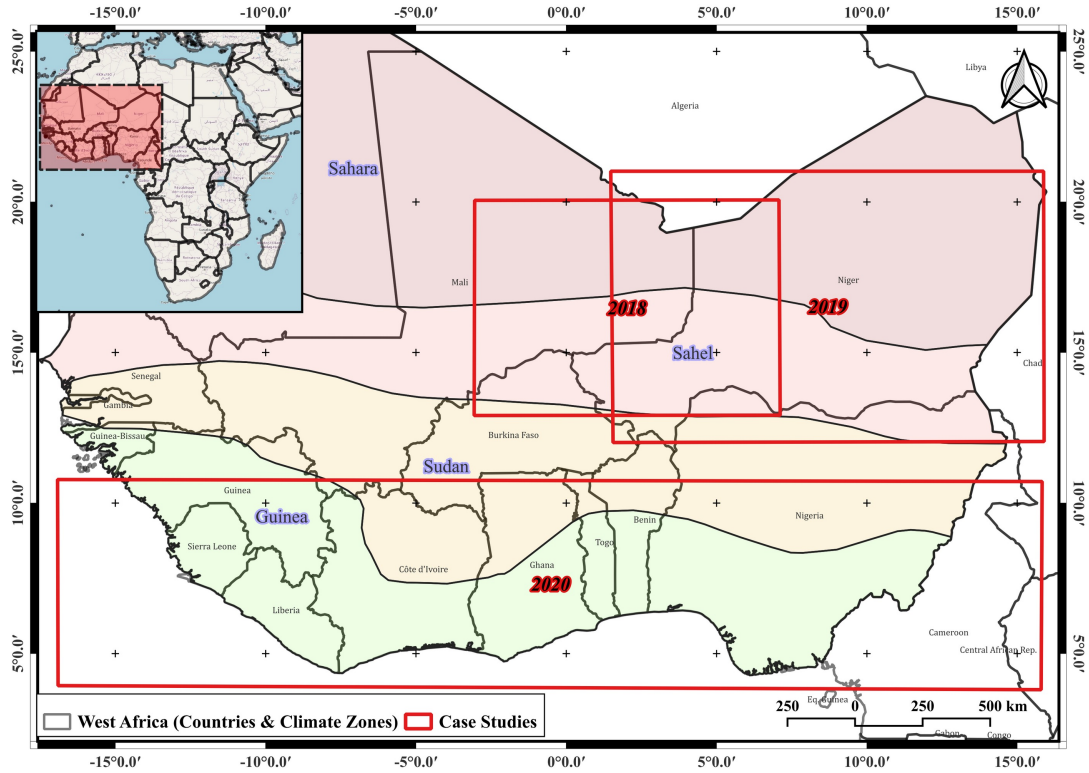


Figure 5.5: Selected Heatwave Case Studies (red boxes) on the year of occurrence

Among the three indices that are used in the present study, almost all of them present occurrences at the periods selected for the case study. The maximum temperature CumHeat, the UTCI and the WBGT recorded daytime heatwave events respectively from 01st to 15th March 2018, 28th February to 16th March 2018 and the 22nd February to 03rd March 2018. The night-time heatwaves are recorded roughly from the 23rd February to the 4th March 2018. The Table 5.1 presents the different start and end dates considered for the heatwaves indices used for the case study analysis and their. The years 2019 and 2020 can easily be read in the table.

Table 5.1: Table Presenting the Heatwave Occurrence in the Case Study periods and for all the heatwave indices

| | | 2018 (Jan-Mar) | | 2019 (Oct-Dec) | | 2020 (Jan-Mar) | |
|------------|---------|-----------------------|------------|-----------------------|------------|-----------------------|-------------|
| | | Start | End | Start | End | Start* | End* |
| Daytime | CumHeat | 01-Mar | 15-Mar | 19-Nov | 29-Nov | 21-Jan | 26-Feb |
| | UTCI | 28-Feb | 16-Mar | 17-Nov | 30-Nov | 14-Jan | 28-Feb |
| | WBGT | 22-Feb | 03-Mar | 18-Nov | 27-Nov | 14-Jan | 26-Feb |
| night-time | CumHeat | 24-Feb | 04-Mar | 14-Nov | 29-Nov | 15-Feb | 05-Mar |
| | UTCI | 22-Feb | 03-Mar | 14-Nov | 29-Nov | 19-Feb | 05-Mar |
| | WBGT | 22-Feb | 03-Mar | 18-Nov | 27-Nov | 21-Feb | 26-Mar |

* The red coloured dates indicates differences in the start and end date of daytime and night-time heatwaves

The 2020 case study in the Table 5.1, even though the dates do not perfectly overlap in the start and end dates for the daytime and the night-time events, they have overlapping periods in the heatwave development that is used. A prior selection of the tendency terms was done and a total of 7 variables are kept for further analysis: the temperature tendency by dynamics (ttendd), temperature tendency by radiation (ttendr) and the temperature tendency by turbulent diffusion (ttendt) are selected. The total tendency (totaltt) is also computed as well as the Meridional (Merid), Zonal (Zonal) advections and the temperature tendency from dynamics minus the total advection ($rttd = ttendd - total.adv$).

5.3.1 Principal Component Analysis (PCA): Dimensionality reduction of the variables and Pattern Detection

The Principal Component Analysis (PCA) reveals a good percentage of the total variation in the dataset can be explained by each principal component. Generally, for the case studies, the first two component could explain more than 50% of the variations in the dataset. The 2018 heatwave PCA is summarized in Figure 5.6. The

scree plot (total variance explained by the PC) in Figure 5.6a shows that the first two dimensions of the analysis express 60.8% of the total variation (inertia) in the dataset, which means that 60.8% of the individuals (records here) or variables (tendency terms, advections and derived terms) cloud total variability is explained by the plane Figure 5.6b-d. In the biplots (Figure 5.6b-d), each variable is represented by an arrow, and the length and direction of the arrow indicate the variable's contribution to the first two principal components. The individuals are represented by dots, and their position in the biplot reflects their scores on the first two principal components. In addition to the variables and individuals, the biplot can also show the quality of the individuals (\cos^2 - Figure 5.6b) and individual groups with ellipses (Figure 5.6c,d). The \cos^2 values represent the quality of the individuals in the biplot, and they indicate the proportion of the total variance of the data that is explained by the first two principal components. Higher \cos^2 values indicate that the individual is well represented in the biplot. The ellipses in the biplot are used to group similar individuals together. They are constructed based on the standard deviation of the individuals' scores on the first two principal components. Individuals that are close to each other within an ellipse are considered to be similar.

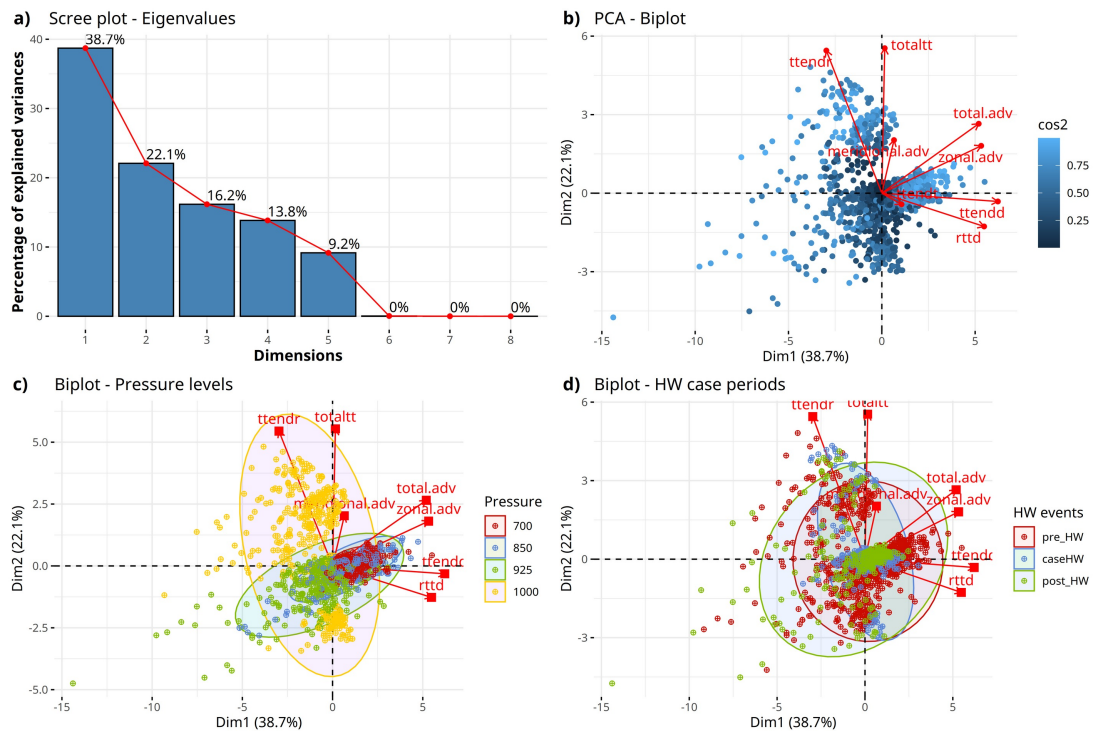


Figure 5.6: PCA Applied to the 2018 Heatwave case study. Shown here are the (a) the scree plot that explain the total variation in the dataset by each component; (b) the biplot that give the direction of the individuals and the variables; (c) the biplot with classes focussed on the pressure levels and (d) the biplot with classes focused on the HW event periods

According to Figure 5.6b, a first group of high values for the variables total advection (total.adv), ttendd, zonal.adv, rttdd and ttendr (variables are sorted from the strongest). In the dimension 2, the variables that explain the variations are ttendr and totaltt. It can be noticed that the total.adv and ttendd highly contributes to the explanation of the changes. The Figure 5.6c,d is identical to the Figure 5.6b in explanation but grouping variable is added to show the contributions of individuals (grouped colours) per pressure levels (Figure 5.6c) to the variables and per data phases (before the heatwaves case, during and after the heatwave case period Figure 5.6d). The results show that the 1000 hPa groups the ttendr and ttendr while 925 hPa is likely to be related to the ttendr and towards ttendd and the advectons. On the

contrary, the 850 hPa will call more onto the tt_{endd} and the temperature advection variables (zonal and total – the zonal might have a good influence in the total advection in general in the area at that period). The 700 hPa is better grouped around the tt_{endd} , $rttd$ and also the zonal advection. These results could indicate that the advection plays a huge role in the temperature change. On the period of occurrence of the heatwaves in 2018, the heatwave period tend to be more influenced by the tt_{endd} in altitude, tt_{endt} and the tt_{endr} at the surface. Note the opposition between the tt_{endd} with the tt_{endd} and tt_{endr} . This calls to the fact that the tt_{endd} generally increases when the tt_{endr} reduces with altitude. The heatwaves occurrences are splitted into two parts following the groups of tendencies. A part influenced by the $total_{tt}$ and the tt_{endr} . And the other part influenced by tt_{endd} , $rttd$ and the temperature advections passing by the tt_{endt} .

In 2019, the pattern is not very much different (see Figure 5.7). Here again the scree plot shows that the first two dimensions could explain the total variation in the dataset at 61.6%. The $total_{adv}$, $zonal_{adv}$, tt_{endd} , $meridional_{adv}$ and $rttd$ (variables are sorted from the strongest) are the highest contributing variables in the first group and in the dimension 2 it is noticed that the $total_{tt}$, tt_{endr} , and tt_{endt} have good influence. As in 2018, the 1000 hpa is more influenced by the $total_{tt}$, tt_{endr} and the tt_{endt} and more of tt_{endt} and the advections for 925 hPa. The advections and tt_{endd} are characteristic of the 850 hPa processes.

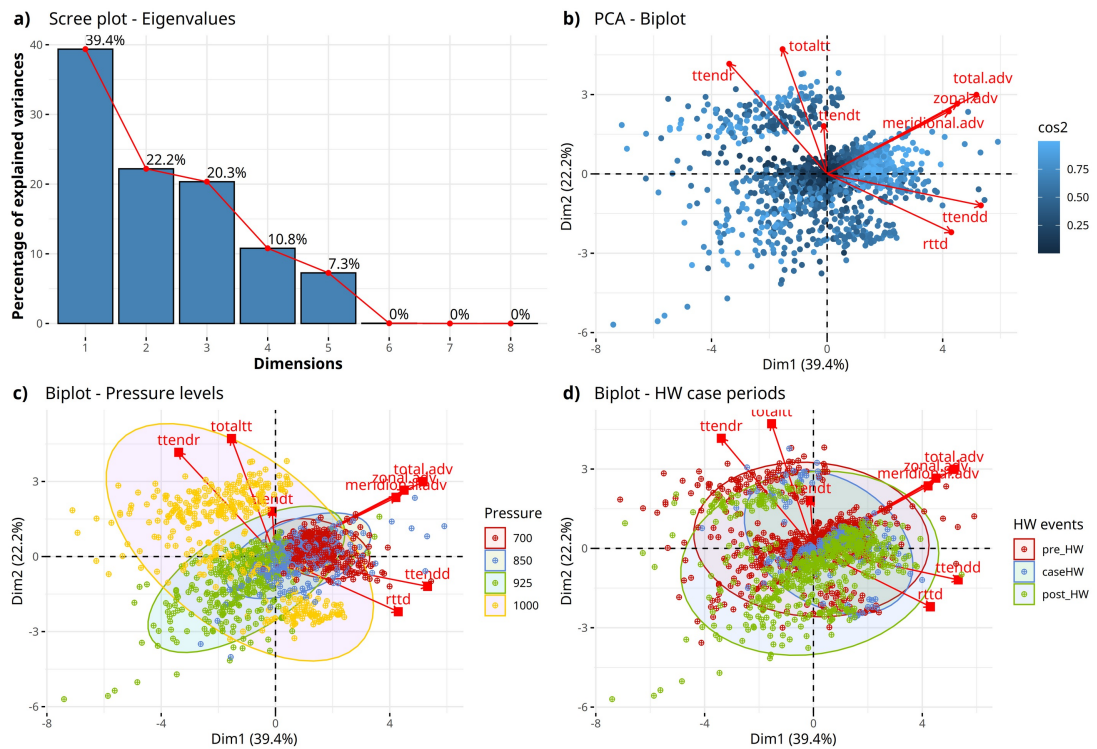


Figure 5.7: PCA Applied to the 2019 Heatwave case study. read as in Figure 5.6

And finally, the 700 hPa is exclusively marked by the horizontal and vertical motion of the atmosphere due to changes in pressure (ttendd) and the temperature advections. The 2019 heatwave is more influenced by the zonal advection, the ttendd and the ttendt sometimes. The 2019 heatwaves are more influenced by the temperature advections and the ttendd with the residual temperature tendency.

The last case study (2020) is presented in Figure 5.8 with a plane representation of the first two PCs (scree plot shows 78.2%). This is the highest score from all cases. Here, there is a clear distinction between the groups of influencing variables, totaltt, ttendr and ttendt on one side and all the other terms on the other side.

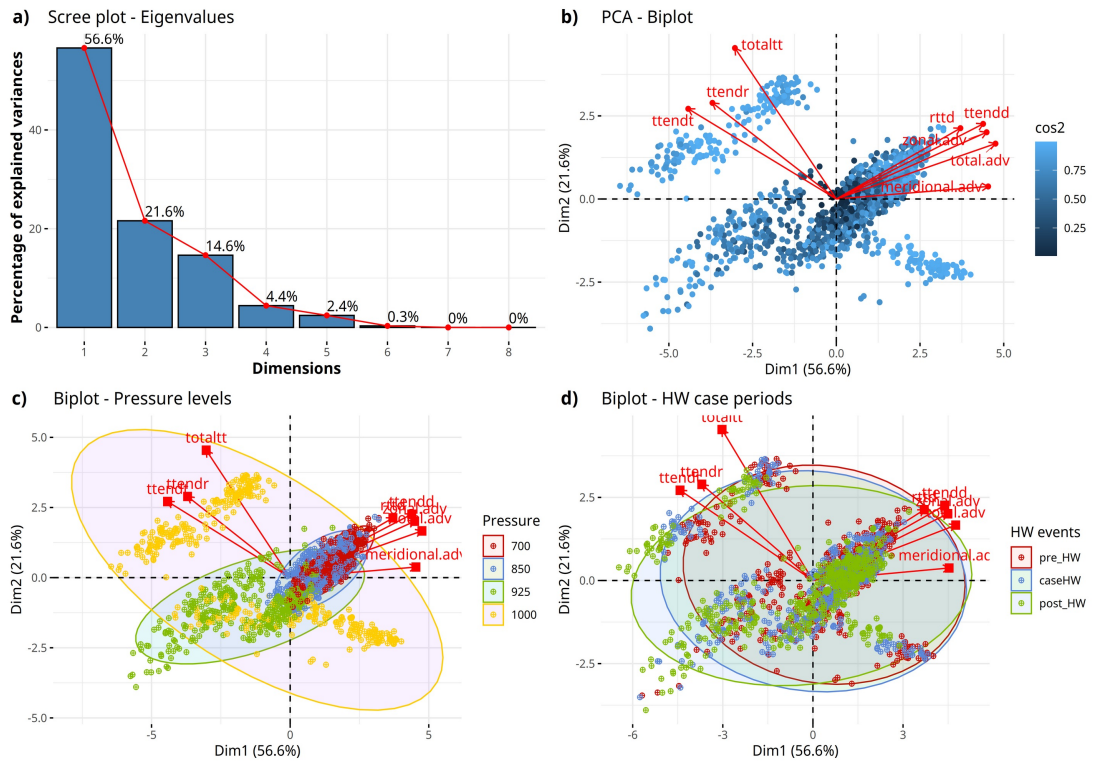


Figure 5.8: PCA Applied to the 2020 Heatwave case study. read as in Figure 5.6

Again the 1000 hPa is scattered but oriented toward the absorption and emission of radiation by atmospheric gases, clouds, and the Earth's surface and the turbulent mixing of air molecules which contribute more to the total tendency. From 925 hPa to the altitude the groups become more shaped around the situation of rising warm air leading to cooling and sinking cool air leading to warming (ttendd), its residuals and the temperature advectons. Indeed, the 800 and 700 hPa levels are more influenced by the ttendd, rttdd, and advectons even though they contribute less to the total advection. The higher the altitude (lower the pressure level), the closer the concentration of the dataset to a single pattern revealing the probable effect of the surface (radiation effect, friction effect on the wind making the variable scattered and hardly discernible). The heatwave period of occurrence is more affected in 2020 by ttentd and ttendr at the surface and ttendd with the advectons in upper levels of the

layer. But in this particular case, the pre-heatwave and post-heatwave seem to be influenced as well by the $ttendd$ and the advections in preparation. Further analysis could reveal this pattern more clearly.

Heatwaves in the region, looking at the different PCA results from the case analysis, reveal that the $ttendr$ and $ttendt$ at the surface and $ttendd$ and $rttd$ with the advections in the upper levels are closely related to the events (temperature related analysis). The higher pressure levels reveal features more clearly compared to the lower pressure levels, reason why the 1000 hPa could be skipped from this analysis and the subsequent ones to avoid the high influence of the radiation at the very surface. From a complete analysis, the 1000 hPa and the 700 hPa will be used in the subsequent analysis for a holistic view of the processes.

5.3.2 Temperature tendency and temperature advection analysis: Trends and Patterns before, during and after Regional heatwaves

The temperature tendency showed an importance in the $ttendd$, $ttenddt$ and the temperature advections (Zonal and Meridional). The trend and evolution of the different variable is considered here, in this section, to understand the underlying causes of heatwaves in West Africa relative to the thermodynamics. In 2018, the Figure 5.9 and Figure 5.12 show the atmospheric conditions obtained from the aggregation of the different variables over the box area where the heatwaves were detected. At 925 hPa, there have been high fluctuations in the $ttendd$ and the $ttendt$ with the zonal and total advection following the same pattern over the days. Before and after the heatwave event, a dip is noticed.

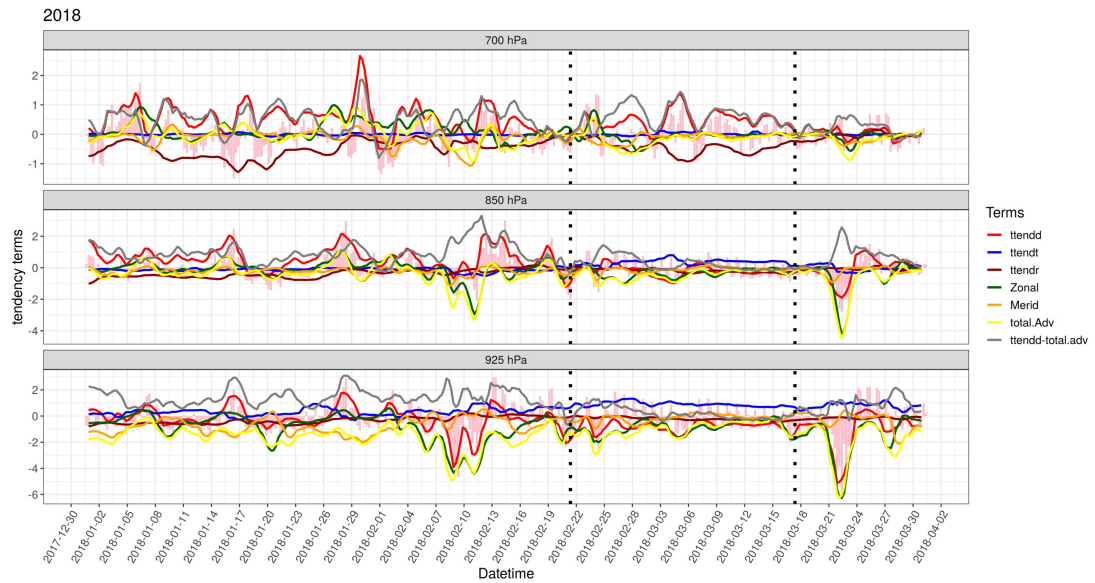


Figure 5.9: Variables evolution at 6 hourly over the whole selected period for heatwave case study in 2018. The values have been smoothed to daily for clarity. The pink bars are the totaltt. The black dotted vertical lines show the section of the beginning and the end of the detected heatwaves highest event in this particular period.

The pattern is similar for the 850 hPa but the 700 hPa show some shifts. In the Figure 5.10 there is a good correlation between the ttendd and the totaltt which denotes that at 850 hPa, the ttendd contributes more to the totaltt amongst the selected temperature tendency terms.

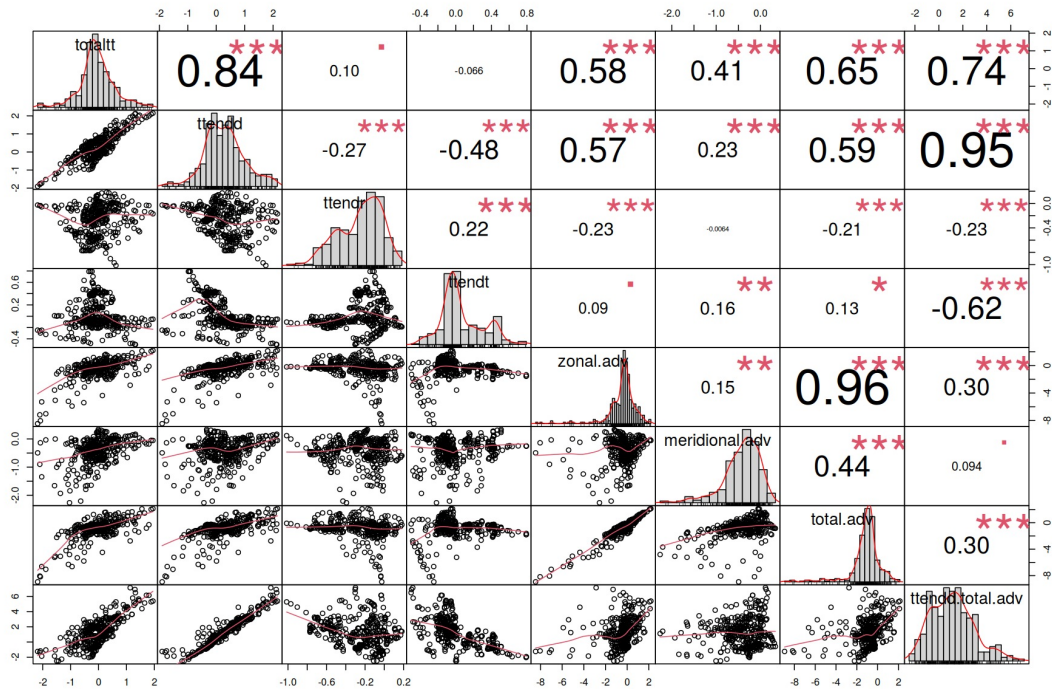


Figure 5.10: 6 hourly correlation of variable at 850 hPa over the whole selected period for heatwave case study in 2018. On top the (absolute) value of the correlation plus the result of the correlation test as stars. On bottom, the bivariate scatter-plots, with a fitted line. The bigger the absolute values the better the correlation (both positive or negative). The red crosses (correlation test) show the significance level of the p-values (0, 0.001, 0.01, 0.05, 0.1, 1) \Leftrightarrow symbols (“****”, “***”, “**”, “*”, “.”, “.”)

Furthermore, the ttendd is negatively correlated with the ttendt and positively well correlated with the zonal advection (zonal.adv) and the total advection (total.adv). These values give a hint on the contribution of the zonal advection in the heatwave formation in the area. The same information could be true for the 925 hPa.

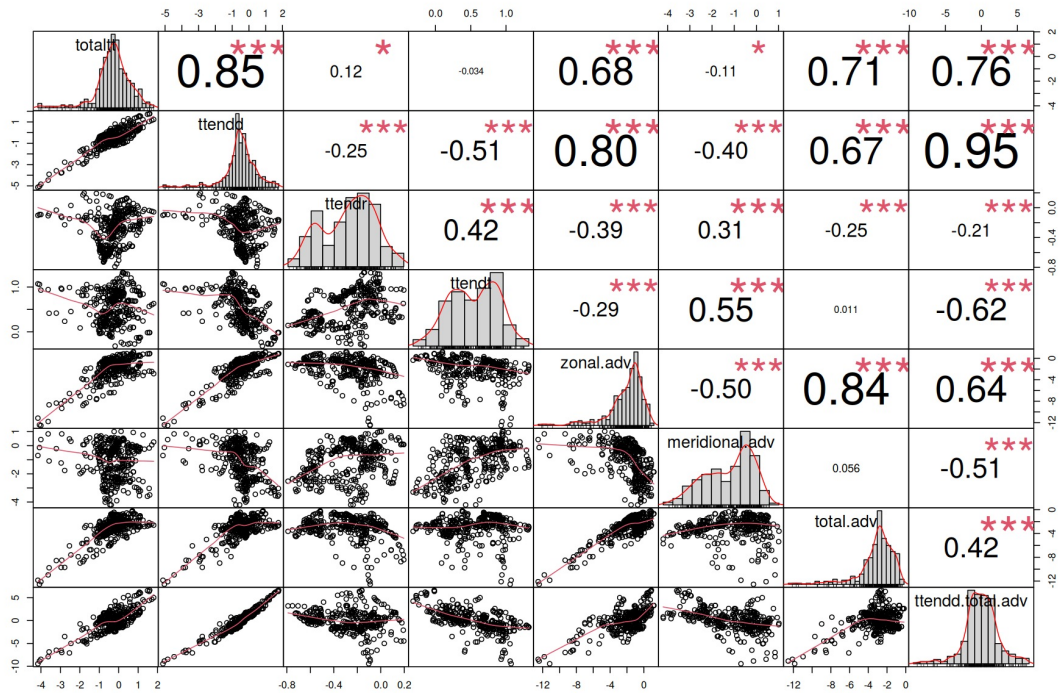


Figure 5.11: 6 hourly correlation of variable at 925 hPa over the whole selected period for heatwave case study in 2018. Read as in Figure 5.10

At 925 hPa (closer to the earth surface), the same scenario is observed, but the correlation values are higher for the ttendd and totaltt as well as the correlation between the ttendd and the zonal advection (total advection). This implies the zonal advection of temperature in the building of heatwaves in the region.

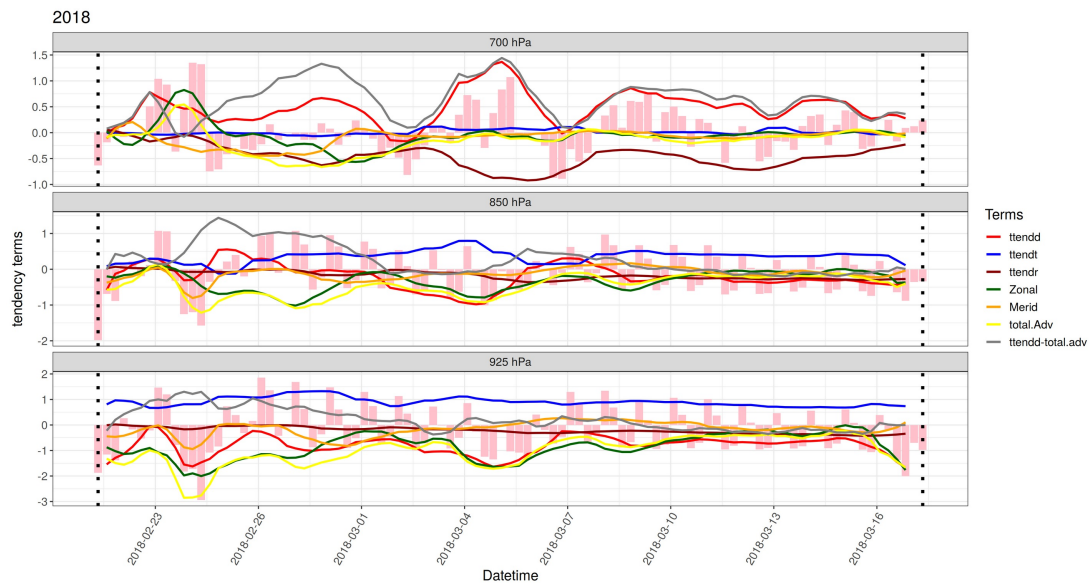


Figure 5.12: 6 hourly smoothed evolution over the 2018 detected heatwaves highest event in this particular period. Read as in Figure 5.9

Indeed, an increase in the $ttendd$ is noticed during the period of the heatwave denoting a change in the temperature dynamics, but this is something that was also present and active before the beginning of the event. The total advection as well as the zonal advection perfectly align with the $ttendd$ and the $rttd$ in the lower atmosphere. At different pressure levels, different variables play different roles in the total tendency, but the $ttendd$ tend to contribute more as the altitude increases. There is at the starting point of the heat event, a warming air due to zonal temperature advection, but it is not maintained over the period of the event.

The 2019 heatwave is a well synchronized period for the daytime and night-time heatwaves, as occurrence periods coincide together. The tendency terms start accumulating from the beginning of the month of October up to the end of the year (see Figure 5.13) for all the pressure levels. Before the start date of the heatwave, the advections (especially the total advection) is correlated to the $ttendd$ and the $rttd$, but

this is observed mainly for the 925 hPa and the 850 hPa. In the 700 hPa this link is not observed or has faltered. This denotes a temperature advection in preparation and during the heatwave period in November in the boundary layer (BL). The similar observation was made for the 2018 heatwave, but the 700 hPa kept a relatively good link between the total advection and the ttendd.

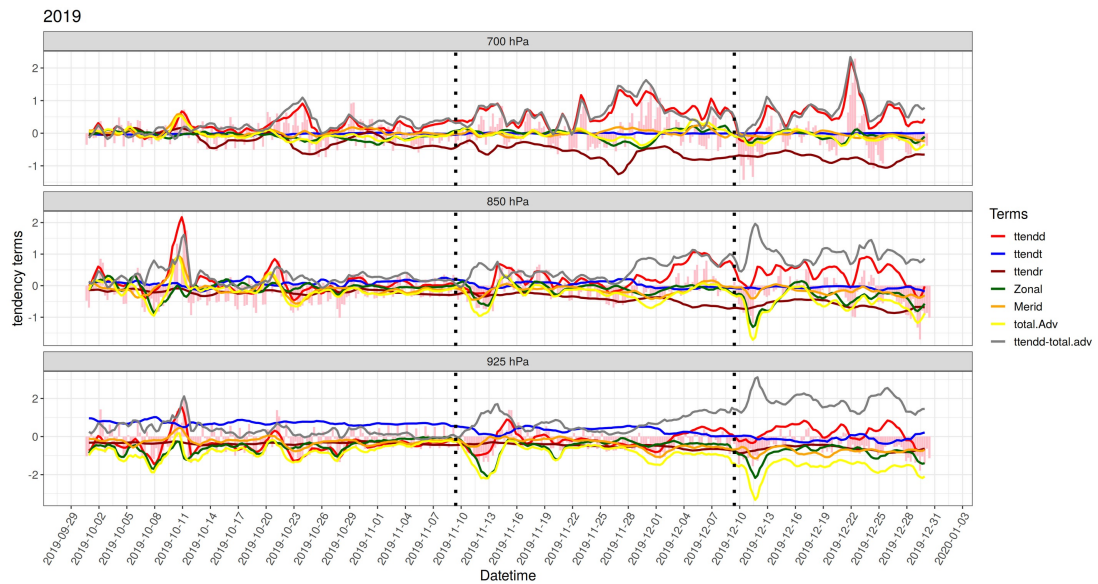


Figure 5.13: Variables evolution at 6 hourly over the whole selected period for heatwave case study in 2019. Read as in Figure 5.9

The 2019 heatwave is here pushed by the ttendd and driven by the temperature advection. The correlation coefficients (see Figure 5.14) remain high for the ttendd (in contributing to the total tendency) but for the ttendd and the advection, there is a tendency for good correlation with the meridional advection. This implies a meridional of the heat in the area. The same is observed with the total advection and the total tendency term, even though the correlation between the total tendency and the zonal advection is also good. At that level, there is good agreement between the ttendr and the ttendd.

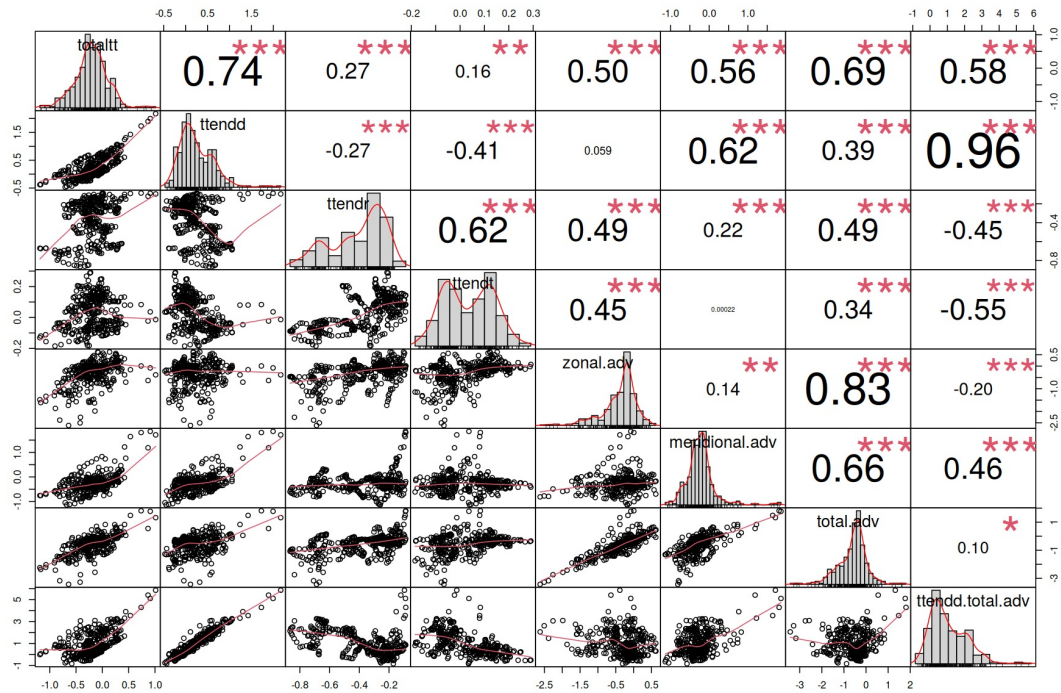


Figure 5.14: Correlation of 6-hourly variables at 850 hPa over the whole selected period for heatwave case study in 2019. Read as in Figure 5.10

At 925 hPa in the Eastern West Africa region, the ttendd still contribute hugely to the total tendency but has weaker correlations with the temperate advection. But the total tendency (totaltt) is well correlated to the zonal advection, the meridional advection and even very well with the total advection. Individually, the ttendr and the ttendt are well correlated with the meridional advection but contribute less to the total advection, especially the ttendt. Although they have good correlations with the meridional advection, their correlation with the total advection is reduced because the zonal advection contributes a lot to the total advection.

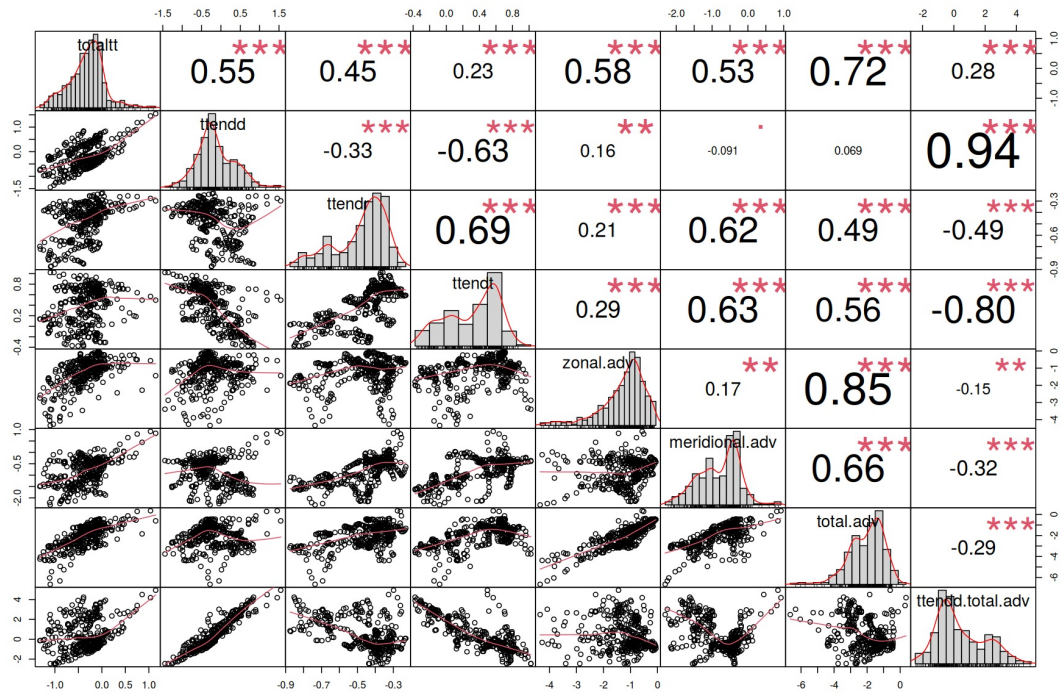


Figure 5.15: Correlation of 6-hourly variables at 925 hPa over the whole selected period for heatwave case study in 2019. Read as in Figure 5.10

It is also interesting to notice the good agreement between the ttendt and the ttendr. There is strong influence of the radiation (turbulence) when coming down to the earth surface.

During the period of the heatwave event, a fluctuation is noticed in the ttendd, yet increasing trend in the different pressure levels where the beginning and the end record peaks. The turbulent diffusion reduces as the pressure level increases in altitude (Figure 5.16). The 850 hPa present a better correlation between the ttendd and the zonal (total) advection, with some slight shifts per moment.

The total tendency and the total advection (mainly meridional advection) are paramount for the development and maintenance of heatwave in the Eastern region of West Africa.

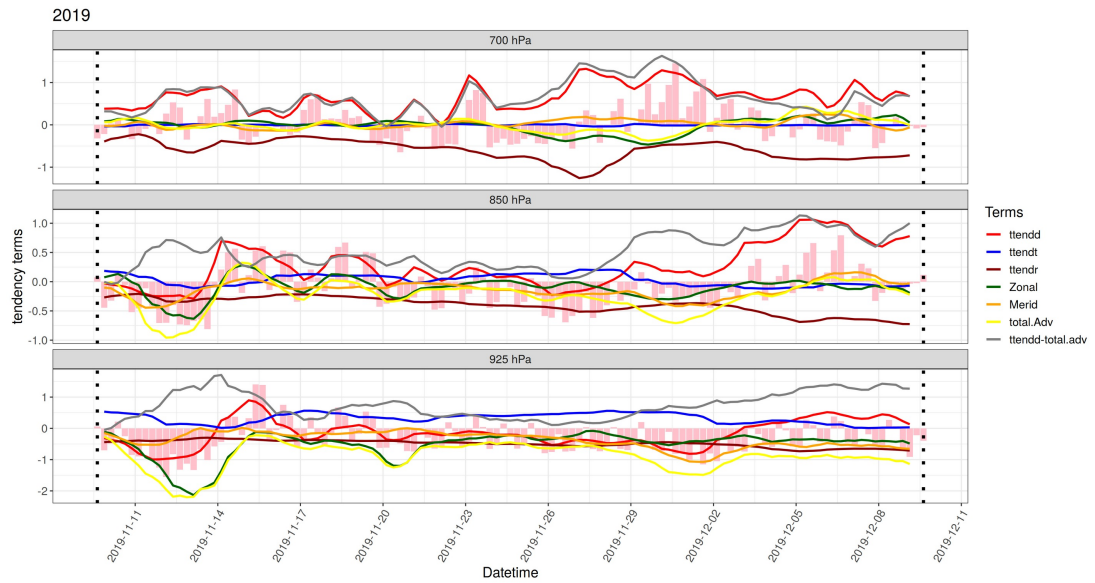


Figure 5.16: 6 hourly smoothed evolution over the 2019 detected heatwaves highest event in this particular period. Read as in Figure 5.9

When considering the 2020 (Figure 5.17 and Figure 5.20) event of heatwave in the region, a particularity is captured here as the area is mainly a coastal area.

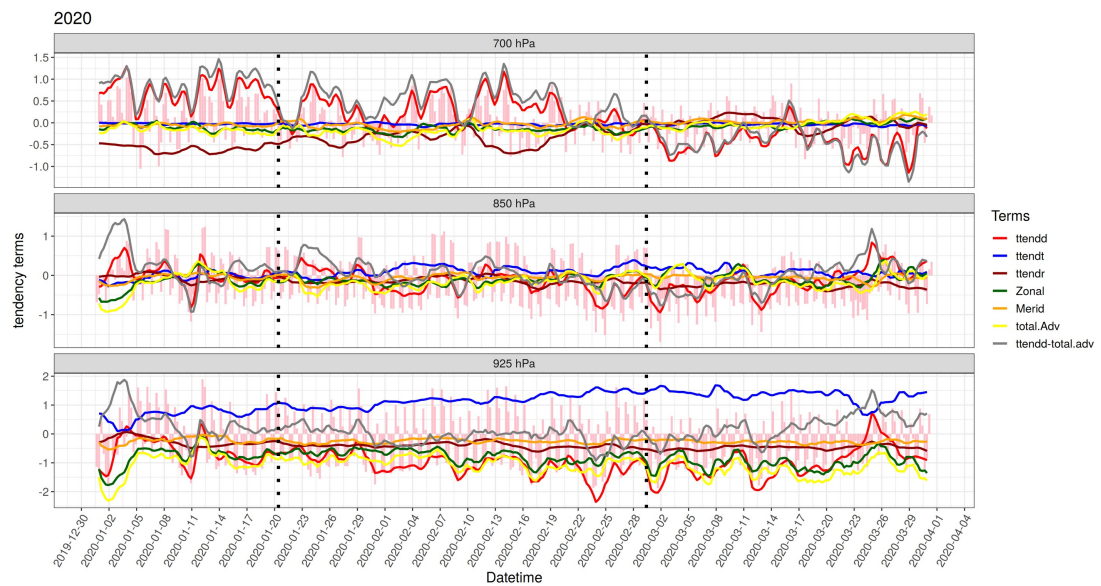


Figure 5.17: Variables evolution at 6 hourly over the whole selected period for heatwave case study in 2020. Read as in Figure 5.9

The main observation in the Figure 5.17 is that the period before and during the heatwave is marked by high turbulent diffusion (ttendt at 925 hPa), ttendt, rttd and ttendd (at 850 hPa and 700 hPa).

The advection (zonal and total) remains unstable in correlation with the $ttedd$ ($rttd$) and the $ttendt$ that are the major drivers of the heatwave at 925 hPa and 850 hPa. During the heatwave, the total tendency ($totaltt$) is balanced in the 850 hPa and more positive in the 700 hPa with increasing $ttedd$ ($rttd$) and zonal (total) advections (notice the meridional advection remains around 0).

Accordingly, correlations at 850 hPa (Figure 5.18), are good for the $ttedd$ (0.70) and $ttendr$ (0.58) respectively as contributing to the total tendency.

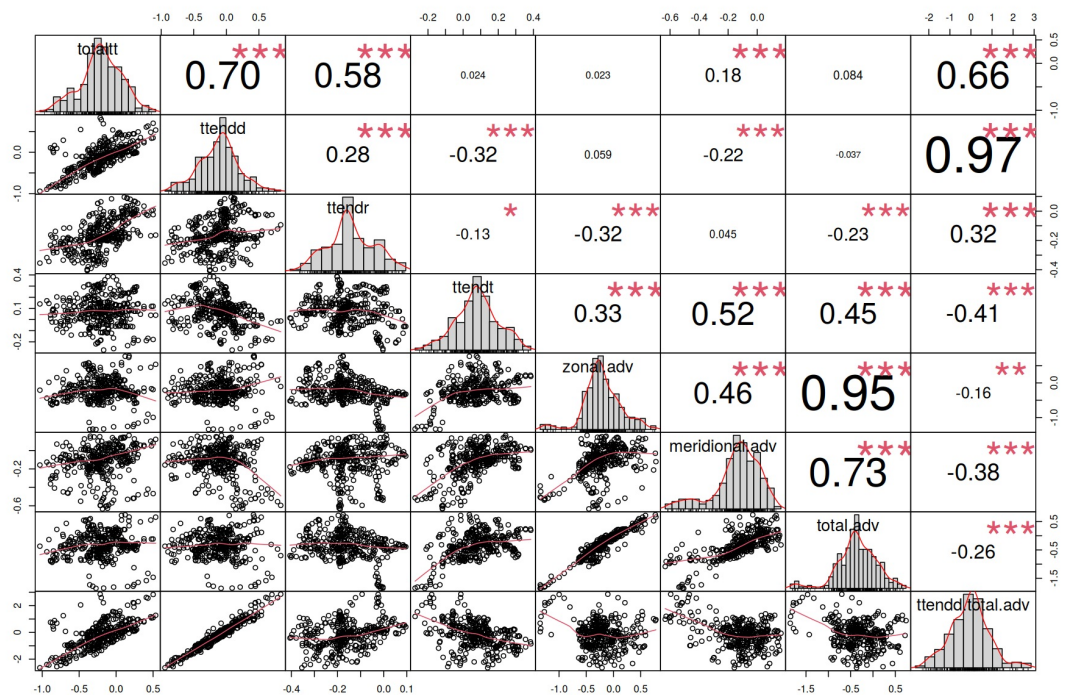


Figure 5.18: Correlation of 6 hourly variables at 850 hPa over the whole selected period for heatwave case study in 2020. Read as in Figure 5.10

In the southern part of the West African region (that is the Guinea or Coastal part). Interestingly, there seemingly is no good correlation between $ttedd$ or $ttendr$ with the advection variables, neither with the total advection. Only the $ttendt$ (which does not really contribute to the total tendency) has a good correlation (0.52) with the meridional advection and a closely good correlation with the total advection (0.45).

Even though the turbulence does not really contribute to the total change in temperature in humid part of the region, it does contribute in the change of temperature per unit of time following the meridional flow.

When having a close look at the 925 hPa correlations, close to surface, the tendency dynamics (ttendd) remain the main contributor to the total temperature change (totaltt) coupled with the zonal advection. Even the total tendency is moved by the zonal advection and the total advection flows.

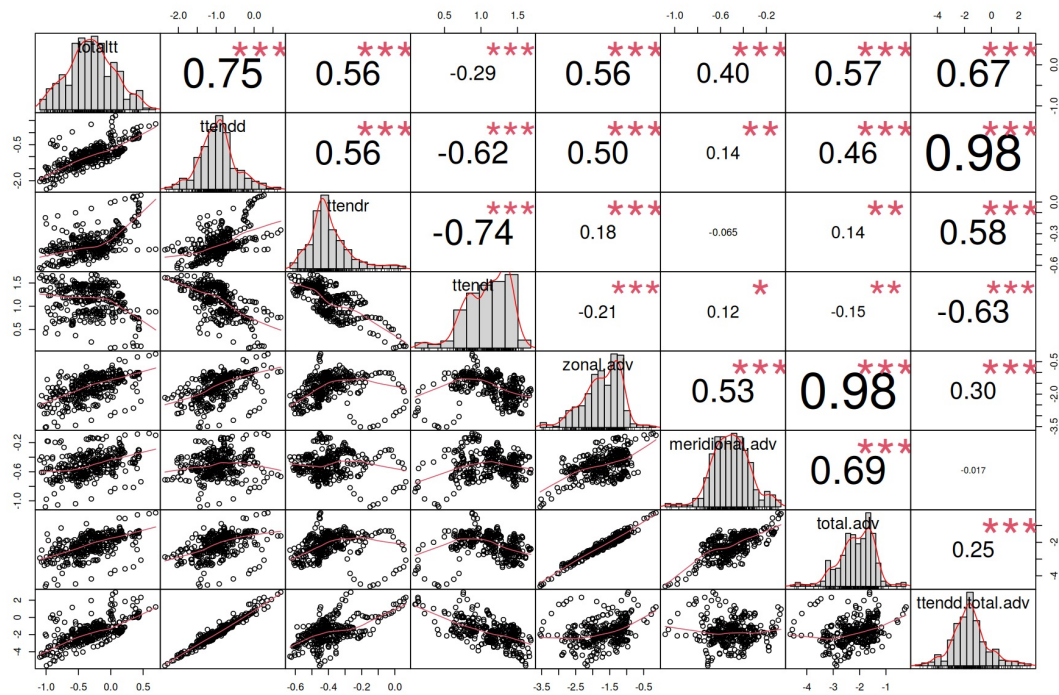


Figure 5.19: Correlation of 6 hourly variables at 925 hPa over the whole selected period for heatwave case study in 2020. Read as in Figure 5.10

If the heat is zonally moved at 925 hPa for the ttendd and the totaltt, it is hardly the same at the higher altitude (850 hPa). But the ttendt seems to be advected, even though it barely contributes to the temperature change in the region. The correlations at 850 hPa show very small but very significant values for the correlations between

ttendd (totaltt) and the meridional advection (total.adv). So there is advection, even though it is a delayed or localized advections per moments.

The highest values are recorded for ttendd (rttd, Figure 5.20) but the advection nullifies in the altitude around 700 hPa. Furthermore, the drop of the ttendd in the 700 hPa marks the end of the heatwave period as well. In this context, the 700 hPa dynamics seems to be determinant in the construction of a heatwave in the Coastal area where humidity is high, and the convection is mostly continuous.

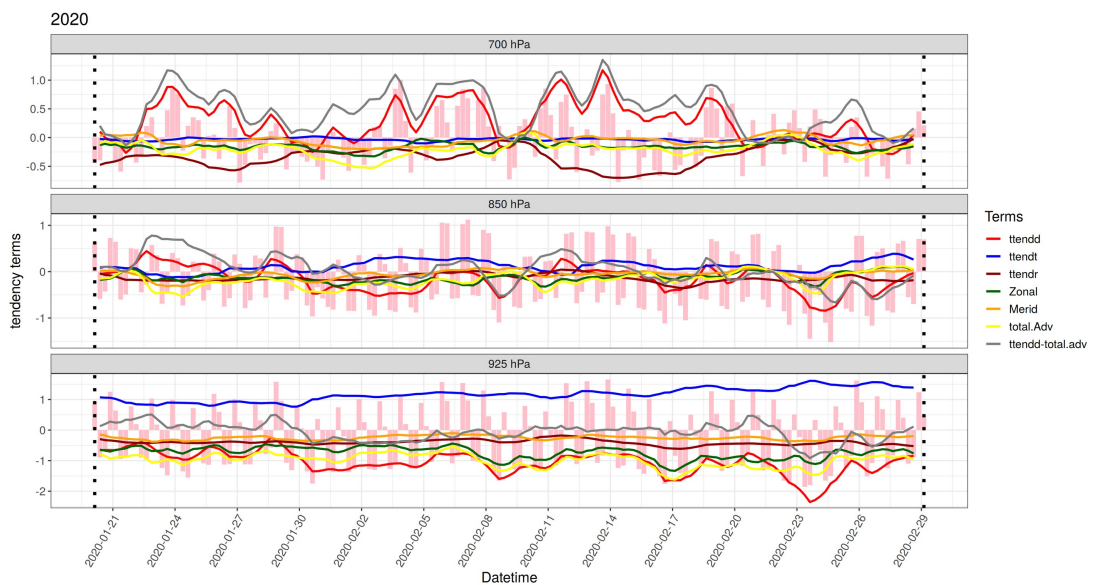


Figure 5.20: 6 hourly smoothed evolution over the detected 2020 heatwaves highest event in this particular period. Read as in Figure 5.9

The development of heatwaves is generally conditioned by a high ttendd (rttd) and/or of ttendt with temperature advection.

5.3.3 The Vertical Profile of tendency terms and advections

The vertical profile presented here in Figure 5.21 illustrates that the temperature tendencies, ttendt and ttendr, are positive and remain the primary contributors to

changes at the surface and 925 hPa levels, but they become negative at higher altitudes. In the 2020 case study, it could be noticed the high positive influence of the $ttend_t$.

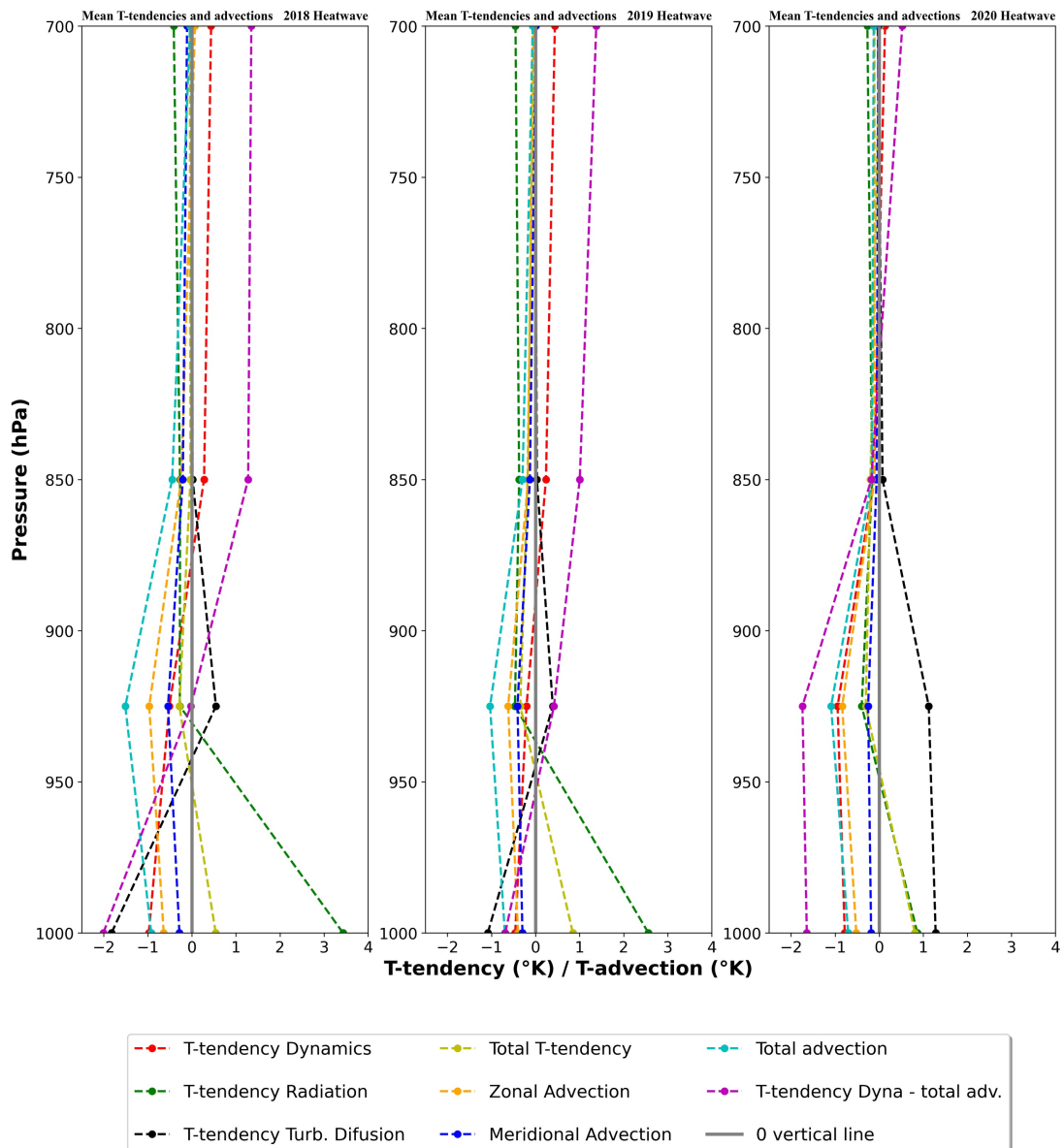


Figure 5.21: Vertical profile of the different tendency terms and the computed advections during the selected heatwave events in West Africa. The lower troposphere is considered here (up to 700 hPa)

Conversely, the temperature tendency from dynamics ($ttend_d$) and the residual temperature tendency dynamics ($rttd$) are the primary contributors to changes

observed at higher altitudes. The zonal (meridional) advection is negative throughout, as is the total advection, but the zonal (total) advection exhibits a pattern similar to that observed by the tt_{end} . The findings suggest that temperature changes at different levels of the atmosphere are influenced by a combination of temperature tendencies and advection processes, with the relative contributions varying with altitude. These findings suggest that dynamic processes and total advection play an important role in determining the changes in temperature at higher altitude regions of the atmosphere in West Africa.

In the analysis of atmospheric conditions during heatwave events, it is observed that in addition to early noticed tt such as the tt_{end} and $rttd$, the zonal (total) advection exhibits positive values beyond the 700 hPa level (Figure 5.22). Specifically, in the case studies of 2018 and 2020, this trend is observed just after the 700 hPa level, whereas in 2019 it is observed at the 500 hPa level. At the surface, the tt_{end} and tt_{end} play a dominant role in temperature changes, owing to slow motion winds, which are a type of wind motion that occurs at a slower speed compared to other wind movements influenced by factors such as friction, turbulence, and radiative effects. Furthermore, it is worth noting that the total advection also contributes to temperature changes at the surface. In contrast, in the altitude from 925 hPa upwards, the tt_{end} and its derivative ($rttd$) have a more significant influence on temperature changes, controlling the changes in temperature advection.

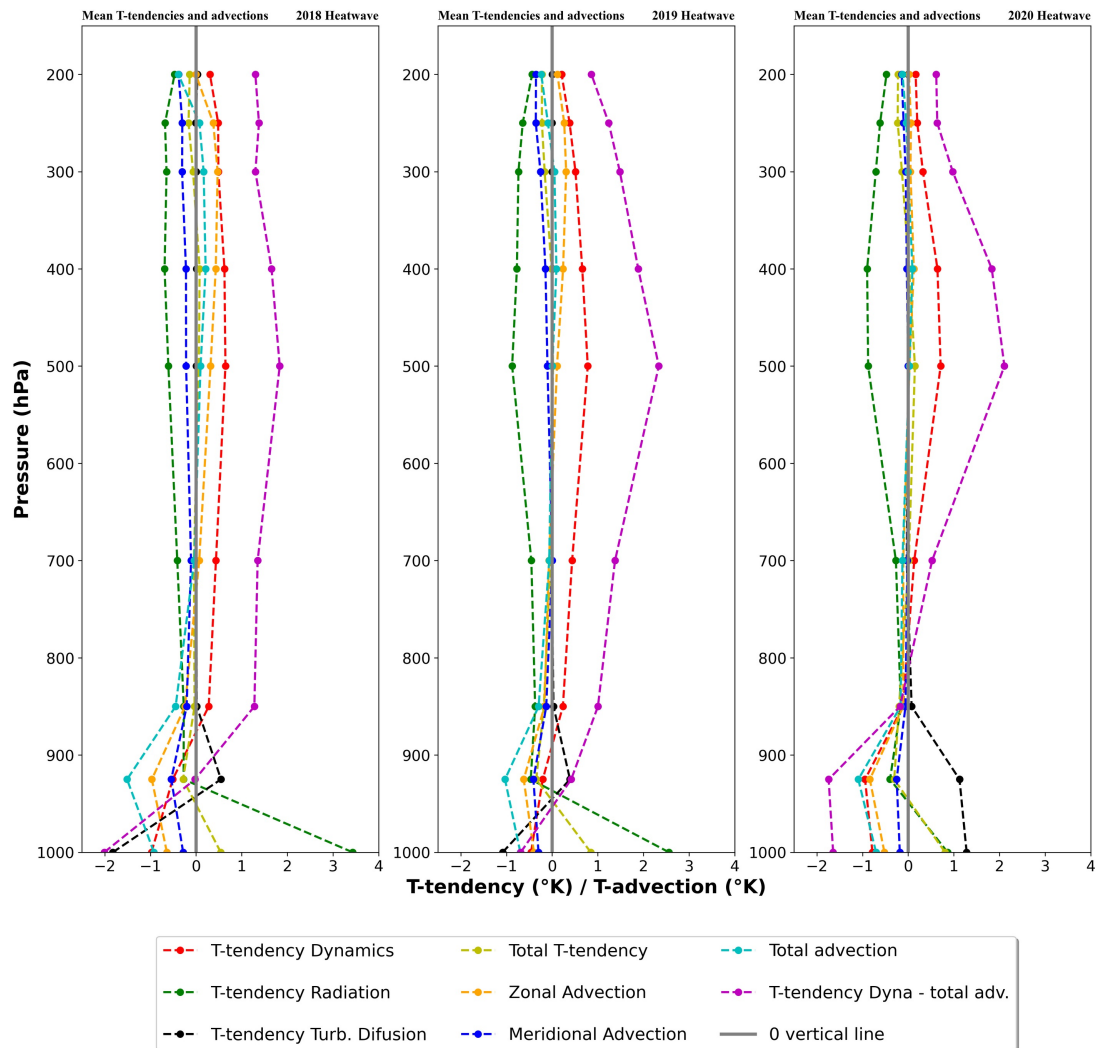


Figure 5.22: Vertical profile of the different tendency terms and the computed advections during the selected heatwave events in West Africa. The lower troposphere is considered here (up to 200 hPa)

These findings have several implications for understanding temperature changes and dynamics in the atmosphere. The dominance of the $ttend_t$ and $ttend_r$ at the surface and the increasing role of the $ttend_d$ with altitude suggest that different processes are at work at different levels of the atmosphere. The positive zonal (total) advection observed at higher altitudes in some case studies indicates the importance of horizontal advection in these events. The effects of friction, turbulence, slow motion wind, and radiative effects on temperature changes at the surface highlight the

complexity of atmospheric dynamics in this region. Understanding these processes is critical for accurately modelling and predicting weather patterns and extreme events, such as heatwaves. Overall, these findings contribute to our knowledge of the complex interactions between various atmospheric processes and provide insights for improving weather and climate models.

5.4 Discussion

Heatwaves' dynamics in West Africa remains bare, nonetheless, it is important to acknowledge the works of some researchers already who established the heatwave records over West Africa (Guichard et al., 2009; Guigma et al., 2020; Largeron et al., 2020; Oueslati et al., 2017; Russo et al., 2016). There is today a clear and significant warming (about 1 °C – 3 °C) has been observed since the 1990s in all seasons over the whole northern Africa. The key points from this investigation are as follows:

- The different zones in West Africa have strong records of heatwaves and these are becoming more intense and frequent in the last decades as presented in the work.
- Heatwave indices are fundamentally different in West Africa and consider different parameters, but have a lot of similarities in their occurrence. Even though the UTCI and the WBGT are thermal indices, they present some important spatial differences due to their sensitivity to humidity (moisture) and wind speed. West Africa presents also some orography that affect the local climate, as in Western part of the Sahel (Senegal). The case studies are selected using the maximum heatwave of the year (intensity), but also the

duration and spatial extent. This was possible across the 3 years because there is an agreement between the occurrence of the different heatwave indices,

- The case studies have records of heatwaves in the pre-monsoon phase (January-May) and the post-monsoon phase (October-December). The most intense heatwaves are recorded in the pre-monsoon phase as compared to the post-monsoon, but the spatial extent and contiguity of the heatwaves cells are observed in the post-monsoon heatwaves. In addition, the late season heatwaves have the characteristic to be generally located in Sudan or in the East Sahel where the land (orography) affects much the radiation and temperature.
- Three major temperature tendency terms that contribute to the onset and cessation of a heatwave in the region are the temperature tendency due to dynamics ($ttendd$ – more in altitude), the temperature tendency due to turbulent diffusion ($ttendt$ – always there as a transition) and the temperature tendency ($ttendr$ – at the surface) due to radiation. They all depend on the considered pressure level but contribute all to temperature change over an area affected by a heatwave. Associated to the zonal advection and the total advection in a given area in the region, heatwaves occur and move Westward or Eastward depending on the motion. The vertical motion is to be accounted for, because the subsidence of the air and thus cooling dissipate heatwaves in a region. The cessation of heatwave is not made clear by the tendencies and the temperature advection in the present study. But in the 2020 case study at 850 and 700 hPa, there is dropped down of the $ttendd$ and $rttd$ coinciding with the cessation of the 2020 heatwave.

- The vertical profile of the different tendency terms along with the calculated terms (total temperature tendency and total tendency dynamics minus total advection) and advections (zonal, meridional and total) reveal that the surface variables are unstable and produce varied values where the $ttendd$ is negative. But from the 925 hPa a clear pattern is set up where the $rttd$ and the $ttendd$ are positive all through. The $rttd$ become very high around 500 hPa. While the meridional advection remain low (below 0) the zonal advection is close to the $totaltt$ and the $ttendd$, making the zonal advection a key process in the physical formation of heatwaves. The $ttendt$ was negative above ground but increases to positive at 925 hPa and quickly went back to close to 0 upward. In 2019, the differences between the positive terms (described above) and the negative terms become larger around the 500 hPa, the same in 2020. The January-March dynamics have increased from 2018 to 2020 to present increased gap between positively contributing terms and the negative terms.

Most heatwave studies focused on the Sahara and/or the Sahel, but the present investigation goes beyond and include the Guinea coast. Heatwaves happen in the spring, which is the hottest period of the year in the region, by the mid-1960s over the continental Sahara and Sahel, eastward to the 0° longitude (Fontaine et al., 2013). Indeed, the duration and intensity of heatwaves has been increasing over the northern Africa but also in the Sudan and the Sahara (as depicted in the present study). West Africa's climate is prone to heatwaves of high intensity due to the position and the direct sunshine hitting the area. As specified by Russo et al. (2016), heatwaves have the potential to occur in the region at any given time; however, they tend to be more concentrated over the Sahel and Southern Sahara between March and June. These

occurrences are primarily observed in proximity to the Saharan Heat Low, as well as in the eastern equatorial Atlantic region where the installation of a cold tongue is impeded, as indicated by Fontaine et al. (2013). The presence of South-Westerly anomalies in low levels over the West Sahara, along with the reinforcement of subsidence in the mid-troposphere, are known to be associated with these events. In August, heatwaves tend to be located over the Northern eastern Saharan, Arabian deserts, and western Southern Europe. Later in the year, during October to December, heatwaves are present further afield. The use of different indices (Cumulative Excess Heat (CumHeat) from Temperature, UTCI and the WBGT) and their normalization is with the intention to compare them and evaluate their performance over the whole West Africa for reference. They use different meteorological variables, but the UTCI and the WBGT remain close by the integration of humidity and wind speed, which are important parameters in biometeorology study. The daytime results show that UTCI has more heatwave cumulative intensity followed by the WBGT which most of them are observed in the coastal part, the Sudan and the East Sahel, denoting the influence of humidity in the detection of heatwaves. The night-time heatwaves recorded the highest intensity over the years for the WBGT followed by the UTCI. But here the highest number of heatwave days are observed in the WBGT followed by the temperature and UTCI. The values for the night-time heatwave are higher than the daytime heatwaves This could be explained by the fact that WBGT is more sensitive to humidity than UTCI, and the latter is more influenced by wind (Becker et al., 2022). These are some of the differences in the indices, even though temperature is the main driver of heatwaves in the region. Some additional parameters can change the results.

Two main patterns are observed in the differences of heatwaves occurrence and their normalized cumulative intensity. The periods of January-May and October-December show high relative differences in time and space. Between the temperature and the thermal indices, the differences are mainly negative in the Sudan and the Sahel and positive in the Guinea (especially the Coastal part including Senegal). This reveals that the thermal indices record highest heatwaves in the Guinea where the humidity is available with high temperatures in January-May and also in October-December. The WBGT rather show a negative difference with temperature in October-December in the Guinea and a positive one in the Sudan and the East Sahel. The sensitivity of the WBGT to humidity could explain this behaviour that is opposite to what is observed in the WBGT. The wind speed could also have an impact on the WBGT. The thermal indices are mostly positive between March and June and negative between October and February, especially in coastal areas. The fact that UTCI recorded highest values for daytime heatwaves confirms that UTCI occurs more in the Sudan and the Sahel while the WBGT is more sensitive to the humidity in the Coastal part. The night-time heatwave has a similar pattern, but the WBGT seem to cover more of the Sudan and the East Sahel. The synchronicity of the heatwaves in January-May and October-December show that these periods of pre-monsoon and post-monsoon to dry season are prone to more frequent and more intense heatwaves (Balogun et al., 2019). This led to the selection of the case studies.

The selected case studies then considered this information and covered the periods (January-May and October-December) the highest heatwaves in the YOPP available data period (2020). The selected case studies include the Western part of the Sudan-Sahel in the 2018 (Westward development of the heatwave) case, even though the

box does not show it. Then the 2019 case is a post-monsoon period in the Eastern Sahel and the 2020 is a Coastal area case during the spring time (the hottest period). By utilising the tendencies, users can systematically analyse the contribution of each process to the overall state change. The tendencies facilitate the breakdown of the state change into individual processes, thus providing a comprehensive understanding of the mechanisms that govern the overall change. The PCA analysis pinpointed the important role of the $ttend_d$, $ttend_t$ and the advections (Meridional and Zonal) in the heatwave process. The $ttend_r$ is more observed at the surface (~ 1000 hPa) and was not considered for the analysis as the friction and scattering of the information could not help to determine true patterns. From the 925 hPa to the 700 hPa, information become clearer. The heatwave pattern at each level differ, but the first two PCs direct to the $ttend_d$ and the $ttend_t$ with the advection. The temperature is more related to the turbulent diffusion ($ttend_t$) in all the selected case studies. As outlined by Fontaine et al. (2013) the March-May heatwaves are characterised by a significant 2 m temperature anomaly that is primarily located over the Western Sahara region. These events are found to be associated with a low-level cyclonic rotation anomaly observed in Morocco. Additionally, these heatwaves are often associated with a warm episode that is abnormal, as well as with the presence of south-westerly anomalies in low levels over the West Sahara, which further reinforce subsidence and anticyclonic rotation. There is a temperature (moisture) advection during heatwaves (Largeron et al., 2020) that are important for high intensity heatwaves in the Sahel. The tendency evolution confirm this information with the temperature advection (mainly zonal and total) in the selected and a possible warming prior to the heatwave (well captured at 850 and 700 hPa). In the Coastal

part, the heating prior to the heatwave is an accumulation in the upper troposphere that could lead to subsidence (vertical advection) in the BL and heating. However, the Eastern Sahel heatwave in 2019 (post-monsoon) there was no prior accumulation of the heat and no major change in the total tendency was observed (except for some fluctuations that peak and come back). Even at the end of the recorded event, the temperature change due to dynamics remain on the increase at all levels. This motion is observed also for the $rttd$. The shift in the progression of the major tendency terms ($ttendd$ and $ttendt$) with the temperature advections (mainly zonal) could be due to the forecast errors in the model (Bauer et al., 2020). According to Bauer et al. (2020), a warmer air advecting into the air column will lead to a positive dynamic tendency.

5.5 Summary

The present chapter analysed and compared daytime (night-time) heatwaves indices (Cumulative Excess Heat of temperature, UTCI and WBGT) over West Africa. The period of analysis covered 1981 to 2020. The duration and cumulative intensity of the heatwaves are investigated, and case studies are selected for in-depth analysis of the root caused of heatwaves in West Africa using the YOPP dataset encompassing the specified period from the ECMWF archives. Temperature dynamics (temperature tendency from dynamics — $ttendd$ with its residual from the total horizontal advection, $rttd$) is the main driver of heatwaves in West Africa. There is also the need to look into models and parametrization to simulate these events. Another aspect is to investigate the role of moisture (atmospheric and soil moisture) in heatwaves formation. It is established that they contribute to heatwaves intensification over an area (Herold et al., 2016; Miralles et al., 2012; Muñoz-Sabater et al., 2021). Then the

effective impact of heatwaves on health is required to channel this information to the target population that are seriously affected and vulnerable.

**CHAPTER 6: LAND-ATMOSPHERE MOISTURE (ENERGY)
INTERACTION IN DIFFERENT LAND-USE AND LAND COVER TYPES
DURING HEATWAVES**

This chapter assesses the energy and moisture exchanges of the atmosphere during heatwaves in West Africa. The Universal Thermal Climate (UTCI), the Wet-Bulb-Globe Temperature (WBGT) and Cumulative Excess Heat (CumHeat) on maximum and minimum temperature are defined and compared as heatwave indices from the model output. night-time (daytime) heatwaves are also considered in this work in the lower atmosphere (Planetary Boundary Layer, PBL). Heatwave case studies are selected for in-depth analysis of temperature tendencies in 2018, 2019 and 2020. This investigation is part of a manuscript under review.

6.1 Introduction

Land-atmosphere interactions play a crucial role in determining the weather and climate of a region by influencing energy and moisture exchange at the land-atmosphere interface. In the case of the West African monsoon (WAM) in West Africa, researchers have extensively studied WAM-specific features, such as the behaviour of albedo over time and space (Nicholson, 2000b). For instance, the high albedo in a desert area contributes to a net radiative heat loss when compared to its surroundings (Charney, 1975). While earlier studies had attributed changes in land surface to human activity, recent research has demonstrated that soil-surface-vegetation-atmosphere interactions and climatic variability are much more complex factors (Guichard et al., 2009). As a result, a number of modelling studies have focused on the role of land-atmosphere interactions in the WAM process. However,

integrating parametrized processes such as radiative, surface, vegetation, boundary layer, convection, and cloud processes remains a challenging task when attempting to reproduce results using surface-atmosphere coupled models. This shows that land surface properties play a significant role in the land-atmosphere interactions that are taking place and appear to be very important to depict with accuracy some surface fluxes. Fluxes are very important in such processes. The mega-heatwaves that occurred in 2003 and 2010 in the mid-latitudes regions were linked to atmospheric blocking patterns, decreased cloud cover, and the transport of warm air (Miralles et al., 2014). When these persistent synoptic conditions occur in the mid-latitudes, the reduction of soil moisture and consequent decrease in evaporative cooling can further exacerbate high air temperatures. This could possibly be the same in the Guinea and Sudan zone (soil moisture is abundant in the Guinea and highly variable in the Sudan) but unlikely in the Sahel (the area is already dry and can quickly dry up) in West Africa. On that aspect, the Sahel might experience such moisture depletion except if the event is a humid heatwave. Black (2004) and Xoplaki (2003) have suggested that heatwaves are associated with anticyclonic circulation patterns, which result in clear skies and a subsidence of warm air from the upper atmosphere. The coupling between land and atmosphere also plays a crucial role in the formation and persistence of heatwaves over an area. For example, Fischer et al (2007) described the soil-moisture atmosphere interactions during the 2003 European summer heatwave. Different land surfaces have varying effects on fluxes, such as those found in urban areas compared to non-urban or forest areas. Built surfaces have low moisture retention capacity, leading to an increase in the Bowen ratio (the ratio of sensible heat flux to latent heat flux) (Ramamurthy et al., 2017). The reduced

evapotranspirative cooling in urban areas results in elevated near-surface air temperatures compared to the surrounding rural areas, and has been proposed as a significant contributor to elevated urban temperatures (Li and Bou-Zeid, 2013). Due to their high concentration of infrastructure, cities are particularly vulnerable to the threats posed by heatwaves.

With Regional Climate Models, it becomes easier to model with accuracy the land-atmosphere processes. The coupled atmospheric model, Regional Climate model from the Abdus Salam International Centre for Theoretical Physics is an international research institute for physical and mathematical sciences (Trieste; (Giorgi et al., 1993a, 1993b)) with the Community Land Model (CLM; (Oleson et al., 2013)), a commonly used Land Surface Model (LSM) of which the performance has already been evaluated in various studies with observational data (RegCM-CLM; (Kumar et al., 2020; Rai et al., 2020; Steiner et al., 2005)). This work investigates the RegCM sensitivity to detects heatwaves and the energy and moisture fluxes during heatwaves events in West Africa.

6.2 Coupled RegCM-CLM Sensitivity analysis of Regional Heatwaves

6.2.1 Regional heatwaves in West Africa

Regional heatwaves are computed towards inter-comparison (Figure 6.1) between the Cumulative excess heat (CumHeat), the Wet-Bulb Globe Temperature (WBGT) and the Universal Thermal Climate Index (UTCI) for the entire period of time (1981-2020).

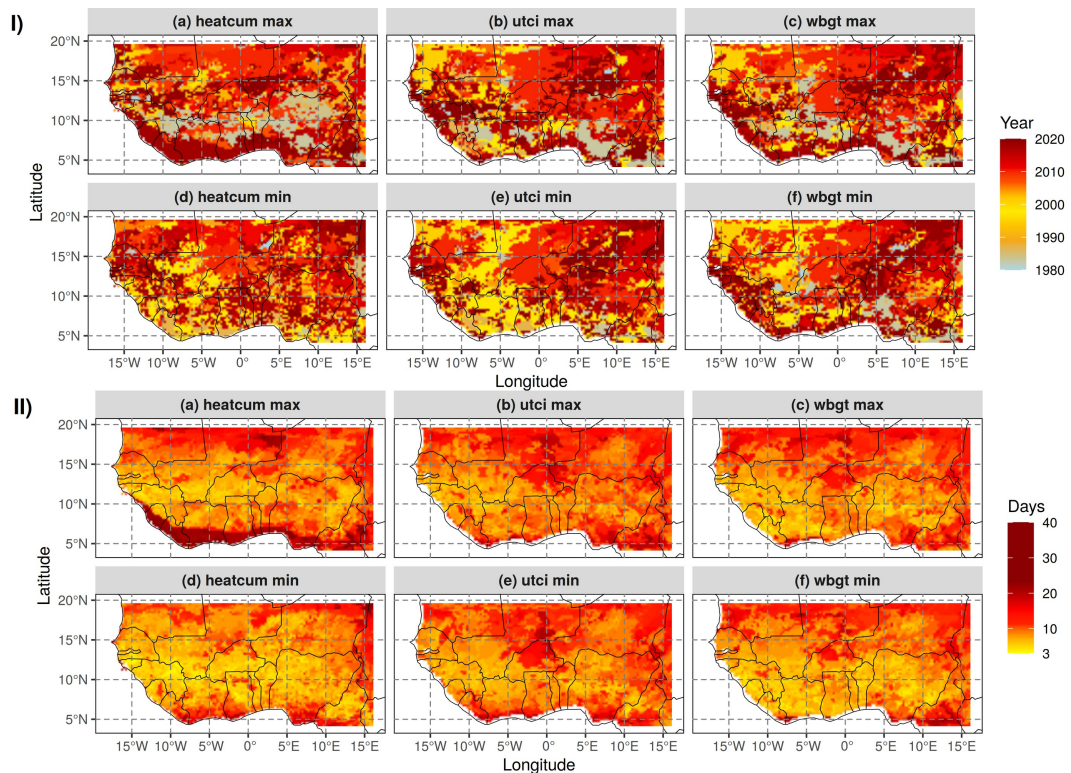


Figure 6.1: Regional Heatwave duration and year of spatial occurrence. Comparison of the year of occurrence of the duration (upper panel I) and the duration (down panel - II). All three indices are presented (CumHeat, UTCI and WBGT for maximum and minimum of the day)

The longest heatwave in Figure 6.1 for maximum values of the day is registered with CumHeat (37 days), then with UTCI (28 days) and finally for the WBGT (27 days) respectively in 2015, 2018 and 2013. The gap between CumHeat and the thermal comfort values can be noticed here. This gap is even more pronounced for minimum values of the day are 53 days, 27 and 27 days respectively for CumHeat, UTCI and WBGT. They are recorded in 1987 and 2020 respectively for CumHeat and the thermal comfort indices. The duration here has increased in the last decade (2010-2020). Even though the highest durations are recorded in those years, the largest coverage remains 2010 for all the maximum values followed by 1983 (CumHeat and WBGT) and 2020 (UTCI). But for the minimum values, the years fluctuate between 1998 (the highest coverage year for CumHeat and UTCI followed by 2010) and 2010

(the highest coverage for the WBGT followed by 1998) for the highest coverage of heat.

The normalized cumulative intensity in Figure 6.2 shows the years of the highest cumulative intensity and their coverage.

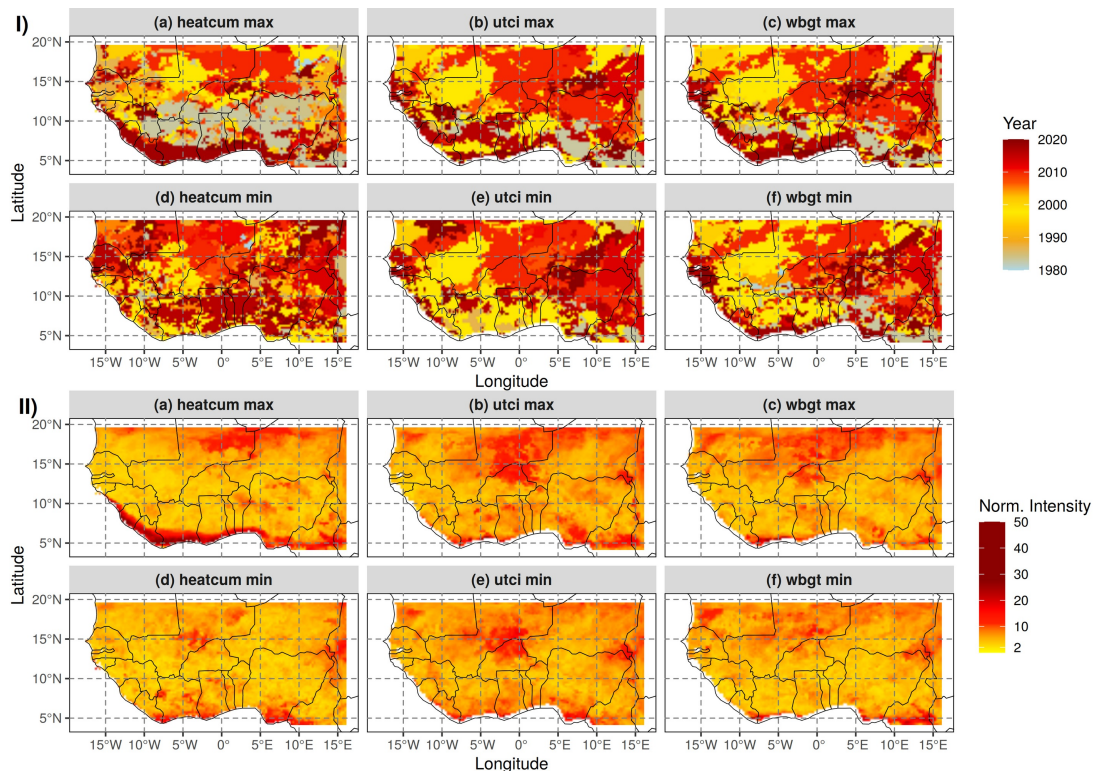


Figure 6.2: Regional Heatwave duration. Comparison of the year of occurrence of the cumulative intensity. read as in Figure 6.1

The values vary from 34 to 32 and 27 for CumHeat, WBGT and UTCI maximum of the day. The minimum values range from 40 for CumHeat to 27 for UTCI through 31 for the WBGT. From the coverage of the heatwave indices, it can be seen that the highest coverage years for maximum values are 1983 (followed by 2010) for CumHeat and 1998 for UTCI (followed by 2010) and the WBGT (followed by 2010). For the minimum values 1998 presents the highest coverage followed generally by the 2010 heatwave except for the CumHeat (2016). The coastal area

shows high cumulative intensity, but it is more pronounced in the maximum CumHeat index in 2018 particularly as for the WBGT and in 2020 for UTCI.

6.2.2 Model sensitivity

The indices' comparison is done using the difference between them. The absolute and relative difference are employed from 2018 to 2020. For comparison, ERA5 data heatwaves are used to against the computed heatwaves from the model outputs for the selected case studies. The comparison is done on 2018 to 2020 maximum heatwaves on monthly bases.

The Figure 6.3 and Figure 6.4 is present the relative difference between the different indices over the months of the years (seasonal difference). The difference is computed on the normalized cumulative intensity. An interesting thing is that in July and September, the differences are almost non-existent for all the compared indices. The major differences are recorded in January to April-May and October to December as the occurrence pattern of the different indices.

There is mostly a negative difference between CumHeat and UTCI (Figure 6.3a-i) in the coastal part in January and February, and this goes up in March-April and start dissipating in May-June. The same pattern is observed between CumHeat and WBGT. The month of March covers the whole Sahel with $\pm 50\%$ ($\pm 1-4$) of difference as if the heatwaves move from the coastal part of the region and moves with the time to the Sahel region covering Senegal. Between the thermal indices (UTCI and WBGT), the stress seems to be there from January to June and from October to December.

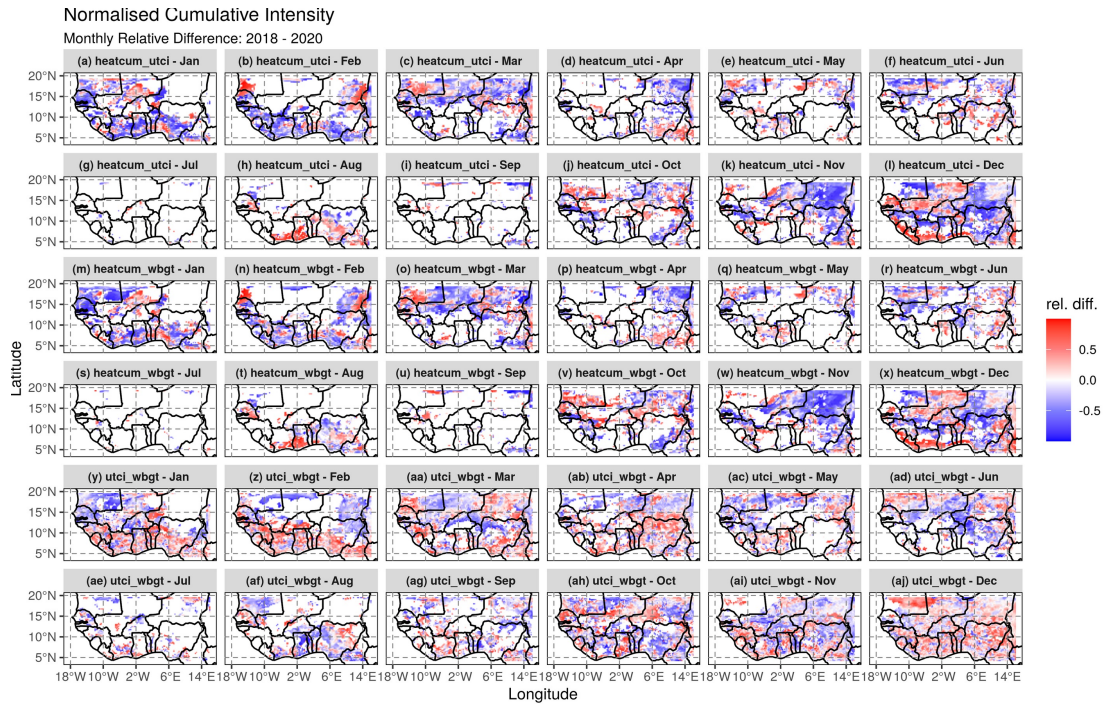


Figure 6.3: Monthly relative difference between daytime heatwave indices. Case study from 2018 to 2020. Normalised Cumulative indices: (a-i) Temperature and UTCI; (m-x) Temperature and WBGT; (y-aj) UTCI and WBGT

UTCI has higher values in coastal area and even toward the Sahel. The difference is higher in December. This is explained by the fact that WBGT is more sensitive to humidity (water vapour) than the UTCI which is largely affected by the wind speed. The Figure 6.4 shows the relative difference between minimum indices. The configuration a similar to the one observed with maximum daily indices.

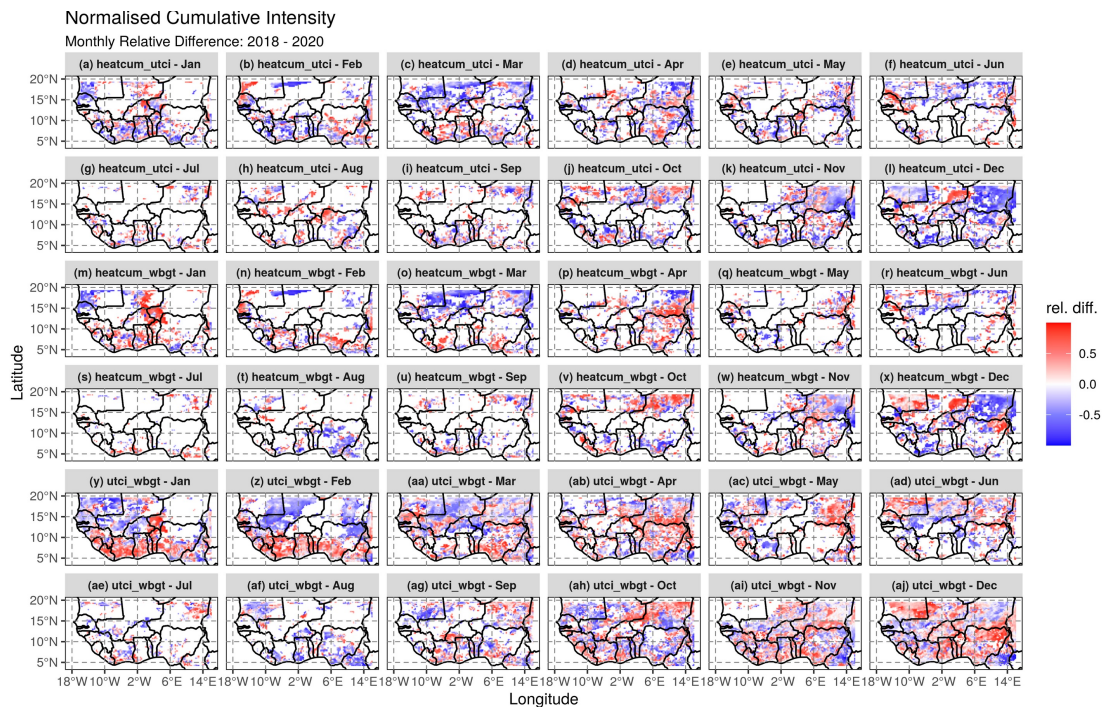


Figure 6.4: Monthly relative difference between night-time heatwave indices. Case study from 2018 to 2020. Normalised Cumulative indices: (a-i) Temperature and UTCI; (m-x) Temperature and WBGT; (y-aj) UTCI and WBGT

The differences here are sparse but remain seasonal. The differences between the thermal comfort indices are observed in all the regions. January and February show positive difference in the coastal area and negative difference in the Sudan and the Sahel. But the positive difference takes over the negative in the northern part in the last months of the years. This could denote that UTCI is higher than the WBGT in the coastal parts at the beginning of the years and at the end of the year in the Sudan and Sahel. The Heat_{Cum} is generally higher than the UTCI and the WBGT but these thermal comfort show higher values in the areas of Niger (South-East mainly).

When comparing the results of the differences between indices computed from the model output with the ones obtained from the ERA5 archives (absolute difference of both relative differences), one notice that the differences are small and seen in the Coastal area and the horizontal band from Senegal covering the Sudan and the Sahel

around 14°N and 20°N. Between the daytime temperature and the WBGT (Figure 6.5m, n, o), the difference is positive meaning that the daytime T_{max} and WBGT from the Model underestimate these indices as compared to ERA5 dataset. The same is observed for the UTCI and the WBGT where the model underestimate the UTCI and WBGT (Figure 6.5aa, ab, ad, ai, aj). At some points in the Sahel (Niger), the model overestimate the values of the indices (Figure 6.5c, k, i, w).

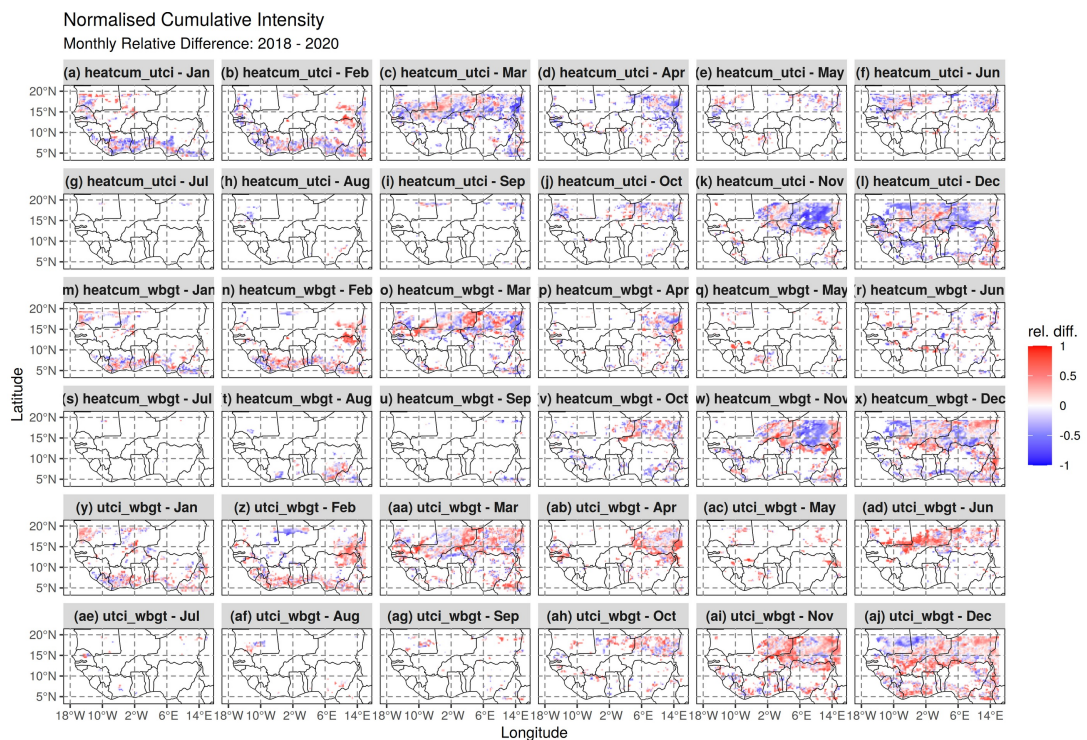


Figure 6.5: Monthly Comparison of the relative difference between daytime heatwave indices from ERA5 computations and the RegCM-CLM model output. Case study from 2018 to 2020. Normalised Cumulative indices: (a-i) Temperature and UTCI; (m-x) Temperature and WBGT; (y-aj) UTCI and WBGT

On the contrary, the night-time differences show an underestimation where there are large differences both at the Coastal and Sudan-Sahel area (Figure 6.6k, i, w, x, y-aa, ai, aj). The UTCI and WBGT combination difference is mainly positive, denoting an underestimation over the whole year except for the Figure 6.6ah in Niger.

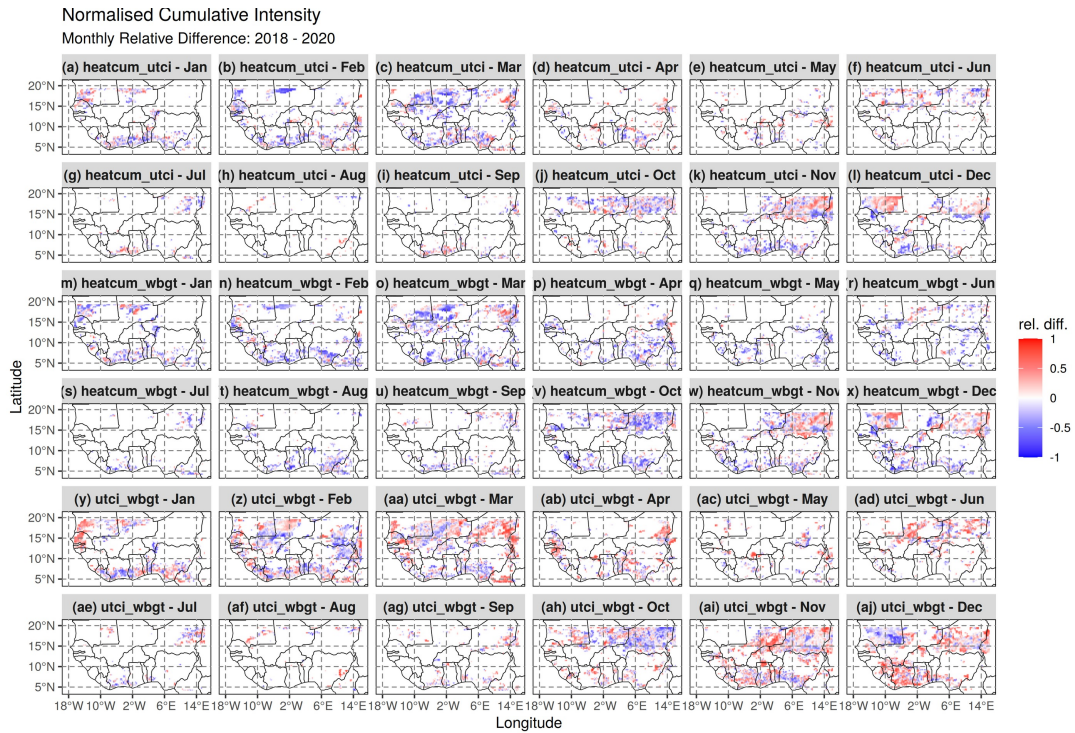


Figure 6.6: Monthly Comparison of the relative difference between night-time heatwave indices from ERA5 computations and the RegCM-CLM model output. Case study from 2018 to 2020. Normalised Cumulative indices: (a-i) Temperature and UTCI; (m-x) Temperature and WBGT; (y-aj) UTCI and WBGT

The differences between ERA5 and the model output show an underestimation of the model indices for the night-time heatwaves and an overestimation of the daytime heatwaves. The daytime heatwaves differences are more negative between T_{\max} and UTCI and positive between UTCI and the WBGT. It was found that the surface temperature and precipitation are better represented in the Community Land Model (CLM – which is used in the present study) scheme than in the Biosphere-Atmosphere transfer Scheme (BATS). Even though the temperature is better represented in the CLM than the BATS by 10-20% (Tiwari et al., 2015), it remains true that the temperature is not well captured yet in the coupled RegCM-CLM model. The differences are probably due to the topography integration in the parametrization.

6.3 The Moisture role during Selected Heatwave cases over West Africa

Here, the relationship between moisture and the heatwave indices is investigated for the whole time series (1981-2020).

6.3.1 Surface Soil moisture with Temperature CumHeat

This relationship (Figure 6.7 for instance) considers the monthly maximum heatwave and the corresponding moisture (surface moisture and soil moisture) available for the month. A correlation is also made on the antecedent moisture to the heatwave available. All months are considered on the basis that a heatwave can happen any time in the region.

Both surface moisture represented by the Standardized Precipitation Evapotranspiration Index (SPEI) and Soil moisture extracted from the model are investigated to check whether the role of moisture during heatwaves in West Africa.

The analysis considered only the normalised cumulative intensity for the maximum and minimum of each index (CumHeat, UTCI and WBGT). The Figure 6.7 shows the Spearman correlation between surface soil moisture (SPEI) and the normalised maximum temperature cumulative heat index.

The 3-month scale shows good correlation (at 95% confidence, blue cross) between the current heatwave month and the soil moisture in the Guinea coastal zone, in the central Sudan and towards the Sahel. The extreme east is also correlated. The correlation here is negative, expressing a decreasing soil moisture during heatwave months, especially in the coastal zone where precipitation is high, the moisture relatively high too and the temperature vary less. At the 6-month scale the same pattern is established but with reduce significant correlation and even more at the 12-

month scale. In the Figure 6.7b, d, f the antecedent soil moisture shows a decreasing correlation and significance from the 3-month scale to the 12-month scale.

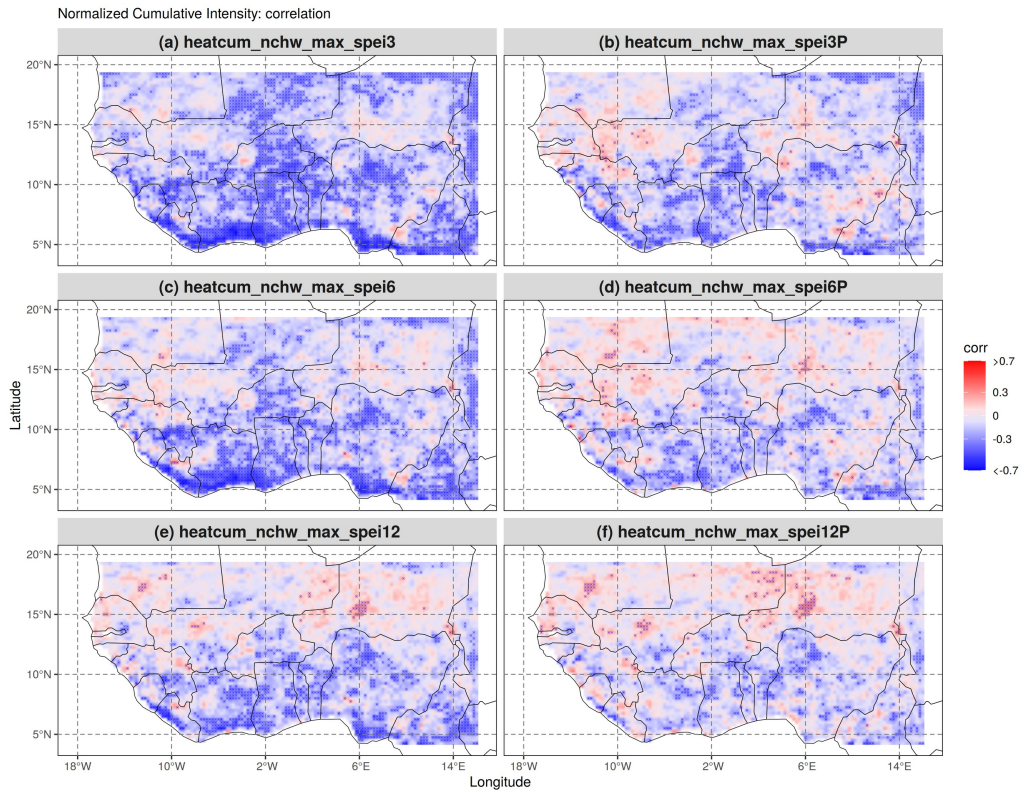


Figure 6.7: Spearman rank correlations between normalised maximum CumHeat temperature months and current (a, c, e) and antecedent (b, d, f) surface moisture (SPEI) at 3-, 6- and 12 months scales. Cross-marked regions indicate significant correlations with a confidence level of 95%

There is a predominance of anti-correlation in the Guinea zone and the eastern part of the Sahel in general. This denotes also an influence of soil moisture in heatwave formation, even though this influence is weak. The influence remain mainly in the Coastal area. Anti-correlations are higher in the Guinea coast and a little bit in the central Sudan. But some positive correlations appear in East and West of Sudan and Sahel zones from the 6-month scale to the 12-month scale, where it is more pronounced. These positive correlations are significant in some area, meaning that there could be an increased soil moisture in those areas during heatwave events. They

are more pronounced with the antecedent month correlation. An increased moisture in this area could be related to the moisture burst in March-April between the end of dry season and the monsoon season, precisely the pre-monsoon moisture.

For the minimum temperature, it is easily observed in Figure 6.8 that heatwaves in the northern part of Nigeria, the southern part of Niger and the Eastern and Western part of the region, including Senegal, are positively correlated to soil moisture. Most of these are significantly correlated and increase area coverage (in a scattered way) as the SPEI scale increases. Those specific areas could receive moisture before and during heatwave events such as air advection or onset of precipitation. Current and antecedent soil moisture can predict heatwaves in the Guinea in general, the central Sudan and the central and northern Sahel. It could also be for the extreme West of the region (e.g., Senegal), in the northern part of Nigeria and in the Southern part of Niger.

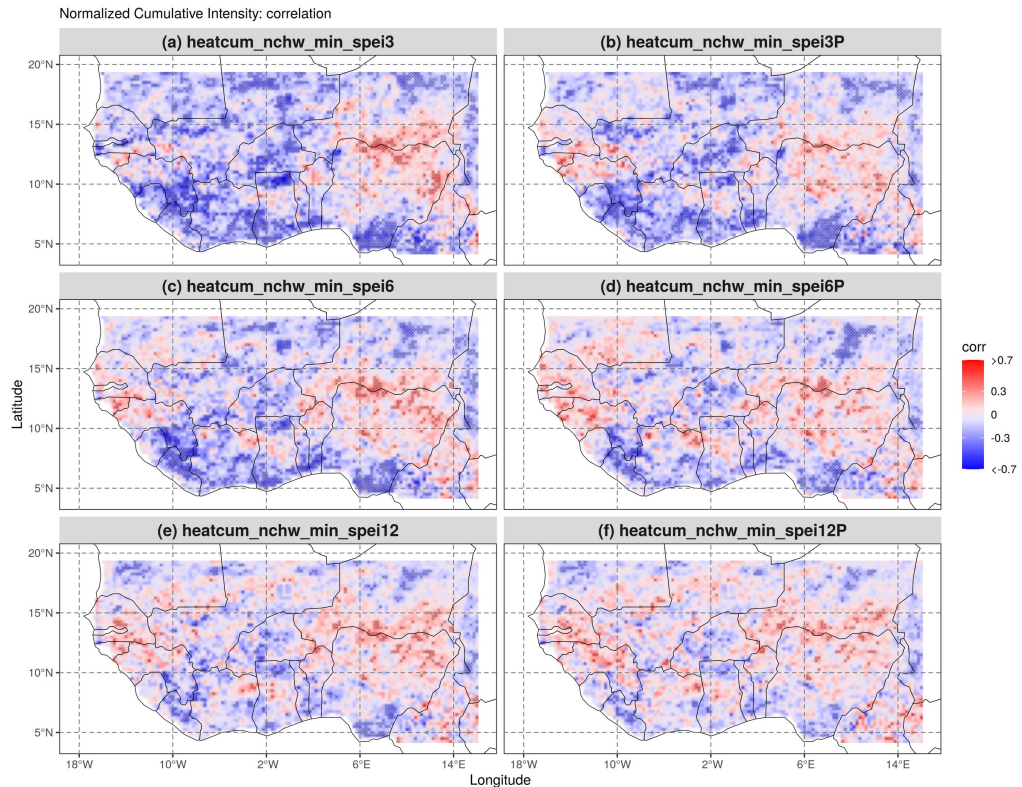


Figure 6.8: Spearman rank correlations between normalised minimum CumHeat temperature months and current (a, c, e) and antecedent (b, d, f) surface moisture (SPEI) at 3-, 6- and 12 months scales. Read as in Figure 6.7

6.3.2 Surface Soil moisture with UTCI CumHeat

For UTCI (Figure 6.9 and 6.10), the same pattern applies with more significant anti-correlation in the Guinea zone at 3-month scale. This reduces and give place to positive correlation at the 12-month scale in the northern part (Niger and Mali in the Sahel) of West Africa. This pattern in the Sahel is also observed and is even more pronounced in the 12-month SPEI heatwave correlation for the antecedent month in maximum heatwave. The southern part of the continent experiences for almost all the

figures an anti-correlation, this is especially where the temperature varies less, and the precipitation record is higher.

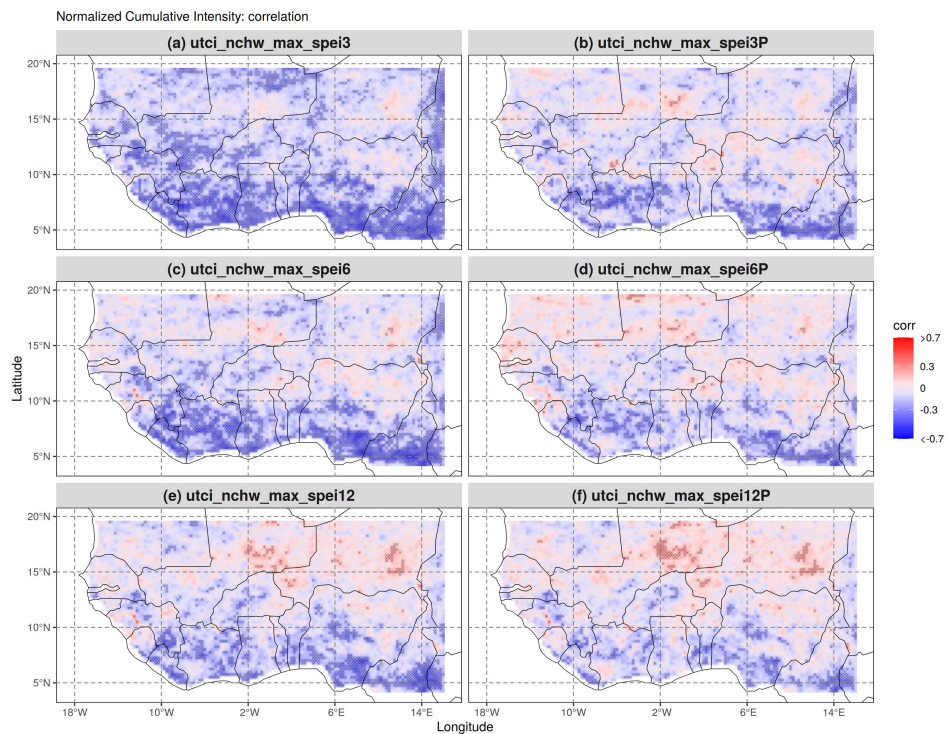


Figure 6.9: Spearman rank correlations between normalised maximum Cumheat UTCI months and current (a, c, e) and antecedent (b, d, f) surface moisture (SPEI) at 3-, 6- and 12 months scales. Read as in Figure 6.7

The minimum UTCI correlation with the soil moisture shows more pronounced positive correlation all over the continent, especially for the SPEI at 12-month scale antecedent correlation. The Northern part of Nigeria and the Senegal remain the areas of positive correlation with the surface soil moisture.

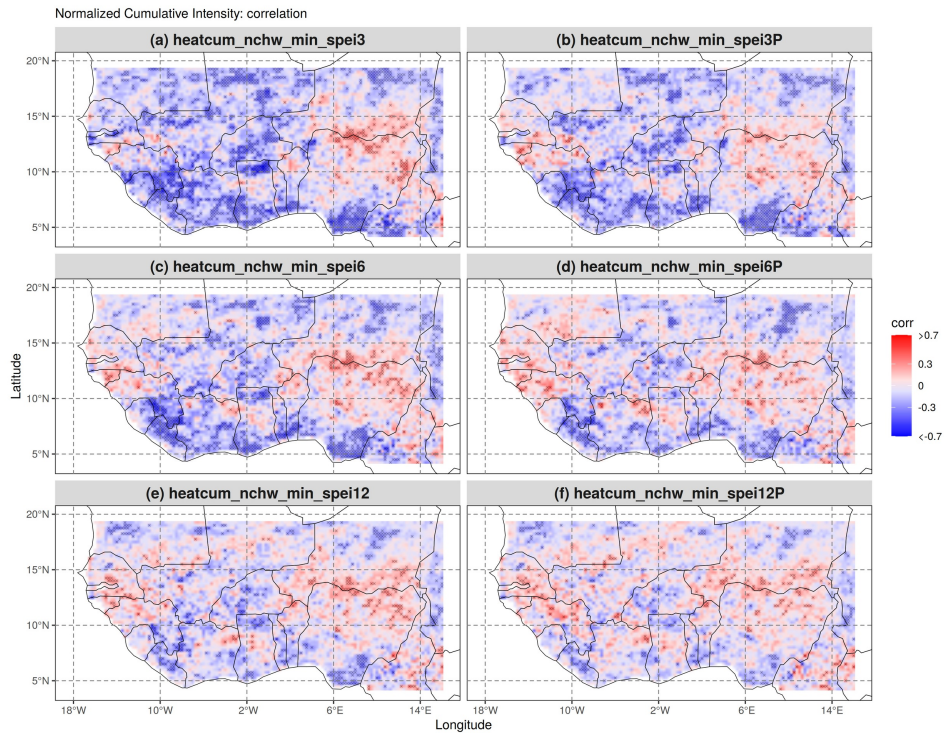


Figure 6.10: Spearman rank correlations between normalised minimum CumHeat UTCI months and current (a, c, e) and antecedent (b, d, f) surface moisture (SPEI) at 3-, 6- and 12 months scales. Read as in Figure 6.7

6.3.3 Surface Soil moisture with the WBGT CumHeat

A close pattern is observed for the WBGT maximum and minimum. The maximum temperature always showed higher values of positive correlation, especially for the antecedent moisture. In details (see Figure 6.11), the southern part from Nigeria towards the Central Africa and from Western Ghana to Sierra Leone is negatively influence by surface moisture. And these are areas where the precipitation is high. The moisture reduces a lot when the heatwave is of high intensity. It is also important to notice the presence of relative humidity and water vapour in the computation of the Wet-Bulb Globe Temperature. The WBGT is influenced by moisture presence.

The Sudan and Sahel are mainly showing some sparse spot where the correlation is positive but not significant. The only spot that shows a positive correlation is in the North-East of Mali at 3-month scale. This is amplified in the antecedent soil moisture correlation. As the scale increases, the positive correlation spots increase in the Sudan and the Sahel and the negative ones decrease in the Guinea. This effect is even amplified in the antecedent moisture.

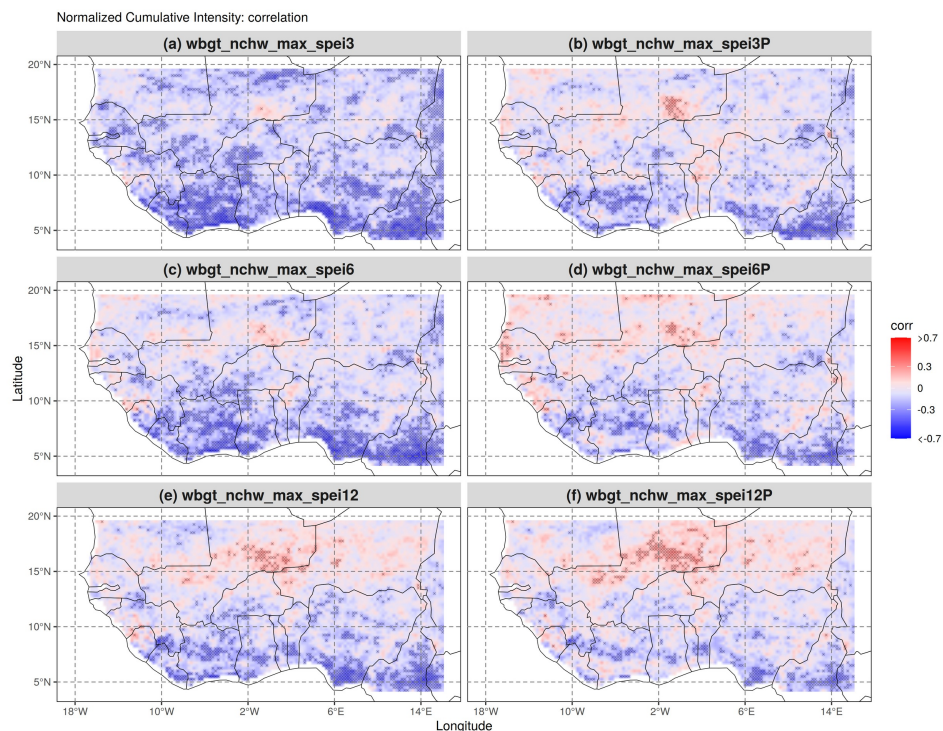


Figure 6.11: Spearman rank correlations between normalised maximum CumHeat WBGT months and current (a, c, e) and antecedent (b, d, f) surface moisture (SPEI) at 3-, 6- and 12 months scales. Read as in Figure 6.7

In the Figure 6.12, the minimum WBGT anti-correlation with the soil surface moisture is mostly felt in the extreme South-East of the region in Cameroon. This pattern is maintained all through the time scales with slight reduction of the significant correlations in the south giving place to positive correlations. In the case of 6-month scale for the antecedent correlation, the positive correlation are mostly

found in the extreme North-west covering the Senegal, Mauritania, and Mali. At 12-month scale this moves from there to Mali and Niger. The antecedent correlation of heatwave month shows more pronounced positive correlation and more accentuated anti-correlation.

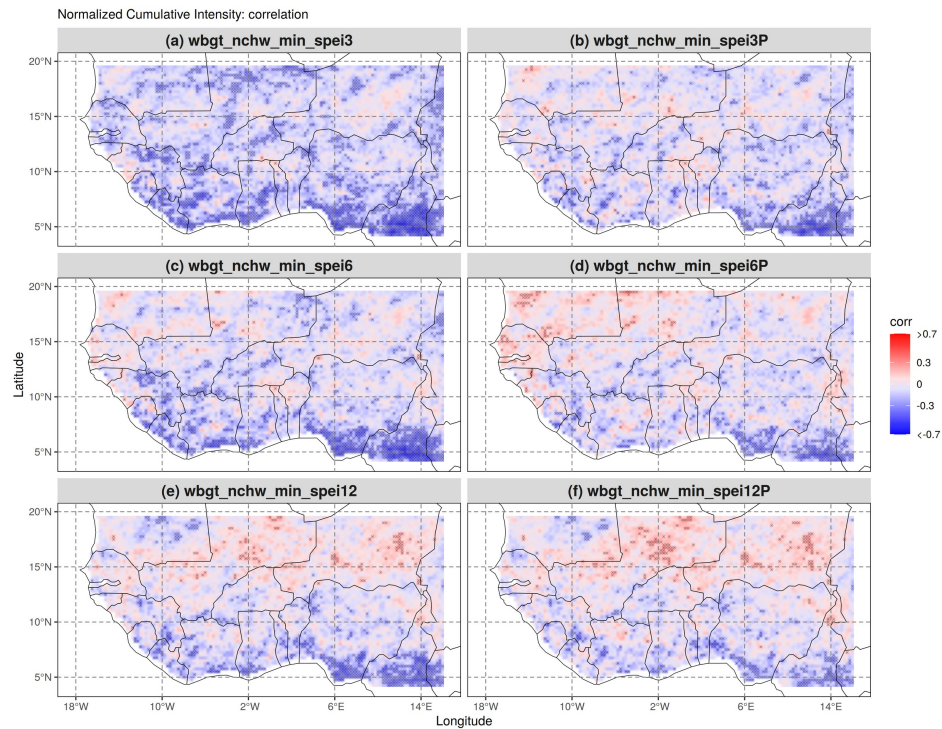


Figure 6.12: Spearman rank correlations between normalised minimum CumHeat WBGT months and current (a, c, e) and antecedent (b, d, f) surface moisture (SPEI) at 3-, 6- and 12 months scales. Read as in Figure 6.7

On the other side, the soil moisture content at different levels in the soil are used for the correlation and the results show different patterns.

6.3.4 Normalised Temperature CumHeat Correlation with Soil Moisture Content (SMC) at different levels

The monthly mean soil moisture content (SMC) was extracted from the 6-hour soil moisture from the RegCM-CLM model output (see Table 6.1 for layer levels and depth).

Table 6.1: Soil layer levels and their depth from the Model Simulation (see Figure 6.13)

| Soil layer | Depth (m) |
|------------|----------------|
| 1 | 0 – 0.018 |
| 2 | 0.018 – 0.045 |
| 3 | 0.045 – 0.091 |
| 4 | 0.091 – 0.166 |
| 5 | 0.1656 – 0.290 |
| 6 | 0.290 – 0.492 |
| 7 | 0.492 – 0.829 |
| 8 | 0.829 – 1.382 |
| 9 | 1.382 – 2.297 |
| 10 | 2.297 – 3.801 |

The model simulation is done by initiating soil moisture in the model configuration.

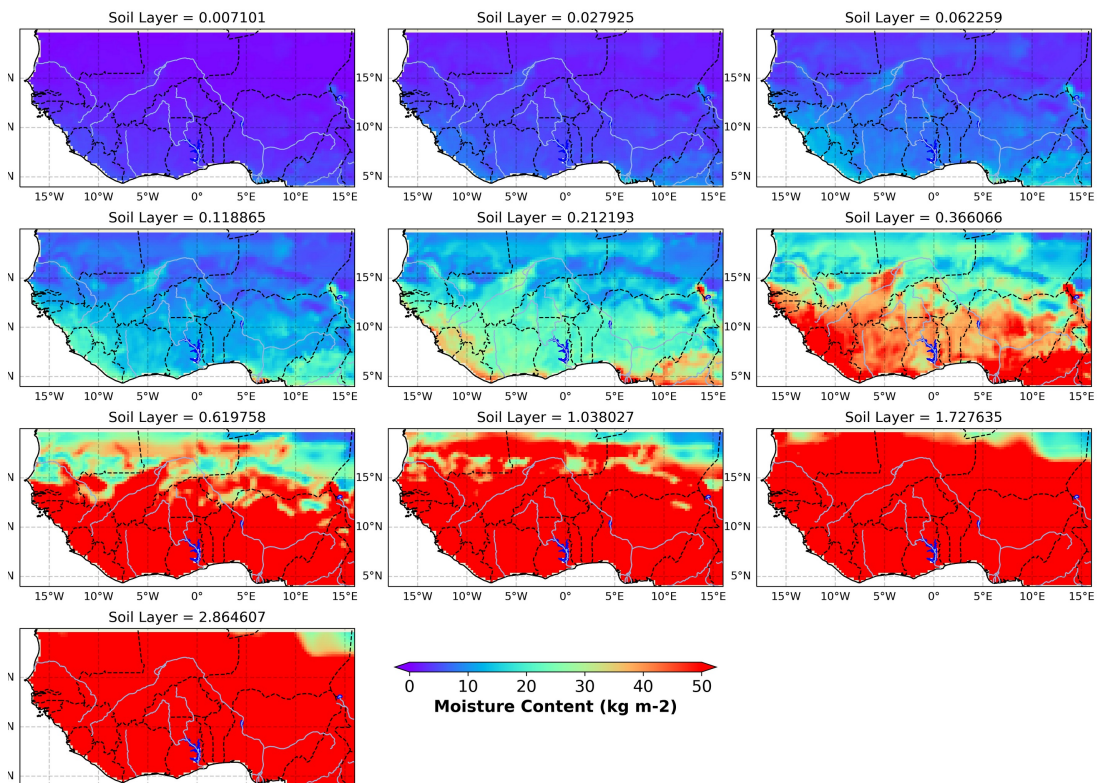


Figure 6.13: Mean soil moisture showing different levels with moisture content extracted from the RegCM-CLM model.

The model produced 10 soil layer levels with soil moisture content for each layer.

The layers are organised from the surface down deep into the soil. The soil generally

increases with the soil layer depth. The range of soil moisture in the 10 layers is from 19.4 kg/m² to 1087.7 kg/m².

The correlation with the SMC shows in Figure 6.14, an anti-correlation in the coastal area confirming the results from SPEI. But Nigeria, Northern part of Ghana, Côte d'Ivoire and Guinea are positively correlated with the maximum CumHeat. The intersection of Burkina Faso, Mali and Niger are also has an anti-correlation. This pattern is observed for both the antecedent soil moisture correlation and the concurrent heatwave-soil moisture content month. In the first layer, the anti-correlation is as described earlier but from the level 6 to 8 the anti-correlation moves toward the Sahel where it is positive in the previous soil layer content. The layers 9 and 10 have almost no significant correlation, and the correlation seem to be more positive than negative. The difference between the antecedent soil moisture content correlation with CumHeat is negligible, even though the coincident month correlation has higher and more significant positive correlations (see Figure 6.14a, b).

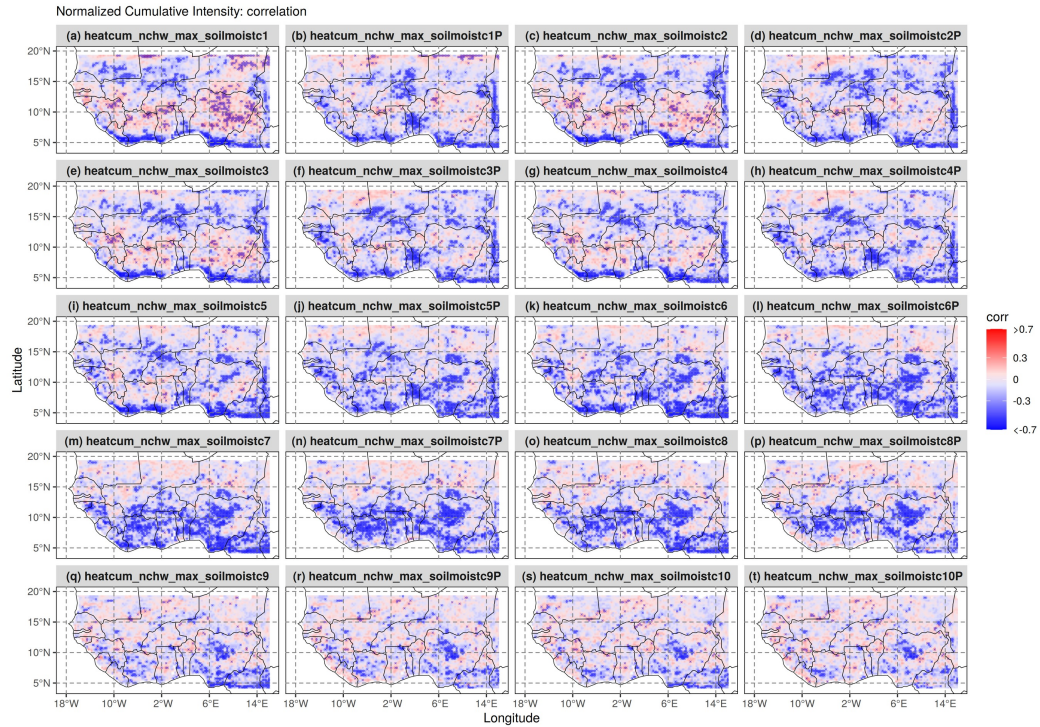


Figure 6.14: Spearman rank correlations between normalised maximum CumHeat T_{max} months and current (a, c, e, g, i, k, m, o, q, s) and antecedent (b, d, f, h, j, l, n, p, r, t) depth layer moisture content at 3-, 6- and 12 months scales. Read as in Figure 6.7

The maximum temperature Cumheat show a moderate correlation, but the minimum temperature (Figure 6.15) is presenting a strong and significant anti-correlation in the Guinea up to the Sudan and a positive correlation from the extreme Northern part of the region. This positive correlation is fading down to the Sudan. Both the anti-correlation and the positive correlation are reducing in significance and strength as the layer level increases. This show that the top layer levels influence more the night-time heatwaves in the Guinea and the Sudan especially while the Sahel seem to be driven by some moisture content. For the night-time heatwaves, the pattern changes from 6th soil layer where the correlation becomes positive almost everywhere, but the significance is observed mainly in the coastal area (layer 8-10 of Figure 6.15), Guinea, Sierra Leone up to the central part of Nigeria.

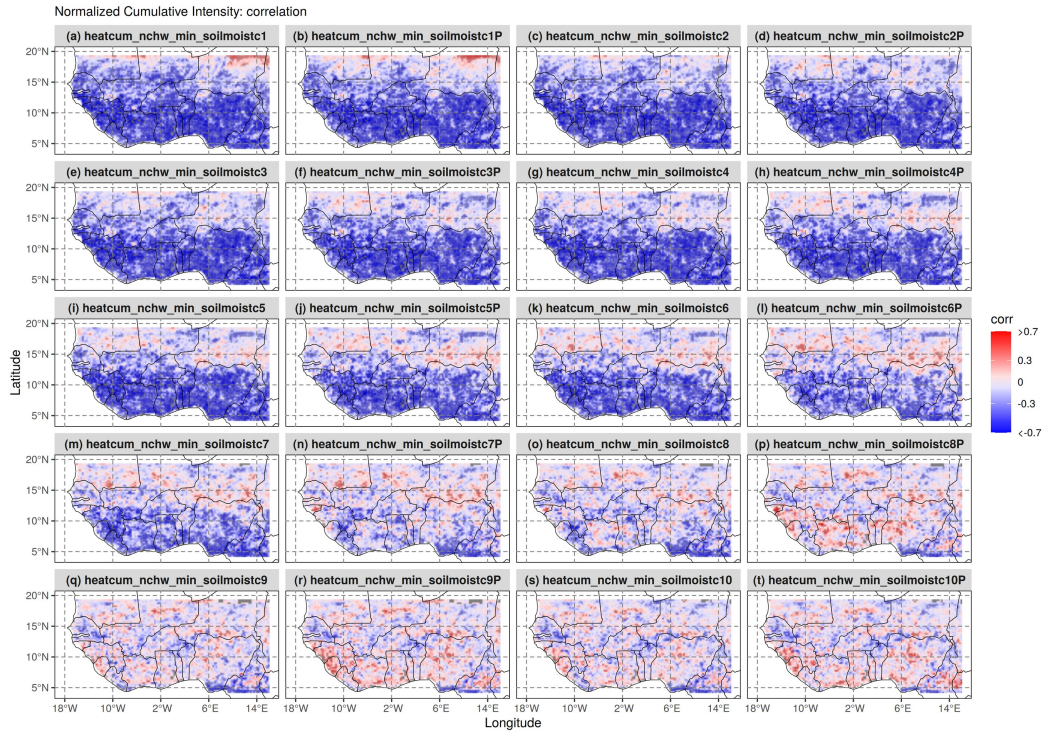


Figure 6.15: Spearman rank correlations between normalised minimum Cumheat T_{\max} months and current (a, c, e, g, i, k, m, o, q, s) and antecedent (b, d, f, h, j, l, n, p, r, t) depth layer moisture content at 3-, 6- and 12 months scales. Read as in Figure 6.7

6.3.4.1 Normalised UTCI Correlation with Soil moisture Content (SMC) at different levels

With UTCI, the pattern of the daytime heatwave correlation with soil moisture content show anti-correlation for the Guinea up to the Sahel (Southern part) but the extreme Northern part of the Sahel presents a strongly positive correlation for both the antecedent and current heatwave month correlation with soil moisture. This pattern changes as the layer levels increase as in with the T_{\max} and T_{\min} Cumheat. The UTCI presents a pattern closer to the T_{\min} Cumheat.

There is no important difference in the behaviour of daytime and night-time UTCI correlation to the SMC. The whole region gradually becomes positively correlated with the increase in the level of soil moisture. UTCI has no variation in the influence

of the soil moisture. The difference between the antecedent month and the current month correlation is very negligible, as they show quite the same patterns. The gap in the central and northern Nigeria is noticed here too.

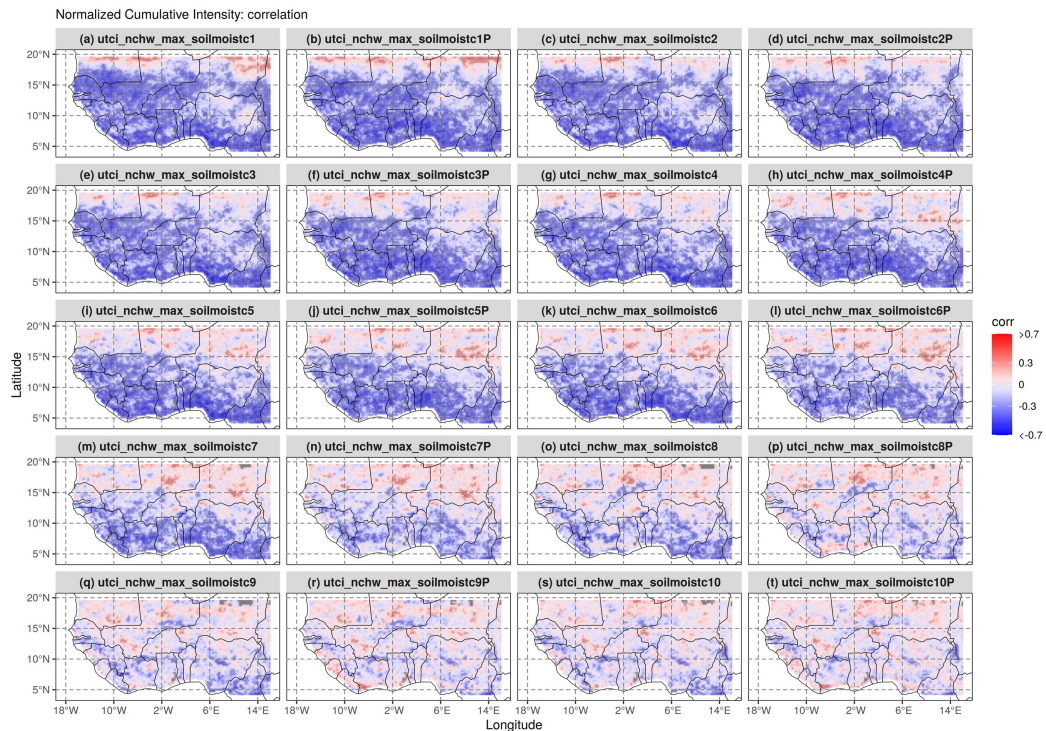


Figure 6.16: Spearman rank correlations between normalised maximum CumHeat UTCI months and current (a, c, e, g, i, k, m, o, q, s) and antecedent (b, d, f, h, j, l, n, p, r, t) depth layer moisture content at 3-, 6- and 12 months scales. Read as in Figure 6.7

6.3.4.2 Normalised WBGT Correlation with Soil moisture Content (SMC) at different levels

The WBGT correlation with soil moisture at different levels in West Africa reveals that an anti-correlation located in the coastal area and a horizontal band covering Senegal around latitude 12°N to 16°N . The band is maintained in the first two layers. The maximum WBGT of the day present a reduction in the correlational in the Southern part of the region, shrinking towards the Guinea coast up to the level 6, that

is 0.492912 m in depth. The pattern reveals that the Western part of the region is more affected by the negative correlation with the soil moisture.

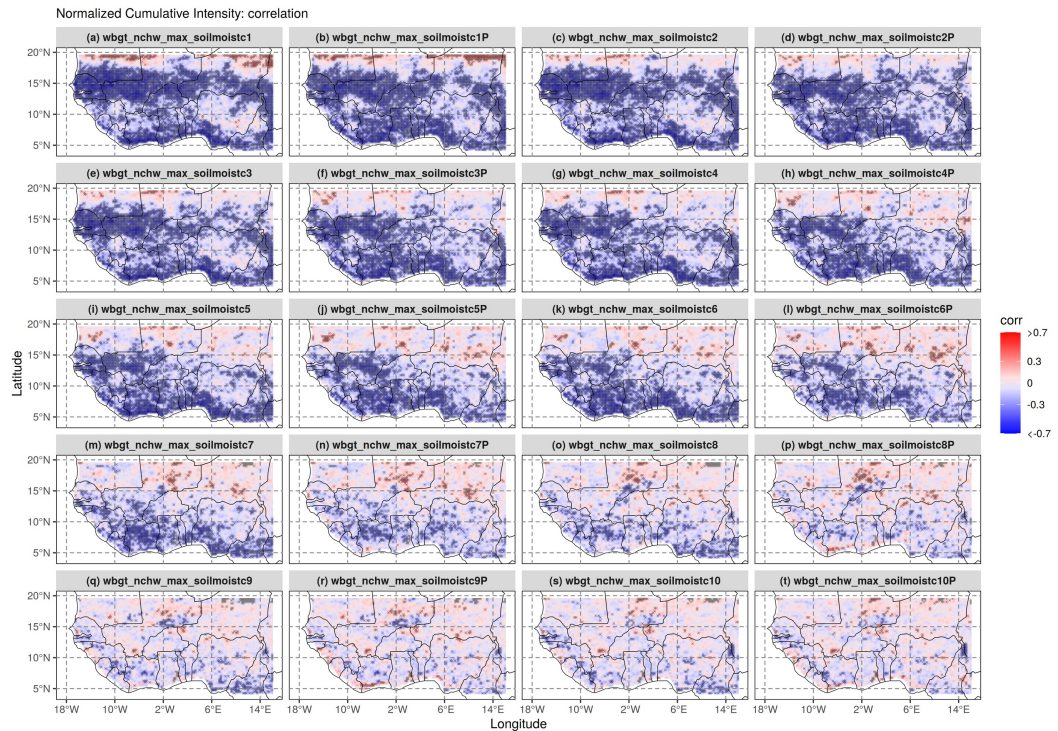


Figure 6.17: Spearman rank correlations between normalised maximum CumHeat WBGT months and current (a, c, e, g, i, k, m, o, q, s) and antecedent (b, d, f, h, j, l, n, p, r, t) depth layer moisture content at 3-, 6- and 12 months scales. Read as in Figure 6.7

There are a few differences between the soil moisture antecedent and current month correlation with the WBGT, but in general the antecedent month correlation reveals dryer conditions compared to the current month. The dryer conditions in the antecedent month could reveal a moisture restoration in the regions affected by the heatwave (Coastal area in the Guinea zone with the Western part in Senegal coast, Mali and Burkina Faso). From 0.492912 m to 3.80188 m in the considered simulation, the soil moisture seems to have limited (confidence) influence on heatwaves in the region as the correlation is not significant.

The minimum WBGT of the day presents similar patterns as in the described daily maximum WBGT. THE 12°N to 16°N horizontal band is kept especially from soil moisture level 1 to 3 where it has reduced. This pattern is similar to the characterization of the West African agro-ecological zones with an influence in Senegal. The Minimum WBGT presents in Figure 6.18 a weaker influence compared to the maximum, but the extreme east area presents an increased influence (anti-correlation) of the soil moisture content. The precipitation in that region is high and the temperature variation is minimized with high relative humidity. This particular influence of the SMC is maintained – even though reducing, from the level 7 up to soil layer level 10 in the Cameroon area and in the Southern part of Senegal.

Even though the influence is generally higher in the maximum WBGT, it is maintained in Cameroon and Senegal more into deeper layers of the soil in the minimum WBGT. The Northern part remains positively correlated (soil moisture increase), revealing an increased soil moisture at the same time as the heatwave occurs in the area. This positive correlation is mainly observed in the Eastern part of the West Africa, especially Niger and towards Chad.

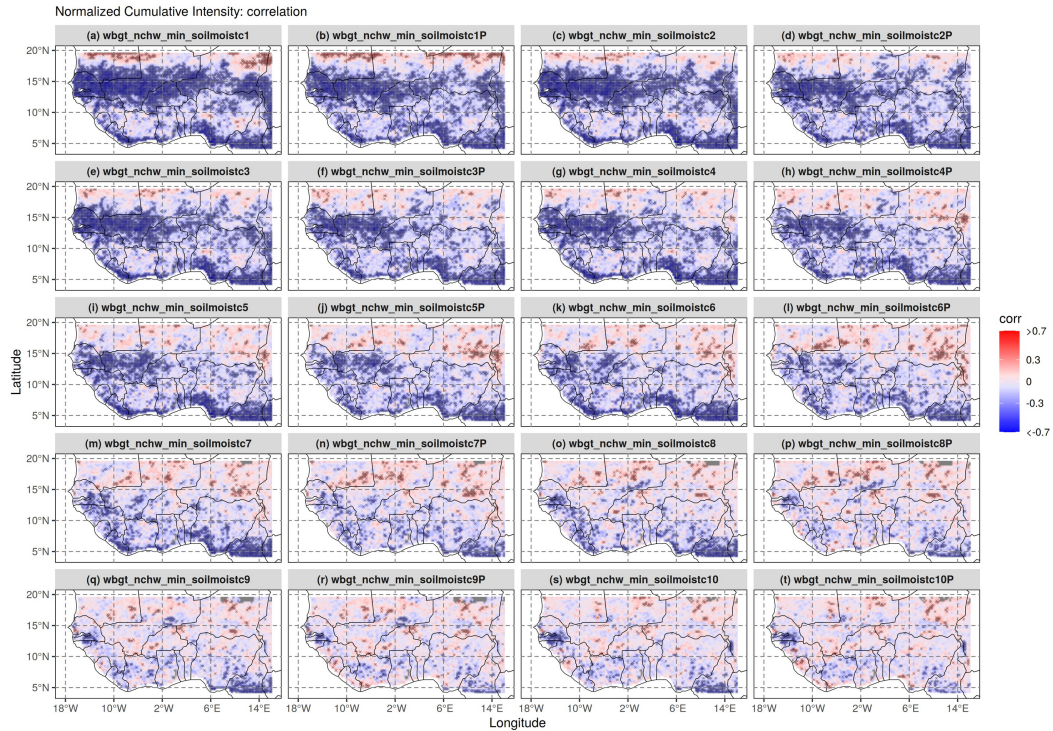


Figure 6.18: Spearman rank correlations between normalised minimum CumHeat WBGW months and current (a, c, e, g, i, k, m, o, q, s) and antecedent (b, d, f, h, j, l, n, p, r, t) depth layer moisture content at 3-, 6- and 12 months scales. Read as in Figure 6.7

The soil layer that influence more the WBGW as in the UTCI and the CumHeat are from the first (topsoil layer) up to the 6th level of soil moisture content.

6.3.5 Moisture Advection during Heatwaves in West Africa

Coupled RegCM-CLM results for specific and relative humidity roles during heatwaves. The individuals here are located around the air temperature anomaly (ta_canom) and the zonal and total advection from relative (rh) and specific humidity (hus). When the individuals in a PCA plot are located at the centre of the biplot, it means that they are not strongly correlated with any of the principal components. In other words, they do not have a significant impact on the variance explained by the principal components. From the Figure 6.19c, it appears that the 700 hPa pressure

level is slightly more strongly correlated with temperature advection than the other pressure levels. The parameters are listed in descending order from top to bottom and include specific humidity anomaly (hus_anom_avg), total relative humidity advection (adv_total_rh), relative humidity zonal advection (adv_zonal_rh), relative humidity meridional advection (adv_meridional_rh), total temperature advection (adv_total_temp), and temperature zonal and meridional advection (adv_zonal_temp and adv_meridional_temp, respectively).

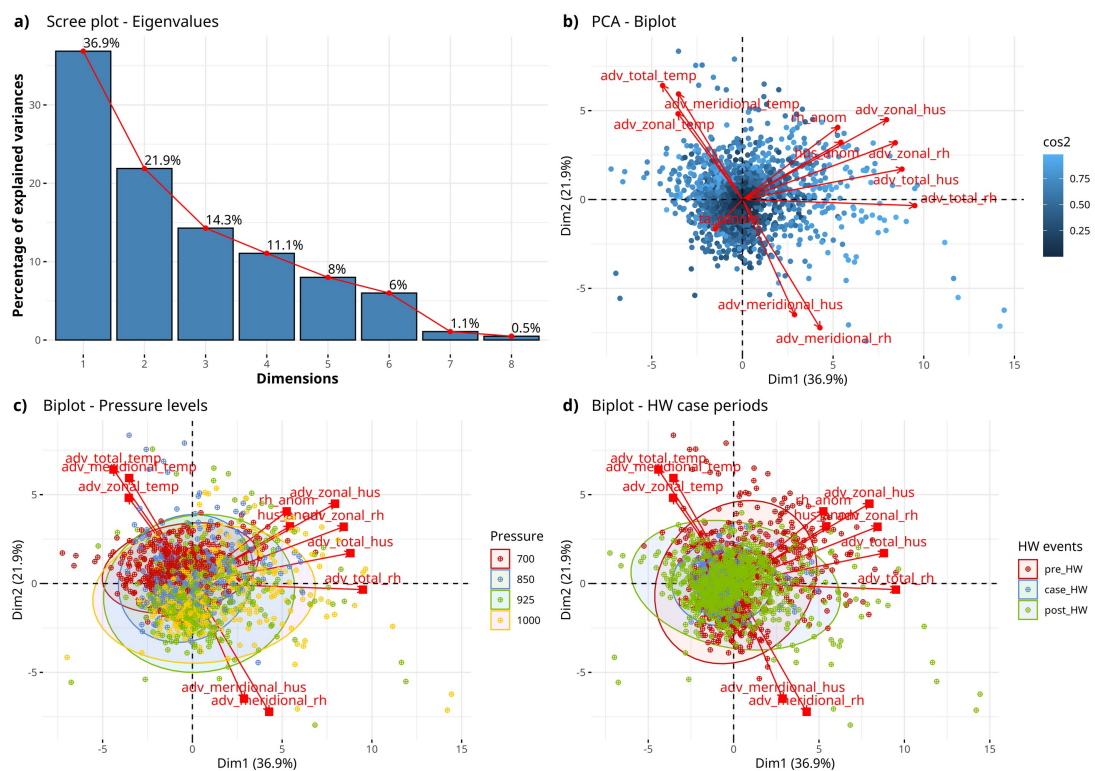


Figure 6.19: PCA applied to the 2018 Heatwave case study. Shown here are the (a) the scree plot that explain the total variation in the dataset by each component (relative and specific humidity, temperature, humidity advection); (b) the biplot that give the direction of the individuals and the variables; (c) the biplot with classes focussed on the pressure levels and (d) the biplot with classes focused on the HW event periods

However, the other pressure levels are mainly centred in the plot and appear to be associated with total and zonal advection from relative and specific humidity. This suggests that temperature advection may not be the dominant factor influencing the

atmospheric variables at these pressure levels, while total and zonal advection from humidity may be more significant.

The PCA biplot of the first and second dimensions reveals that prior to the occurrence of heatwaves, there is a significant moisture advection that tends to dissolve during the heatwave period. The individuals in the biplot are centred around this point, indicating that they all contribute to this phenomenon, but not strongly, except for the temperature anomaly. This finding is consistent with existing studies in the field. Specifically, Figure 6.20d, the individuals are observed to be centred, suggesting that the different variables are not strongly correlated with one another during the heatwave events.

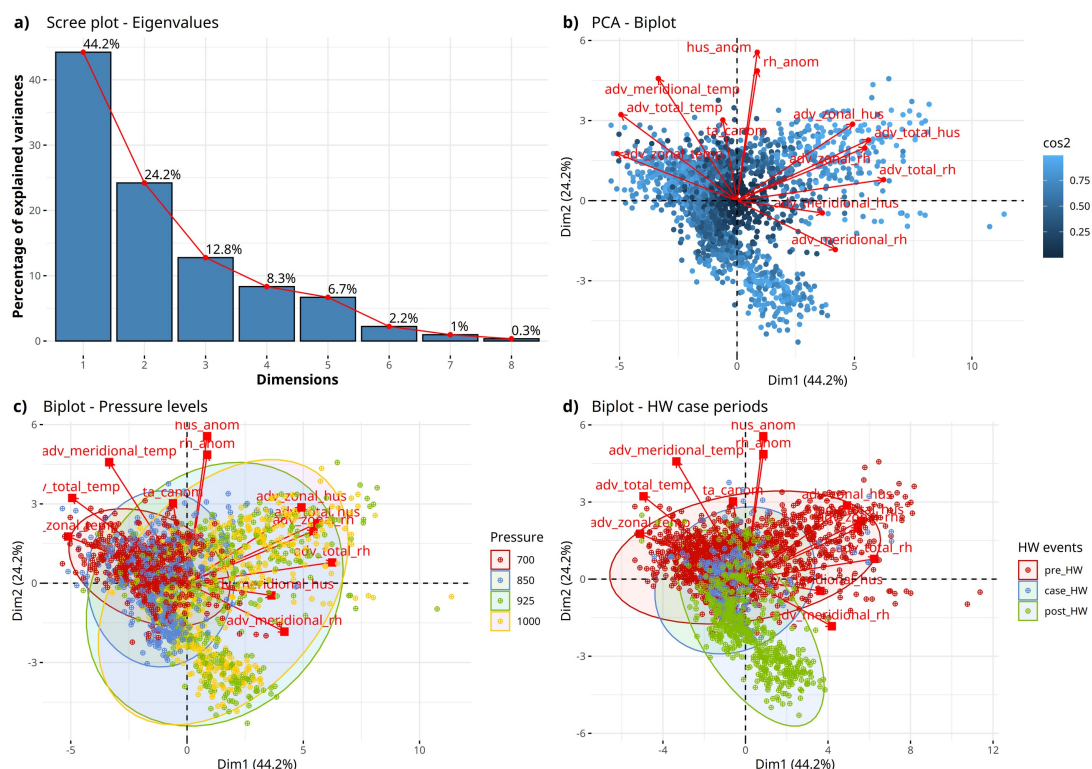


Figure 6.20: PCA applied to the 2019 Heatwave case study. Descriptions are read as in Figure 6.19

However, the temperature anomaly appears to have a greater association with the moisture advection. Overall, the results of the biplot analysis suggest that moisture

advection plays a critical role in the onset of heatwaves, and this relationship is primarily mediated by temperature anomalies. The same is observed in Figure 6.21.

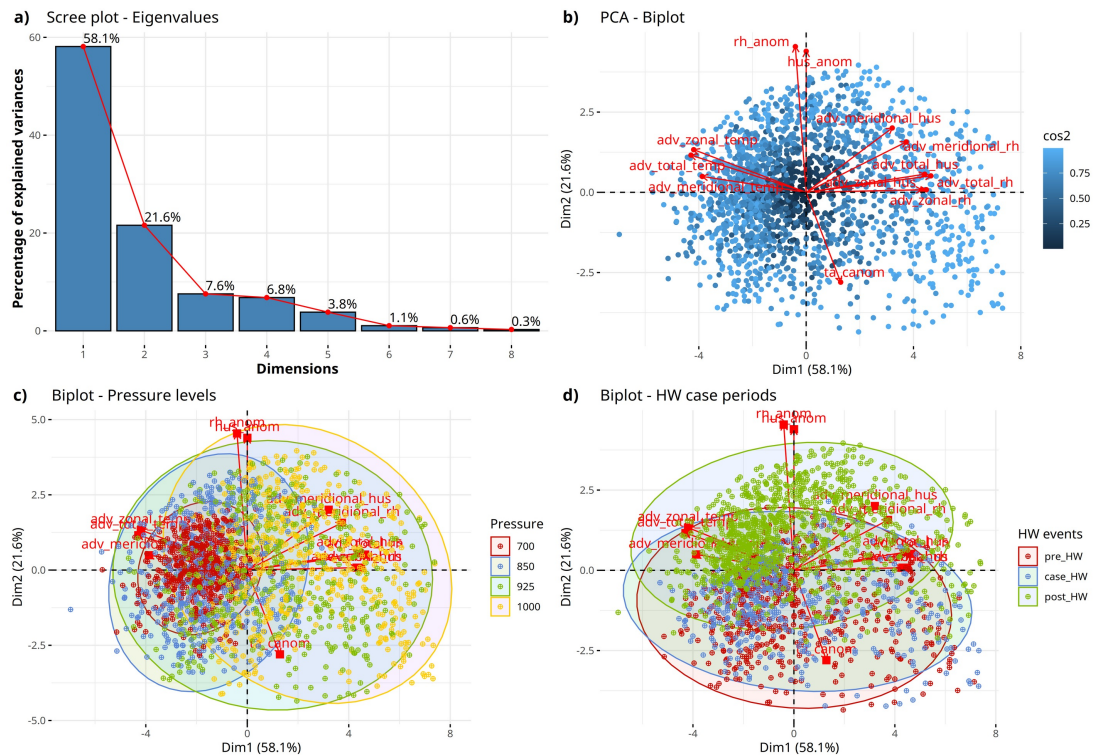


Figure 6.21: PCA applied to the 2020 Heatwave case study. Descriptions are read as in Figure 6.19

The time series plot in Figure 6.22 is accompanied by a legend that provides a comprehensive description of its parameters. It should be noted that specific humidity advection was excluded from the plot due to its low values, which require a separate figure to be presented. Overall, the legend provides a clear and concise description of the parameters used in the time series plot, allowing for better interpretation and analysis of the results.

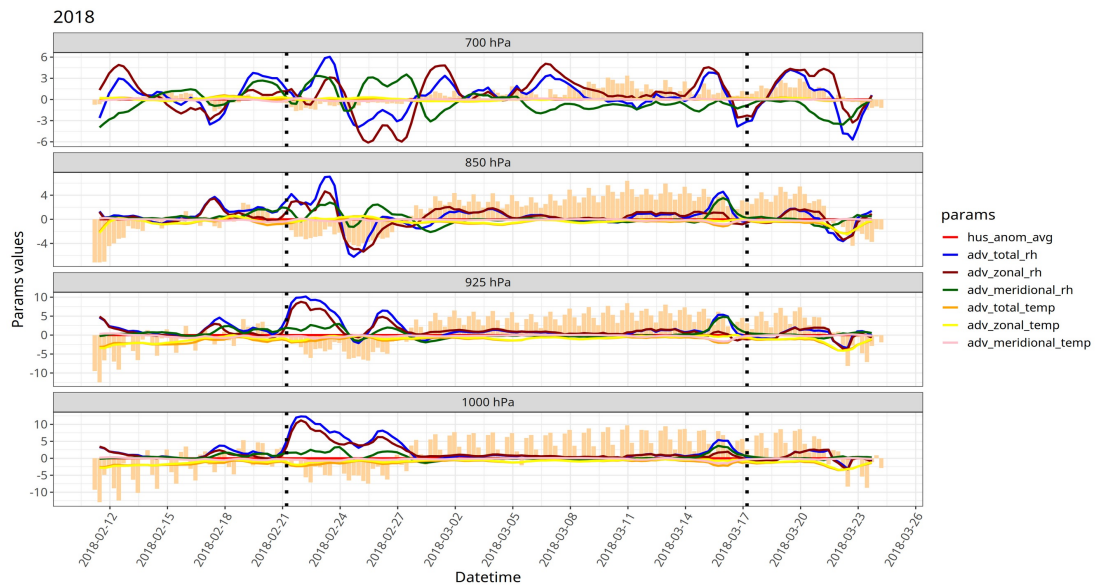


Figure 6.22: 6 hourly smoothed evolution over the 2018 detected heatwave highest event case study. The values have been smoothed to daily for clarity and plotted at 925 hPa, 850 hPa and 700 hPa. The pink bars are the temperature anomaly ($^{\circ}\text{C}$). The black dotted vertical lines show the section of the beginning and the end of the detected heatwaves detected event in this particular period. Horizontal lines represent the parameters as indicated in the legend

The time series plot displays the evolution of seven variables at different pressure levels before, during, and after a heatwave event. At 1000 hPa, there is an initial rise in the variables, including specific humidity anomaly, total, zonal and meridional relative humidity advection, and zonal temperature advection, followed by a decrease to negative values and a subsequent rise, but at a lower rate than the first rise. At the beginning of the heatwave event, the variables fluctuate at very low levels (around 0). Towards the end of the heatwave event, there is a slight increase in the variables, followed by a decrease again. This pattern is also observed at 925 hPa. At 850 hPa, the fluctuations during the heatwave event are much more frequent compared to 1000 and 925 hPa levels. At 700 hPa, the fluctuations are even more pronounced and continue even after the heatwave event has ended, similar to the pattern observed before the heatwave event.

In 2019 (Figure 6.23), the same is observed with a small rise when the temperature anomaly is negative.

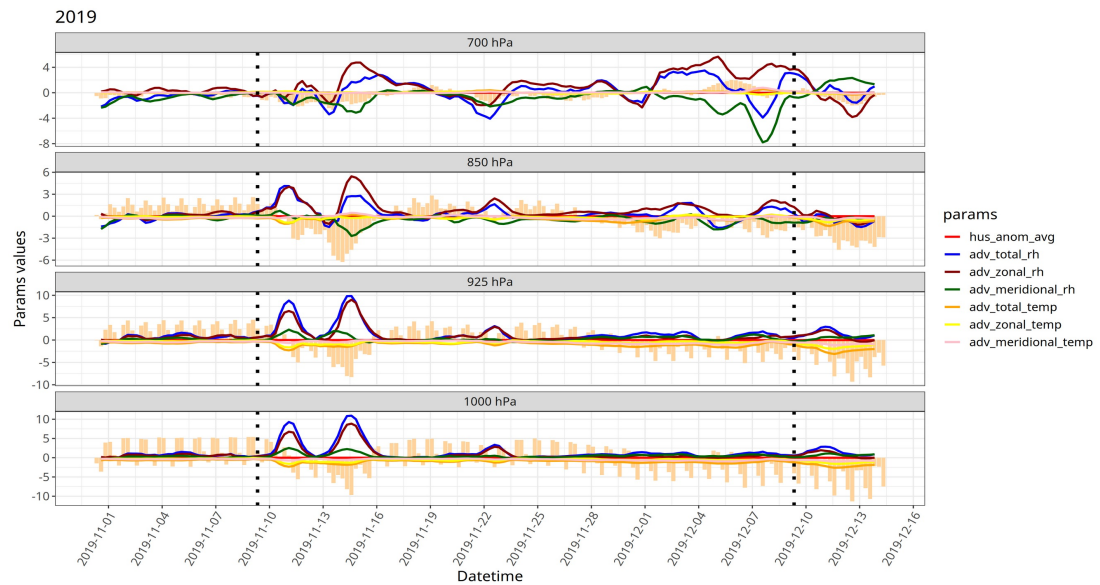


Figure 6.23: 6 hourly smoothed evolution over the 2019 detected heatwaves highest event in this particular period. Descriptions are read as in Figure 6.22

This pattern of evolution in the variables suggests that there are changes in the atmospheric conditions during and after the heatwave event. Specifically, the rise in specific humidity and relative humidity advection before the heatwave period suggests that there is an increase in moisture content in the atmosphere. However, during the heatwave event, there is a decrease in these variables which indicates that the atmosphere has become drier. Additionally, the fluctuations observed at 850 hPa and 700 hPa during and after the heatwave period suggest that there are ongoing changes in the atmospheric conditions at these levels, even after the heatwave event has ended. Overall, this interpretation suggests that the heatwave event has significant effects on the atmospheric conditions, which could have broader implications for weather and climate.

An increase in total and zonal advectations during a heatwave in the coastal area (see 2020 case study, Figure 6.24) with a negative zonal temperature advection would indicate that warm and humid air from the ocean is being transported over the land, which can contribute to the intensification of the heatwave. The negative zonal temperature advection suggests that the air transported from the ocean is warmer than the air already present over the land. This can lead to an increase in temperature and humidity, which can exacerbate the heatwave conditions.

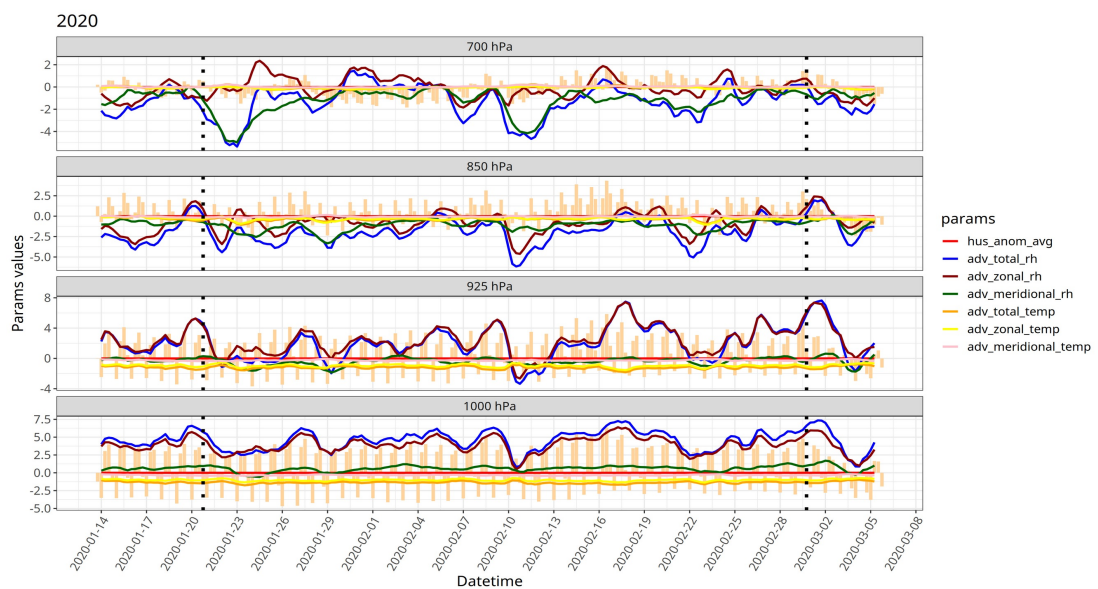


Figure 6.24: 6 hourly smoothed evolution over the 2020 detected heatwaves highest event in this particular period. Descriptions are read as in Figure 6.22

Overall, the plot provides insight into how the variables evolve over time and pressure levels during the heatwave event. The fluctuations and patterns observed at different pressure levels can provide information on the atmospheric dynamics and the processes involved in heatwave formation and dissipation. In the 2020 case, the combination of such factors can lead to an increased risk of heat-related illnesses and other adverse impacts on human health, agriculture, and ecosystems.

6.4 Discussion

The geographic position of West Africa, located in the tropics, from close to the equator to the Northern Hemisphere, makes it a region that receives high solar radiation almost all the year with low variations over the year. With such a condition, heatwaves can happen at any time of the year, in contrast to Europe where the highest impacts predominately occur in summer (Russo et al., 2016). Nevertheless, it is almost found that the strong warming increasingly and more significantly occur during the hottest months of the year (April, May). That period corresponds to the end of the dry season and the onset of the West African monsoon (Largeron et al., 2020). Even though the multi-day soil desiccation is not the major driver of the intensification (in Europe this is the case, (Fischer et al., 2014; Miralles et al., 2014)) of the springtime highest intensity heatwaves in the Sahel (soils are already dry, (Baup et al., 2007)), there are evidences of associated increased moisture during Sahelian heatwaves (Guichard et al., 2009; Largeron et al., 2020). Towards the southern part of West Africa, this remains possible. The present study found that:

- RegCM-CLM coupled dynamic model with non-hydrostatic core run establishes the land-atmosphere interaction in West Africa and reproduces heatwave episodes quite well in West Africa;
- Soil moisture has an influence on heatwaves where there is intense desiccation from the antecedent soil moisture to the current soil moisture;
- SPEI agrees with the model SMC in establishing the relationship (correlation or anti-correlation) with heatwaves in West Africa. SPEI could be used as a proxy for soil moisture in the region;

- Focusing on the 3-month scale soil moisture as depicted in previous studies, temperatures rise because an increasing sensible heat flux to the atmosphere compensates a decreasing latent heat flux is the normal effect to low soil moisture.
- From the moisture advection, it is important to note that atmospheric conditions during a heatwave are complex and can vary at different altitudes. Specifically, at the surface (1000 hPa and 925 hPa), the variables show a relatively consistent pattern of rising before the heatwave, decreasing during the heatwave, and rising again after the heatwave. However, at higher altitudes (850 hPa and particularly 700 hPa), the fluctuations are more frequent and intense, both during and after the heatwave.

The quantification of the influence of soil moisture in the formation of heatwaves in West Africa is evident from the conducted analysis. This highlights the potential importance of soil moisture in more or less amplifying heatwave events in the region. Given the link between SPEI and soil moisture availability (in Mueller and Seneviratne (2012) and in the present work), the correlation with the maximum heatwaves depicts the relationship between land surface and the atmosphere. Following the results given by Mueller and Seneviratne (2012), the correlations reduce for the 6-month and 12-month but at 3-month, the correlation is at the highest in the southern part including the Guinea Coast and parts of the Sudan zone (including the central part around 2° to 1° longitude West and 5° to 15° latitude) around -0.6. But in the present study, the antecedent SPEI 3-month values present fewer significant anti-correlation compared to the current 3-month values. This indicates the decrease of moisture during high heatwave months in the coastal areas.

On the other hand, the Sudan-Sahel, especially the intersection of Senegal, Mali and Guinea and the Eastern part of Nigeria, present either no correlation or positive correlations even though not significant in most cases. This denotes that in those cited area there is an increased moisture during heatwaves in the antecedent months and a slight desiccation (anti-correlation) of the moisture in the same month correlation with the heatwave. These results are similar to the Mueller and Seneviratne (2012) on the use of the Global Precipitation Climatology Project (GPCP) and ERA-Interim, as they provide slightly more constant correlation results. So, the Guinea zone with some area in the Sudan zone presents a configuration similar to that described by Perkins *et al.* (2015), in the Australian heatwave correlation with antecedent soil moisture. For all the considered daytime and night-time heatwave indices (CumHeat Temperature, UTCI and WBGT), there is anti-correlation in the Guinea and some specific area in the Sudan and even in the Sahel (central longitudes) denoting the influence of surface soil moisture and even soil layer moisture content for daytime and night-time normalised cumulative index at 3-month scale. There is a desiccation of the soil moisture in the Coastal area and the central part of the region that decreases with timescale before the maximum of the heatwave. Numerous severe heatwave phases occur after dried soil moisture at different levels, but some still exist after “normal” or “increased” soil moisture, indicating that it does not always have to be very dry for an extreme heatwave event to occur. It can even occur after an increased soil moisture. The current correlation reveals more anti-correlation in the Guinea zone and in the Sudan and the Sahel. The “positive” heatwave reduces a lot, denoting a higher decrease in the heatwave maximum event. There is also an increased positive correlation as the timescale

increases, meaning that there is a regain of soil moisture as the timescale increases, but the correlations are mostly not significant. The soil layer moisture content reveals a particularly “increasing” daytime soil moisture content availability in Nigeria in the month when the heat event is maximum. This correlation is maintained up to the 6th - 8th layer, depending on the time and index. The 9th and 10th soil moisture content are too far and present very weak correlations, and only a few are significant. This “increasing” daytime correlation is manifested in the night-time events correlation with the surface soil moisture (SPEI).

UTCI and the WBGT include humidity in the equation, making them somehow sensitive to humidity in an area. But their correlations with the soil moisture is mainly observed in the Guinea zone and has less coverage. The antecedent correlation reveal almost no significant correlations except for the Guinea zone. UTCI is more sensitive to the soil moisture availability (SPEI) than the WBGT even though similar in general. In contrast to the WBGT, which is less sensitive to soil moisture availability at greater depths, the UTCI takes into account thermal, solar, and convective heat transfers from ambient temperature, humidity, solar radiation, and wind speed. The UTCI is more representative of specific climates, weather, and locations than the WBGT. Additionally, like the human body, the UTCI is highly responsive to changes in temperature, solar radiation, wind, and humidity, making it better suited for describing temporal variability of thermal conditions than the WBGT. The UTCI is also capable of detecting even small differences in the intensity of meteorological stimuli (Blazejczyk et al., 2012). Notably, there are substantial differences between the UTCI and WBGT, with the UTCI being more sensitive to wind speed and the WBGT considering humidity almost as important as temperature.

In humid environments, the correlation between them is relatively high, whereas in dry environments, there is little to no significant correlation between them (Golbabaei et al., 2015; Kampmann et al., 2012).

The strong land-atmosphere coupling under dry soil conditions over Europe is not as strong in the Sudan and the Sahel as was already depicted by Baup *et al.* and Largeron *et al.* (2007; 2020). This is effectively due to the fact that the Sahel especially is dry and remains so until the monsoon season. The higher relationship in the Guinea is unmistakable, there is soil moisture in the region especially the soil layer content is mostly filled up to 0.492912 m (6th level) or 1.38283 m (8th level). In West Africa, the antecedent soil moisture conditions could enhance heatwave occurrence and intensity following the dry-up intensity. However, this is not always the case as some area showed “normal” and “increasing” SMC in the Sudan and particularly the Sahel. The net radiation budget is majorly responsible for this mechanism at the land surface. Indeed, the impact of soil moisture conditions on sensible fluxes is strong in West Africa (Koné et al., 2022). When the soil is wet (i.e. Guinea zone), the latent heat flux dominates, initiating and enhancing cloud formation that in return cools the temperatures of the affected area. Dry soils reverse the mechanism and the sensible heat flux dominate with an increase in the heat that is felt, generally associated to heatwaves. According to Koné et al. (2022) soil moisture initial conditions impact on precipitation in West Africa is linear over the Central and West Sahel regions, dry (wet) experiments lead to a rainfall decrease (increase). This is observed in the present case where the Central and the West Sahel region has strong anti-correlation with temperature CumHeat and SPEI, receiving much rainfall. Furthermore, the behaviour of specific variables such as the zonal temperature

advection can be opposite to what might be expected during a heatwave, knowing that there is an inflow of moisture before heatwave events in West Africa. Overall, the moisture advection results highlight the importance of considering atmospheric variables at multiple altitudes when studying heatwaves and their impacts.

Similar to the previous chapter (Chapter 5 –using ERA5-Land and YOPP datasets), the key findings reveal that heatwaves in West Africa have become more intense and frequent in recent decades. These heatwaves are fundamentally different in West Africa due to the region's unique parameters, including humidity, wind speed, and orography. The study used the maximum heatwave of the year, considering intensity, duration, and spatial extent, to select case studies. These heatwaves typically occur in the pre-monsoon phase (January-May) and the post-monsoon phase (October-December), with the most intense heatwaves recorded in the pre-monsoon. When we put these findings together, it becomes clear that soil moisture and atmospheric dynamics are interconnected in the formation and progression of heatwaves. Changes in soil moisture can influence atmospheric conditions, which in turn affect temperature tendencies and wind dynamics, influencing the intensity, frequency, and duration of heatwaves. This complex interplay highlights the need for comprehensive, multi-factor models to accurately predict and understand heatwaves in West Africa.

According to several studies, such as those found in Anjileli et al. (2021), Felsche et al. (2023) and Zhang et al. (2015), reduced soil moisture contributes to more intense and frequent heatwaves. This is because when soil moisture levels are low, an increasing sensible heat flux to the atmosphere compensates for a decreasing latent

heat flux, leading to higher temperatures. This suggests that monitoring soil moisture levels could be crucial for predicting and managing heatwaves in West Africa.

6.5 Summary

The study analysed the sensitivity of the RegCM-CLM coupled model to detect heatwaves in West Africa and the role of soil moisture during heatwave events. The non-hydrostatic core is used, driven by ERA5. The NOAA Climate Prediction Center (CPC) soil moisture dataset was used to initiate the model (van den Dool et al., 2003). The model can identify heatwaves in the region, although there are biases in the extreme North when compared to ERA5 results. However, in general, the RegCM-CLM coupled model simulation is capable of reproducing different heatwave indices at different time periods. The soil moisture is also utilised to assess the impact of soil moisture on heatwave events in West Africa. Soil moisture conditions have a relatively significant impact on heatwave events and, therefore, on surface energy fluxes. In wet (dry) experiments, a cooling (warming) of the surface temperature is observed in association with a decrease (increase) in sensible heat flux, an increase (decrease) in latent heat flux, and a decrease (increase) in the boundary layer depth. It is also shown that there is a moisture advection before a heatwave event and another inflow just before the cessation, especially in the Sudan and Sahel. Hirschi et al. (2011) suggest that regional climate model simulations successfully capture the connection between the intensity of extreme events and the magnitude of prior soil moisture deficits, but only for areas where moisture is limited. However, for wetter regions like Central Europe, there appears to be a weak association between extreme temperature events and preceding soil moisture

conditions, and models tend to overestimate the impact of soil moisture on temperature. This may also be the case for the Guinea Coast in West Africa.

CHAPTER 7: CONCLUSIONS AND RECOMMENDATIONS

7.1 Introduction

Described as periods of excessively (abnormally) high temperatures (hot weather), heatwaves have had and continue to have devastating impacts on human and animal life, agriculture, and water resources and also infrastructures. Weather and atmospheric conditions lead to two types of heatwaves: dry heatwaves occur when the skies are clear, exposing the area to large amounts of solar radiation, while moist heatwaves occur when water vapour traps heat due to cloudy and/or humid conditions. Both heatwaves have tremendous impacts, especially when they are compounded with drought phases or dry spells. Extreme heat events have become more severe and frequent due to global warming, and climate simulations predict that they will continue to increase in frequency, duration and intensity in the future, largely due to rising greenhouse gas emissions.

According to the emergency events' database (EM-DAT), there have been no significant impacts of heatwaves in sub-Saharan Africa since 1900. However, various studies with different measures have reported several heatwaves in the region. As global warming continues, the Sub-Saharan African region is already and will continue to be disproportionately affected by heatwaves. Therefore, it is essential to address this discrepancy in reporting to accurately evaluate the future impacts of extreme heat in the region.

Such a situation makes it very critical to quantify heatwaves, monitor and even predict them, so populations are always prepared ahead of the event. Mapping out vulnerable regions is also crucial so that adequate plans can be made to deal with

them in the future. The present study investigates the “Drought-heatwaves” dynamics with land use/cover change under the West African monsoon system. The central questions of this research work are:

- i. What are the discernible patterns governing the occurrence of drought-heatwaves under the ambit of the West African Monsoon?
- ii. To what extent do the synoptic and boundary layer scale temperature components contribute to explicating the dynamics of heatwaves in the West African region?
- iii. How does the coupled Regional Climate Model with a Land Model (RegCM-CLM) respond to heatwaves, considering the interplay of moisture roles within different Land Use Land Cover Types (LULCT)?

7.2 Conclusion and Summary of Key Findings

This study aimed to deepen our understanding of Drought and heatwaves occurrence in West Africa, the dynamics and influence of temperature tendencies responsible for heatwaves, and to assess the sensitivity of the Regional Climate Model (RCM) with the Land Community Model (RegCM-CLM) to these extreme events. After conducting a thorough analysis of temperature tendencies and heatwave indices, and studying the root causes of heatwaves in the region, we arrived at several key findings and conclusions that shed light on the nature and implications of drought and heatwaves in West Africa. The research work is conducted on the research questions related to the specific objectives. Research questions that have been raised were investigated for answers.

7.2.1 What are the patterns of drought-heatwaves under the WAM?

Here, the gridded and observational data were compared to assess the drought and heatwave indices, primarily focusing on the Standardized Precipitation (Evapotranspiration) Index (SPI) for drought and the Cumulative Excess Heat (CumHeat) and Universal Thermal Climate Index (UTCI) for heatwave detection. Although the within-dataset correlation showed good agreement, there were slight differences observed. The Guinea zone generally recorded mild to moderate SPEI values, with a few extreme values. Similarly, Sudan and Sahel recorded extreme dry events. The comparison between station and gridded data revealed that some stations had fewer heatwaves and lower intensity as compared to the gridded data, with extreme values present in the station data. In terms of heatwaves, the Sahel region was found to experience greater stress compared to the other two zones. The same was observed for maximum temperature (T_{\max} CumHeat) in some stations from both datasets (station and gridded). Heatwave/heat-stress intensity and duration are increasing (for both datasets) and going up to very extreme heatwaves/heat-stress. Finally, the Sahel reveals particular tendencies of Drought-Heatwave (D-HW). The frequency increases or decreases depending on the index (T_{\max} /UTCI), the zones and the dataset. Heatwave/heat-stress do not frequently occur during severe drought conditions with the highest intensity. This aspect is relatively new information in the region but agrees with some previous work (Guigma et al., 2020) on UTCI or T_{\max} heatwaves occurrence in the Sahel at specific periods of the year that could be considered drought periods.

7.2.2 How well do synoptic and boundary layer scale temperature components explain heatwaves' dynamics in West Africa?

The study analysed and compared diurnal heatwaves indices to understand temperature tendencies at synoptic and boundary layer scales that contribute most to the heatwaves' dynamics in West Africa. The spatio-temporal duration and cumulative intensity of the heatwaves were investigated, and specific cases studied. The study used data from the Year Of Polar Prediction (YOPP) to understand the root causes of heatwaves in the region. The results showed that different heatwave indices were based on different parameters and had similar patterns of occurrence. The differences in thermal indices (UTCI and WBGT) were mainly due to their sensitivity to humidity (moisture) and wind speed. The geography of West Africa, with its proximity to the ocean and local orography, also plays a role in the local climate, as seen in the case of Senegal. The study found that heatwaves in West Africa occurred in two main phases: the pre-monsoon phase (January-May) and the post-monsoon phase (October-December). The most intense heatwaves were recorded in the pre-monsoon phase, and the late season heatwaves were generally located in the Sudan country or in the Eastern Sahel, where the land has a significant effect on radiation and temperature. The study also identified three key temperature tendency terms that contribute to the onset and cessation of heatwaves in the region: temperature tendency due to dynamics ($ttend_d$), temperature tendency due to turbulent diffusion ($ttend_t$), and temperature tendency due to radiation ($ttend_r$). The radiation and the turbulent diffusion seem to maintain the heatwave and the dynamics initiate and dissipates the heatwave, but it also contributes in maintaining the heatwave. These tendencies depend on the pressure levels and contribute to the

temperature change over an area affected by a heatwave. Additionally, the direction and intensity of the zonal and total advection in a given area play a critical role in the physical formation of heatwaves and determine whether they move westward or eastward. The cessation of heatwaves in the region was not clearly defined by the tendencies and temperature advection in the present study, but the vertical profile of the different tendency terms revealed that the boundary layer (BL) is turbulent and produces varying values. However, a clear pattern was established above 925 hPa, where the $ttendd$, $total.adv$ (horizontal advection), and $ttendr$ are positive and increase even further around 500 hPa. The zonal advection is particularly critical in the physical formation of heatwaves, as it is close to the $totaltt$ and the $ttendd$. The dynamics of the heatwaves in January-March have increased from 2018 to 2020, resulting in a larger gap between positive and negative contributing temperature terms.

7.2.3 How sensitive is the coupled Regional Climate Model with a Land Model (RegCM-CLM) to heatwaves with moisture role in the different LULC types?

The study finally investigated the sensitivity of the Regional Climate Model (RCM) combined with the Land Community Model (RegCM-CLM) to heatwaves in West Africa. The focus is on the role of moisture initialization in different land-use and land-cover types (LULCT) in West Africa. The outcomes of this investigation provide nuanced insights into the intricate interactions shaping heatwave dynamics within the context of West Africa. The integrated Regional Climate Model (RCM) coupled with the Land Community Model (RegCM-CLM) and driven by ERA5 demonstrates good capabilities in identifying and characterizing heatwave

occurrences across the diverse landscape of West Africa. However, discernible disparities in model performance surface when examining the northern regions, necessitating further scrutiny. An intrinsic synchronization between heatwave indices derived from RegCM-CLM and those obtained through ERA5 is unveiled, attesting to the model's capability to capture the temporal intricacies of heatwave events across this region. Crucially, the role of soil moisture content emerges as a pivotal determinant in shaping the spatio-temporal evolution of heatwave. Elevation in soil moisture content corresponds to a possible dampened rise in surface temperature, mitigated sensible heat flux, intensified latent heat flux, and confined boundary layer depth. Conversely, reduced soil moisture content aligns with elevated surface temperatures, amplified sensible heat flux, diminished latent heat flux, and expanded boundary layer depth. Furthermore, this study establishes a robust linkage between the SPEI and the occurrences of heatwaves across a 3-month time-frame, underscoring the potential utility of SPEI as an indicative proxy for soil moisture content within the West African context. Additionally, significant correlations manifest within soil moisture datasets, albeit primarily within the initial 6th to 8th soil moisture levels. The potential of employing SPEI as a surrogate for soil moisture content in regional heatwave analyses holds promise, enabling a deeper comprehension of the intricate coupling between land surface properties and atmospheric dynamics. A notable observation is the amplification of sensible heat flux directed towards the atmosphere, concomitant with a simultaneous decrease in latent heat flux, resulting from elevated soil moisture content over a 3-month interval. This highlights the intricate interplay between land surface characteristics and atmospheric heat exchange processes. While correlations between extreme event

severity and antecedent soil-moisture deficits are perceptible within moisture-limited domains, such a linkage does not uniformly hold across the entirety of the West African landscape. Drawing parallels with temperate latitudes, a parallel relationship is evident in the Guinea Coast region, where diminished soil moisture content corresponds to a heightened incidence of elevated stress days. Case studies centred in the Sudan and Sahel regions during 2018 and 2019 unveil distinct instances of moisture inflow preceding and following heatwave episodes, indicative of complex temporal patterns. Contrasting this, the Guinea region (2020) exhibits sporadic moisture fluctuations, particularly along the coastal expanse. These intricate findings encapsulate the multifaceted interplay between soil moisture and heatwave dynamics. This comprehensive investigation, grounded in West Africa's unique climatic context, contributes valuable insights into the mechanisms underlying heatwave occurrences, enhancing our comprehension of this complex phenomenon within the region.

7.3 Limitations of the Research Work

The thesis work encountered several limitations that warrant discussion. The comprehensive analysis of heatwaves necessitates a continuous and well-distributed temporal dataset across the region. However, certain countries lacked adequate data availability, with some possessing less than 60% of the required series of data over time. Utilizing hourly datasets could yield deeper insights into diurnal heatwave fluctuations; however, the absence of such data remains a constraint in this study. Consequently, establishing an extensive network of reliable data sources and capturing detailed temporal observations emerges as imperative for a nuanced

understanding of processes at hourly scales. The application of the Year of Polar Prediction (YOPP) temperature tendencies revealed limitations inherent to the dataset. The restricted historical data availability (spanning 2018 to 2020) could introduce limitations in terms of the selection of the most intense, longer heatwave and larger in coverage over the whole period as use cases with the YOPP temperature tendencies. Additionally, the YOPP model biases introduced a shift between total temperature tendencies and temperature advection components. Furthermore, the study's reliance on a single climate model (RegCM4.7-CLM4.5) might inadequately capture the intricate atmospheric and land-surface interactions contributing to heatwaves and droughts in West Africa. This limitation extends to the soil moisture initialization, which could potentially benefit from enhanced spatio-temporal resolution for more detailed results. Lastly, a promising avenue for future investigation involves employing updated versions such as RegCM5-CLM5 or the Weather Research and Forecasting Model (WRF) alongside thoroughly evaluated land surface models (LSMs). This approach holds the potential to yield more accurate outcomes within the distinct climate zones under scrutiny, offering a refined comprehension of heatwave and drought dynamics in West Africa.

7.4 Key Messages

West Africa's climate is based on the monsoon system with low-temperature variations and an average high temperature over the year. The high temperatures classify the region as exceptionally prone to heatwaves. The West African Heatwaves and drought are associated with global warming variability. Droughts become more intense as heatwaves in some areas, and both could have unprecedented impact on

health, crop yields and infrastructures. Heatwaves' intensity differ in the three climatological zones (Guinea, Sudan and the Sahel). Therefore, particular aspects in each climate zone make it interesting to study, knowing that heatwaves and drought have different impacts depending on the particular climate of an area. The research findings highlight the importance of understanding the changing patterns of D-HW:

- Some areas have experienced an increase in drought-heatwaves (D-HW), while others have experienced a decrease. The intensity of heatwaves in the Guinea zone is lower than those observed in the Sudan and Sahel regions. The Sahel region has shown a more significant impact, and the potential for frequent occurrence of D-HW in this region could be increased or decreased by the restoration of forests and landscapes.
- The temperature dynamics responsible for heatwaves in West Africa are consistent across all climate zones. There is an increase in temperature tendency due to dynamics (ttendd) with the vertical advection (rttd), to radiation (ttendr) and to turbulent diffusion (ttendt). These factors are associated with temperature tendency terms and temperature advection, which can lead to westward movement, subsidence. Subsidence, in turn, leads to compression and heating during heatwave events. All three tendencies together initiate, maintain and dissipate the heatwave. It is important to understand these temperature dynamics and their impact on heatwaves in order to better comprehend the behaviour of heatwaves in West Africa.
- Soil moisture plays a significant role in the occurrence and driver of heatwaves. The RegCM-CLM model simulation used for heatwave detection and soil moisture role during heatwave events showed that heatwaves are

influenced by antecedent soil moisture desiccation from the surface to 0.36 or 1.03 m depth (6th to 8th levels). Deeper levels do not have a significant influence. Positive correlations also influence the Eastern-Sudan and East-Sahel parts, while the other part (significantly in Guinea) is affected by an anti-correlation (a reduction of the previous month's moisture before a high-intensity heatwave). The sensitivity to initial soil moisture for three severe cases of heatwaves studied, indicating that warm extremes can be amplified by pre-existing dry soil conditions and the persistence of soil moisture anomalies. It is important to understand the role of soil moisture in heatwaves to better comprehend the behaviour of heatwaves and their impact on agriculture, forest mortality, and drinking water scarcity.

7.5 Recommendations

The recommendations presented in this section aim to address the research problem and key findings of the study. Based on the analysis and results, several practical suggestions are made to improve the understanding and management of compound drought-heatwaves. These recommendations are intended to be useful for stakeholders and decision-makers, government agencies, non-government organisations, academia, private sector, as well as to provide guidance for future research in this field.

7.5.1 Future Research

- Conduct further research on the changing patterns of D-HW in different climate zones and their potential consequences for sector specific activities

such as food security. This research should focus on region-specific analysis and adaptation strategies to mitigate the adverse effects of D-HW.

- Develop targeted model evaluations for climate services to evaluate the simulation of heatwaves in different regions. This research should focus on the evaluation of several climate models and the identification of anomalous dry soil moisture conditions and low accumulated heatwaves.
- Design heatwave early warning systems (HEWS) to reduce the avoidable human health consequences of heatwaves through timely notification of prevention measures to vulnerable populations. This research should focus on the development of HEWS that are tailored to the specific needs of different regions and populations.
- Further investigate the land-atmospheric feedbacks during droughts and heatwaves and their impact on agricultural loss, forest destruction, and drinking water scarcity. This research should focus on the identification of combined events and the development of adaptation strategies to mitigate their impact.
- For further advancement, this study could consider investigating the interplay between heatwaves and the Urban Heat Island (UHI) phenomenon. This exploration would provide insights into the impacts of factors like albedo, construction materials, and localized heat pockets within urban areas that are increasingly susceptible to high temperatures. Integrating this UHI information into building models and urban planning frameworks, as they become accessible, could contribute to a more comprehensive understanding of heatwave dynamics in urban environments.

- Future research should prioritize the use of observation network data in the region, as they provide more accurate and reliable information for local-scale analysis of heatwaves and soil moisture.
- The computed UTCI from the Rayman model is very close to the ERA5-HEAT archives dataset (1.37 ± 0.21 °C). There is agreement between the datasets. This model could be used for thermal comfort indices in the region.

This work contributes to the development of an early warning system dedicated for each part of the region for the vulnerable population to be prepared and get ready with measures that are already applied for heatwaves periods.

7.5.2 Policy Actions

Existing policies on heatwaves need to be updated and effectively implemented to reduce their adverse impacts on the city populations. Studies have showed the non-availability of data on extreme heat and drought in the Emergency Events Database (EM-DAT) proving that heatwaves often go unnoticed or unreported. More attention is needed unto these events. Developing countries as in West Africa are peculiarly vulnerable to sustained high temperatures, due to the location, the urban design and poverty levels (including the elderly, children, and those with underlying health conditions, during heatwaves). Decisions on infrastructure investment in urban areas are central to managing chronic heat exposure and to avoiding it in the future.

Key recommendations for policy action based on the work results are to:

- Promote and implement the development of drought and heatwave early warning systems (EWS) to help communities prepare for and respond to drought or heatwave events. The EWS should include both short-term and

long-term measures to address the impacts of heatwaves on human health, including provisions for access to cooling centres, improved public awareness and education, and training for healthcare workers.

- Encourage the adoption of smart agriculture practices (mulching, heat-resistant crops, etc.) and water-saving technologies in industry and households to reduce water usage and minimize the impact of drought and heatwaves.
- Implement measures to reduce greenhouse gas emissions, such as transitioning to renewable energy sources, to slow down climate change, which contributes to increased frequency and intensity of heatwaves and droughts.
- Promote reforestation and afforestation initiatives: Encourage the planting of trees in urban and rural areas to increase vegetation coverage, reduce carbon emissions, and provide multiple ecosystem services such as soil conservation, water regulation, and wildlife habitat. Also encourage the use of native plant species in urban and rural areas for landscaping, erosion control, and reforestation efforts.
- Implement policies that promote sustainable land use practices, such as agroforestry, conservation agriculture, and the integration of trees in agricultural landscapes.
- Foster collaboration and engagement between different stakeholders, including government agencies, non-government organizations, academia, and the private sector (businesses), to ensure effective and sustainable vegetation management and address drought and heatwave issues.

- Develop and implement contingency plans to address the impacts of drought and heatwaves on human health, such as increasing access to clean drinking water and medical care.

The recommendations presented in this thesis provide valuable insights for policymakers and stakeholders (including government agencies, non-government organisations, academia, private sector etc.) to consider as they work towards addressing the challenges posed by drought and heatwaves in the region. Further research and action are needed to ensure the long-term sustainability of the region's ecosystems and communities.

7.6 Final Thoughts

This study has enriched our comprehension of the intricate interactions and underlying physical mechanisms that characterize the relationship between droughts and heatwaves, thereby offering quantitative insights into their potential impacts on human populations, the temperature tendencies mechanisms around heatwaves and the role of soil and atmospheric moisture during heatwaves in West Africa. The overarching aim is to furnish a more robust and sustainable strategy for land management, effectively mitigating the adverse consequences of these events. The findings of this research bear significant implications for multiple Sustainable Development Goals (SDGs), including but not limited to Sustainable Cities and Communities (SDG 11), Climate Action (SDG 13), and Life on Land (SDG 15). Building upon these outcomes, future research endeavours can be directed towards forging a comprehensive heatwave early warning system tailored to the West African context. Such a system holds substantial promise for bolstering disaster-risk

management strategies when faced with the dual challenges of droughts and heatwaves. Moreover, the study's findings will furnish valuable insights for the formulation of tailored adaptation and mitigation tactics aimed at addressing urban heat, particularly within densely populated urban centres. By further enriching our understanding of the intricacies of the West African climate system, this research not only contributes to the scientific discourse but also extends its relevance to the corridors of policy-making and decision-shaping. The outcomes will be instrumental in quantifying the ramifications of drought-heatwave events across a spectrum of socioeconomic activities, human health, and overall security within the West African region. The ultimate aspiration remains steadfast — to curtail the adverse impacts of these occurrences and cultivate a more resilient and prepared society. As we progress, a continuous dialogue between research, policy, and practice will be imperative to ensure a sustainable and harmonious coexistence with the dynamic climate patterns of West Africa.

REFERENCES

- Agnew, C.T., Chappell, A., 1999. Drought in the Sahel 13.
- Ahmad, B., Ali, S., Khan, T., Hasson, S., Bukhari, S.A.A., 2021. Simulating the Urban Heat Island Augmented with a Heat Wave Episode Using ICTP RegCM4.7 in a Mega-Urban Structure of Karachi, Pakistan. *J. Soft Comput. Civ. Eng.* 5. <https://doi.org/10.22115/scce.2021.237606.1243>
- Ahmadalipour, A., 2017. Multi-Dimensional Drought Risk Assessment Based on Socio- Economic Vulnerabilities and Hydro-Climatological Factors (PhD Thesis).
- Ahmadalipour, A., Moradkhani, H., 2018. Escalating heat-stress mortality risk due to global warming in the Middle East and North Africa (MENA). *Environment International* 117, 215–225. <https://doi.org/10.1016/j.envint.2018.05.014>
- Aid, F., Stroke, H., Severe, I.S.A., Or, A., The, G.E.T., To, V., 1978. Preventing Heat-Related Illness Heat Index / Heat Disorders Heat Index Chart NOAA ' s National Weather Service Heat Index Program How Heat Affects the Body Summary of NWS ' s Alert Procedures.
- Akinbobola, A., Njoku, C.A., Balogun, I.A., 2017. Basic Evaluation of Bioclimatic Conditions over Southwest Nigeria 11.
- Alexander, L.V., Zhang, X., Peterson, T.C., Caesar, J., Gleason, B., Klein Tank, A.M.G., Haylock, M., Collins, D., Trewin, B., Rahimzadeh, F., Tagipour, A., Rupa Kumar, K., Revadekar, J., Griffiths, G., Vincent, L., Stephenson, D.B., Burn, J., Aguilar, E., Brunet, M., Taylor, M., New, M., Zhai, P., Rusticucci, M., Vazquez-Aguirre, J.L., 2006. Global observed changes in daily climate extremes of temperature and precipitation. *Journal of Geophysical Research Atmospheres* 111, 1–22. <https://doi.org/10.1029/2005JD006290>
- Almazroui, M., Saeed, F., Saeed, S., Nazrul Islam, M., Ismail, M., Klutse, N.A.B., Siddiqui, M.H., 2020. Projected Change in Temperature and Precipitation Over Africa from CMIP6. *Earth Syst Environ.* <https://doi.org/10/gg38gt>
- Anjileli, H., Huning, L.S., Moftehari, H., Ashraf, S., Asanjan, A.A., Norouzi, H., AghaKouchak, A., 2021. Extreme heat events heighten soil respiration. *Sci Rep* 11, 6632. <https://doi.org/10.1038/s41598-021-85764-8>
- Anwar, S.A., Reboita, M.S., Llopart, M., 2022. On the sensitivity of the Amazon surface climate to two land-surface hydrology schemes using a high-resolution regional climate model (RegCM4). *International Journal of Climatology* 42, 2311–2327. <https://doi.org/10.1002/joc.7367>
- Aryee, J.N.A., Amekudzi, L.K., Preko, K., Atiah, W.A., Danuor, S.K., 2020. Estimation of planetary boundary layer height from radiosonde profiles over

West Africa during the AMMA field campaign: Intercomparison of different methods. *Scientific African* 7, e00228. <https://doi.org/10.1016/j.sciaf.2019.e00228>

- Babst, F., Carrer, M., Poulter, B., Urbinati, C., Neuwirth, B., Frank, D., 2012. 500 years of regional forest growth variability and links to climatic extreme events in Europe. *Environ. Res. Lett.* 7, 045705. <https://doi.org/10/gf2pkz>
- Ballester, J., Quijal-Zamorano, M., Méndez Turrubiates, R.F., Pegenaute, F., Herrmann, F.R., Robine, J.M., Basagaña, X., Tonne, C., Antó, J.M., Achebak, H., 2023. Heat-related mortality in Europe during the summer of 2022. *Nat Med* 29, 1857–1866. <https://doi.org/10.1038/s41591-023-02419-z>
- Balogun, I.A., Ntekop, A.A., Daramola, M.T., 2019. Assessment of the bioclimatic conditions over some selected stations in Nigeria. *SN Appl. Sci.* 1, 610. <https://doi.org/10.1007/s42452-019-0589-y>
- Bamba, A., Dieppois, B., Konaré, A., Pellarin, T., Balogun, A., Dessay, N., Kamagaté, B., Savané, I., Diédhiou, A., 2015. Changes in Vegetation and Rainfall over West Africa during the Last Three Decades (1981-2010). *Atmospheric and Climate Sciences* 05, 367. <https://doi.org/10.4236/acs.2015.54028>
- Barbier, J., Guichard, F., Bouniol, D., Couvreur, F., Roehrig, R., 2018. Detection of Intraseasonal Large-Scale Heat Waves: Characteristics and Historical Trends during the Sahelian Spring. *Journal of Climate* 31, 61–80. <https://doi.org/10/gdfd55>
- Barbosa, S., Scotto, M.G., 2022. Extreme heat events in the Iberia Peninsula from extreme value mixture modeling of ERA5-Land air temperature. *Weather and Climate Extremes* 36, 100448. <https://doi.org/10.1016/j.wace.2022.100448>
- Bastos, A., Ciais, P., Friedlingstein, P., Sitch, S., Pongratz, J., Fan, L., Wigneron, J.P., Weber, U., Reichstein, M., Fu, Z., Anthoni, P., Arneeth, A., Haverd, V., Jain, A.K., Joetzjer, E., Knauer, J., Lienert, S., Loughran, T., McGuire, P.C., Tian, H., Viovy, N., Zaehle, S., 2020. Direct and seasonal legacy effects of the 2018 heat wave and drought on European ecosystem productivity. *Sci. Adv.* 6, eaba2724. <https://doi.org/10/gg34d2>
- Bauer, P., Sandu, I., Magnusson, L., Mladek, R., Fuentes, M., 2020. ECMWF global coupled atmosphere, ocean and sea-ice dataset for the Year of Polar Prediction 2017–2020. *Sci Data* 7, 427. <https://doi.org/10.1038/s41597-020-00765-y>
- Baup, F., Mougín, E., de Rosnay, P., Timouk, F., Chênerie, I., 2007. Surface soil moisture estimation over the AMMA Sahelian site in Mali using ENVISAT/ASAR data. *Remote Sensing of Environment* 109, 473–481. <https://doi.org/10.1016/j.rse.2007.01.015>

- Becker, F.N., Fink, A.H., Bissolli, P., Pinto, J.G., 2022. Towards a more comprehensive assessment of the intensity of historical European Heat Waves (1979-2019) 15.
- Beguiría, S., Vicente-Serrano, S.M., Reig, F., Latorre, B., 2014. Standardized precipitation evapotranspiration index (SPEI) revisited: parameter fitting, evapotranspiration models, tools, datasets and drought monitoring. *International Journal of Climatology* 34, 3001–3023. <https://doi.org/10.1002/joc.3887>
- Black, E., Blackburn, M., Harrison, G., Hoskins, B., Methven, J., 2004. Factors contributing to the summer 2003 European heatwave. *wea* 59, 217–223. <https://doi.org/10.1256/wea.74.04>
- Blazejczyk, K., Epstein, Y., Jendritzky, G., Staiger, H., Tinz, B., 2012. Comparison of UTCI to selected thermal indices. *Int J Biometeorol* 56, 515–535. <https://doi.org/10/cssh8t>
- Błażejczyk, K., Jendritzky, G., Bröde, P., Fiala, D., Havenith, G., Epstein, Y., Psikuta, A., Kampmann, B., 2013. An introduction to the Universal Thermal Climate Index (UTCI). *Geogr. Pol.* 86, 5–10. <https://doi.org/10/ghpbz4>
- Bobadoye, A., 2018. Assessing vulnerability to Climate Change and the impact of drought on vegetation productivity in West Africa. <https://doi.org/10.13140/RG.2.2.21932.92800>
- Bonan, G.B., Lawrence, P.J., Oleson, K.W., Levis, S., Jung, M., Reichstein, M., Lawrence, D.M., Swenson, S.C., 2011. Improving canopy processes in the Community Land Model version 4 (CLM4) using global flux fields empirically inferred from FLUXNET data. *J. Geophys. Res.* 116, G02014. <https://doi.org/10.1029/2010JG001593>
- Bonan, G.B., Oleson, K.W., Fisher, R.A., Lasslop, G., Reichstein, M., 2012. Reconciling leaf physiological traits and canopy flux data: Use of the TRY and FLUXNET databases in the Community Land Model version 4: COMMUNITY LAND MODEL CANOPY SCALING. *J. Geophys. Res.* 117, n/a-n/a. <https://doi.org/10.1029/2011JG001913>
- Boone, A., De Rosnay, P., Balsamo, G., Beljaars, A., Chopin, F., Decharme, B., Delire, C., Ducharne, A., Gascoin, S., Grippa, M., Guichard, F., Gusev, Y., Harris, P., Jarlan, L., Kergoat, L., Mougin, E., Nasonova, O., Norgaard, A., Orgeval, T., Ottlé, C., Poccard-Leclercq, I., Polcher, J., Sandholt, I., Saux-Picart, S., Taylor, C., Xue, Y., 2009. The AMMA land surface model intercomparison project (ALMIP). *Bulletin of the American Meteorological Society* 90, 1865–1880. <https://doi.org/10.1175/2009BAMS2786.1>
- Bröde, P., Fiala, D., Błażejczyk, K., Holmér, I., Jendritzky, G., Kampmann, B., Tinz, B., Havenith, G., 2012. Deriving the operational procedure for the Universal

- Thermal Climate Index (UTCI). *International journal of biometeorology* 56, 481–494. <https://doi.org/10/bv7qwf>
- Bröde, P., Jendritzky, G., Fiala, D., Havenith, G., 2010. The Universal Thermal Climate Index UTCI in Operational Use, in: *Adapting to Change: New Thinking on Comfort*. Presented at the Network for Comfort and Energy Use in Buildings, Cumberland Lodge, Windsor, UK, p. 6.
- Brubaker, K.L., Entekhabi, D., 1996. Analysis of Feedback Mechanisms in Land-Atmosphere Interaction. *Water Resour. Res.* 32, 1343–1357. <https://doi.org/10/c68h66>
- Budd, G.M., 2008. Wet-bulb globe temperature (WBGT)—its history and its limitations. *Journal of Science and Medicine in Sport* 11, 20–32. <https://doi.org/10/ct4qqp>
- Cabin, R.J., Mitchell, R.J., 2000. To Bonferroni or not to Bonferroni: when and how are the questions. *Bulletin of the ecological society of America* 81, 246–248.
- Cameron, D.A., 2001. The extent of soil desiccation near trees in a semi-arid environment, in: Toll, D.G. (Ed.), *Unsaturated Soil Concepts and Their Application in Geotechnical Practice*. Springer Netherlands, Dordrecht, pp. 357–370. https://doi.org/10.1007/978-94-015-9775-3_7
- Cattiaux, J., Chauvin, F., Douville, H., Ribes, A., 2020. Weather Extremes and Climate Change, *Encyclopedia of the Environment*. Encyclopédie de l'environnement.
- CDKN Global, 2022. Fact Sheet - West Africa The IPCC'S Sixth Assessment Report: Impacts, adaptation options and investment areas for a climate-resilient West Africa (Guides and working papers).
- Ceccherini, Guido, Russo, S., Amezttoy, I., Francesco Marchese, A., Carmona-Moreno, C., 2017. Heat waves in Africa 1981-2015, observations and reanalysis. *Natural Hazards and Earth System Sciences* 17, 115–125. <https://doi.org/10.5194/nhess-17-115-2017>
- Ceccherini, G., Russo, S., Amezttoy, I., Marchese, A.F., Carmona-Moreno, C., 2017. Heat waves in Africa 1981-2015, observations and reanalysis. *Natural Hazards and Earth System Sciences Discussions* 1–17. <https://doi.org/10.5194/nhess-2016-90>
- Ceccherini, G., Russo, S., Amezttoy, I., Patricia, C.R., Carmona-Moreno, C., 2016. Magnitude and frequency of heat and cold waves in recent decades: the case of South America. *Natural Hazards and Earth System Sciences* 16, 821–831. <https://doi.org/10.5194/nhess-16-821-2016>
- Ceccherini, G., Russo, S., Amezttoy, I., Romero, C.P., Carmona-Moreno, C., 2015. Magnitude and frequency of heat and cold waves in recent decades: the case

of South America. *Natural Hazards and Earth System Sciences Discussions* 3, 7379–7409. <https://doi.org/10.5194/nhessd-3-7379-2015>

Charney, J.G., 1975. Dynamics of deserts and drought in the Sahel. *Q.J Royal Met. Soc.* 101, 193–202. <https://doi.org/10/fncdh9>

Cheng, J., Xu, Z., Bambrick, H., Prescott, V., Wang, N., Zhang, Y., Su, H., Tong, S., Hu, W., 2019. Cardiorespiratory effects of heatwaves: A systematic review and meta-analysis of global epidemiological evidence. *Environmental Research* 177, 108610. <https://doi.org/10.1016/j.envres.2019.108610>

Ciais, P., Reichstein, M., Viovy, N., Granier, A., Ogee, J., Allard, V., Aubinet, M., Buchmann, N., Bernhofer, C., Carrara, A., Chevallier, F., De Noblet, N., Friend, A.D., Friedlingstein, P., Grünwald, T., Heinesch, B., Keronen, P., Knohl, A., Krinner, G., Loustau, D., Manca, G., Matteucci, G., Miglietta, F., Ourcival, J.M., Papale, D., Pilegaard, K., Rambal, S., Seufert, G., Soussana, J.F., Sanz, M.J., Schulze, E.D., Vesala, T., Valentini, R., 2005. Europe-wide reduction in primary productivity caused by the heat and drought in 2003. *Nature* 437, 529–533. <https://doi.org/10.1038/nature03972>

Couvreux, F., Guichard, F., Gounou, A., Bouniol, D., Peyrillé, P., Köhler, M., 2014. Modelling of the Thermodynamical Diurnal Cycle in the Lower Atmosphere: A Joint Evaluation of Four Contrasted Regimes in the Tropics Over Land. *Boundary-Layer Meteorol* 150, 185–214. <https://doi.org/10/f5qf29>

Dai, Y., Zeng, X., Dickinson, R.E., Baker, I., Bonan, G.B., Bosilovich, M.G., Denning, A.S., Dirmeyer, P.A., Houser, P.R., Niu, G., 2003. The common land model. *Bulletin of the American Meteorological Society* 84, 1013–1024.

Danso, D.K., Anquetin, S., Diedhiou, A., Lavaysse, C., Koba, A., Touré, N.E., 2019. Spatio-temporal variability of cloud cover types in West Africa with satellite-based and reanalysis data. *Quarterly Journal of the Royal Meteorological Society* 145, 3715–3731. <https://doi.org/10.1002/qj.3651>

Danuor, S., Gaye, A., Yacouba, H., Mariko, A., Bouzou, M.I., Maiga, M., Da, D., Ginoux, K., Parker, D.J., Polcher, J., Laval, K., Diallo, D., Bourles, B., 2011. Education in meteorology and climate sciences in West Africa. *Atmospheric Science Letters* 12, 155–159. <https://doi.org/10.1002/asl.326>

de Freitas, C.R., 1994. THEORIES ON PROGRESSIVE DESICCATION AND DESERTIFICATION: REASSESSING THE DROUGHT HAZARD. *Weather and Climate* 14, 11–21. <https://doi.org/10/gg7fkr>

Dee, D.P., Uppala, S.M., Simmons, A.J., Berrisford, P., Poli, P., Kobayashi, S., Andrae, U., Balmaseda, M.A., Balsamo, G., Bauer, P., Bechtold, P., Beljaars, A.C.M., van de Berg, L., Bidlot, J., Bormann, N., Delsol, C., Dragani, R., Fuentes, M., Geer, A.J., Haimberger, L., Healy, S.B., Hersbach, H., Hólm, E.V., Isaksen, I., Kållberg, P., Köhler, M., Matricardi, M., McNally, A.P., Monge-Sanz, B.M., Morcrette, J.-J., Park, B.-K., Peubey, C., de Rosnay, P.,

- Tavolato, C., Thépaut, J.-N., Vitart, F., 2011. The ERA-Interim reanalysis: configuration and performance of the data assimilation system. *Q.J.R. Meteorol. Soc.* 137, 553–597. <https://doi.org/10/cz2w58>
- Deme, A., Gaye, A.T., Hourdin, F., 2020. Climate projections in West Africa: the obvious and the uncertain, in: Lalou, R., Oumarou, A., Sanni, M.A., Sultan, B., Arame Soumaré, M. (Eds.), *Rural Societies in the Face of Climatic and Environmental Changes in West Africa, Synthèses*. IRD Éditions, Marseille, pp. 61–86.
- Demuzere, M., Harshan, S., Järvi, L., Roth, M., Grimmond, C.S.B., Masson, V., Oleson, K.W., Velasco, E., Wouters, H., 2017. Impact of urban canopy models and external parameters on the modelled urban energy balance in a tropical city. *Quarterly Journal of the Royal Meteorological Society* 143, 1581–1596. <https://doi.org/10/gbh5z>
- Deng, X., Zhan, J., Su, H., 2014. Land Use Impacts on Climate. <https://doi.org/10.1007/978-3-642-54876-5>
- Di Napoli, C., Barnard, C., Prudhomme, C., Cloke, H.L., Pappenberger, F., 2020. ERA5-HEAT: A global gridded historical dataset of human thermal comfort indices from climate reanalysis. *Geoscience Data Journal* n/a. <https://doi.org/10.1002/gdj3.102>
- Di Napoli, C., Pappenberger, F., Cloke, H.L., 2018. Assessing heat-related health risk in Europe via the Universal Thermal Climate Index (UTCI). *Int J Biometeorol* 62, 1155–1165. <https://doi.org/10.1007/s00484-018-1518-2>
- Diba, I., Camara, M., Diedhiou, A., 2019. Investigating West African Monsoon features in warm years using the Regional Climate Model RegCM4. *Atmosphere* 10. <https://doi.org/10.3390/atmos10010023>
- Dickinson, E., Henderson-Sellers, A., Kennedy, J., 1993. Biosphere-atmosphere Transfer Scheme (BATS) Version 1e as Coupled to the NCAR Community Climate Model. <https://doi.org/10.5065/D67W6959>
- Dickinson, R.E., 1995. Land-atmosphere interaction 6. <https://doi.org/10/d86xv2>
- Dirmeyer, P.A., Balsamo, G., Blyth, E., Morrison, R., Cooper, H., 2020. Land-Atmosphere Interactions Exacerbated the Drought and Heatwave over Northern Europe during Summer 2018 [WWW Document]. *Earth and Space Science Open Archive*. <https://doi.org/10.1002/essoar.10503148.1>; <http://web.archive.org/web/20200709003223/https://www.essoar.org/action/cookieAbsent>
- Doughty, C.E., Metcalfe, D.B., Girardin, C.A.J., Amézquita, F.F., Cabrera, D.G., Huasco, W.H., Silva-Espejo, J.E., Araujo-Murakami, A., da Costa, M.C., Rocha, W., Feldpausch, T.R., Mendoza, A.L.M., da Costa, A.C.L., Meir, P.,

- Phillips, O.L., Malhi, Y., 2015. Drought impact on forest carbon dynamics and fluxes in Amazonia. *Nature* 519, 78–82. <https://doi.org/10/f3nn75>
- Dousset, B., Gourmelon, F., 2003. Satellite multi-sensor data analysis of urban surface temperatures and landcover. *ISPRS journal of photogrammetry and remote sensing* 58, 43–54.
- Droogers, P., Allen, R., 2002. Estimating Reference Evapotranspiration Under Inaccurate Data Conditions. *Irrigation and Drainage Systems* 16, 33–45. <https://doi.org/10.1023/A:1015508322413>
- Easterling, D.R., 2000. Climate Extremes: Observations, Modeling, and Impacts. *Science* 289, 2068–2074. <https://doi.org/10.1126/science.289.5487.2068>
- Elguindi, N., Bi, X., Giorgi, F., Nagarajan, B., Pal, J., Solmon, F., Rauscher, S., Zakey, A., O'Brien, T., Nogherotto, R., 2014. Regional climate model RegCM: reference manual version 4.5. Abdus Salam ICTP, Trieste 33.
- Eltahir, E.A.B., 1998. A Soil Moisture–Rainfall Feedback Mechanism: 1. Theory and observations. *Water Resources Research* 34, 765–776. <https://doi.org/10/crhw25>
- Emanuel, K.A., 1991. A Scheme for Representing Cumulus Convection in Large-Scale Models. *Journal of the Atmospheric Sciences* 48, 2313–2329. [https://doi.org/10.1175/1520-0469\(1991\)048<2313:ASFRCC>2.0.CO;2](https://doi.org/10.1175/1520-0469(1991)048<2313:ASFRCC>2.0.CO;2)
- Engdaw, M.M., Ballinger, A.P., Hegerl, G.C., Steiner, A.K., 2022. Changes in temperature and heat waves over Africa using observational and reanalysis data sets. *International Journal of Climatology* 42, 1165–1180. <https://doi.org/10.1002/joc.7295>
- Environmental Audit Committee, 2018. Heatwaves: adapting to climate change Ninth Report of Session 2017-19 Report. the House of Commons 1–51.
- Feller, U., Vaseva, I.I., 2014. Extreme climatic events: Impacts of drought and high temperature on physiological processes in agronomically important plants. *Frontiers in Environmental Science* 2, 1–17. <https://doi.org/10/gg3rwq>
- Felsche, E., Böhnisch, A., Ludwig, R., 2023. Inter-seasonal connection of typical European heatwave patterns to soil moisture. *npj Clim Atmos Sci* 6, 1–11. <https://doi.org/10.1038/s41612-023-00330-5>
- Ferguson, C.R., Wood, E.F., 2011. Observed land–atmosphere coupling from satellite remote sensing and reanalysis. *Journal of Hydrometeorology* 12, 1221–1254. <https://doi.org/10/bv2hwp>
- Fink, A.H., Agustí-Panareda, A., Parker, D.J., Lafore, J.-P., Ngamini, J.-B., Afiesimama, E., Beljaars, A., Bock, O., Christoph, M., Didé, F., Faccani, C., Fourrié, N., Karbou, F., Polcher, J., Mumba, Z., Nuret, M., Pohle, S., Rabier,

- F., Tompkins, A.M., Wilson, G., 2011. Operational meteorology in West Africa: observational networks, weather analysis and forecasting. *Atmospheric Science Letters* 12, 135–141. <https://doi.org/10.1002/asl.324>
- Fink, A.H., Brücher, T., Krüger, A., Leckebusch, G.C., Pinto, J.G., Ulbrich, U., 2004. The 2003 European summer heatwaves and drought –synoptic diagnosis and impacts. *Weather* 59, 209–216. <https://doi.org/10.1256/wea.73.04>
- Fink, A.H., Engel, T., Ermert, V., Linden, R. van der, Schneidewind, M., Redl, R., Afiesimama, E., Thiaw, W.M., Yorke, C., Evans, M., Janicot, S., 2017. Mean Climate and Seasonal Cycle, in: *Meteorology of Tropical West Africa*. John Wiley & Sons, Ltd, pp. 1–39. <https://doi.org/10.1002/9781118391297.ch1>; <http://web.archive.org/web/20200806191835/https://onlinelibrary.wiley.com/doi/abs/10.1002/9781118391297.ch1>; <http://web.archive.org/web/20200806191841/https://onlinelibrary.wiley.com/doi/abs/10.1002/9781118391297.ch1>
- Fischer, E.M., Oleson, K.W., Lawrence, D.M., 2012. Contrasting urban and rural heat stress responses to climate change: HEAT STRESS RESPONSE TO CLIMATE CHANGE. *Geophysical Research Letters* 39, n/a-n/a. <https://doi.org/10/fxvz3g>
- Fischer, E.M., Seneviratne, S.I., Vidale, P.L., Lüthi, D., Schär, C., 2007. Soil moisture-atmosphere interactions during the 2003 European summer heat wave. *Journal of Climate* 20, 5081–5099. <https://doi.org/10.1175/JCLI4288.1>
- Fischer, K., Klockmann, M., Reim, E., 2014. Strong negative effects of simulated heat waves in a tropical butterfly. *Journal of Experimental Biology* 217, 2892–2898. <https://doi.org/10.1242/jeb.106245>
- Flaounas, E., Kelemen, F.D., Wernli, H., Gaertner, M.A., Reale, M., Sanchez-Gomez, E., Lionello, P., Calmanti, S., Podrascanin, Z., Somot, S., Akhtar, N., Romera, R., Conte, D., 2018. Assessment of an ensemble of ocean–atmosphere coupled and uncoupled regional climate models to reproduce the climatology of Mediterranean cyclones. *Clim Dyn* 51, 1023–1040. <https://doi.org/10.1007/s00382-016-3398-7>
- Flato, G., Marotzke, J., Abiodun, B., Braconnot, P., Chou, S.C., Collins, W., Cox, P., Driouech, F., Emori, S., Eyring, V., 2014. Evaluation of climate models, in: *Climate Change 2013: The Physical Science Basis. Contribution of Working Group I to the Fifth Assessment Report of the Intergovernmental Panel on Climate Change*. Cambridge University Press, pp. 741–866.
- Fontaine, B., Janicot, S., Monerie, P.-A., 2013. Recent changes in air temperature, heat waves occurrences, and atmospheric circulation in Northern Africa: HEAT WAVES AND ATMOSPHERIC CIRCULATION. *J. Geophys. Res. Atmos.* 118, 8536–8552. <https://doi.org/10/ggwczs>

- Founda, D., Santamouris, M., 2017. Synergies between Urban Heat Island and Heat Waves in Athens (Greece), during an extremely hot summer (2012). *Sci Rep* 7, 10973. <https://doi.org/10/gddhfg>
- Frich, P., Alexander, L.V., Della-Marta, P., Gleason, B., Haylock, M., Tank Klein, A.M.G., Peterson, T., 2002. Observed coherent changes in climatic extremes during the second half of the twentieth century. *Climate Research* 19, 193–212. <https://doi.org/10.3354/cr019193>
- Fu, C., Freney, J.R., Stewart, J.W.B., 2008. Changes in the Human-monsoon System of East Asia in the Context of Global Change. <https://doi.org/10.1142/6924>
- Funk, C., Peterson, P., Landsfeld, M., Pedreros, D., Verdin, J., Shukla, S., Husak, G., Rowland, J., Harrison, L., Hoell, A., Michaelsen, J., 2015. The climate hazards infrared precipitation with stations—a new environmental record for monitoring extremes. *Sci Data* 2, 150066. <https://doi.org/10.1038/sdata.2015.66>
- Gabriel, K.M.A., Endlicher, W.R., 2011. Urban and rural mortality rates during heat waves in Berlin and Brandenburg, Germany. *Environmental Pollution* 159, 2044–2050. <https://doi.org/10.1016/j.envpol.2011.01.016>
- Gao, X., Shi, Y., Song, R., Giorgi, F., Wang, Y., Zhang, D., 2008. Reduction of future monsoon precipitation over China: comparison between a high resolution RCM simulation and the driving GCM. *Meteorol Atmos Phys* 100, 73–86. <https://doi.org/10.1007/s00703-008-0296-5>
- Garcia-Herrera, R., Díaz, J., Trigo, R.M., Luterbacher, J., Fischer, E.M., 2010. A review of the european summer heat wave of 2003. *Critical Reviews in Environmental Science and Technology* 40, 267–306. <https://doi.org/10/csmhdk>
- Geirinhas, J.L., Russo, A., Libonati, R., Sousa, P.M., Miralles, D.G., Trigo, R.M., 2021. Recent increasing frequency of compound summer drought and heatwaves in Southeast Brazil. *Environ. Res. Lett.* 16, 034036. <https://doi.org/10.1088/1748-9326/abe0eb>
- Geirinhas, J.L., Trigo, R.M., Libonati, R., Castro, L.C.O., Sousa, P.M., Coelho, C.A.S., Peres, L.F., Magalhães, M. de A.F.M., 2019. Characterizing the atmospheric conditions during the 2010 heatwave in Rio de Janeiro marked by excessive mortality rates. *Science of The Total Environment* 650, 796–808. <https://doi.org/10/gg4jdz>
- Giorgi, F., Marinucci, M.R., Bates, G.T., 1993a. Development of a second-generation regional climate model (RegCM2). Part I: Boundary-layer and radiative transfer processes. *Monthly Weather Review* 121, 2794–2813.
- Giorgi, F., Marinucci, M.R., Bates, G.T., De Canio, G., 1993b. Development of a second-generation regional climate model (RegCM2). Part II: Convective

- processes and assimilation of lateral boundary conditions. *Monthly Weather Review* 121, 2814–2832.
- Giorgi, F., Shields, C., 1999. Tests of precipitation parameterizations available in latest version of NCAR regional climate model (RegCM) over continental United States. *Journal of Geophysical Research: Atmospheres* 104, 6353–6375. <https://doi.org/10/bc6zgr>
- Giorgi, F., Solmon, F., Giuliani, G., 2016. Regional Climatic Model RegCM User's Guide Version 4.5 (No. May).
- Golbabaie, F., Rostami Aghdam Shendi, M., Monazzam, M.R., Hosseini, M., Yazdani avval, M., 2015. Investigation of heat stress based on WBGT index and its relationship with physiological parameters among outdoor workers of Shabestar city. *J Health Saf Work* 5, 85–94.
- GreenFacts, 2006. Scientific Facts on Climate Change and Global Warming [WWW Document]. URL http://www.greenfacts.org/en/studies/climate_change/1-2/2.htm (accessed 11.10.22).
- Guerreiro, S.B., Dawson, R.J., Kilsby, C., Lewis, E., Ford, A., 2018. Future heat-waves, droughts and floods in 571 European cities. *Environ. Res. Lett.* 13, 034009. <https://doi.org/10/gf659h>
- Guichard, F., Kergoat, L., Mougín, E., Timouk, F., Baup, F., Hiernaux, P., Lavenu, F., 2009. Surface thermodynamics and radiative budget in the Sahelian Gourma: Seasonal and diurnal cycles. *Journal of Hydrology* 375, 161–177. <https://doi.org/10/csdzkv>
- Guigma, K.H., 2021. Heat waves in the West African Sahel: nature, drivers and predictability (doctoral). University of Sussex.
- Guigma, K.H., Todd, M., Wang, Y., 2020. Characteristics and thermodynamics of Sahelian heatwaves analysed using various thermal indices. *Clim Dyn.* <https://doi.org/10.1007/s00382-020-05438-5>
- Haddow, G.D., Bullock, J.A., Coppola, D.P., 2017. Natural and Technological Hazards and Risk Assessment, in: *Introduction to Emergency Management*. Elsevier, pp. 33–77. <https://doi.org/10.1016/B978-0-12-803064-6.00002-0>; <http://web.archive.org/web/20200707100825/https://linkinghub.elsevier.com/retrieve/pii/B9780128030646000020>
- Hao, Z., Singh, V.P., Hao, F., 2018. Compound Extremes in Hydroclimatology: A Review. *Water* 10, 718. <https://doi.org/10/gd2rhk>
- Hargreaves, G.H., 1994. Defining and Using Reference Evapotranspiration. *Journal of Irrigation and Drainage Engineering* 120, 1132–1139. [https://doi.org/10.1061/\(ASCE\)0733-9437\(1994\)120:6\(1132\)](https://doi.org/10.1061/(ASCE)0733-9437(1994)120:6(1132))

- Harrington, L.J., Otto, F.E.L., 2020. Reconciling theory with the reality of African heatwaves. *Nat. Clim. Chang.* <https://doi.org/10/gg5txn>
- Henderson-Sellers, A., Dickinson, R.E., 1993. Atmospheric-land surface fluxes. *Modelling change in environmental systems.* John Wiley and Sons 387–405.
- Herold, N., Kala, J., Alexander, L.V., 2016. The influence of soil moisture deficits on Australian heatwaves. *Environ. Res. Lett.* 11, 064003. <https://doi.org/10/ghpb3g>
- Hersbach, H., Bell, B., Berrisford, P., Hirahara, S., Horányi, A., Muñoz-Sabater, J., Nicolas, J., Peubey, C., Radu, R., Schepers, D., Simmons, A., Soci, C., Abdalla, S., Abellan, X., Balsamo, G., Bechtold, P., Biavati, G., Bidlot, J., Bonavita, M., De Chiara, G., Dahlgren, P., Dee, D., Diamantakis, M., Dragani, R., Flemming, J., Forbes, R., Fuentes, M., Geer, A., Haimberger, L., Healy, S., Hogan, R.J., Hólm, E., Janisková, M., Keeley, S., Laloyaux, P., Lopez, P., Lupu, C., Radnoti, G., de Rosnay, P., Rozum, I., Vamborg, F., Villaume, S., Thépaut, J.-N., 2020. The ERA5 global reanalysis. *Quarterly Journal of the Royal Meteorological Society* 146, 1999–2049. <https://doi.org/10.1002/qj.3803>
- Hirschi, M., Seneviratne, S.I., Alexandrov, V., Boberg, F., Boroneant, C., Christensen, O.B., Formayer, H., Orłowsky, B., Stepanek, P., 2011. Observational evidence for soil-moisture impact on hot extremes in southeastern Europe. *Nature Geosci* 4, 17–21. <https://doi.org/10.1038/ngeo1032>
- Hobday, A.J., Oliver, E.C.J., Gupta, A.S., Benthuisen, J.A., Burrows, M.T., Donat, M.G., Holbrook, N.J., Moore, P.J., Thomsen, M.S., Wernberg, T., Smale, D.A., 2015. Categorizing and Naming Marine HeatWaves 34, 0–29. <https://doi.org/10.1007/s00376-014-4097-0>
- Holtslag, A.A.M., De Bruijn, E.I.F., Pan, H.L., 1990. A high resolution air mass transformation model for short-range weather forecasting. *Monthly Weather Review* 118, 1561–1575.
- Honnert, R., 2019. Grey-Zone Turbulence in the Neutral Atmospheric Boundary Layer. *Boundary-Layer Meteorol* 170, 191–204. <https://doi.org/10.1007/s10546-018-0394-y>
- Hourdin, F., Musat, I., Guichard, F., Ruti, P.M., Favot, F., Filiberti, M.A., Pham, M.A.İ., Grandpeix, J.Y., Polcher, J.A.N., Marquet, P., Boone, A., Lafore, J.P., Redelsperger, J.L., Dell’Aquila, A., Doval, T.L., Traore, A.K., Gallée, H., 2010. Amma-Model intercomparison project. *Bulletin of the American Meteorological Society* 91, 95–104. <https://doi.org/10.1175/2009BAMS2791.1>
- IFRC, 2022. IFRC and C40 Cities urge cities to prepare for more dangerous and deadly heat waves | IFRC [WWW Document]. URL

<https://www.ifrc.org/press-release/ifrc-and-c40-cities-urge-cities-prepare-more-dangerous-and-deadly-heat-waves> (accessed 12.17.22).

- IPCC, 2021a. Summary for Policymakers. In: *Climate Change 2021: The Physical Science Basis. Contribution of Working Group I to the Sixth Assessment Report of the Intergovernmental Panel on Climate Change*. IPCC, Switzerland.
- IPCC, 2021b. *Climate Change 2021: The Physical Science Basis. Contribution of Working Group I to the Sixth Assessment Report of the Intergovernmental Panel on Climate Change*. IPCC.
- IPCC, 2019. *Climate Change and Land An IPCC Special Report on climate change, desertification, land degradation, sustainable land management, food security, and greenhouse gas fluxes in terrestrial ecosystems (Special Report)*. WMO; UNEP.
- IPCC, 2018. *Global Warming of 1.5°C. An IPCC Special Report on the impacts of global warming of 1.5°C above pre-industrial levels and related global greenhouse gas emission pathways, in the context of strengthening the global response to the threat of climate change, sustainable development, and efforts to eradicate poverty*. IPCC.
- IPCC, 2012a. Glossary of terms. In: *Managing the Risks of Extreme Events and Disasters to Advance Climate Change Adaptation*.
- IPCC, 2012b. *Managing the risks of extreme events and disasters to advance climate change adaptation*. <https://doi.org/10.1596/978-0-8213-8845-7>
- IPCC, 2001. *Climate Change 2001: The Scientific Basis*. IPCC, Cambridge, United Kingdom and New York, NY, USA.
- Jackson, T.L., Feddema, J.J., Oleson, K.W., Bonan, G.B., Bauer, J.T., 2013. Parameterization of urban characteristics for global climate modeling, in: *Geography of Climate Change*. Routledge, pp. 141–158.
- Jakob, C., 1999. Cloud Cover in the ECMWF Reanalysis. *Journal of Climate* 12, 947–959. [https://doi.org/10.1175/1520-0442\(1999\)012<0947:CCITER>2.0.CO;2](https://doi.org/10.1175/1520-0442(1999)012<0947:CCITER>2.0.CO;2)
- Janicot, S., Thorncroft, C.D., Ali, A., Asencio, N., Berry, G., Bock, O., Bourles, B., Caniaux, G., Chauvin, F., Deme, A., Kergoat, L., Lafore, J.P., Lavaysse, C., Lebel, T., Marticorena, B., Mounier, F., Nedelec, P., Redelsperger, J.L., Ravegnani, F., Reeves, C.E., Roca, R., De Rosnay, P., Schlager, H., Sultan, B., Tomasini, M., Ulanovsky, A., 2008. Large-scale overview of the summer monsoon over West Africa during the AMMA field experiment in 2006. *Annales Geophysicae* 26, 2569–2595. <https://doi.org/10.5194/angeo-26-2569-2008>

- Jendritzky, G., de Dear, R., Havenith, G., 2012. UTCI—Why another thermal index? *Int J Biometeorol* 56, 421–428. <https://doi.org/10/fzmrn5>
- Jesus, E.T. de, Amorim, J. da S., Junqueira, R., Viola, M.R., Mello, C.R. de, 2020. Meteorological and hydrological drought from 1987 to 2017 in Doce River Basin, Southeastern Brazil. *RBRH* 25, e29. <https://doi.org/10/gg34fc>
- Jiang, Y., Cooley, D., Wehner, M.F., 2020. Principal Component Analysis for Extremes and Application to U.S. Precipitation. *Journal of Climate* 33, 6441–6451. <https://doi.org/10.1175/JCLI-D-19-0413.1>
- Jiménez, P.A., De Arellano, J.V.G., Gonzá Lez-Rouco, J.F., Navarro, J., Montá Vez, J.P., García-Bustamante, E., Dudhia, J., 2011. The effect of heat waves and drought on surface wind circulations in the Northeast of the Iberian Peninsula during the summer of 2003. *Journal of Climate* 24, 5416–5422. <https://doi.org/10.1175/2011JCLI4061.1>
- Jones, H., 2018. Heat and Drought.
- Kampmann, B., Bröde, P., Fiala, D., 2012. Physiological responses to temperature and humidity compared to the assessment by UTCI, WGBT and PHS. *Int J Biometeorol* 56, 505–513. <https://doi.org/10.1007/s00484-011-0410-0>
- Katavoutas, G., Founda, D., 2019. Response of Urban Heat Stress to Heat Waves in Athens (1960–2017). *Atmosphere* 10, 483. <https://doi.org/10/gg34k7>
- Kendall, M.G., 1970. Rank Correlation Methods, CHARLES GRIFFIN&COMPANY LIMITED. ed.
- Kendon, E.J., Stratton, R.A., Tucker, S., Marsham, J.H., Berthou, S., Rowell, D.P., Senior, C.A., 2019. Enhanced future changes in wet and dry extremes over Africa at convection-permitting scale. *Nat Commun* 10, 1–14. <https://doi.org/10.1038/s41467-019-09776-9>
- Kergoat, L., Grippa, M., Baille, A., Eymard, L., Lacaze, R., Mougin, E., Ottlé, C., Pellarin, T., Polcher, J., De Rosnay, P., Roujean, J.L., Sandholt, I., Taylor, C.M., Zin, I., Zribi, M., 2011. Remote sensing of the land surface during the African Monsoon Multidisciplinary Analysis (AMMA). *Atmospheric Science Letters* 12, 129–134. <https://doi.org/10.1002/asl.325>
- Kiehl, J.T., Hack, J.J., Bonan, G.B., Boville, B.A., Williamson, D.L., Rasch, P.J., 1998. The National Center for Atmospheric Research Community Climate Model: CCM3*. *J. Climate* 11, 1131–1149. [https://doi.org/10.1175/1520-0442\(1998\)011<1131:TNCFAR>2.0.CO;2](https://doi.org/10.1175/1520-0442(1998)011<1131:TNCFAR>2.0.CO;2)
- Kim, J.H., Castroverde, C.D.M., Huang, S., Li, C., Hilleary, R., Seroka, A., Sohrabi, R., Medina-Yerena, D., Huot, B., Wang, J., Nomura, K., Marr, S.K., Wildermuth, M.C., Chen, T., MacMicking, J.D., He, S.Y., 2022. Increasing

- the resilience of plant immunity to a warming climate. *Nature* 607, 339–344. <https://doi.org/10.1038/s41586-022-04902-y>
- Klein, C., 2016. Interactions of regional atmospheric and land surface processes with the West African monsoon system 173.
- Kniffka, A., Knippertz, P., Fink, A.H., 2019. The role of low-level clouds in the West African monsoon system. *Atmospheric Chemistry and Physics* 19. <https://doi.org/10.5194/acp-19-1623-2019>
- Knippertz, P., Fink, A.H., 2006. Synoptic and dynamic aspects of an extreme springtime Saharan dust outbreak. *Q. J. R. Meteorol. Soc.* 132, 1153–1177. <https://doi.org/10/d79mwt>
- Knippertz, P., Martin, J.E., 2005. Tropical plumes and extreme precipitation in subtropical and tropical West Africa. *Quarterly Journal of the Royal Meteorological Society* 131, 2337–2365. <https://doi.org/10/btqztb>
- Koné, B., Diedhiou, A., Diawara, A., Anquetin, S., Touré, N.E., Bamba, A., Koba, A.T., 2022. Influence of initial soil moisture in a regional climate model study over West Africa – Part 1: Impact on the climate mean. *Hydrol. Earth Syst. Sci.* 26, 711–730. <https://doi.org/10.5194/hess-26-711-2022>
- Koné, B., Diedhiou, A., Touré, N.E., Sylla, M.B., Giorgi, F., Anquetin, S., Bamba, A., Diawara, A., Koba, A.T., 2018. Sensitivity study of the regional climate model RegCM4 to different convective schemes over West Africa. *Earth Syst. Dynam.* 9, 1261–1278. <https://doi.org/10/gfnkr8>
- Kozubek, M., Krizan, P., Lastovicka, J., 2020. Homogeneity of the Temperature Data Series from ERA5 and MERRA2 and Temperature Trends. *Atmosphere* 11, 235. <https://doi.org/10.3390/atmos11030235>
- Kumar, D., Rai, P., Dimri, A.P., 2020. Investigating Indian summer monsoon in coupled regional land–atmosphere downscaling experiments using RegCM4. *Climate Dynamics* 1–22.
- Kusaka, H., Kondo, H., Kikegawa, Y., Kimura, F., 2001. A simple single-layer urban canopy model for atmospheric models: Comparison with multi-layer and slab models. *Boundary-layer meteorology* 101, 329–358.
- Lafore, J.P., Flamant, C., Giraud, V., Guichard, F., Knippertz, P., Mahfouf, J.F., Mascart, P., Williams, E.R., 2010. Introduction to the AMMA Special Issue on “Advances in understanding atmospheric processes over West Africa through the AMMA field campaign.” *Quarterly Journal of the Royal Meteorological Society* 136, 2–7. <https://doi.org/10.1002/qj.583>
- Lambin, E.F., Geist, H., 2006. *Land-Use and Land-Cover Change Local Processes and Global Impacts*.

- Lambin, E.F., Meyfroidt, P., 2011. Global land use change, economic globalization, and the looming land scarcity. *Proc Natl Acad Sci USA* 108, 3465–3472. <https://doi.org/10/cxqb7q>
- Langlois, N., Herbst, J., Mason, K., Nairn, J., Byard, R.W., 2013. Using the Excess Heat Factor (EHF) to predict the risk of heat related deaths. *Journal of Forensic and Legal Medicine* 20, 408–411. <https://doi.org/10.1016/j.jflm.2012.12.005>
- Largerone, Y., Guichard, F., Roehrig, R., Couvreur, F., Barbier, J., 2020. The April 2010 North African heatwave: when the water vapor greenhouse effect drives nighttime temperatures. *Clim Dyn* 54, 3879–3905. <https://doi.org/10/gg44xw>
- Lavigne, T., Liu, C., 2022. Validity of Global Fog-Day Trends Indicated by the Global Surface Summary of the Day (GSOD) Data Set. *JGR Atmospheres* 127. <https://doi.org/10.1029/2021JD035881>
- Lebel, T., Parker, D.J., Flamant, C., Bourlès, B., Marticorena, B., Mougin, E., Peugeot, C., Diedhiou, A., Haywood, J.M., Ngamini, J.B., Polcher, J., Redelsperger, J.L., Thorncroft, C.D., 2010. The AMMA field campaigns: Multiscale and multidisciplinary observations in the West African region. *Quarterly Journal of the Royal Meteorological Society* 136, 8–33. <https://doi.org/10.1002/qj.486>
- Lemke, B., Kjellstrom, T., 2012. Calculating workplace WBGT from meteorological data: a tool for climate change assessment. *Industrial Health* 50, 267–278.
- Leonard, M., Westra, S., Phatak, A., Lambert, M., van den Hurk, B., McInnes, K., Risbey, J., Schuster, S., Jakob, D., Stafford-Smith, M., 2014. A compound event framework for understanding extreme impacts. *Wiley Interdisciplinary Reviews: Climate Change* 5, 113–128. <https://doi.org/10/gg64nk>
- Lester, P.F., 2013. *Aviation Weather*. Jeppesen.
- Li, D., Bou-Zeid, E., 2013. Synergistic interactions between urban heat islands and heat waves: The impact in cities is larger than the sum of its parts. *Journal of Applied Meteorology and Climatology* 52, 2051–2064. <https://doi.org/10.1175/JAMC-D-13-02.1>
- Li, L., Qian, R., Wang, W., Kang, X., Ran, Q., Zheng, Z., Zhang, B., Xu, C., Che, R., Dong, J., Xu, Z., Cui, X., Hao, Y., Wang, Y., 2020. The intra- and inter-annual responses of soil respiration to climate extremes in a semiarid grassland. *Geoderma* 378, 114629. <https://doi.org/10/gg7hq2>
- Li, X., Wang, S., 2022. Recent Increase in the Occurrence of Snow Droughts Followed by Extreme Heatwaves in a Warmer World. *Geophysical Research Letters* 49, e2022GL099925. <https://doi.org/10.1029/2022GL099925>

- Liu, C., Yang, C., Yang, Q., Wang, J., 2021. Spatiotemporal drought analysis by the standardized precipitation index (SPI) and standardized precipitation evapotranspiration index (SPEI) in Sichuan Province, China. *Sci Rep* 11, 1280. <https://doi.org/10.1038/s41598-020-80527-3>
- Lorenz, R., Jaeger, E.B., Seneviratne, S.I., 2010. Persistence of heat waves and its link to soil moisture memory: PERSISTENCE OF HEAT WAVES. *Geophys. Res. Lett.* 37, n/a-n/a. <https://doi.org/10/dh7tpb>
- Lybbert, T.J., Carter, M.R., 2015. Bundling drought tolerance and index insurance to reduce rural household vulnerability to drought, in: *Sustainable Economic Development*. Elsevier, pp. 401–414.
- Lyngsie, G., Olsen, J.L., Awadzi, T.W., Fensholt, R., Breuning-Madsen, H., 2013. Influence of the inter tropical discontinuity on Harmattan dust deposition in Ghana. *Geochemistry, Geophysics, Geosystems* 14, 3425–3435. <https://doi.org/10/f5fm9z>
- Maharana, P., Kumar, D., Dimri, A.P., 2019. Assessment of coupled regional climate model (RegCM4.6–CLM4.5) for Indian summer monsoon. *Clim Dyn* 53, 6543–6558. <https://doi.org/10/gg4mfp>
- Mann, H.B., 1945. Nonparametric Tests Against Trend. *Econometrica* 13, 245. <https://doi.org/10.2307/1907187>
- Markewitz, D., Devine, S., Davidson, E.A., Brando, P., Nepstad, D.C., 2010. Soil moisture depletion under simulated drought in the Amazon: impacts on deep root uptake. *New Phytologist* 187, 592–607. <https://doi.org/10/fq7dht>
- Matsuura, K., Willmott, C.J., 2012. Terrestrial Precipitation: 1900-2010 Gridded Monthly Time Series [WWW Document]. URL http://climate.geog.udel.edu/~climate/html_pages/Global2011/Precip_revised_3.02/README.GlobalTsP2011.html (accessed 4.22.21).
- Matzarakis, A., Nastos, P.T., 2011. Human-biometeorological assessment of heat waves in Athens. *Theoretical and Applied Climatology* 105, 99–106. <https://doi.org/10.1007/s00704-010-0379-3>
- Matzarakis, A., Rutz, F., Mayer, H., 2010. Modelling radiation fluxes in simple and complex environments: basics of the RayMan model. *International journal of biometeorology* 54, 131–139.
- Matzarakis, A., Rutz, F., Mayer, H., 2007. Modelling radiation fluxes in simple and complex environments—application of the RayMan model. *International journal of biometeorology* 51, 323–334.
- Maurya, R.K.S., Sinha, P., Mohanty, M.R., Mohanty, U.C., 2017. Coupling of Community Land Model with RegCM4 for Indian Summer Monsoon Simulation. *Pure Appl. Geophys.* 174, 4251–4270. <https://doi.org/10/gck467>

- McGarigal, K., Cushman, S.A., Ene, E., 2012. Spatial pattern analysis program for categorical and continuous maps. Computer software program produced by the authors at the University of Massachusetts, Amherst. FRAGSTATS v4. See <http://www.umass.edu/landeco/research/fragstats/fragstats.html>.
- McKee, T.B., Doesken, N.J., Kleist, J., 1993. THE RELATIONSHIP OF DROUGHT FREQUENCY AND DURATION TO TIME SCALES. p. 6.
- Meehl, G.A., Tebaldi, C., 2004. More intense, more frequent, and longer lasting heat waves in the 21st century. *Science* 305, 994–997.
- Miralles, D.G., Gentile, P., Seneviratne, S.I., Teuling, A.J., 2019. Land–atmospheric feedbacks during droughts and heatwaves: state of the science and current challenges. *Annals of the New York Academy of Sciences* 1436, 19–35. <https://doi.org/10.1111/nyas.13912>
- Miralles, D.G., Teuling, A.J., van Heerwaarden, C.C., Vilà-Guerau de Arellano, J., 2014. Mega-heatwave temperatures due to combined soil desiccation and atmospheric heat accumulation. *Nature Geosci* 7, 345–349. <https://doi.org/10/gc3fn5>
- Miralles, D.G., Van Den Berg, M.J., Teuling, A.J., De Jeu, R.A.M., 2012. Soil moisture-temperature coupling: A multiscale observational analysis. *Geophysical Research Letters* 39, 2–7. <https://doi.org/10.1029/2012GL053703>
- Mishra, A.K., Singh, V.P., 2010. A review of drought concepts. *Journal of Hydrology* 391, 202–216. <https://doi.org/10.1016/j.jhydrol.2010.07.012>
- Molina, M.O., Gutiérrez, C., Sánchez, E., 2021. Comparison of ERA5 surface wind speed climatologies over Europe with observations from the HadISD dataset. *International Journal of Climatology* 41, 4864–4878. <https://doi.org/10.1002/joc.7103>
- Morel, R., 1995. La sécheresse en Afrique de l’Ouest / The drought in West Africa. *geoca* 70, 215–222. <https://doi.org/10/bqqr7f>
- Moron, V., Oueslati, B., Pohl, B., Rome, S., Janicot, S., 2016. Trends of mean temperatures and warm extremes in northern tropical Africa (1961-2014) from observed and PPCA-reconstructed time series: TEMPERATURES IN NORTH TROPICAL AFRICA. *J. Geophys. Res. Atmos.* 121, 5298–5319. <https://doi.org/10/gg44xx>
- Mueller, B., Seneviratne, S.I., 2012. Hot days induced by precipitation deficits at the global scale. *Proc. Natl. Acad. Sci. U.S.A.* 109, 12398–12403. <https://doi.org/10.1073/pnas.1204330109>

- Mukherjee, S., Mishra, A.K., 2021. Increase in Compound Drought and Heatwaves in a Warming World. *Geophys. Res. Lett.* 48. <https://doi.org/10.1029/2020GL090617>
- Muñoz-Sabater, J., Dutra, E., Agustí-Panareda, A., Albergel, C., Arduini, G., Balsamo, G., Boussetta, S., Choulga, M., Harrigan, S., Hersbach, H., Martens, B., Miralles, D.G., Piles, M., Rodríguez-Fernández, N.J., Zsoter, E., Buontempo, C., Thépaut, J.-N., 2021. ERA5-Land: a state-of-the-art global reanalysis dataset for land applications. *Earth System Science Data* 13, 4349–4383. <https://doi.org/10.5194/essd-13-4349-2021>
- Ngoungue Langué, C.G., Lavaysse, C., Vrac, M., Flamant, C., 2022. Heat waves monitoring over West African cities: uncertainties, characterization and recent trends (preprint). *Atmospheric, Meteorological and Climatological Hazards*. <https://doi.org/10.5194/nhess-2022-192>
- Nicholson, S., 2000a. Land surface processes and Sahel climate. *Reviews of Geophysics* 38, 117–139. <https://doi.org/10/fcsmbg>
- Nicholson, S., 2000b. Land surface processes and Sahel climate. *Reviews of Geophysics* 38, 117–139. <https://doi.org/10/fcsmbg>
- Nicholson, S.E., 2018. Climate of the Sahel and West Africa, in: *Oxford Research Encyclopedia of Climate Science*. Oxford University Press. <https://doi.org/10.1093/acrefore/9780190228620.013.510>
- Njoku, C.A., Orisakwe, I., Ojeh, V.N., 2021. Mid-afternoon Outdoor Biometeorological Conditions in a Hot-humid Climate of Minna in Nigeria, West Africa during the Year 2012. *JGEESI* 52–62. <https://doi.org/10.9734/jgeesi/2021/v25i230271>
- Odoulami, R.C., Abiodun, B.J., Ajayi, A.E., Diasso, U.J., Mounkaila Saley, M., 2017. Potential impacts of forestation on heatwaves over West Africa in the future. *Ecological Engineering* 102, 546–556. <https://doi.org/10.1016/j.ecoleng.2017.02.054>
- Offerle, B., Jonsson, P., Eliasson, I., Grimmond, C.S.B., 2005. Urban Modification of the Surface Energy Balance in the West African Sahel: Ouagadougou, Burkina Faso. *Journal of Climate* 18, 3983–3995. <https://doi.org/10/cqsqx2>
- Oke, T.R., 1987. *Boundary layer climates*.
- Oleson, K.W., Lawrence, D.M., Bonan, G.B., Drewniak, B., Huang, M., Levis, S., Li, F., Riley, W.J., Swenson, S.C., Thornton, P.E., Bozbiyik, A., Fisher, R., Heald, C.L., Kluzek, E., Lamarque, F., Lawrence, P.J., Leung, L.R., Muszala, S., Ricciuto, D.M., Sacks, W., Sun, Y., Tang, J., Yang, Z.-L., 2013. Technical Description of version 4.5 of the Community Land Model (CLM) 434.

- Oleson, K.W., Niu, G.-Y., Yang, Z.-L., Lawrence, D.M., Thornton, P.E., Lawrence, P.J., Stöckli, R., Dickinson, R.E., Bonan, G.B., Levis, S., Dai, A., Qian, T., 2008. Improvements to the Community Land Model and their impact on the hydrological cycle. *Journal of Geophysical Research: Biogeosciences* 113. <https://doi.org/10.1029/2007JG000563>
- Oueslati, B., Pohl, B., Moron, V., Rome, S., Janicot, S., 2017. Characterization of Heat Waves in the Sahel and Associated Physical Mechanisms. *J. Climate* 30, 3095–3115. <https://doi.org/10/f97x8g>
- Pal, J.S., Small, E.E., Eltahir, E.A.B., 2000. Simulation of regional-scale water and energy budgets: Representation of subgrid cloud and precipitation processes within RegCM. *Journal of Geophysical Research: Atmospheres* 105, 29579–29594. <https://doi.org/10/b2jgm2>
- Pante, G., Knippertz, P., Fink, A.H., Kniffka, A., 2021. The potential of increasing man-made air pollution to reduce rainfall over southern West Africa. *Atmos. Chem. Phys.* 21, 35–55. <https://doi.org/10/ghstzm>
- Panthou, G., Mailhot, A., Laurence, E., Talbot, G., 2014. Relationship between surface temperature and extreme rainfalls: A multi-time-scale and event-based analysis. *Journal of hydrometeorology* 15, 1999–2011.
- Parker, D.J., Burton, R.R., Diongue-Niang, A., Ellis, R.J., Felton, M., Taylor, C.M., Thorncroft, C.D., Bessemoulin, P., Tompkins, A.M., 2005. The diurnal cycle of the West African monsoon circulation. *Quarterly Journal of the Royal Meteorological Society* 131, 2839–2860. <https://doi.org/10/cxkd96>
- Partey, S.T., Zougmore, R.B., Ramasamy, J., 2021. DROUGHT IN WEST AFRICA.
- Patil, I., 2021. Visualizations with statistical details: The “ggstatsplot” approach. *JOSS* 6, 3167. <https://doi.org/10.21105/joss.03167>
- Pei, Z., Fang, S., Wang, L., Yang, W., 2020. Comparative Analysis of Drought Indicated by the SPI and SPEI at Various Timescales in Inner Mongolia, China. *Water* 12, 1925. <https://doi.org/10/ghqfbd>
- Perkins, S.E., 2015. A review on the scientific understanding of heatwaves—Their measurement, driving mechanisms, and changes at the global scale. *Atmospheric Research* 164–165, 242–267. <https://doi.org/10/gg8fs5>
- Perkins, S.E., Alexander, L.V., 2012. On the Measurement of Heat Waves. *Journal of Climate* 26, 4500–4517. <https://doi.org/10.1175/JCLI-D-12-00383.1>
- Perkins, S.E., Alexander, L.V., Nairn, J.R., 2012. Increasing frequency, intensity and duration of observed global heatwaves and warm spells. *Geophysical Research Letters* 39, 1–5. <https://doi.org/10.1029/2012GL053361>

- Perkins, S.E., Argüeso, D., White, C.J., 2015. Relationships between climate variability, soil moisture, and Australian heatwaves. *J. Geophys. Res. Atmos.* 120, 8144–8164. <https://doi.org/10/ghpb5j>
- Perkins-Kirkpatrick, S.E., Lewis, S.C., 2020. Increasing trends in regional heatwaves. *Nat Commun* 11, 3357. <https://doi.org/10.1038/s41467-020-16970-7>
- Phillips, O.L., Aragão, L.E.O.C., Lewis, S.L., Fisher, J.B., Lloyd, J., López-González, G., Malhi, Y., Monteagudo, A., Peacock, J., Quesada, C.A., van der Heijden, G., Almeida, S., Amaral, I., Arroyo, L., Aymard, G., Baker, T.R., Bánki, O., Blanc, L., Bonal, D., Brando, P., Chave, J., de Oliveira, Á.C.A., Cardozo, N.D., Czimczik, C.I., Feldpausch, T.R., Freitas, M.A., Gloor, E., Higuchi, N., Jiménez, E., Lloyd, G., Meir, P., Mendoza, C., Morel, A., Neill, D.A., Nepstad, D., Patiño, S., Peñuela, M.C., Prieto, A., Ramírez, F., Schwarz, M., Silva, J., Silveira, M., Thomas, A.S., Steege, H. ter, Stropp, J., Vásquez, R., Zelazowski, P., Dávila, E.A., Andelman, S., Andrade, A., Chao, K.-J., Erwin, T., Di Fiore, A., C., E.H., Keeling, H., Killeen, T.J., Laurance, W.F., Cruz, A.P., Pitman, N.C.A., Vargas, P.N., Ramírez-Angulo, H., Rudas, A., Salamão, R., Silva, N., Terborgh, J., Torres-Lezama, A., 2009. Drought Sensitivity of the Amazon Rainforest. *Science* 323, 1344–1347. <https://doi.org/10/fhrvnh>
- Polcher, J., Parker, D.J., Gaye, A.T., 2011. African Monsoon Multidisciplinary Analysis: An integrated project for understanding of the West African climate system and its human dimension. *Atmospheric Science Letters* 12, 1–1. <https://doi.org/10/d3vqkf>
- Pongratz, J., Reick, C.H., Raddatz, T., Claussen, M., 2009. Effects of anthropogenic land cover change on the carbon cycle of the last millennium. *Global Biogeochemical Cycles* 23. <https://doi.org/10/cb89mn>
- Pospichal, B., Karam, D., Crewell, S., Flamant, C., Hünerbein, A., Bock, O., Saïd, F., 2010. Diurnal cycle of the intertropical discontinuity over West Africa analysed by remote sensing and mesoscale modelling. *Q.J.R. Meteorol. Soc.* 136, 92–106. <https://doi.org/10/d72gw7>
- Quenum, G.M.L.D., Klutse, N.A.B., Dieng, D., Laux, P., Arnault, J., Kodja, Japhet.D., Oguntunde, P.G., 2019. Identification of Potential Drought Areas in West Africa Under Climate Change and Variability. *Earth Syst Environ* 3, 429–444. <https://doi.org/10/gg5m65>
- Ragatoa, D.S., Ogunjobi, K.O., Klutse, N.A.B., Okhimamhe, A.A., Eichie, J.O., 2019. A change comparison of heat wave aspects in climatic zones of Nigeria. *Environmental Earth Sciences* 78, 0. <https://doi.org/10.1007/s12665-019-8112-8>
- Ragatoa, D.S., Ogunjobi, K.O., Okhimamhe, A.A., Ama, N., Klutse, B., Lamptey, B.L., 2018. A predictive study of heat wave characteristics and their spatio-

- temporal trends in climatic zones of Nigeria. *Model. Earth Syst. Environ* 4, 27. <https://doi.org/10.1007/s40808-018-0480-7>
- Rai, P., Maharana, P., Kumar, D., Dimri, A.P., Paeth, H., 2020. Study of Northeast Monsoon over India using a coupled land-atmosphere model RegCM4-CLM4.5 (other). oral. <https://doi.org/10.5194/egusphere-egu2020-7772>
- Raj, J., Bangalath, H.K., Stenchikov, G., 2019. West African Monsoon: current state and future projections in a high-resolution AGCM. *Climate Dynamics* 52, 6441–6461. <https://doi.org/10.1007/s00382-018-4522-7>
- Ramamurthy, P., Li, D., Bou-Zeid, E., 2017. High-resolution simulation of heatwave events in New York City. *Theor Appl Climatol* 128, 89–102. <https://doi.org/10.1007/s00704-015-1703-8>
- Rasmijn, L.M., van der Schrier, G., Bintanja, R., Barkmeijer, J., Sterl, A., Hazeleger, W., 2018. Future equivalent of 2010 Russian heatwave intensified by weakening soil moisture constraints. *Nature Clim Change* 8, 381–385. <https://doi.org/10/gdhksm>
- Ratnam, J.V., Behera, S.K., Ratna, S.B., Rajeevan, M., Yamagata, T., 2016. Anatomy of Indian heatwaves. *Sci Rep* 6, 24395. <https://doi.org/10/f8htzj>
- Rhee, J., Park, S., Lu, Z., 2014. Relationship between land cover patterns and surface temperature in urban areas. *GIScience & Remote Sensing* 51, 521–536. <https://doi.org/10/gg35t7>
- Roberts, A.J., Marsham, J.H., Knippertz, P., 2015. Disagreements in Low-Level Moisture between (Re)Analyses over Summertime West Africa. *Monthly Weather Review* 143, 1193–1211. <https://doi.org/10/f677m4>
- Roehrig, R., Bouniol, D., Guichard, F., Hourdin, F., Redelsperger, J.-L., 2013. The Present and Future of the West African Monsoon: A Process-Oriented Assessment of CMIP5 Simulations along the AMMA Transect. *Journal of Climate* 26, 6471–6505. <https://doi.org/10/f468kn>
- Rohde, R., Muller, R., Jacobsen, R., Perlmutter, S., Mosher, S., 2013. Berkeley Earth Temperature Averaging Process. *Geoinfor Geostat: An Overview* 01. <https://doi.org/10.4172/2327-4581.1000103>
- Rossato, L., Alvalá, R.C. dos S., Marengo, J.A., Zeri, M., Cunha, A.P.M. do A., Pires, L.B.M., Barbosa, H.A., 2017. Impact of Soil Moisture on Crop Yields over Brazilian Semiarid. *Front. Environ. Sci.* 5, 73. <https://doi.org/10/gg7hrj>
- Russo, S., Dosio, A., Graversen, R.G., Sillmann, J., Carrao, H., Dunbar, M.B., Singleton, A., Montagna, P., Barbola, P., Vogt, J.V., 2014. Magnitude of extreme heat waves in present climate and their projection in a warming world. *Journal of Geophysical Research Atmospheres* 119, 12500–12512. <https://doi.org/10.1002/2014JD022098>

- Russo, S., Dosio, A., Sterl, A., Barbosa, P., Vogt, J., 2013. Projection of occurrence of extreme dry-wet years and seasons in Europe with stationary and nonstationary Standardized Precipitation Indices. *Journal of Geophysical Research Atmospheres* 118, 7628–7639. <https://doi.org/10.1002/jgrd.50571>
- Russo, S., Marchese, A.F., Sillmann, J., Immé, G., 2016. When will unusual heat waves become normal in a warming Africa? *Environmental Research Letters* 11. <https://doi.org/10.1088/1748-9326/11/5/054016>
- Russo, S., Sillmann, J., Fischer, E.M., 2015. Top ten European heatwaves since 1950 and their occurrence in the coming decades. *Environ. Res. Lett.* 10, 124003. <https://doi.org/10.1088/1748-9326/10/12/124003>
- Russo, S., Sillmann, J., Sterl, A., 2017a. Humid heat waves at different warming levels. *Scientific Reports* 7, 7477. <https://doi.org/10/gbskj7>
- Russo, S., Sillmann, J., Sterl, A., 2017b. Humid heat waves at different warming levels. *Sci Rep* 7, 7477. <https://doi.org/10/gbskj7>
- Russo, S., Sterl, A., 2011. Global changes in indices describing moderate temperature extremes from the daily output of a climate model. *Journal of Geophysical Research Atmospheres* 116, 1–12. <https://doi.org/10.1029/2010JD014727>
- Salack, S., Klein, C., Giannini, A., Sarr, B., Worou, O.N., Belko, N., Jan Bliedernicht, Kunstman, H., 2016. Global warming induced hybrid rainy seasons in the Sahel. *Environ. Res. Lett.* 11, 104008. <https://doi.org/10.1088/1748-9326/11/10/104008>
- Sanogo, S., Fink, A.H., Omotosho, J.A., Ba, A., Redl, R., Ermert, V., 2015. Spatio-temporal characteristics of the recent rainfall recovery in West Africa: RECENT RAINFALL RECOVERY IN WEST AFRICA. *Int. J. Climatol.* 35, 4589–4605. <https://doi.org/10.1002/joc.4309>
- Saroha, J., 2017. Indian Monsoon : Origin and Mechanism. *International Journal of Research and Analytical Reviews* 4.
- Sauder, D.C., DeMars, C.E., 2019. An Updated Recommendation for Multiple Comparisons. *Advances in Methods and Practices in Psychological Science* 2, 26–44. <https://doi.org/10.1177/2515245918808784>
- Schär, C., Vidale, P.L., Lüthi, D., Frei, C., Häberli, C., Liniger, M.A., Appenzeller, C., 2004. The role of increasing temperature variability in European summer heatwaves. *Nature*. <https://doi.org/10.1038/nature02300>
- Schwalm, C.R., Anderegg, W.R., Michalak, A.M., Fisher, J.B., Biondi, F., Koch, G., Litvak, M., Ogle, K., Shaw, J.D., Wolf, A., 2017. Global patterns of drought recovery. *Nature* 548, 202–205.

- Sen, P.K., 1968. Estimates of the Regression Coefficient Based on Kendall's Tau. *Journal of the American Statistical Association* American Statistical Association American Statistical Association American Statistical Association American Statistical Association 63, 1379–1389.
- Seneviratne, S., Nicholls, N., Easterling, D., Goodess, C., Kanae, S., Kossin, J., Luo, Y., Marengo, J., McInnes, K., Rahimi, M., Reichstein, M., Sorteberg, A., Vera, C., Zhang, X., 2012. Changes in climate extremes and their impacts on the natural physical environment. *Managing the Risk of Extreme Events and Disasters to Advance Climate Change Adaptation*. 109–230.
- Seneviratne, S.I., Wartenburger, R., Guillod, B.P., Hirsch, A.L., Vogel, M.M., Brovkin, V., Van Vuuren, D.P., Schaller, N., Boysen, L., Calvin, K.V., Doelman, J., Greve, P., Havlik, P., Humpenöder, F., Krisztin, T., Mitchell, D., Popp, A., Riahi, K., Rogelj, J., Schleussner, C.F., Sillmann, J., Stehfest, E., 2018. Climate extremes, land-climate feedbacks and land-use forcing at 1.5°C. *Philosophical Transactions of the Royal Society A: Mathematical, Physical and Engineering Sciences* 376. <https://doi.org/10.1098/rsta.2016.0450>
- Shanahan, T.M., Overpeck, J.T., Anchukaitis, K.J., Beck, J.W., Cole, J.E., Dettman, D.L., Peck, J.A., Scholz, C.A., King, J.W., 2009. Atlantic Forcing of Persistent Drought in West Africa. *Science* 324, 377–380. <https://doi.org/10/fkp654>
- Sharma, S., Mujumdar, P., 2017. Increasing frequency and spatial extent of concurrent meteorological droughts and heatwaves in India. *Scientific Reports* 7, 1–9. <https://doi.org/10.1038/s41598-017-15896-3>
- Shinoda, M., 1986. Wind and Moisture Anomalies Drought of the in the Early Sahelian 1980's.
- Smoyer-Tomic, K.E., Kuhn, R., Hudson, A., 2003. Heat Wave Hazards: An Overview of Heat Wave Impacts in Canada. *Natural Hazards* 28, 465–486. <https://doi.org/10.1023/A:1022946528157>
- Stefanon, M., D'Andrea, F., Drobinski, P., 2012. Heatwave classification over Europe and the Mediterranean region. *Environ. Res. Lett.* 7, 014023. <https://doi.org/10/gg3rt7>
- Steiner, A.L., Pal, J.S., Giorgi, F., Dickinson, R.E., Chameides, W.L., 2005. The coupling of the Common Land Model (CLM0) to a regional climate model (RegCM). *Theor. Appl. Climatol.* 82, 225–243. <https://doi.org/10.1007/s00704-005-0132-5>
- Stull, R., 2005. *The Atmospheric Boundary Layer* 44.
- Sutanto, S.J., Vitolo, C., Di Napoli, C., D'Andrea, M., Van Lanen, H.A.J., 2020. Heatwaves, droughts, and fires: Exploring compound and cascading dry

- hazards at the pan-European scale. *Environment International* 134, 105276. <https://doi.org/10.1016/j.envint.2019.105276>
- Tan, J., Zheng, Y., Tang, X., Guo, C., Li, L., Song, G., Zhen, X., Yuan, D., Kalkstein, A.J., Li, F., Chen, H., 2010. The urban heat island and its impact on heat waves and human health in Shanghai. *International Journal of Biometeorology* 54, 75–84. <https://doi.org/10.1007/s00484-009-0256-x>
- Tefera, A.S., Ayoade, J.O., Bello, N.J., 2019. Comparative analyses of SPI and SPEI as drought assessment tools in Tigray Region, Northern Ethiopia. *SN Appl. Sci.* 1, 1–14. <https://doi.org/10.1007/s42452-019-1326-2>
- Teuling, A.J., Seneviratne, S.I., Stöckli, R., Reichstein, M., Moors, E., Ciais, P., Luysaert, S., van den Hurk, B., Ammann, C., Bernhofer, C., Dellwik, E., Gianelle, D., Gielen, B., Grünwald, T., Klumpp, K., Montagnani, L., Moureaux, C., Sottocornola, M., Wohlfahrt, G., 2010. Contrasting response of European forest and grassland energy exchange to heatwaves. *Nature Geosci* 3, 722–727. <https://doi.org/10/ftnk6g>
- Tiwari, P.R., Kar, S.C., Mohanty, U.C., Dey, S., Sinha, P., Raju, P.V.S., Shekhar, M.S., 2015. The role of land surface schemes in the regional climate model (RegCM) for seasonal scale simulations over Western Himalaya. *Atmósfera* 28, 129–142. [https://doi.org/10.1016/S0187-6236\(15\)30005-9](https://doi.org/10.1016/S0187-6236(15)30005-9)
- Tomasini, M., Guichard, F., Couvreur, F., Roehrig, R., Barbier, J., 2022. Spurious effects of the deep convection parameterization on the simulation of a Sahelian heatwave. *Quart J Royal Meteor Soc* *qj.4365*. <https://doi.org/10.1002/qj.4365>
- Tompkins, A.M., Feudale, L., 2010. Seasonal ensemble predictions of West African monsoon precipitation in the ECMWF system 3 with a focus on the AMMA special observing period in 2006. *Weather and Forecasting* 25, 768–788. <https://doi.org/10.1175/2009WAF2222236.1>
- Tsige, T.D., Uddameri, V., Forghanparast, Farhang., Hernandez, E.Annette., Ekwaro-Osire, Stephen., 2019. Comparison of Meteorological- and Agriculture-Related Drought Indicators across Ethiopia. *Water* 11, 2218. <https://doi.org/10/gg34gk>
- UNFCCC, 1992. UNITED NATIONS FRAMEWORK CONVENTION.
- van den Dool, H., Huang, J., Fan, Y., 2003. Performance and analysis of the constructed analogue method applied to U.S. soil moisture over 1981–2001. *Journal of Geophysical Research: Atmospheres* 108. <https://doi.org/10.1029/2002JD003114>
- Varentsov, M., Wouters, H., Platonov, V., Konstantinov, P., 2018. Investigation of urban-induced mesoclimatic anomalies in the lower atmosphere over

Moscow megacity based on simulations with COSMO-CLM model for multiple summers 1.

- Varghese, B.M., Barnett, A.G., Hansen, A.L., Bi, P., Nairn, J., Rowett, S., Nitschke, M., Hanson-Easey, S., Heyworth, J.S., Sim, M.R., Pisaniello, D.L., 2019. Characterising the impact of heatwaves on work-related injuries and illnesses in three Australian cities using a standard heatwave definition- Excess Heat Factor (EHF). *J Expo Sci Environ Epidemiol* 29, 821–830. <https://doi.org/10/gg34hs>
- Vatani, J., Golbabaee, F., Dehghan, S.F., Yousefi, A., 2016. Applicability of Universal Thermal Climate Index (UTCI) in occupational heat stress assessment: a case study in brick industries. *Ind Health* 54, 14–19. <https://doi.org/10.2486/indhealth.2015-0069>
- Vicente-Serrano, S.M., 2007. Evaluating the impact of drought using remote sensing in a Mediterranean, semi-arid region. *Natural Hazards* 40, 173–208. <https://doi.org/10/d6jfhv>
- Vicente-Serrano, S.M., Beguería, S., López-Moreno, J.I., 2010a. A multiscalar drought index sensitive to global warming: The standardized precipitation evapotranspiration index. *Journal of Climate* 23, 1696–1718. <https://doi.org/10.1175/2009JCLI2909.1>
- Vicente-Serrano, S.M., Beguería, S., López-Moreno, J.I., García-Vera, M.A., Stepanek, P., 2010b. A complete daily precipitation database for northeast Spain: Reconstruction, quality control, and homogeneity. *International Journal of Climatology* 30, 1146–1163. <https://doi.org/10.1002/joc.1850>
- Wajid, A., Hussain, K., Maqsood, M., Ahmad, A., Hussain, A., 2007. Influence of drought on water use efficiency in wheat in semi-arid regions of Punjab. *Soil & Environment* 26, 64–68.
- Wang, C., Li, Z., Chen, Y., Li, Y., Liu, X., Hou, Y., Wang, X., Kulaixi, Z., Sun, F., 2022. Increased Compound Droughts and Heatwaves in a Double Pack in Central Asia. *Remote Sensing* 14, 2959. <https://doi.org/10.3390/rs14132959>
- Wang, Q., Zeng, J., Qi, J., Zhang, X., Zeng, Y., Shui, W., Xu, Z., Zhang, R., Wu, X., 2020. A Multi-Scale Daily SPEI Dataset for Drought Monitoring at Observation Stations over the Mainland China from 1961 to 2018 (preprint). *Atmosphere – Meteorology*. <https://doi.org/10.5194/essd-2020-172>
- Wang, S., Davidson, A., 2007. Impact of climate variations on surface albedo of a temperate grassland. *Agricultural and Forest Meteorology* 142, 133–142. <https://doi.org/10.1016/j.agrformet.2006.03.027>
- Wenda, W.I., Hanks, R.J., 1981. Corn yield and evapotranspiration under simulated drought conditions. *Irrig Sci* 2. <https://doi.org/10/fm9v4w>

- Wilson, A., Boulder, C., 2019. Investigating CESM1 Ability to Predict Extreme Temperature Events 1–14.
- WMO, 2012. Standardized precipitation index user guide.
- WMO, GWP, 2016. Handbook of Drought Indicators and Indices, Integrated Drought Management Programme (IDMP), Integrated Drought Management Tools and Guidelines. ed, WMO. WMO, Geneva.
- Wreford, A., Adger, W.N., 2010. Adaptation in agriculture: Historic effects of heat waves and droughts on UK agriculture. *International Journal of Agricultural Sustainability* 8, 278–289. <https://doi.org/10/bbqmn6>
- Xiao, R., Ouyang, Z., Zheng, H., Li, W., Schienke, E.W., Wang, X., 2007. Spatial pattern of impervious surfaces and their impacts on land surface temperature in Beijing, China. *Journal of Environmental Sciences* 19, 250–256. [https://doi.org/10.1016/S1001-0742\(07\)60041-2](https://doi.org/10.1016/S1001-0742(07)60041-2)
- Xoplaki, E., González-Rouco, J.F., Luterbacher, J., Wanner, H., 2003. Mediterranean summer air temperature variability and its connection to the large-scale atmospheric circulation and SSTs. *Climate Dynamics* 20, 723–739. <https://doi.org/10.1007/s00382-003-0304-x>
- Yang, M., Zuo, R., Wang, L., Hu, F., Wang, C., Ge, W., 2019. An experiment to improve the capability of the regional climate model RegCM4. 5 to simulate the land surface climate in dense vegetation areas. *Journal of Earth System Science* 128, 184. <https://doi.org/10/gg4shp>
- Yaro, J.A., Hesselberg, J. (Eds.), 2016. *Adaptation to Climate Change and Variability in Rural West Africa*. Springer International Publishing, Cham. <https://doi.org/10.1007/978-3-319-31499-0>
- Ye, Z., Im, U., Christensen, J., Geels, C., Sandstad, M., Iles, C., Schwingshackl, C., 2022. Near-past and future trends of European extreme heat and heat waves from WRF downscaling experiments. <https://doi.org/10.5194/egusphere-egu22-11296>
- York, G., 2012. Drought in West Africa threatens millions.
- Zare, S., Hasheminejad, N., Shirvan, H.E., Hemmatjo, R., Sarebanzadeh, K., Ahmadi, S., 2018. Comparing Universal Thermal Climate Index (UTCI) with selected thermal indices/environmental parameters during 12 months of the year. *Weather and Climate Extremes* 19, 49–57. <https://doi.org/10.1016/j.wace.2018.01.004>
- Zare, S., Shirvan, H.E., Hemmatjo, R., Nadri, F., Jahani, Y., Jamshidzadeh, K., Paydar, P., 2019. A comparison of the correlation between heat stress indices (UTCI, WBGT, WBDT, TSI) and physiological parameters of workers in

Iran. Weather and Climate Extremes 26, 100213.
<https://doi.org/10.1016/j.wace.2019.100213>

Zeng, X., Zhao, M., Dickinson, R.E., 1998. Intercomparison of Bulk Aerodynamic Algorithms for the Computation of Sea Surface Fluxes Using TOGA COARE and TAO Data. *Journal of Climate* 11, 2628–2644.
[https://doi.org/10.1175/1520-0442\(1998\)011<2628:IOBAAF>2.0.CO;2](https://doi.org/10.1175/1520-0442(1998)011<2628:IOBAAF>2.0.CO;2)

Zhang, J., Liu, Z., Chen, L., 2015. Reduced soil moisture contributes to more intense and more frequent heat waves in northern China. *Adv. Atmos. Sci.* 32, 1197–1207. <https://doi.org/10.1007/s00376-014-4175-3>

Zittis, G., Hadjinicolaou, P., Almazroui, M., Bucchignani, E., Driouech, F., El Rhaz, K., Kurnaz, L., Nikulin, G., Ntoumos, A., Ozturk, T., Proestos, Y., Stenchikov, G., Zaaboul, R., Lelieveld, J., 2021. Business-as-usual will lead to super and ultra-extreme heatwaves in the Middle East and North Africa. *npj Clim Atmos Sci* 4, 1–9. <https://doi.org/10.1038/s41612-021-00178-7>

APPENDIXES

The appendices contain additional material that supplements the main discussion in this thesis. Appendix A provides additional results from the objective 1. Appendix B includes additional results from the objective 2 and Appendix C, results from the objective 3.

APPENDIX A

The analysis of the Heatwave Magnitude index daily (HWMI_d) and the Apparent heatwave index (AWHI) for gridded (.grd) and observation (.obs) gives different results from what was used in the Cumulative (excess) Heat (CumHeat) and that informed the use of the CumHeat.

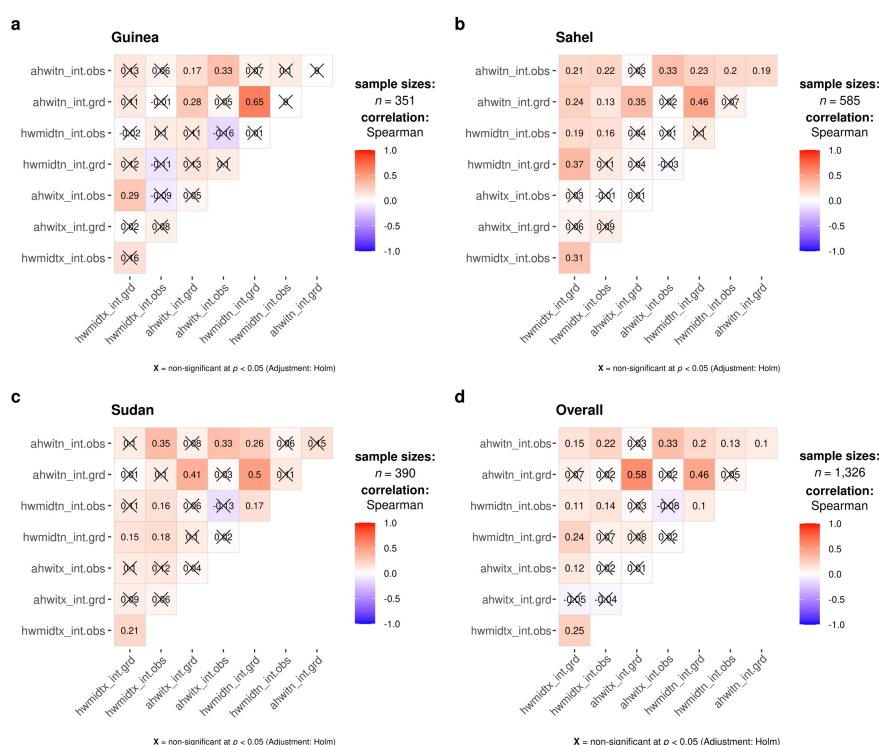


Figure A.1: Heatwave (HWMI_d and AWHI) intensity (int) Correlation for the climate zones in West Africa (a- Guinea; b- Sahel; c- Sudan and d- overall average)

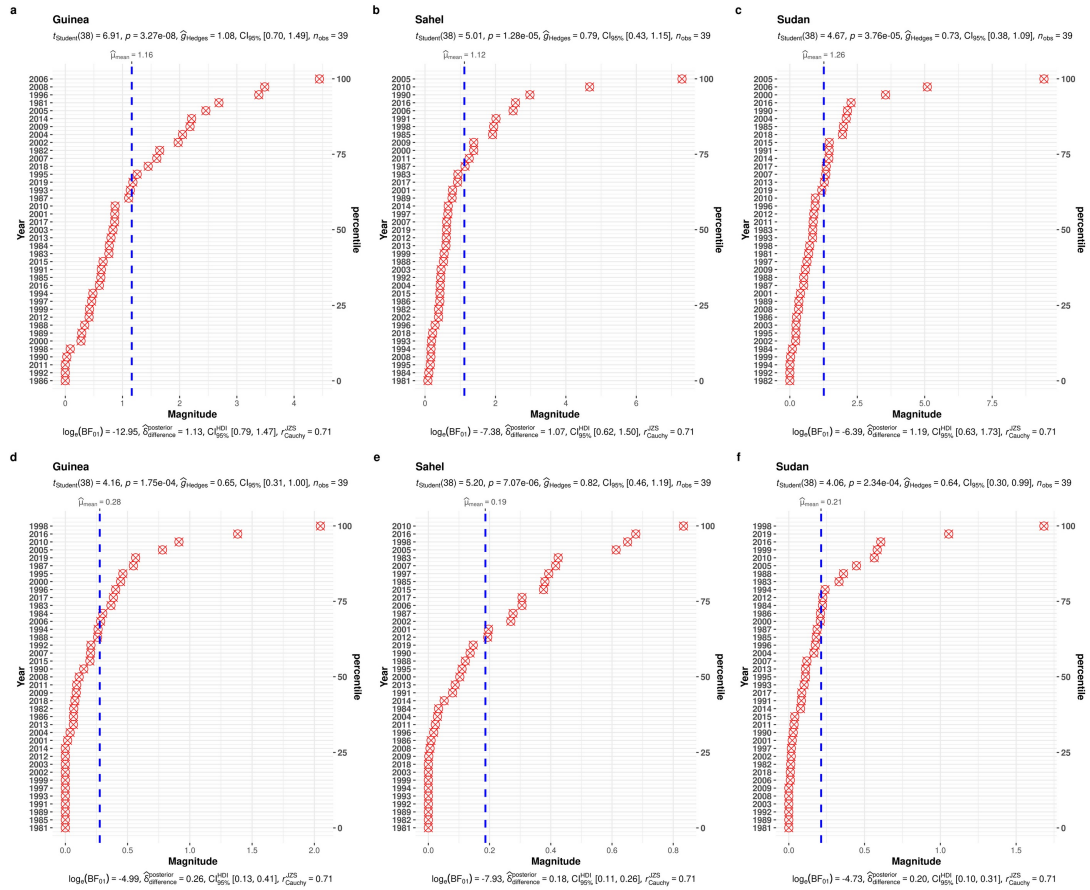


Figure A.2: HWMId zonal comparison; Gridded (a, b, c) and observation (d, e, f) datasets. BF10 is the Bayes Factor; The Highest Density Interval (HDI) formed from the posterior gives the 95% most credible values; r is the prior

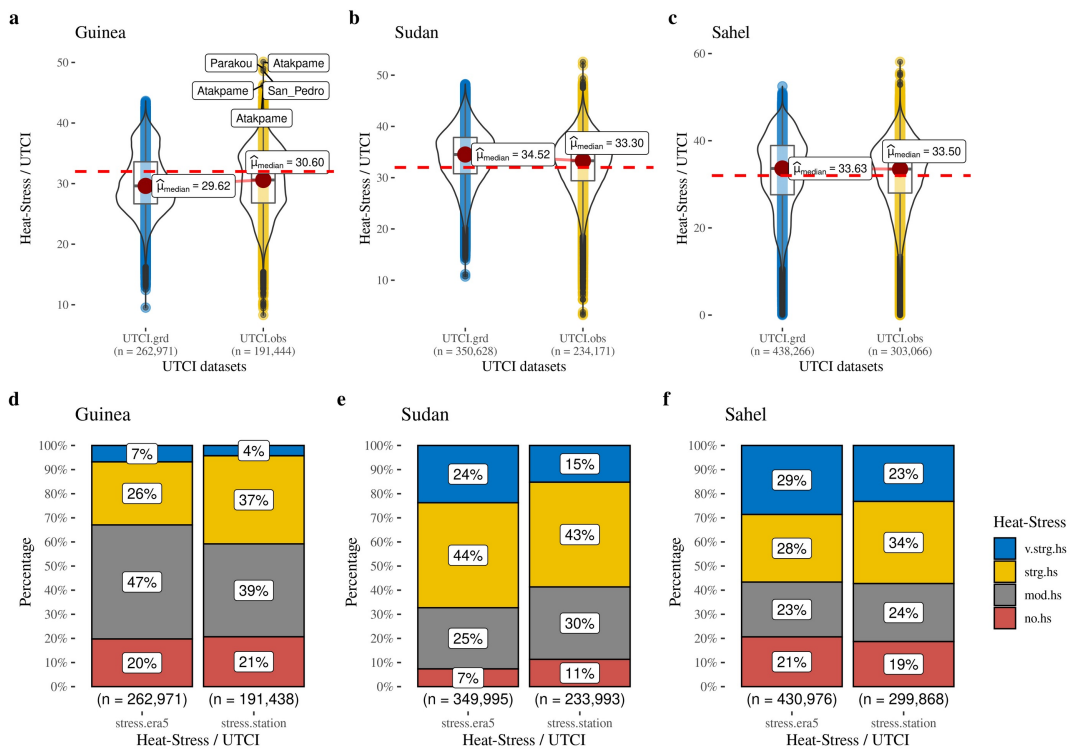


Figure A.3: UTCI Gridded and Station comparison; dataset distribution in the climatic zones and their relative level of heat stress at 32 °C strong heat stress in red dotted line (upper panel); Percentage of occurrence comparison in each climate zone with p-values at the top (lower panel)

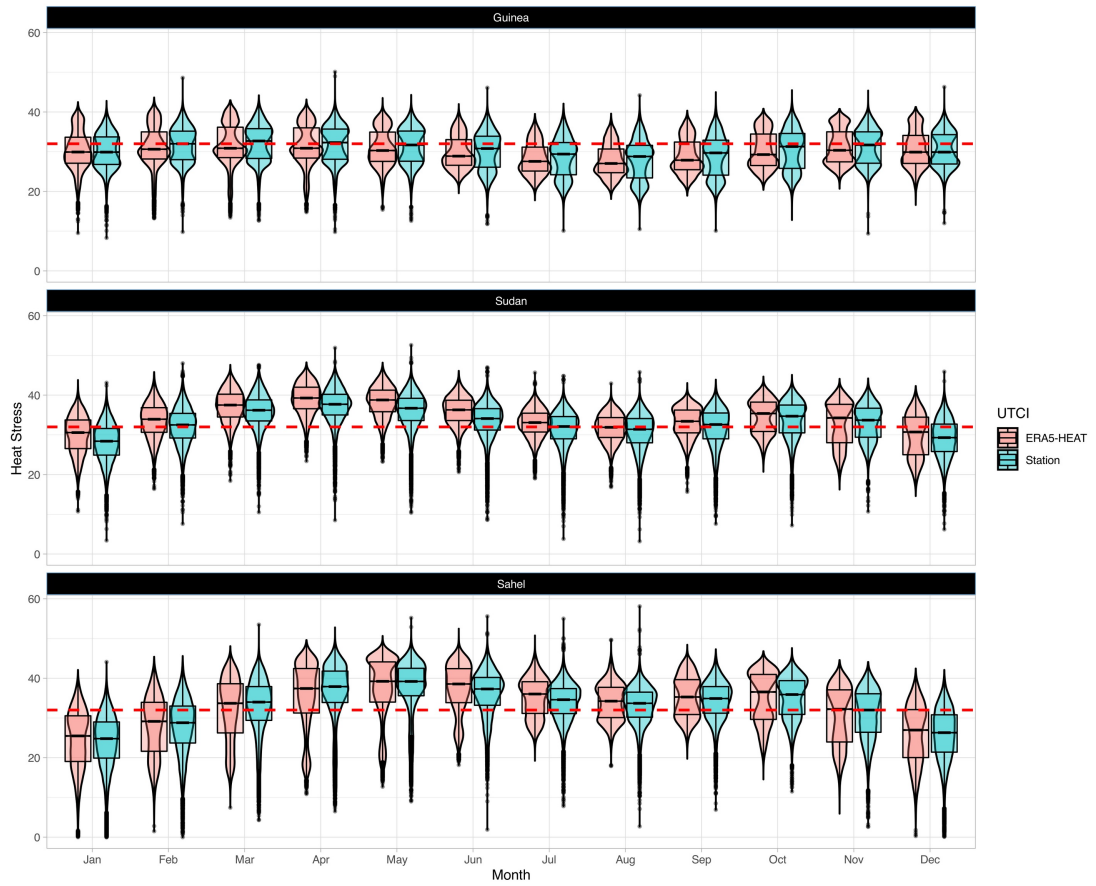


Figure A.4: Seasonal Variation and distribution of UTCI (Gridded and Station) compared over the period 1981 to 2020 in the climate zones (Guinea, Sudan and Sahel). Red dotted line is the 32 °C strong heat stress

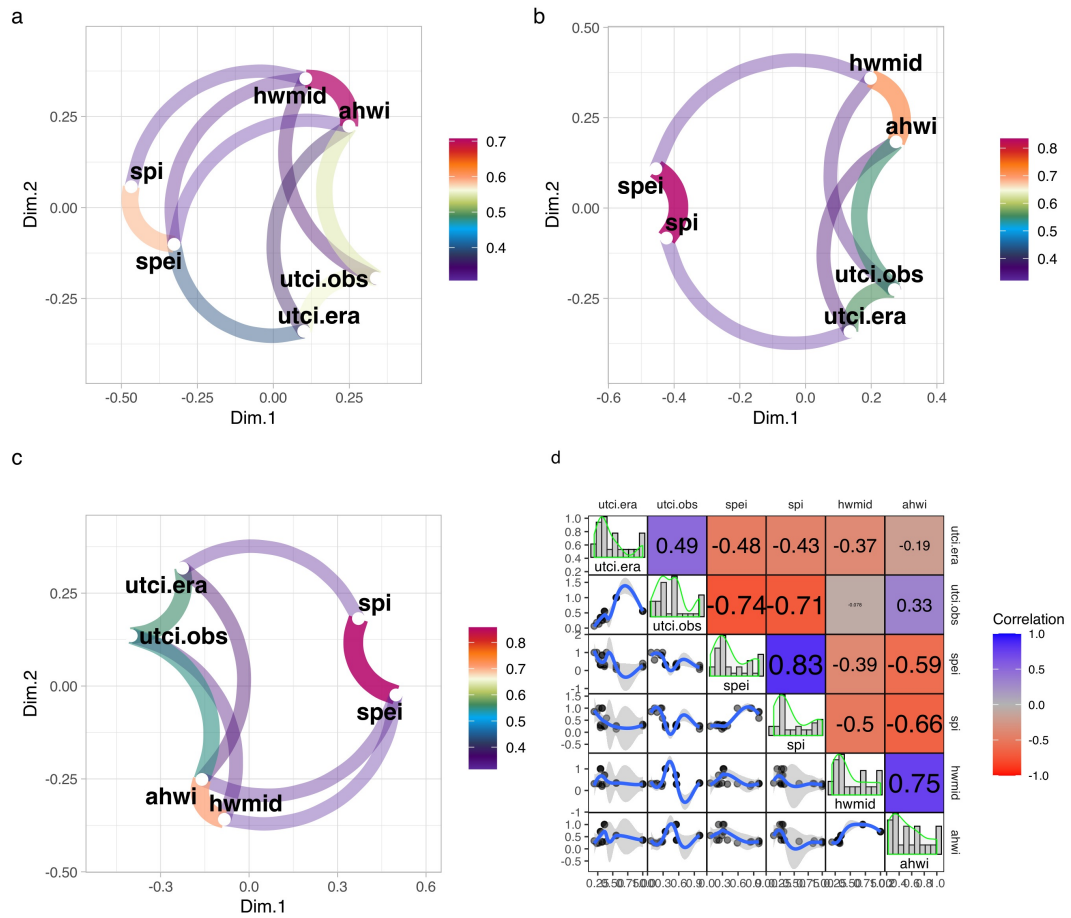


Figure A.5: Drought Heatwaves relationship and association in the Guinea Zone;association of heatwave / heat stress and drought at 3- (a), 6-(b) and 12-(c) months;each point represent an index, the path is the correlation between variable and the colours are the correlation strength; d- is the overall correlation between the indices,with correlation values in the upper triangle, a regression line on lower triangle and histogram with density on the diagonal

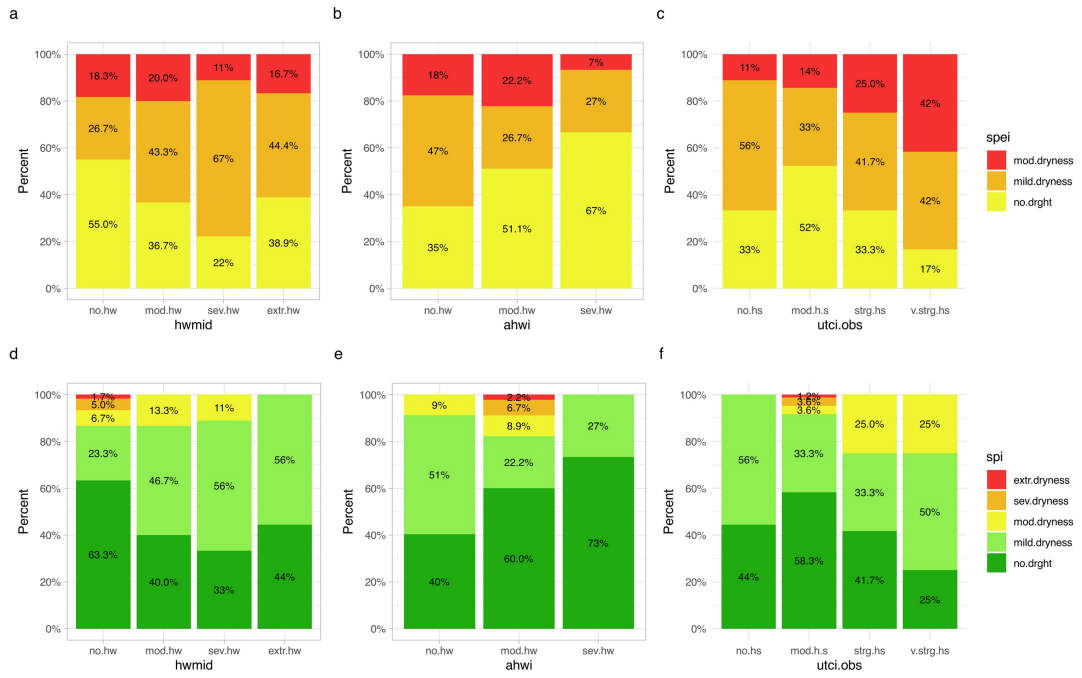


Figure A.6: Heatwave and Heat Stress Occurrence during Droughts in the Guinea zone;SPEI – HWMId (a), AHWI (b) and UTCI (c); SPI – HWMId (d), AHWI (e) and UTCI (f)

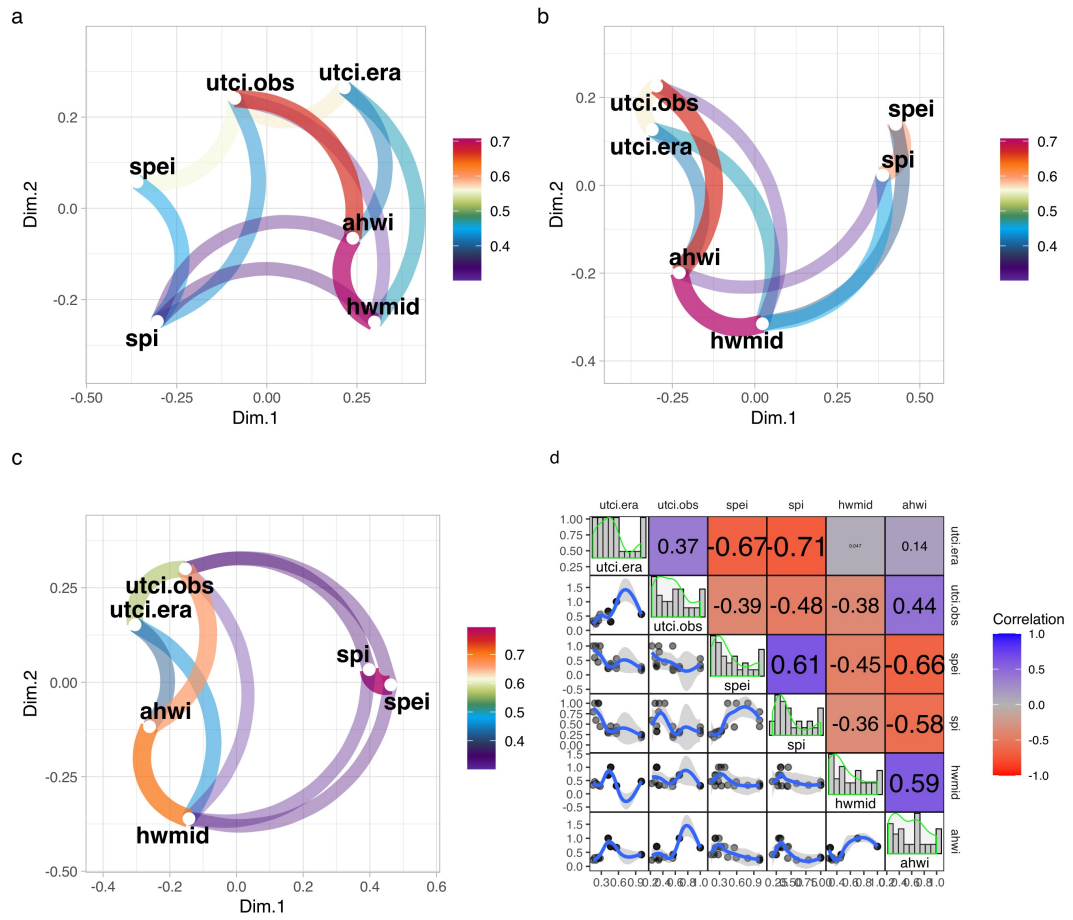


Figure A.7: Drought Heatwaves relationship and association in the Sudan Zone; Presented as Figure A.5

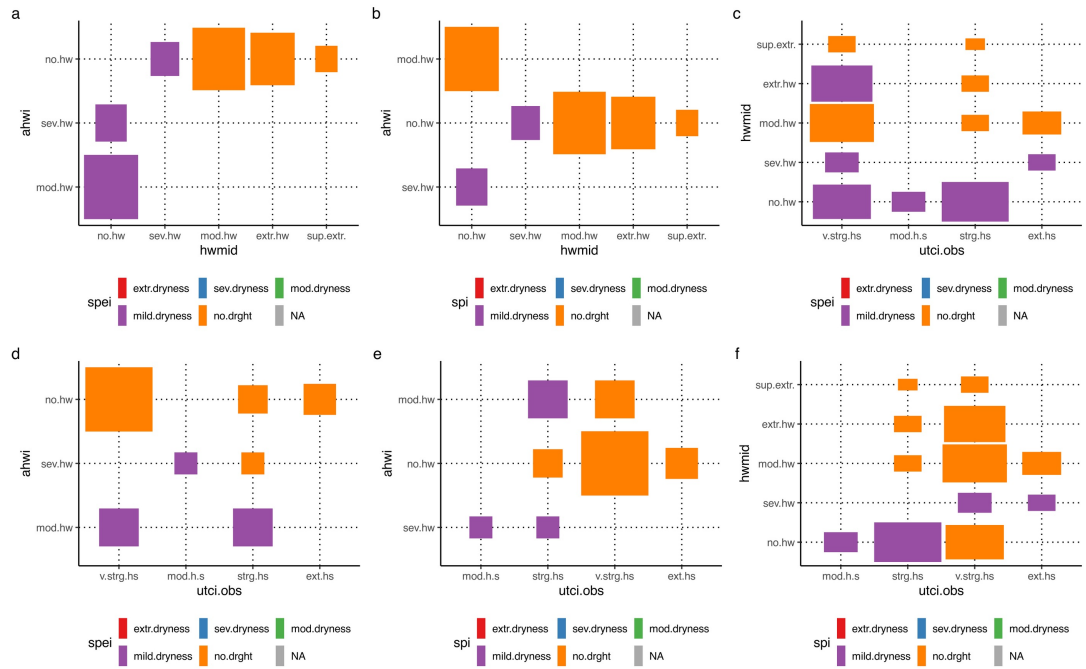


Figure A.8: Heatwave and Heat Stress Occurrence during Droughts in the Sudan zone; SPEI:AHWI vs HWMId (a), HWMId vs UTci (c) and AHWI vs UTci (d); SPI: AHWI vs HWMId(b), AHWI vs UTci (e) and HWMId vs UTci (f). The colours represent different drought intensity and the size represent the relative proportion of occurrence from the total series.

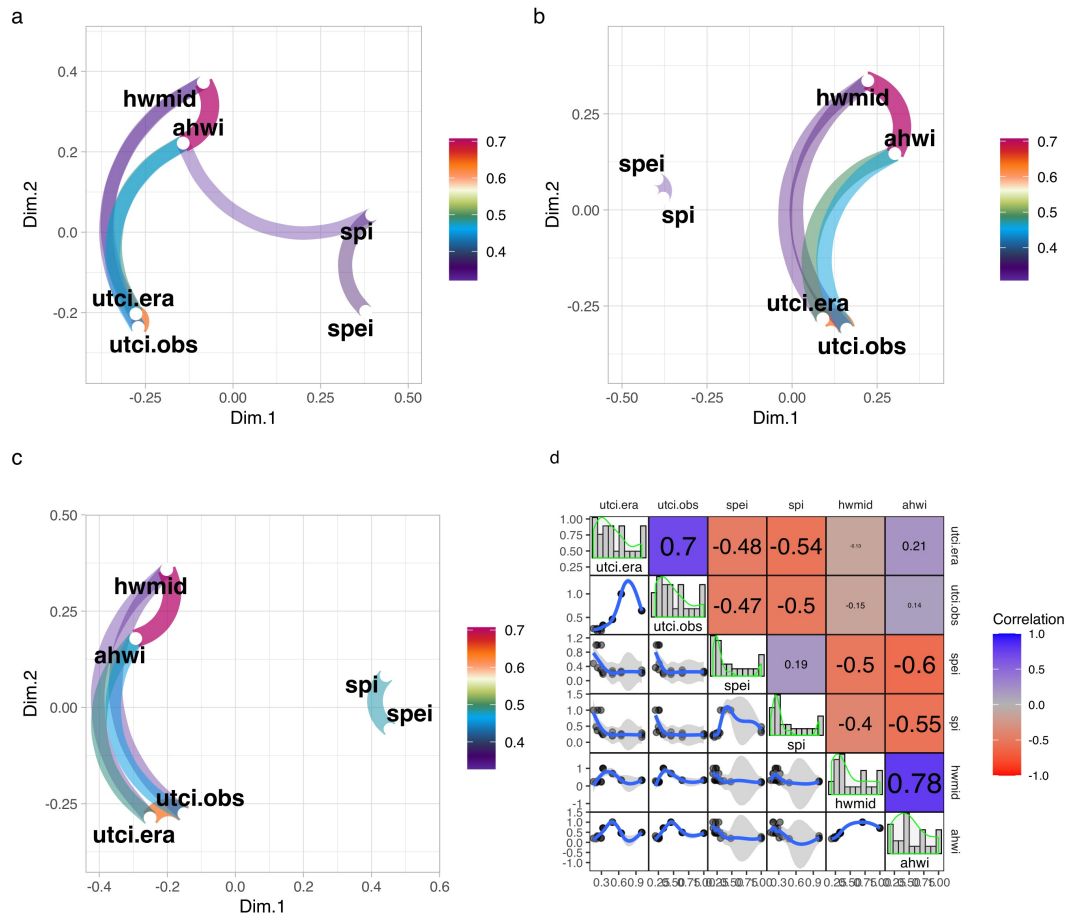


Figure A.9: Drought Heatwaves relationship and association in the Sudan Zone; Presented as Figure A.5

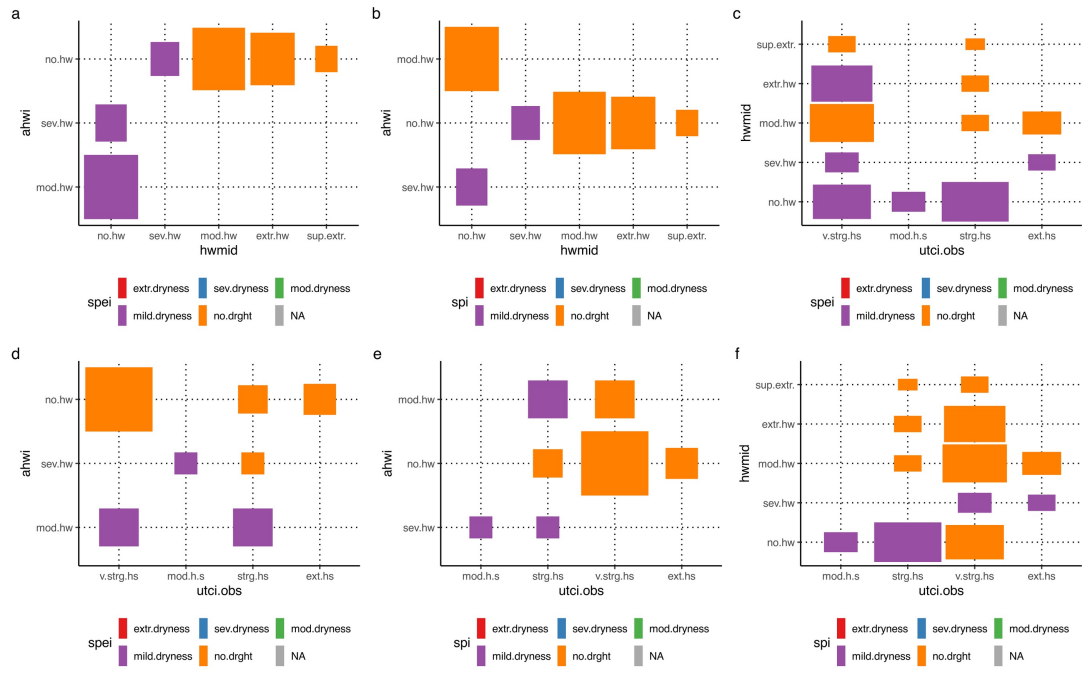


Figure A10: Heatwave and Heat Stress Occurrence during Droughts in the Sahel ; Presented as in Figure A.8

APPENDIX B

The appendix B provides supplementary information and data that support the analysis and conclusions presented in the objective 2.

Table B1: Mean Frequency and Trend of heatwave (Heat stress) in West Africa. Presented per index and climate zones

| Index | Zone | Parameter | Frequency | Trend |
|--------------|-------------|------------------|------------------|--------------|
| HeatCum | Guinea | nchw (day) | 0.1900 | 0.0001 |
| | | nchw (night) | 0.1200 | 0.0001 |
| | | dur (day) | 0.5200 | 0.0004 |
| | | dur (night) | 0.4400 | 0.0002 |
| | Sudan | nchw (day) | 0.2300 | 0.0003 |
| | | nchw (night) | 0.1700 | 0.0002 |
| | | dur (day) | 0.5200 | 0.0005 |
| | | dur (night) | 0.4600 | 0.0002 |
| | Sahel | nchw (day) | 0.3700 | 0.0006 |
| | | nchw (night) | 0.2300 | 0.0002 |
| | | dur (day) | 0.6700 | 0.0009 |
| | | dur (night) | 0.5400 | 0.0002 |
| UTCI | Guinea | nchw (day) | 0.3700 | 0.0008 |
| | | nchw (night) | 0.2600 | 0.0008 |
| | | dur (day) | 0.5500 | 0.0009 |
| | | dur (night) | 0.5600 | 0.0011 |
| | Sudan | nchw (day) | 0.2500 | 0.0002 |
| | | nchw (night) | 0.3000 | 0.0004 |
| | | dur (day) | 0.5100 | 0.0006 |
| | | dur (night) | 0.5000 | 0.0007 |
| | Sahel | nchw (day) | 0.1700 | 0.0001 |
| | | nchw (night) | 0.1800 | 0.0001 |
| | | dur (day) | 0.4700 | 0.0003 |
| | | dur (night) | 0.5000 | 0.0002 |
| WBGT | Guinea | nchw (day) | 0.2600 | 0.0001 |
| | | nchw (night) | 0.3000 | 0.0001 |

| Index | Zone | Parameter | Frequency | Trend |
|-------|-------|--------------|-----------|--------|
| | | dur (day) | 0.6000 | 0.0002 |
| | | dur (night) | 0.5800 | 0.0003 |
| | | nchw (day) | 0.1700 | 0.0003 |
| | | nchw (night) | 0.1900 | 0.0003 |
| | Sudan | dur (day) | 0.4400 | 0.0005 |
| | | dur (night) | 0.5100 | 0.0004 |
| | | nchw (day) | 0.1900 | 0.0006 |
| | | nchw (night) | 0.1500 | 0.0006 |
| | Sahel | dur (day) | 0.4500 | 0.0008 |
| | | dur (night) | 0.5000 | 0.0008 |

Development of heatwaves in West Africa and the contribution of temperature tendencies (Table B2).

Table B2: Mean Contribution of the temperature tendencies in the selected case studies (2018, 2019 and 2020) for each climate zone. Here are presented only the top 3 contributors irrespective of the model pressure levels

| Year | Zone | Level | Minimum | Mean | Maximum | Parameter |
|------|--------|-------|---------|-------|---------|-----------|
| | | 91 | 23.08 | 43.47 | 90.26 | ttendt |
| | Guinea | 91 | 23.43 | 55.7 | 89.36 | ttendr |
| | | 80 | 32.04 | 48.57 | 81.74 | ttendd |
| | | 91 | 32.9 | 62.02 | 81.43 | ttendr |
| 2018 | Sudan | 80 | 34.52 | 52.85 | 77.85 | ttendd |
| | | 77 | 35.7 | 49.88 | 73.5 | ttendd |
| | | 91 | 32.9 | 61.57 | 80.53 | ttendr |
| | Sahel | 91 | 25.93 | 39.79 | 70.46 | ttendt |
| | | 91 | 15.49 | 30.73 | 67.68 | ttendd |
| 2019 | | 91 | 22.14 | 43.58 | 87.79 | ttendr |
| | Guinea | 91 | 17.36 | 50.14 | 87.07 | ttendt |
| | | 91 | 11.08 | 24.89 | 78.13 | ttendd |
| | Sudan | 91 | 26.81 | 50.09 | 80.96 | ttendt |

| Year | Zone | Level | Minimum | Mean | Maximum | Parameter |
|-------------|-------------|--------------|----------------|-------------|----------------|------------------|
| 2020 | Sahel | 91 | 21.26 | 47 | 69.8 | ttendr |
| | | 80 | 28.95 | 46.77 | 66.51 | ttendr |
| | | 91 | 32.82 | 48.28 | 74.65 | ttendt |
| | | 91 | 14.58 | 30.82 | 68.49 | ttendd |
| | | 80 | 27.5 | 46.01 | 66.23 | ttendr |
| | | 91 | 17.69 | 51.8 | 91.33 | ttendt |
| | Guinea | 91 | 19.24 | 41.76 | 79.89 | ttendr |
| | | 80 | 34.44 | 52.29 | 76.12 | ttendd |
| | | 91 | 24.43 | 53.6 | 85.25 | ttendt |
| | Sudan | 91 | 7.67 | 27.96 | 80.42 | ttendd |
| | | 91 | 18.57 | 44.9 | 78.08 | ttendr |
| | | 80 | 34.31 | 47.96 | 73.67 | ttendd |
| Sahel | 91 | 28.73 | 46.69 | 73.19 | ttendr | |
| | 91 | 13.54 | 29.5 | 70.95 | ttendd | |

Plots showing the development of heatwaves in West Africa (selected heatwaves cases).

Net_Total T-tendency 925 hPa on March 2018 Heatwave (Day)

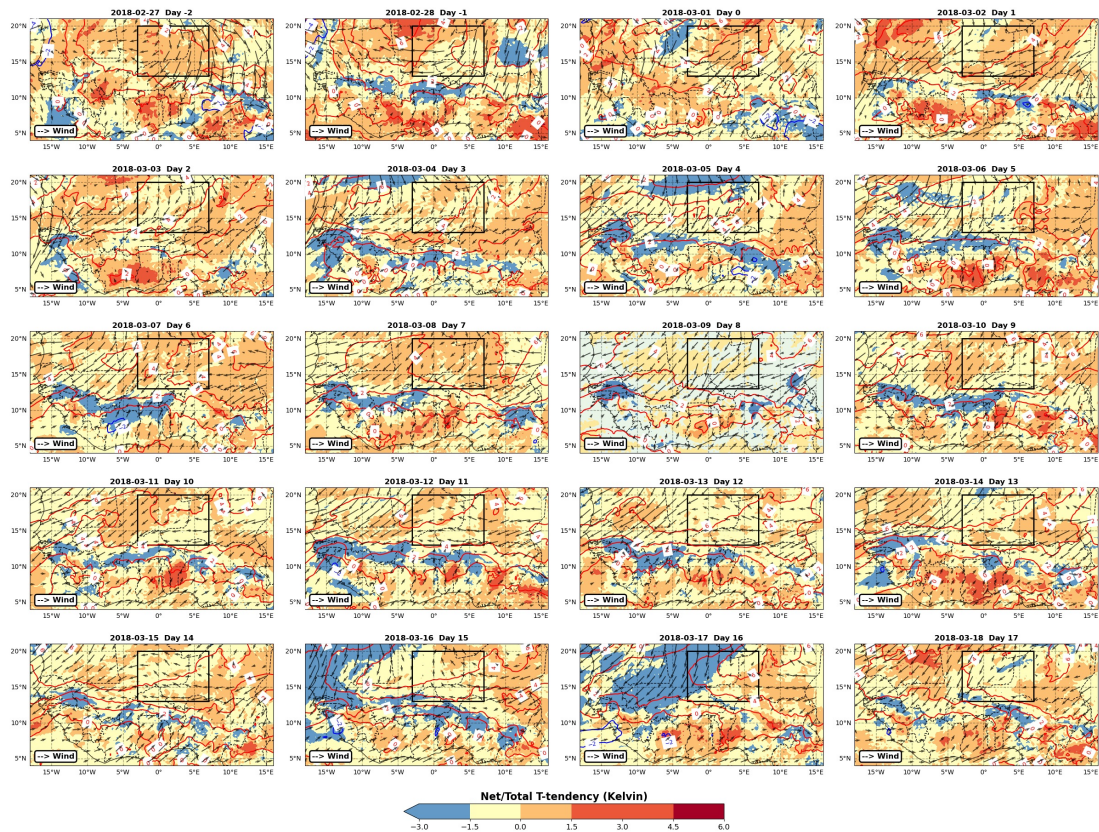


Figure B.11: Net total daytime temperature tendency at 925 hPa in the 2018 (January-March) heatwave case study. Appended are the temperature anomaly in contours (blue and red) and the wind direction (vector). The black box shows the case study

Net_Total T-tendency 925 hPa on March 2018 Heatwave (Night)

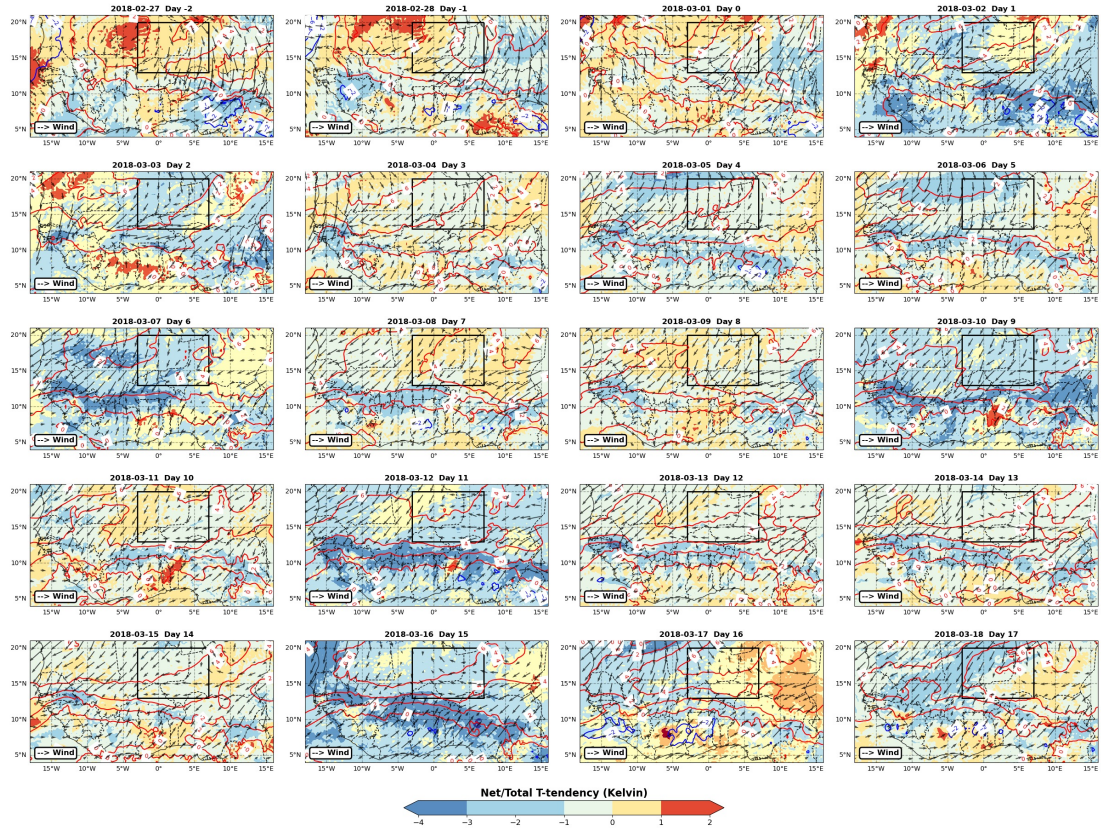


Figure B.12: Net total night-time temperature tendency at 925 hPa in the 2018 (January-March) heatwave case study. Appended are the temperature anomaly in contours (blue and red) and the wind direction (vector). The black box shows the case study

Net_Total T-tendency 925 hPa on November 2019 Heatwave (Day)

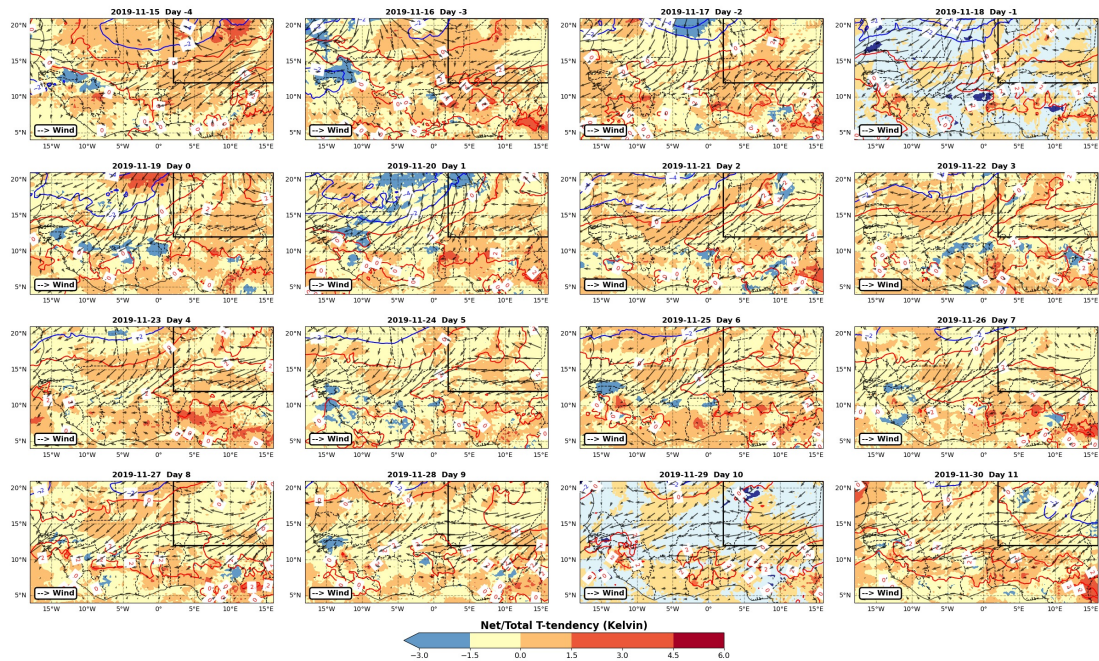


Figure B.13: Net total daytime temperature tendency at 925 hPa in the 2019 (November) heatwave case study. Appended are the temperature anomaly in contours (blue and red) and the wind direction (vector). The black box shows the case study

Net_Total T-tendency 925 hPa on November 2019 Heatwave (Night)

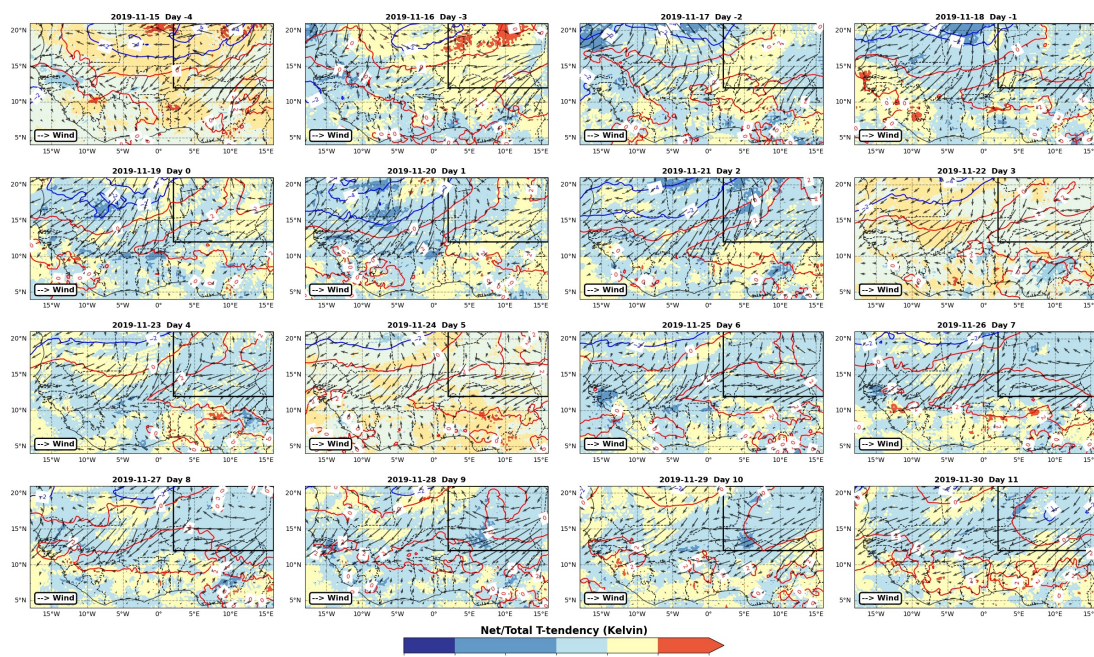


Figure B.14: Net total night-time temperature tendency at 925 hPa in the 2019 (November) heatwave case study. Appended are the temperature anomaly in contours (blue and red) and the wind direction (vector). The black box shows the case study

Net_Total T-tendency 925 hPa on Jan.-Feb 2020 Heatwave (Day)

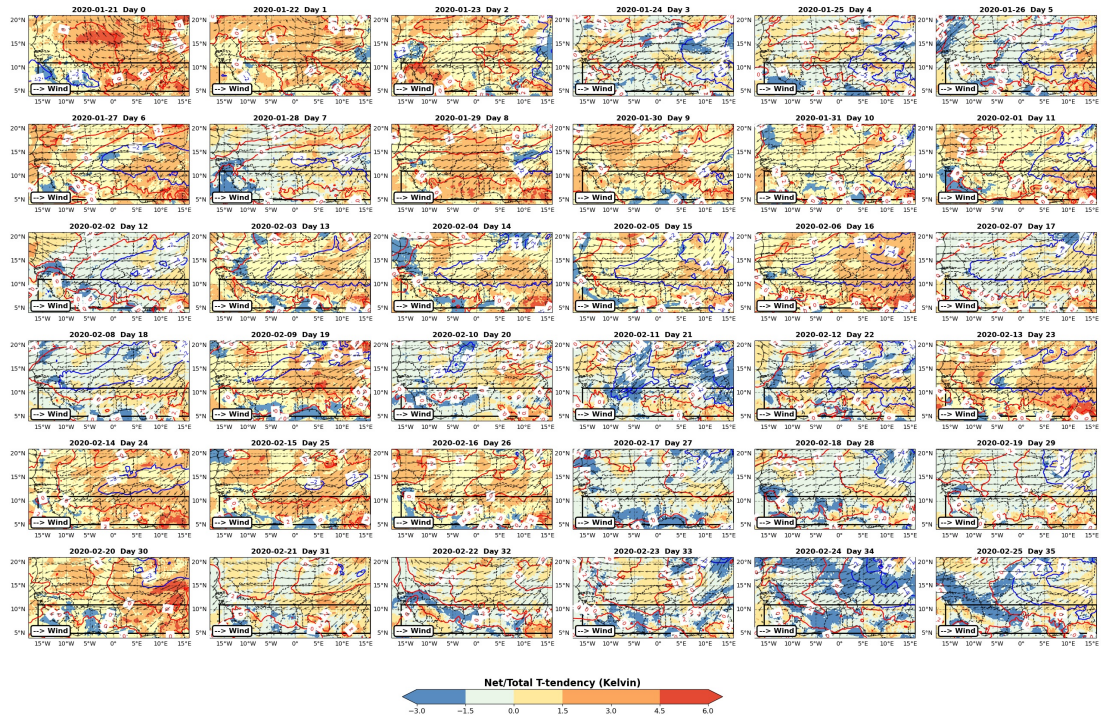


Figure B.15: Net total daytime temperature tendency at 925 hPa in the 2020 (January-March) heatwave case study. Appended are the temperature anomaly in contours (blue and red) and the wind direction (vector). The black box shows the case study

Net_Total T-tendency 925 hPa on Jan.-Feb 2020 Heatwave (Night)

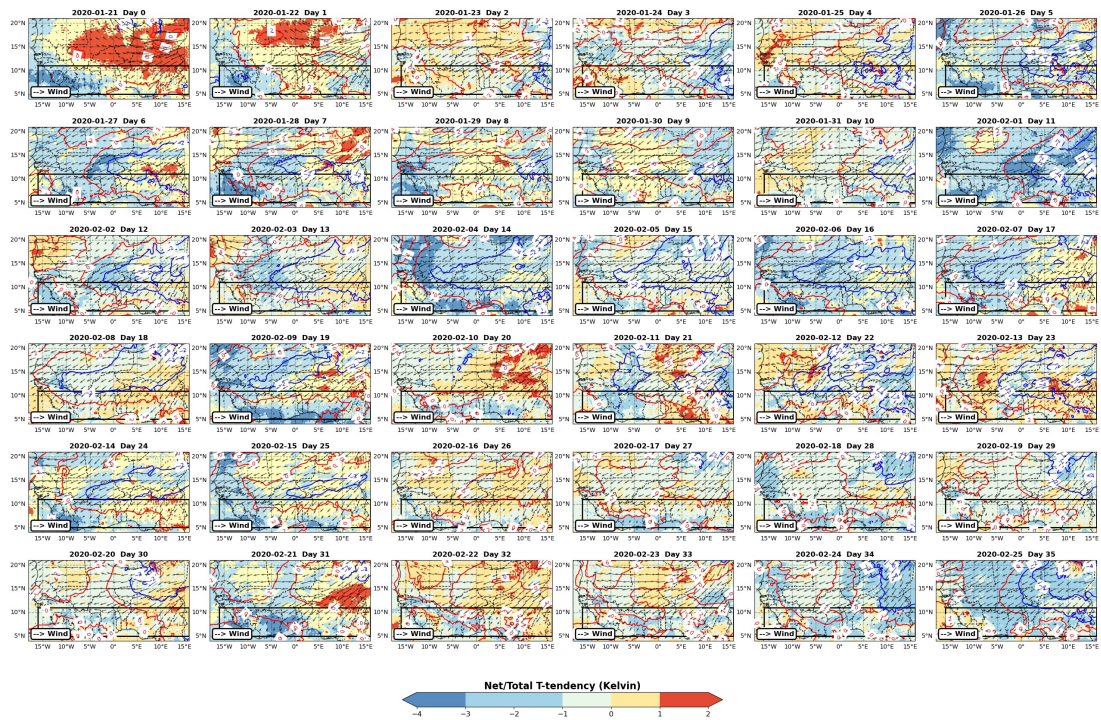


Figure B.16: Net total night-time temperature tendency at 925 hPa in the 2020 (January-March) heatwave case study. Appended are the temperature anomaly in contours (blue and red) and the wind direction (vector). The black box shows the case study

APPENDIX C

The appendix provides supplementary information and data that support the analysis and conclusions presented in the objective 3.

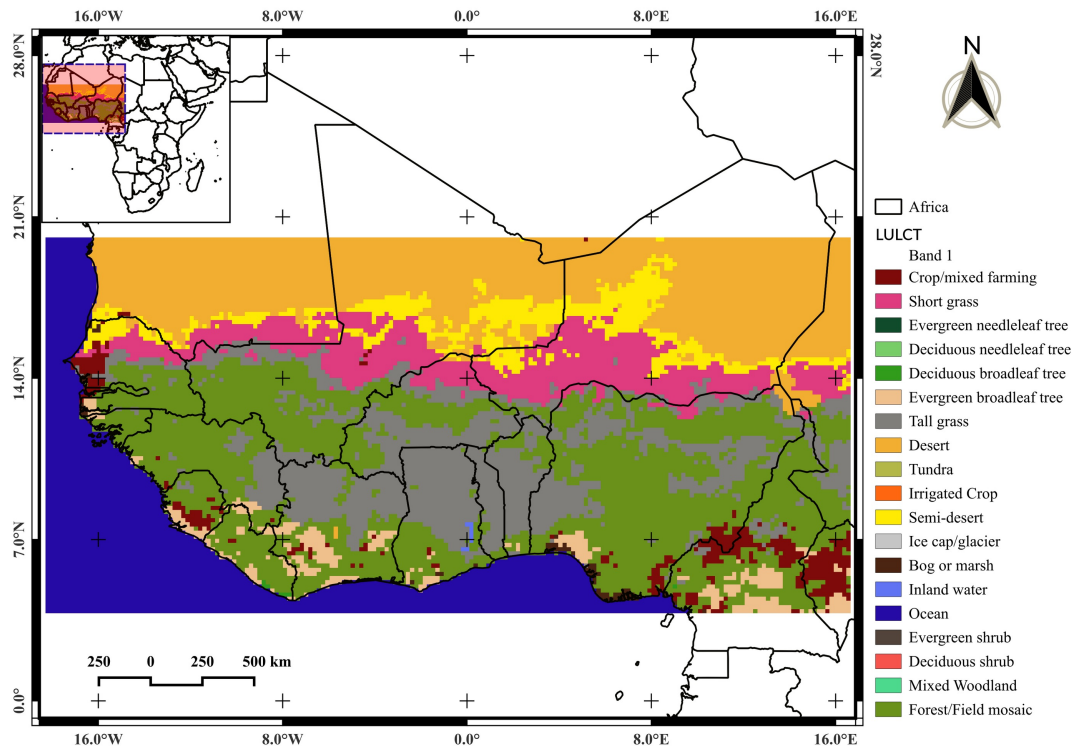


Figure C.17: Geographical Distribution of Vegetation Types and Land Use types in West Africa for Biosphere-Atmosphere Transfer Scheme (BATS) control

This BATS map was associated to the CLM4.5 surface's Urban, PFTs and LULC types configuration to better capture the West African domain complexity.

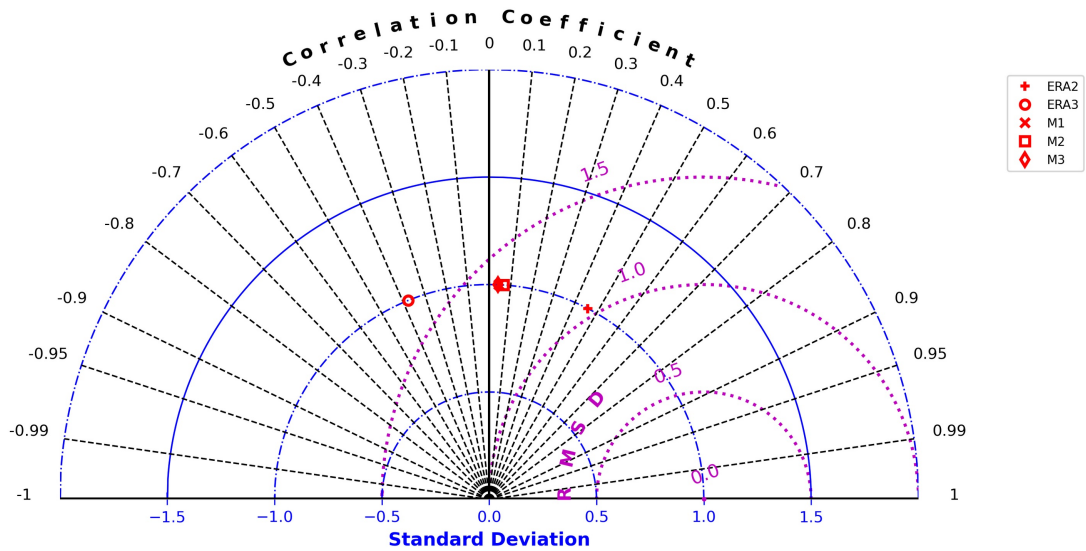


Figure C.18: Taylor Diagram of the 2018-2020 relative differences of Daytime Heatwaves indices. ERA5 HeatCum-UTCI is used as the reference dataset compared to the other ERA5 HeatCum-WBGT (represented as ERA2) and UTCI-WBGT (represented as ERA3) and the indices computed from the RegCM-CML model, HeatCum-UTCI (M1), HeatCum-WBGT (M2) and UTCI-WBGT (M3). The correlation coefficient, the standard deviation, and the root mean square difference between the two datasets are displayed.

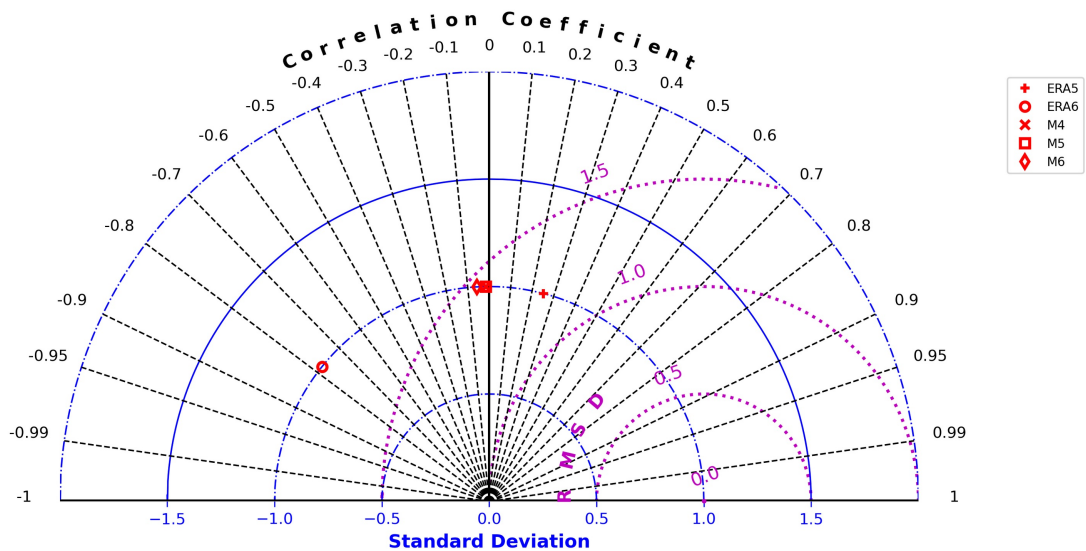


Figure C.19: Taylor Diagram of the 2018-2020 relative differences of night-time Heatwaves indices. Read as in Figure C.18

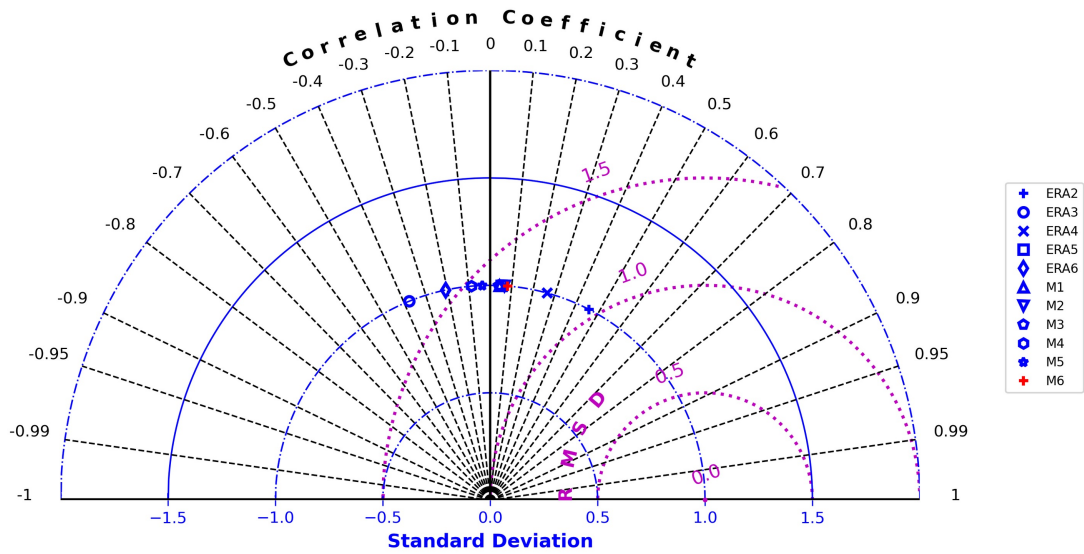


Figure C.20: Taylor Diagram of the 2018-2020 relative differences of Daytime (night-time) Heatwaves indices. ERA and M are the datasets sources (ERA5 and Model output). Numbers that follow them are 1-3 (daytime) and 4-6 (night-time). So HeatCum-UTCI is used as the reference dataset compared to other datasets. The correlation coefficient, the standard deviation, and the root mean square difference between the two datasets are displayed. The ERA4, ERA5 and ERA6 are respectively.

These Taylor diagram plots are from relative differences (-1 to 1) and then normalised before computing the common statistics. The datasets that are being compared, are relative differences, meaning they are deviations from a reference dataset or observations (Which are heatwaves derived from ERA5 dataset). The fact that some values are observed on negative standard deviation -1 and some following the same line to positive standard deviation 1 indicates that some of the datasets are overestimating (ERA2, ERA4 and M6) while others are underestimating (i.e., ERA6 and M4) the reference data or observations. This suggests that there are variations in the occurrence of heatwaves depending on the index and the dataset. The range of RMSD values between 1 and 2 suggests that there are moderates to large differences between the datasets and the reference data or observations. This may indicate that

the datasets are not accurately following the underlying patterns and trends in the HeatCum-UTCI (from ERA5-Land dataset) differences used as baseline. The correlation coefficients between -0.4 to 0.5 suggest that there is a weak to moderate relationship between the datasets and the reference data or observations. Overall, the Taylor diagram suggests that there are differences in the indices and also in the datasets, and the later needs to be addressed in order to improve the RegCM-CLM performance relative to the ERA5-Land data or observations. Further investigation into the sources of these biases and errors may be necessary in order to improve the accuracy and reliability.